EXPLORING GAMMA-RAY BINARIES AT VERY HIGH ENERGIES: VERITAS OBSERVATIONS AND THE DETECTION OF PSR J2032+4127/MT91 213

by

Tyler J. Williamson

A dissertation submitted to the Faculty of the University of Delaware in partial fulfillment of the requirements for the degree of Doctor of Philosophy in Physics

Fall 2024

EXPLORING GAMMA-RAY BINARIES AT VERY HIGH ENERGIES: VERITAS OBSERVATIONS AND THE DETECTION OF PSR J2032+4127/MT91 213

by

Tyler J. Williamson

Approved: _____

Edmund R. Nowak, Ph.D.
Chair of the Department of Physics and Astronomy

Approved: _____

Debra H. Norris
Interim Dean of the College of Arts and Sciences

Approved: _____

Louis F. Rossi, Ph.D.
Vice Provost for Graduate and Professional Education and
Dean of the Graduate College

I certify that I have read this dissertation and that in my opinion it meets the academic and professional standard required by the University as a dissertation for the degree of Doctor of Philosophy.

Signed: _____

Jamie Holder, Ph.D.
Professor in charge of dissertation

I certify that I have read this dissertation and that in my opinion it meets the academic and professional standard required by the University as a dissertation for the degree of Doctor of Philosophy.

Signed: _____

Reshmi Mukherjee, Ph.D.
Member of dissertation committee

I certify that I have read this dissertation and that in my opinion it meets the academic and professional standard required by the University as a dissertation for the degree of Doctor of Philosophy.

Signed: _____

John Clem, Ph.D.
Member of dissertation committee

I certify that I have read this dissertation and that in my opinion it meets the academic and professional standard required by the University as a dissertation for the degree of Doctor of Philosophy.

Signed: _____

James MacDonald, Ph.D.
Member of dissertation committee

ACKNOWLEDGEMENTS

Enough gratitude cannot be given to Jamie Holder, my advisor. Without his guidance, encouragement, and supreme patience this dissertation and the work described therein would not have been possible. Thanks are also due to my committee members: Reshmi Mukherjee, John Clem, and James MacDonald.

I owe a great deal to the members of the VERITAS collaboration, all of whom contributed to this work either directly or indirectly. Though the members of VERITAS are too numerous to enumerate here, I would like to specifically thank Ralph Bird, Michael Daniel, Gareth Hughes, Sajan Kumar, and Greg Richards.

Many thanks are due also to John Millis, who fostered my interest in physics and research during my time as an undergraduate.

I extend thanks to my colleagues and supervisors at Anderson University, whose support and patience was welcome while I endeavored to finish my dissertation while teaching.

Finally, many thanks are owed to my family, who never failed to support and encourage me.

There is a high probability that deserving people were unjustly omitted from this list. Please accept my apologies and know that your contribution was valued even if the author's ignorance left it unnoticed in this document.

DEDICATION

To my family: my parents, Rhonda and Greg, my sister Lauren, my brother Connor, and my sister-in-law Cheyenne.

And to my grandfather, Carl Eugene Graber. June 4, 1937- December 19, 2022.

TABLE OF CONTENTS

LIST OF TABLES

LIST OF FIGURES

ABSTRACT

Gamma-ray binaries consist of a compact object orbiting with a massive star. The violent interactions within these systems, due either to the collision of the pulsar/stellar winds or the relativistic jets of a black hole, are capable of accelerating charged particles to TeV energies. Due to the orbital motion of the binary system, this acceleration occurs in a constantly-evolving environment. Gamma-ray binaries therefore act as "natural laboratories" for the study of non-thermal acceleration and radiation mechanisms, as well as a means to study the physics of compact objects.

This dissertation is concerned primarily with the discovery of a new gamma-ray binary system: PSR J2032+4127/MT91 213. At the time of its discovery, this was only the second gamma-ray binary system with a firmly identified compact object, and just the seventh gamma-ray binary known. This system's unique 50-year orbital period sets it apart from other gamma-ray binary systems and underscores the significance of the 100-hour observing campaign to cover the periastron passage in the autumn of 2017 by VERITAS, MAGIC, and *Swift*-XRT. As a result of these observations, detailed light curves and spectra were constructed which exhibit complex variability. This variability maps the continually-changing environment at the interface of the pulsar and stellar winds, allowing for examination of the underlying physical processes.

The analysis of gamma-ray emission from PSR J2032+4127/MT91 213 was complicated by the fact that the binary system lies in the same area of the sky as another gamma-ray source: TeV J2032+4130. This fact motivated the development of a more sophisticated data analysis method, based on the method of maximum-likelihood estimation, which is capable of simultaneously detecting and characterizing the emission of two or more sources in the same field of view. This analysis was tested on several known sources and shown to be consistent with standard analysis methods.

Its ability to distinguish between multiple sources in the same field was demonstrated in a re-analysis of the PSR J2032+4127/MT91 213 + TeV J2032+4130 system. Finally, the method was used to search for "hidden" sources in the vicinity of other gamma-ray binary systems, yielding negative results but providing insight into the nature of the wind interaction in these systems.

The results presented in this dissertation are based on extensive observations carried out by VERITAS: the Very Energetic Radiation Imaging Telescope Array System. VERITAS, which comprises an array of four Imaging Atmospheric Cherenkov Telescopes (IACTs), is uniquely suited for detecting gamma-ray emission in the GeV-TeV range, providing the high sensitivity and precision needed to track the complex variability in PSR J2032+4127/MT91 213's periastron passage. The physical instrumentation of VERITAS and the standard VERITAS software/data analysis tools, both discussed in detail in this work, were critical in obtaining the results here presented.

Chapter 1

ASTROPHYSICS AT VERY HIGH ENERGIES

The very high-energy (VHE, E > 100 GeV) regime of the Universe, unexplored until the past few decades, contains a rich treasure-trove of information for high-energy physicists. Light emitted at such energies is not due to thermal radiation and thus offers a unique window into the "non-thermal universe". In particular, VHE radiation is often associated with the acceleration of particles in extreme physical environments unattainable to any Earth-bound laboratory. The study of VHE radiation therefore extends the study of particle acceleration and interaction at extreme energies. Because of the association of this radiation with particle acceleration, it also functions as a natural way to examine the production of energetic cosmic rays, which appear to be ubiquitous in the galaxy.

1.1 Cosmic Rays

The particles now known as "cosmic rays" were first discovered by Victor Hess in 1912 during a high-altitude balloon flight [35]. The term now refers to the near isotropic stream of energetic particles which enter Earth's atmosphere at the rate of approximately 1000 particles $m^{-2}s^{-1}$. They consist mostly of ionized nuclei: 90% protons, 9% helium, and 1% heavier nuclei and electrons [36]. The energy spectrum (shown in Figure 1.1) spans more than 10 decades in energy and exhibits a general power-law shape (flux $\propto (E/E_0)^{\gamma}$) with an average spectral index γ close to -3. Cosmic rays are very nearly isotropic due to diffusion in the Galactic magnetic field, though small anisotropies have been reported [37].

Because cosmic rays consist of charged particles which are repeatedly deflected as they traverse the Galaxy, the arrival direction of an observed cosmic ray at Earth is

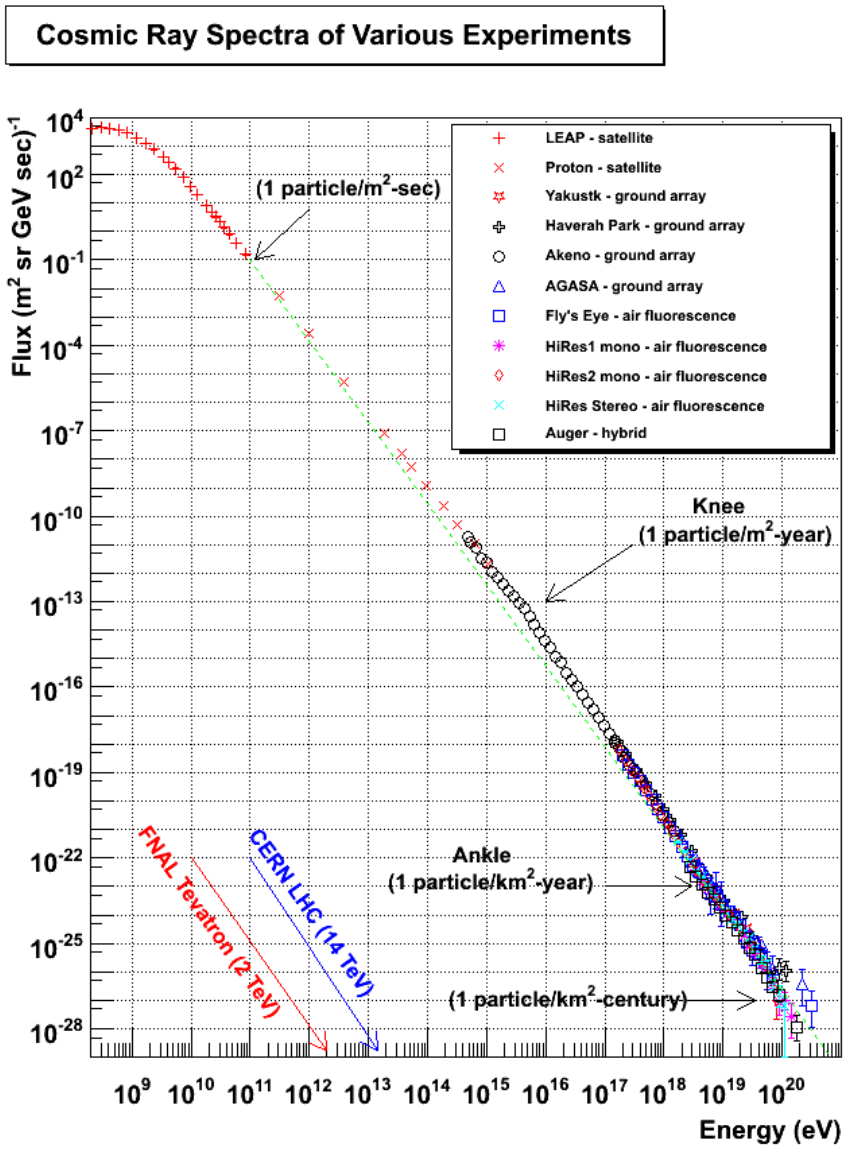

Figure 1.1: The cosmic ray spectrum produced by combining data from various experiments. Image available at https://web.physics.utah.edu/ whanlon/spectrum.html

not indicative of its ultimate source. Cosmic rays do not "point back" to their point of origin. This complicates the question of where the particles originate (where are they accelerated to such high energies?). While the ultimate origin of these cosmic rays remains a mystery, much can be said with confidence. Firstly, the bulk of cosmic rays very likely originate within our own Galaxy. The considerable energy density of cosmic rays observed on Earth makes the prospect of a universal sea of cosmic rays throughout space an unlikely prospect [38]. Moreover, while cosmic rays themselves cannot be traced back to their source, observations of energetic radiation can be used to indirectly map the distribution of cosmic rays. This is because a portion of the accelerated particles will radiate away some of their energy as they interact with the local magnetic field and interstellar medium at the acceleration site. Details of particle acceleration and radiation mechanisms will be discussed later, in Section 1.2. The point is that, while cosmic rays themselves do not point back to their acceleration site, they should generate non-thermal radiation (mostly gamma rays) from the acceleration site. Since electromagnetic radiation is not deflected in the Galactic magnetic fields, this radiation can effectively be used to trace cosmic ray acceleration sites in the Galaxy. Measurements of diffuse gamma-ray emission from instruments such as *Fermi*-LAT indicate that the majority of cosmic rays observed from Earth are accelerated within our Galaxy, rather than diffusing in from outside [39]. Further evidence for a Galactic origin of cosmic rays comes from observations of gamma-ray emission in the Magellanic clouds, which indicate lower levels of cosmic rays in those galaxies than in our own [40, 41]. This contradicts the notion of a largely universal sea of cosmic rays, which would pervade nearby galaxies at nearly equal levels.

While there is firm evidence that most cosmic rays are of galactic origin, there is good reason to believe that at least some of them, particularly those at the highest energies, are of extragalactic origin. The most straightforward argument to this end is that at the highest energies, galaxies should not be able to confine the cosmic rays accelerated within them. Assuming an average galactic magnetic field of $\sim 3\mu$G, the Larmor radius of a proton exceeds 1 kpc for energies greater than $\sim 3 \times 10^{18}$ eV. The

bulk of cosmic rays in this energy range should therefore be of extragalactic origin. The resulting spectrum of cosmic rays observed from Earth should be dominated by particles accelerated within the galaxy up to energies approaching $\sim 10^{18}$ eV, at which point a transition from galactic to extragalactic sources should be observed. The observed spectra of cosmic rays provide evidence for this scenario. While the overall spectrum can be approximated as a simple power law with an index of ≈ -3, closer inspection reveals detailed features in the spectrum. In particular, the power-law index is apparently variable with energy. The all-particle spectrum is observed to steepen from an index of ≈ -2.7 to a new index of ≈ -3.1 beginning at about $\approx 3 \times 10^{15}$ eV [42, 43]. This feature is followed by a flattening back to an index of ≈ -2.7 beginning near 10^{18} eV[44]. These two features have come to be known as the "knee" and the "ankle" in the cosmic-ray spectrum: the former referring to the steepening of the spectrum near 10^{15} eV, the latter referring to the hardening at 10^{18} eV[1]. Taken together, the knee and the ankle are generally thought to support the notion of a transition from galactic to extragalactic origins for cosmic rays. The ankle is most easily interpreted as the energy at which extragalactic sources become dominant of galactic ones, which explains its appearance near the same energy that cosmic-ray escape from the Galaxy becomes significant.

The knee is generally thought to indicate the joint effect of galactic acceleration mechanisms nearing their maximum energy, together with increased "leakage" of particles escaping the Galaxy at higher energies [45]. The specific acceleration sites within the Galaxy have long been suspected to be supernovae. This idea was first suggested by Baade and Zwicky in 1934 [46] and remains prominent for two reasons: 1) supernovae explosions in the Galaxy provide more than enough energy to power the observed cosmic-ray luminosity and 2) the acceleration mechanism at supernovae sites can be shown to reproduce a power-law distribution in energy, in accordance with

[1] These features are not easy to discern from Figure 1.1, but are more easily identified when multiplying the flux by a factor of E^3 to identify deviations from flatness.

observations. Energetically, the luminosity of cosmic rays in the galaxy has been estimated to be about $\approx 7 \times 10^{40}$ erg s^{-1}[47]. Supernovae typically release $\approx 10^{51}$ erg per explosion [48], and occur in the Galaxy at a rate of ≈ 25 per kyr [49], giving an average power output of $\approx 8 \times 10^{41}$ erg s^{-1}. Thus only 10% of the observed supernova energy output is required to explain the luminosity of cosmic rays. The specific mechanism for acceleration will be discussed in a later section, but it can be shown that the most likely acceleration mechanism for charged particles in the vicinity of supernovae is one that produces a power-law distribution in energy, further strengthening the case for supernovae as the dominant source of galactic cosmic rays.

The acceleration site of extragalactic cosmic rays remains a topic of discussion, but is likely associated with active galactic nuclei [50, 51].

While general classes of astrophysical objects have been hypothesized as sites of cosmic-ray acceleration, the proverbial "smoking gun" remains to be found. Since the arrival direction of cosmic rays does not point back to the acceleration site, indirect methods are necessary. Wherever these particles are initially accelerated, they should radiate away some of their energy as they interact with the local magnetic fields and interstellar medium. This radiation is unperturbed by the Galactic magnetic field and thus travels directly from the source. Studies of non-thermal radiation from potential acceleration sites are therefore a fruitful way to search for the origin of cosmic rays.

1.2 Particle Acceleration

Second Order Fermi Acceleration

At the heart of the search for the origin of cosmic rays is the question of how and where they are accelerated to such high energies. The relevant mechanisms are electromagnetic in nature. Of these, two broad categories can be recognized: direct acceleration by a large scale electric field, or stochastic acceleration characterized by small energy gains over long time intervals from small scale fields. In practice, the high conductivity associated with the ionized plasma in many astrophysical environments effectively rules out the prolonged presence of a large electric field, and therefore

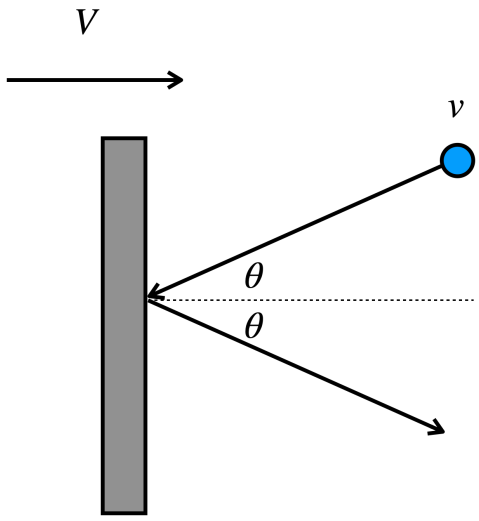

Figure 1.2: A sketch showing a single idealized collision between a particle and a massive interstellar cloud.

stochastic acceleration mechanisms are favored in most phenomenological explanations. The stochastic acceleration approach was first developed by Fermi in 1949 [52]. Fermi showed that random interactions with regions of moving magnetic field will, on average, cause charged particles to gain energy according to a power-law distribution. Here we summarize a derivation of this result, following Longair [53].

Let us consider the collision between a charged particle of mass m with a magnetized interstellar cloud whose mass can be considered infinite in comparison. In the rest frame of the galaxy, the cloud velocity is $\vec{V}$ and the particle velocity is $\vec{v}$. The collision is depicted in Figure 1.2. Let the unprimed frame $\mathcal{S}$ correspond to the galactic rest frame, and the primed frame $\mathcal{S}'$ correspond to the center of mass frame of the cloud and particle, which approximately moves with the cloud's velocity $\vec{V}$.

In the primed frame, the particle's energy and momentum are described by:

$$\begin{aligned} E' &= \gamma_V \left(E + pV\cos\theta\right) \\ p'_x &= -\gamma_V \left(p\cos\theta + \frac{V}{c^2}E\right) \end{aligned} \tag{1.1}$$

During the collision, the particle's energy is unchanged and the x-component of its momentum is reversed:

$$\begin{aligned} E' &= \gamma_V \left(E + pV\cos\theta\right) \\ p'_x &= \gamma_V \left(p\cos\theta + \frac{V}{c^2}E\right) \end{aligned} \tag{1.2}$$

Transforming back into the unprimed frame via a second Lorentz transformation:

$$\begin{aligned} E'' &= \gamma_V^2 \left[E + E\left(\frac{V}{c}\right)^2 + 2Vp\cos\theta\right] \\ &= \gamma_V^2 E \left[1 + \left(\frac{V}{c}\right)^2 + \frac{2Vv\cos\theta}{c^2}\right] \end{aligned} \tag{1.3}$$

Therefore:

$$\Delta E = E'' - E = \gamma_V^2 E \left[\left(\frac{V}{c}\right)^2 + \frac{2Vv\cos\theta}{c^2}\right] + E(\gamma_V^2 - 1)$$

Since it is likely that $V << c$, $\gamma_V^2 \approx 1 + \left(\frac{V}{c}\right)^2$ and

$$\Delta E \approx \gamma_V^2 E \left[2\left(\frac{V}{c}\right)^2 + \frac{2Vv\cos\theta}{c^2}\right] \tag{1.4}$$

Thus in any single collision the particle may either gain or lose energy, depending on the collision angle θ. A "head-on" collision will increase the particle's energy while a "tail-on" collision will decrease it. The average change in energy per collision therefore depends upon the average angle of incidence. This is not isotropic: head-on collisions will tend to happen more frequently due to the greater relative velocity of those clouds in the particle's frame of reference. The probability of a collision at an angle θ should be proportional to the relative velocity of the cloud:

$$P(\theta) \propto \frac{V\cos\theta + v}{1 + \frac{Vv\cos\theta}{c^2}}$$

In the relativistic limit $v \to c$:

$$P(\theta) \propto 1 + \frac{V}{c}\cos\theta$$

The average change in energy is found by integrating Equation 1.4 with the above (normalized) probability distribution for θ over all values of θ:

$$\left\langle \frac{\Delta E}{E} \right\rangle = \frac{8}{3} \left(\frac{V}{c} \right)^2 \tag{1.5}$$

This result indicates that particles colliding randomly with magnetized clouds will, on average, gain energy in proportion to the square of the cloud's velocity. For this reason, this mechanism is known as "second order Fermi acceleration".

Spectrum

If the mean separation distance between clouds is L, then the average time elapsed in between collisions will be approximately L/c. The average rate of energy increase will then be:

$$\frac{dE}{dt} \approx \frac{\Delta E}{L/c} = \frac{8}{3} \frac{V^2}{Lc} E = \alpha E$$

The number of particles per unit volume N with an energy of E)(the particle spectrum produced by this acceleration) obeys the diffusion-loss equation [53]:

$$\frac{dN}{dt} = D\nabla^2 N + \frac{\partial}{\partial E}\left[b(E)N\right] - \frac{N}{\tau_{\rm esc}} + Q(E)$$

Where $b(E)$ is the energy loss rate of the particles, $\tau_{\rm esc}$ is the characteristic time the particle remains within the acceleration region, D is a diffusion coefficient, and $Q(E)$ is the rate at which new particles are injected into the volume. In the steady state, and in the absence of diffusion, $\frac{dN}{dt} = \nabla^2 N = 0$. If we further neglect particle injection ($Q(E) = 0$), then the diffusion-loss equation simplifies (with $b(E) = -\alpha E$) to:

$$-\frac{d}{dE}\left[\alpha E N\right] - \frac{N}{\tau_{\rm esc}} = 0$$

Which has as a solution:

$$N(E) \propto E^{-x} \tag{1.6}$$

Where $x = 1 + \frac{1}{\alpha \tau_{\text{esc}}}$. In the context of cosmic-ray physics, Equation 1.6 is the most important feature of second-order Fermi acceleration, since it predicts a power-law distribution in energy in accordance with the cosmic-ray spectrum observed from Earth.

While this second-order acceleration mechanism successfully explains the power-law shape of the cosmic-ray energy spectrum, it has several shortcomings. The fact that the energy gain per collision is proportional to $(V/c)^2$ makes this a quite inefficient method of accelerating particles to very high energies, given that the typical speeds of interstellar clouds are $V/c \leq 10^{-4}$[53]. Additionally, the theory fails to explain why the observed power-law index should be close to 2.5.

First Order Fermi Acceleration

Decades after Fermi's work, several authors proposed a more efficient mechanism utilizing the same principles of Fermi's original idea [54, 55, 56, 57]. In what has come to be known as "diffusive shock acceleration" or "first-order Fermi acceleration", charged particles repeatedly crossing an astrophysical shock front will consistently experience head-on interactions, resulting in much more efficient acceleration. Furthermore, it can be shown that this process predicts a power-law distribution with an index close to the observed value.

Astrophysical shocks are ubiquitous in the Universe, and are very likely present in supernova remnants and the jets of active galactic nuclei. Such shocks are created when fast-moving outflows are forced into another environment (such as the interstellar medium) at speeds greater than the local speed of sound. The gas in the environment is unable to equilibrate and is generally divided into a "shocked" and an "unshocked" region. The barrier dividing the two regions is the shock front, which propagates forward into the unshocked gas.

Let us consider such a shock front which propagates to the right (the x direction) at a speed U relative to the interstellar medium (Figure 1.3a). Ahead ("upstream") of the shock front, the gas is unshocked and has no bulk speed. The shock front itself acts as a discontinuity between the unshocked gas in the upstream region and the shocked

gas in the "downstream" region. In the rest frame of the shock front, we denote the density, pressure, temperature, and speed of the unshocked gas as ρ_1, P_1, T_1, and v_1. By definition, $v_1 = U$. Gas in the downstream region has density, pressure, temperature, and speed of ρ_2, P_2, T_2, and v_2. While discontinuous, the properties of the shocked and unshocked gas are necessarily related via conservation of mass, energy, and momentum across the shock front ([53]):

$$\begin{aligned} \rho_1 v_1 &= \rho_2 v_2 \\ \rho_1 v_1 \left(\frac{1}{2}v_1^2 + \frac{\Gamma}{\Gamma-1}\frac{P_1}{\rho_1}\right) &= \rho_2 v_2 \left(\frac{1}{2}v_2^2 + \frac{\Gamma}{\Gamma-1}\frac{P_2}{\rho_2}\right) \\ P_1 + \rho_1 v_1^2 &= P_2 + \rho_2 v_2^2 \end{aligned} \tag{1.7}$$

Where the gas is treated as an ideal gas with Γ as the ratio of specific heat capacities. We define the Mach number of the shock wave as $M_1 = U/c_1$, with c_1 being the speed of sound of the unshocked gas. For very strong shocks ($M_1 >> 1$) the conditions 1.7 simplify to [53]:

$$\begin{aligned} \frac{P_2}{P_1} &= \frac{2\Gamma M_1^2}{\Gamma+1} \\ \frac{\rho_2}{\rho_1} &= \frac{\Gamma+1}{\Gamma-1} \\ \frac{T_2}{T_1} &= \frac{2\Gamma\left(\Gamma-1\right)M_1^2}{\left(\Gamma+1\right)^2} \end{aligned} \tag{1.8}$$

As unshocked gas passes through the shock front, it is compressed and heated. The first equation from 1.7 can be combined with the second from 1.8 to give:

$$\frac{v_2}{v_1} = \frac{\rho_1}{\rho_2} = \frac{\Gamma-1}{\Gamma+1} \tag{1.9}$$

In the frame of the shock front therefore, gas is slowed as it crosses the shock from upstream to downstream. To see how this results in particle acceleration, let us consider a mono-atomic ideal gas with $\Gamma = 5/3$. The speeds of the unshocked and shocked gases then relate as:

$$v_2 = \frac{1}{4}v_1 \tag{1.10}$$

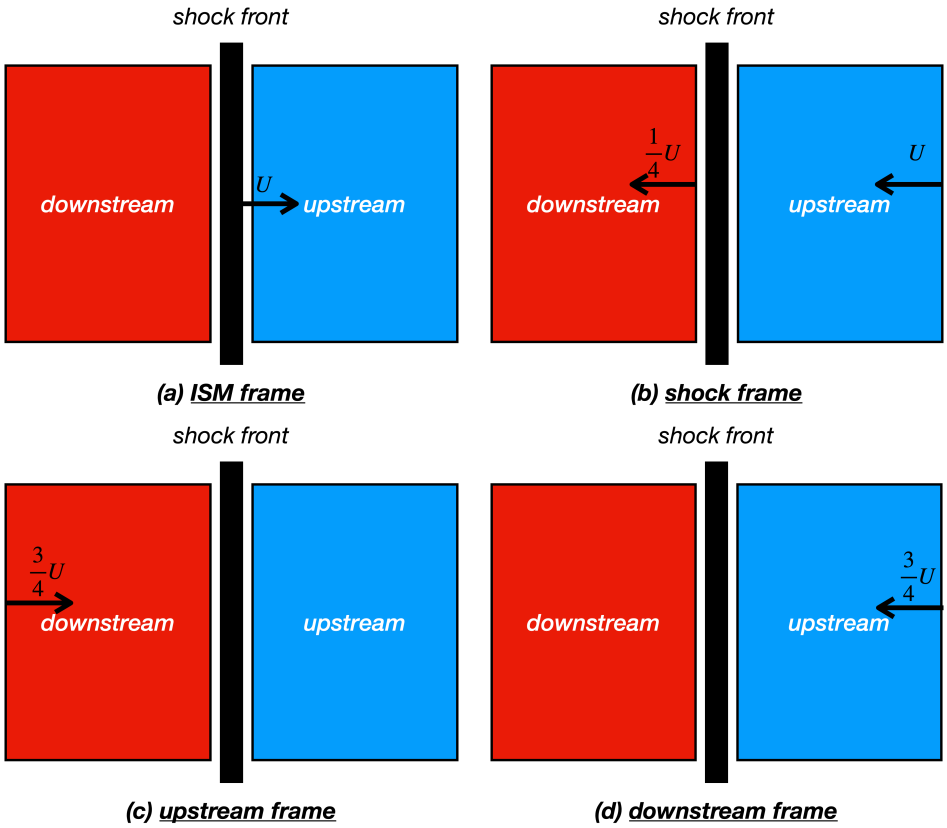

Figure 1.3: The interface between the the shocked and unshocked gases is depicted from different reference frames.

in the frame of the shock front. This is depicted in Figure 1.3b.

We now consider a relativistic particle which is originally upstream of the shock with energy $E = pc$ in the upstream frame. In the frame of the unshocked (upstream) gas, the shock front approaches with a speed of U, followed by the shocked gas (downstream) approaching at a speed of $V = \frac{3}{4}U$ (Figure 1.3c). This is similar to the head-on collision with the magnetic cloud discussed earlier. If the particle is incident upon the shock front with an angle θ_1 to the normal, then its energy in the downstream frame is found via a Lorentz transformation:

$$E' = \gamma_V E \left(1 - \frac{V}{c} \cos\theta_1\right) \tag{1.11}$$

Here, upstream region is the unprimed frame, and the downstream region is the

primed frame. In the downstream region, the unshocked gas approaches with a speed of $\frac{3}{4}U$ (Figure 1.3d). The particle is effectively isotropized by turbulent magnetic fields within the gas and attains an angle of θ_2' to the normal receding shock front (Figure 1.4). The particle's energy remains the same (in the primed frame) while its direction changes. In the unshocked frame, the particle's energy is:

$$E'' = \gamma_V E' \left(1 + \frac{V}{c}\cos\theta_2'\right)$$

If we assume that the shock speed is non-relativistic ($\gamma_V^2 \approx 1 + \frac{V^2}{c^2}$) then:

$$\frac{\Delta E}{E} = \gamma_V^2 \left[\left(\frac{V}{c}\right)^2 + \frac{V}{c}\cos\theta_2' - \frac{V}{c}\cos\theta_1 - \left(\frac{V}{c}\right)^2 \cos\theta_1 \cos\theta_2'\right] \tag{1.12}$$

The average energy gain in such an interaction is found by averaging $\langle\cos\theta_1\rangle$ and $\langle\cos\theta_2'\rangle$. Since the speed of the shock is negligible compared with the speed of the particle, the probability of the particle crossing the shock is proportional to $\cos\theta$. It follows that:

$$\langle\cos\theta\rangle = \frac{\int_{\theta_{\min}}^{\theta_{\max}} \cos^2\theta \sin\theta d\theta}{\int_{\theta_{\min}}^{\theta_{\max}} \cos\theta \sin\theta d\theta} = \frac{\frac{1}{3}\cos^3\theta\Big|_{\theta_{\min}}^{\theta_{\max}}}{\frac{1}{2}\cos^2\theta\Big|_{\theta_{\min}}^{\theta_{\max}}} \tag{1.13}$$

To find $\langle\cos\theta_1\rangle$ we integrate Equation 1.13 over all angles which carry the particle from the upstream region to the downstream: $\theta_{\min} = \pi/2$, $\theta_{\max} = \pi$. This gives:

$$\langle\cos\theta_1\rangle = -\frac{2}{3}$$

Similarly, to cross from downstream back to upstream: $\theta_{\min} = 0$, $\theta_{\max} = \pi/2$, which gives:

$$\langle\cos\theta_2'\rangle = \frac{2}{3}$$

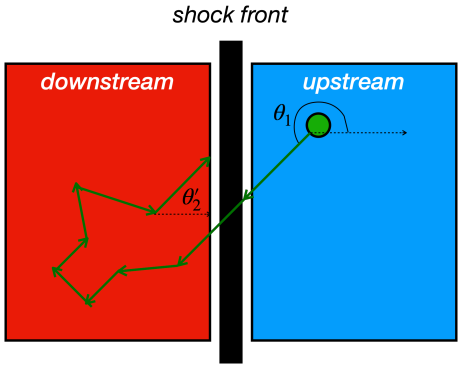

Figure 1.4: The geometry of a charged particle crossing the shock front and being isotropized by the turbulent magnetic field.

Substituting into Equation 1.12 we find, to first order in V/c:

$$\left\langle \frac{\Delta E}{E} \right\rangle = \frac{4}{3}\frac{V}{c}$$

The increase in energy is therefore first order in V/c, hence the name "first order Fermi acceleration".

Spectrum

Particles contained within the shock can repeatedly cross the shock front, gaining energy in each round trip. After a single interaction, the particle's energy is $E = \beta E_0$, where E_0 is the particle's initial energy and $\beta = 1 + \frac{4}{3}\frac{V}{c}$ is the average fractional energy gain of the particle per shock crossing. After each collision there is a finite probability for the particle to escape the acceleration region. Let us define P as the probability of the particle remaining in the acceleration region after each collision. This probability is calculated following Bell [56].

If the size of the acceleration region is not a constraint, particle escape occurs as a result of advection away from the shock front in the downstream region. This is due to the fact that particles in the upstream region will, on average, observe the shock front to be approaching with speed U, while particles in the downstream region observe

the shock front to be receding with speed $\phi_{\rm esc} = 1/4U$. We can therefore estimate the escape probability by comparing the flux of particles entering the downstream region with the flux of particles far downstream of the shock front. The flux of particles through a surface far downstream of the shock will therefore be $\frac{1}{4}nU$, where n is the number density of particles. The flux of particles entering the downstream region across the shock front will be

$$\phi_{\rm enter} = \frac{1}{2}nc\int_{\pi/2}^{\pi}\cos\theta\sin\theta d\theta = \frac{nc}{4}$$

The escape probability can be found by taking the ratio of the two fluxes:

$$P_{\rm esc} = \frac{\phi_{\rm esc}}{\phi_{\rm enter}} = \frac{U}{c}$$

The probability P for the particle to remain in the shock is therefore $P = 1 - P_{\rm esc} = 1 - \frac{U}{c}$, which is energy independent.

If there were initially N_0 particles with identical energy E_0 within the acceleration region, then after k round trips across the shock front, $N = N_0P^k$ particles remain, with average energy $E = \beta^k E_0$. It follows that:

$$\frac{\ln\left(N/N_0\right)}{\ln\left(E/E_0\right)} = \frac{\ln P}{\ln\beta}$$

And therefore:

$$\frac{N}{N_0} = \left(\frac{E}{E_0}\right)^{\ln P/\ln\beta}$$

Which is the integral energy spectrum ($N(\geq E)$). The differential spectrum is then:

$$N(E)dE = \text{constant} \times \left(\frac{E}{E_0}\right)^{\ln P/\ln\beta - 1} dE$$

With $\ln P = \ln\left(1 - \frac{U}{c}\right) \approx -\frac{U}{c}$ and $\ln\beta = \ln\left(1 + \frac{4}{3}\frac{V}{c}\right) \approx \frac{4}{3}\frac{V}{c} = \frac{U}{c}$:

$$N(E)dE = \text{constant} \times \left(\frac{E}{E_0}\right)^{-2} dE \tag{1.14}$$

This acceleration mechanism therefore predicts a specific and unique power-law index regardless of the characteristics of the physical environment, so long as there are

strong shocks present. This is likely to be the case in many astrophysical environments, such as supernova remnants and active galactic nuclei. Because of its relative efficiency (first order in V/c) and because it produces a power-law spectrum with an index close to that which is observed experimentally, first-order Fermi acceleration (diffusive shock acceleration) has prevailed in astrophysical thinking since its development in the 1970s.

Non-linear Effects

The previous derivation assumed that the environment of the shock is not significantly altered by the presence of the energetic cosmic rays accelerated there. In many physical environments, the energy of the accelerated cosmic rays can become comparable to the energy of the surrounding plasma and therefore the cosmic rays can have a significant impact on their acceleration environment. Particle acceleration in such environments is governed by non-linear diffusive shock acceleration (NLDS). In NLDS, particles are still accelerated stochastically by repeatedly crossing the shock front; however the diffusion and scattering of these particles is modified by effects they themselves create. Firstly, the pressure created by accelerating particles can slow down the plasma flowing into the shock from the upstream region. This results in a position-dependent plasma velocity in the upstream region and therefore a position-dependent compression ratio ($v_{\text{upstream}}/v_{\text{downstream}}$), with compression ratio increase with distance upstream of the shock. Assuming that the diffusion length of accelerated particles is energy-dependent, this means that higher-energy particles, which diffuse far into the upstream region, will see a larger compression ratio than lower-energy particles which cannot diffuse as far upstream. The result is curved particle spectrum rather than a simple power-law [36, 58].

Another effect results from the fact that cosmic rays streaming upstream of the shock can create a "streaming instability" which can greatly amplify the magnetic field of the plasma. This was first noticed by Bell [56]. This amplified magnetic field can enhance the scattering efficiency of the plasma, keeping accelerating particles confined

for longer. This broadens the energy spectrum of the accelerated particles and, in particular, increases the maximum energy attained by the accelerated cosmic rays.

1.3 Radiation mechanisms

As charged particles are accelerated, they will lose some of their energy in the form of radiation as they interact with magnetic fields, photon fields, and the physical medium in the acceleration region. Here we summarize the most important radiation mechanisms, restricting our focus to non-thermal radiation.

Synchrotron Radiation

When a charged particle moves with velocity $\vec{v}$ in the vicinity of a magnetic field $\vec{B}$, the Lorentz force will cause the particle to spiral around the magnetic field lines. The radius of this gyration is the Larmor radius:

$$R_L = \frac{p_\perp}{eB} \tag{1.15}$$

And the angular frequency is the Larmor frequency:

$$\omega_L = \frac{eBc}{E} \tag{1.16}$$

While the magnetic field does not work on the particle, the particle will lose energy in the form of radiation due to the fact that it is accelerating. When this process happens with relativistic particles it is known as synchrotron radiation. This radiation is responsible for non-thermal emission from a variety of astrophysical sources across the electromagnetic spectrum, from the radio regime through to the gamma-ray regime. The energy loss rate of a single relativistic electron due to synchrotron radiation can be found by calculating the power in the electron's instantaneous rest frame using the Larmor formula and performing Lorentz transforms to express this power in the observer frame. This calculation can be found in several places, including Longair [53] and Blumenthal & Gould [59]. In terms of the magnetic field energy density u_B, the dimensionless speed $\beta = v/c$, and the Thomson cross section:

$$\sigma_T = \frac{8\pi}{3}\left(\frac{e}{mc^2}\right)^2 \tag{1.17}$$

The energy loss can be obtained:

$$\frac{dE}{dt} = -\frac{4}{3}\sigma_T \beta^2 \gamma^2 c u_B \tag{1.18}$$

Equation 1.18 represents the average energy loss rate over an isotropic distribution of pitch angles between $\vec{v}$ and $\vec{B}$. It should be noted that synchrotron radiation is dominated by electrons (as opposed to protons), due to this much higher energy loss rate and smaller Larmor radius.

The energy radiated by a single electron reaches the observer in the form of narrowly beamed pulses. The radiation is strongly beamed in the direction of motion toward the observer due to relativistic aberration. The synchrotron energy spectrum is the Fourier transform of the time series of these pulses. The full calculation has been done elsewhere [59, 53], the result is:

$$P_{\text{emitted}}(E) = \frac{\sqrt{3} e^3 B \sin\alpha}{m_e c^2} \frac{E}{E_c} \int_{E/E_c}^{\infty} K_{5/3}(\xi)\, d\xi \tag{1.19}$$

Where $K_{5/3}$ is a modified Bessel function, α is the electron pitch angle, and:

$$E_c = \frac{3}{2}\left(\frac{E_e}{m_e c^2}\right)^2 \frac{eB\hbar}{m_e c} \sin\alpha \tag{1.20}$$

in terms of the electron energy E_e. The spectrum is sharply peaked around E_c: most of the energy radiated from electrons of energy E_e will be in the form of photons with energy close to E_c.

We are particularly interested in the photon energy spectrum that would be produced by a distribution of electrons. In particular, let us assume that the electron distribution follows a power law (as is expected from diffusive shock acceleration):

$$n(E)dE = k\left(\frac{E}{E_0}\right)^{-p} dE \tag{1.21}$$

The resulting synchrotron spectrum (power received per unit volume per unit energy) can then be written as [59]:

$$J(E) = \frac{4\pi k e^3 B^{(p+1)/2}}{mc^2} \left(\frac{3e}{4\pi mc}\right)^{(p-1)/2} a(p) \left(\frac{E}{E_0}\right)^{-(p-1)/2} \tag{1.22}$$

Where $a(p)$ is given by Equation 4.60 in [59]. The key result to note is that a power-law distribution of electrons with index p emitting synchrotron radiation will produce a photon power-law distribution with a steeper index of $(p-1)/2$. Measurement of the spectral index of radiation can therefore be used to identify properties of the underlying electron distribution.

Inverse Compton Scattering

Compton scattering occurs when a photon interacts with an electron, resulting in an increase in the kinetic energy of the electron at the expense of a decrease in the photon's energy (and therefore an increase in wavelength) [60]. When the process works in reverse (very energetic electrons scatter photons to very high energies) it is known as inverse Compton scattering.

The classical derivation of inverse Compton scattering is accomplished by applying the standard Compton scattering results in the rest frame of the electron, and then transforming back into the lab frame. The full derivation will not be repeated here; the salient result is that, for near head-on collisions, the photon can gain energy in proportion to γ^2 ($E_{\gamma,f} \sim \gamma^2 E_{\gamma,i}$). Relativistic electrons accelerated at astrophysical shocks can therefore interact with ambient photons (from a nearby star, or from the CMB, for example) and upscatter them to gamma-ray energies.

If the photon energy in the rest frame of the electron is small in comparison to the electron's rest energy (the Thomson limit), the energy loss rate can be written [53]:

$$\frac{dE}{dt} = -\frac{4}{3}\sigma_T \beta^2 \gamma^2 c u_{\text{rad}} \tag{1.23}$$

Where u_{rad} is the radiation energy density. Note that this expression is completely identical to the loss rate for synchrotron radiation (Equation 1.18) except for the substitution $u_B \rightarrow u_{\text{rad}}$.

This result is only valid in the Thomson limit. As the photon energy becomes comparable to the electron energy in the electron's rest frame, the scattering cross section is best described by the Klein-Nishina formula [59]:

$$\frac{d\sigma}{d\Omega} = \frac{1}{2} r_e^2 \left(\frac{E'_{\gamma,f}}{E'_{\gamma,i}} \right)^2 \left(\frac{E'_{\gamma,i}}{E'_{\gamma,f}} + \frac{E'_{\gamma,f}}{E'_{\gamma,i}} - \sin^2 \theta \right) \tag{1.24}$$

Where r_e is the classical electron radius and $E'_{\gamma,i/f}$ is the initial/final energy of the photon in the rest frame of the electron.

The spectrum of scattered photons per electron is given in Equation 2.48-49 of [59]. If the distribution of electrons responsible for upscattering the photons is described by a power-law with index p (Equation 1.21), then the resulting photon spectrum can be calculated. This is again done following [59], who derive two separate results for the Thomson regime and the "Klein-Nishina regime" (where the photon energy dominates the electron rest mass in the electron frame).

In the Thomson regime:

$$\frac{dn}{dtdE} = \pi r_e^2 ck 2^{p+3} \frac{p^2 + 4p + 11}{(p+3)^2(p+1)(p+5)} \left(\frac{E}{E_0} \right)^{-(p+1)/2} \times \int \left(\frac{E'}{E'_0} \right)^{(p-1)/2} n(E') dE' \tag{1.25}$$

Where $n(E')$ is the number density of photons.

In the Klein-Nishina regime:

$$\frac{dn}{dtdE} = \pi r_e^2 ck \left(\frac{E}{mc^2} \right)^{-(p+1)} \times \int \frac{n(E')}{E'} \left(\ln \frac{EE'}{m^2c^4} + C(p) \right) dE' \tag{1.26}$$

Where $C(p)$ is an energy-independent parameter given by Equation 2.85 in [59]. The important note is that a population of electrons described by a power law of index p cooling via inverse Compton scattering will produce a power-law radiation spectrum with an initial index of $(p+1)/2$, steepening to $p+1$ at higher energies.

Non-thermal Bremsstrahlung

Electrons will emit radiation when they are accelerated in the vicinity of the Coulomb field of an atomic nucleus. The resulting radiation is known as "bremsstrahlung" (bremsstrahlung being German for "braking radiation").

From [53], the bremsstrahlung spectrum for a single electron passing through a gas of nuclei of density N can be written:

$$I(E) = \frac{16\pi^3 Z^2 e^6 N}{3c^3 m_e^2 v} \ln\left(\frac{192v}{Z^{1/3}c}\right) \tag{1.27}$$

Where v is the initial speed of the electron. The intensity spectrum radiated by a single electron is therefore energy-independent. This spectrum has the property, as shown in [61], that a power-law distribution of electrons losing energy via bremsstrahlung will produce a power-law photon spectrum with the same spectral index.

Neutral Pion Decay

Relativistic protons can produce high-energy gamma rays as inelastic collisions with the ambient gas or photons facilitate the production of secondary particles such as pions, which can promptly decay into gamma rays.

The kinetic energy of a proton can create a neutral pion π^0 during a collision with an atomic nucleus. This can happen if the proton has at least ≈ 280 MeV of kinetic energy. This is more than twice the mass of the π^0 (135 MeV); the excess kinetic energy is required in order that the momentum of the system be conserved during the collision [61]. The newly created π^0 will almost immediately ($\tau \approx 8.4 \times 10^{-17}$ s) decay into a pair of gamma rays, each with an energy of $m_{\pi^0}c^2/2 = 67.5$ MeV in the rest frame of the pion.

Neutral pions can also be produced via the "photo-pion" interaction whereby the scattering of a proton by a high-energy photon facilitates the production of pions [53]. Neutral pions produced in this way will rapidly decay into gamma rays, as described above.

The energy in the lab frame is obtained by a Lorentz transformation:

$$E_\gamma = \gamma E'_\gamma \left(1 + \beta \cos\theta'\right) = \gamma \frac{m_{\pi^0} c^2}{2} \left(1 + \beta \cos\theta'\right) \tag{1.28}$$

The pion decay is isotropic in its rest frame (due to the fact that π^0 has zero spin):

$$dN' = \frac{1}{4\pi} d\Omega' = \frac{1}{2} d\left(\cos\theta'\right) \tag{1.29}$$

From Equaton 1.28:

$$d\cos\theta' = \frac{2dE_\gamma}{\gamma\beta m_{\pi^0} c^2} \tag{1.30}$$

And therefore:

$$\frac{dN'}{dE_\gamma} = \frac{1}{\gamma\beta m_{\pi^0} c^2} \tag{1.31}$$

In the rest frame of the pion, the energy spectrum is constant from $E_{\min} = \gamma \frac{m_{\pi^0} c^2}{2} (1 - \beta)$ to $E_{\max} = \gamma \frac{m_{\pi^0} c^2}{2} (1 + \beta)$. The observed gamma-ray spectrum for a single event will therefore take the form of a uniform rectangle from $E_{\min}$ to $E_{\max}$, which necessarily includes $E = \frac{m_{\pi^0} c^2}{2} = 67.5$ MeV. The total energy spectrum of a population of protons emitting gamma-rays via neutral pion decay will therefore be a superposition of rectangles of which only the energy $E = \frac{m_{\pi^0} c^2}{2}$ is always present. The result is a characteristic "bump" in the gamma-ray spectrum, corresponding to 67.5 MeV in the pion rest frame. This distinctive feature, known as the "pion bump", is a signature of the presence of relativistic protons at the emission site. Because the bulk of cosmic rays are protons, and neutral pion decay is the only radiation mechanism in which protons dominate, the search for pion bumps in astrophysical spectra has become a major goal in the search for cosmic ray acceleration sites.

1.4 Sources of VHE gamma rays

Particle acceleration is likely to occur in any astrophysical environment where strong shocks are present. The particles will emit some of their energy in the form of one

or several of the radiation mechanisms discussed in the previous section. Observations of nonthermal radiation can therefore identify sources of significant acceleration.

1.4.1 Galactic Sources

Supernova Remnants

A supernova is a catastrophic explosion that occurs either when a massive star exhausts its nuclear fuel and undergoes core collapse, or when a white dwarf in a binary system exceeds its critical mass and undergoes a thermonuclear explosion. The shock front of the explosion and the ejected material of the former star propagate radially away over a period of thousands of years. This leftover material expanding into the interstellar medium is known as a supernova remnant (SNR). SNRs have long been hypothesized as the primary source of Galactic cosmic rays, due to the vast supply of energy available as well as the likely presence of diffusive shock acceleration, which produces a power-law distribution of accelerated particles. An image of the Tycho supernova remnant (which resulted from a white dwarf exceeding its maximum mass [62]) is shown in Figure 1.5.

Some ($\sim 1\%$) of the gravitational binding energy of the star will be converted into bulk kinetic energy of its ejected outer envelope (the remainder of the energy being carried away in the form of neutrinos [63]). For a supernova of energy $E \sim 10^{51}$ erg, and with ejected mass $2 - 10\ M_{\odot}$, the ejected material will form an expanding shell around the former star, expanding outward at $v_{\rm shell} \simeq \sqrt{\frac{2E}{M_{\rm shell}}} \simeq 10^4$ km/s [36]. The ejected material expands outward into the interstellar medium at a bulk speed faster than the sound speed in the medium, forming a strong shock. Particle acceleration can occur in the vicinity of this shock via the diffusive shock acceleration mechanism discussed in Section 1.2.

Non-thermal radiation from across the electromagnetic spectrum including radio, X rays, and gamma rays, has been detected from many supernova remnants.

The detailed structure of this emission is quite sensitive to the specific initial conditions of the explosion, as well as the age of the remnant. As of the time of writing, VHE emission has been observed from 24 SNRs, according to TeVCat ([64], http://tevcat2.uchicago.edu/). Non-thermal radio and X-ray emission likely results from the synchrotron emission of relativistic electrons gyrating in the SNR ambient magnetic field [65]. Evidence indicates that the magnetic field within these shocks can be significantly greater than that of the ambient interstellar medium [66]. This is a result of streaming instabilities causing magnetic field amplification in the plasma upstream of the shock front. The gamma-ray emission is caused in part by non-thermal bremsstrahlung and inverse Compton scattering from relativistic electrons, although the detection of the characteristic pion bump in several SNRs proves that protons are being accelerated as well [67, 68]. While proton acceleration is likely occurring in several SNRs at least up to $\sim$ TeV energies, it is not yet clear if these sources are capable of accelerating particles to the PeV energies at which the "knee" in the cosmic-ray spectrum is observed. The search for astrophysical sources with $\geq$ PeV-energy protons (known colloquially as "PeVatrons") is ongoing, although recent evidence has identified at least one strong candidate (SNR G106.3+2.7)[69, 70]. New instruments such as the Large High Altitude Air Shower Observatory (LHAASO, [71]), which is designed to detect radiation and cosmic rays in the TeV - PeV energy range, will greatly aid in this search.

Pulsars

A massive star which ends its life in a supernova explosion leaves behind the former stellar core in the form of either a neutron star or a black hole, depending upon the mass of the star. A neutron star is formed during the supernova explosion as nuclear fusion in the star's core can no longer support its weight. The increasing density during collapse supplies enough energy for protons and electrons to combine into neutrons via

$$p + e^- \rightarrow n + \nu_e$$

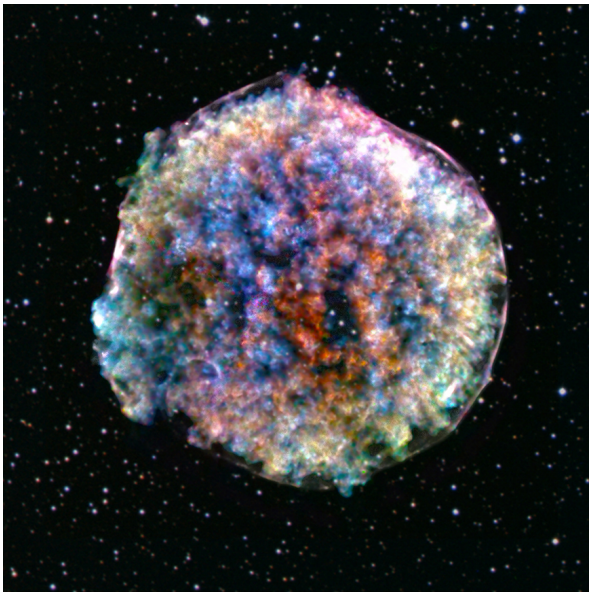

Figure 1.5: A composite X-ray and optical image of the Tycho supernova remnant, from NASA's Chandra X-ray observatory.

A gas of mostly neutrons forms and becomes a neutron star if neutron degeneracy pressure is sufficient to support the weight of the star. A typical neutron star has a mass of $M_{\rm NS} \approx 1.4\ M_\odot$ and radius of $R_{\rm NS} \approx 10^6$ cm $= 10$ km, resulting in a typical average density of $\rho_{\rm NS} \approx 10^{14}$ g cm^{-3}. The star is initially quite hot $T \sim 10^9$ K, but cools over time as there are no means of internal energy production. Conservation of angular momentum and magnetic flux during the collapse often leave the neutron star with a very high rotation rate ($\Omega_{\rm NS} \sim 10 - 1000\ {\rm s}^{-1}$) and magnetic field ($B_{\rm NS} \sim 10^{10} - 10^{13}$ G).

Neutron stars were first predicted by Baade and Zwicky in 1934 [46], only two years after the neutron was discovered by Chadwick [72]. More specific predictions were made by Oppenheimer and Volkoff in 1939 [73]. They were first discovered by Bell in 1968 [74].

As was first suggested by [75], the immense rotational energy associated with the rapidly-rotating neutron star can be released in the form of energetic radiation due to the strong magnetic field of the neutron star. The rotating, magnetized neutron star can generate an extremely large electric potential which accelerates electrons to relativistic energies. As these energetic particles move along the neutron star's curved

magnetic field lines, they radiate away some of their energy in the form of curvature radiation (similar to synchrotron radiation) which is strongly beamed along the magnetic axis of the star. If the rotational and magnetic axes of the star are misaligned, the observed result looks like a lighthouse, where radiation from the star is only seen as one of the magnetic poles sweeps through the observer field of view. Because this creates the illusion of the radiation being pulsed, this type of neutron star has come to be known as a "pulsar". Pulsars emit non-thermal radiation across the electromagnetic spectrum: particularly in the radio, X-ray, and gamma-ray bands.

VHE radiation from pulsars was first observed from the Crab pulsar by VERITAS [2] (Figure 1.6) and VHE emission has now been confirmed from four pulsars [76, 77, 78].

Pulsar Wind Nebulae

Much of the energy from the high rotation rate of a pulsar is dissipated in the form of a relativistic "wind" of electrons and positrons which escape the pulsar to a large distance. Close to the pulsar, charged particles co-rotate with the pulsar magnetic field. At a distance of $r_L = c/\Omega$ from the pulsar this results in luminal co-rotation speeds; beyond this distance particles can escape to infinity along open field lines. The volume enclosed by the cylinder of radius r_L is known as the "light cylinder" and comprises the pulsars magnetosphere. The pulsed emission from the pulsar likely originates from within the magnetosphere. Particles escaping the magnetosphere eventually attain relativistic speeds and form a shock where the wind reaches the interstellar medium [79]. At this "termination shock", electrons and positrons are accelerated through the process of diffusive shock acceleration. As they accelerate, they lose energy by emitting radiation through synchrotron and inverse Compton processes; this radiation is then observed in the form of non-thermal radio, X-ray, and gamma-ray emission. The resulting nebula, known as a "pulsar wind nebula" (PWN) surrounds the central pulsar. PWNe are the most common source of VHE radiation within the Galaxy. The Crab Nebula (Figure 1.7) was the first object ever observed in this energy band [80] and

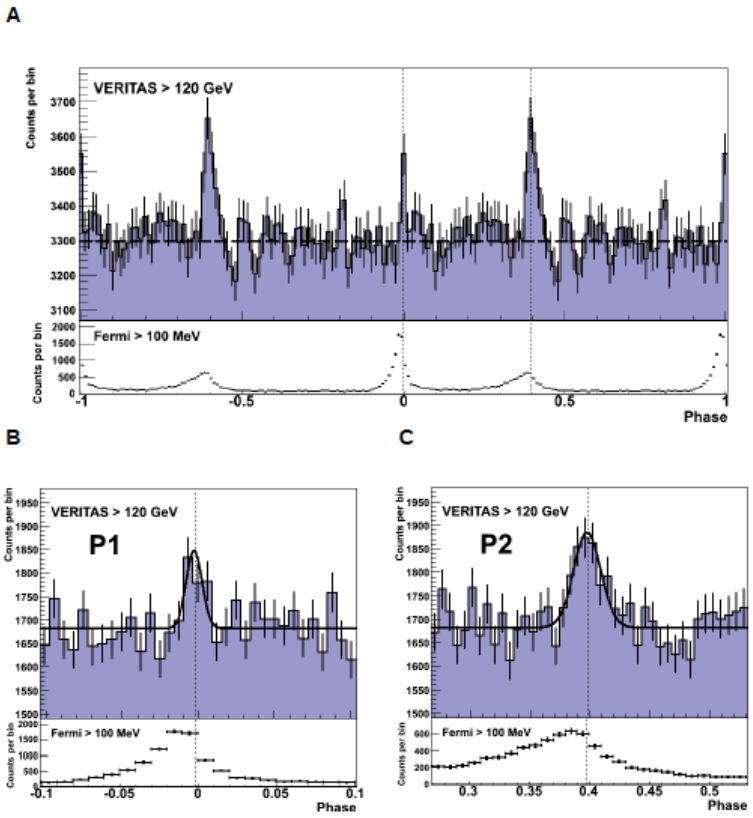

Figure 1.6: The pulsar profile of the Crab pulsar, reproduced from [2]. The top plot shows gamma-ray counts binned by pulsar phase, showing two peaks corresponding to two pulses. The profile is shown twice for clarity. The lower panel shows zoomed in views of each pulse.

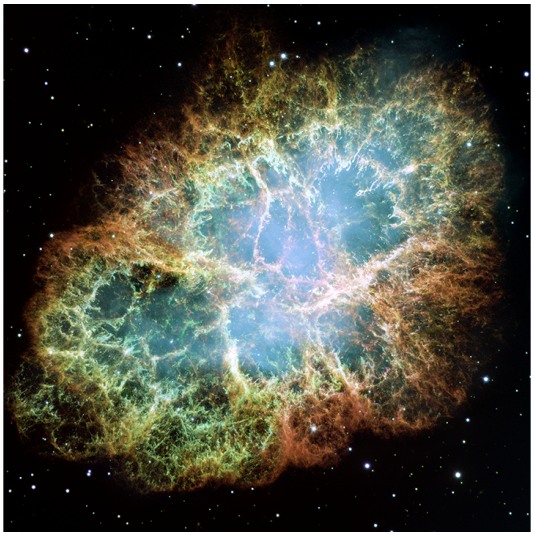

Figure 1.7: An image of the Crab Nebula and supernova remnant, from NASA's Hubble Space Telescope.

has become the "standard candle" of gamma-ray astronomy. According to TeVCat, 34 PWNe have now been observed at VHE energies.

Gamma-ray Binaries

A pulsar wind nebula is formed when the wind from an isolated pulsar shocks the surrounding interstellar medium; resulting in steady non-thermal emission. If the pulsar is not isolated, its wind can interact with and shock the wind of the companion star, leading to non-thermal radiation originating at the interaction surface between the two stars. Shocks can also be generated in the relativistic jet of a black hole companion. In several such instances, the resulting radiation can be observed in the VHE energy band; these objects are known as gamma-ray binaries. Gamma-ray binaries are characterized by synchrotron and inverse Compton radiation which is highly variable in time as a function of the orbit of the system as well as the viewing geometry of the observers. Nine systems have so far been classified as gamma-ray binaries. For a detailed discussion of these systems, see chapter 5.

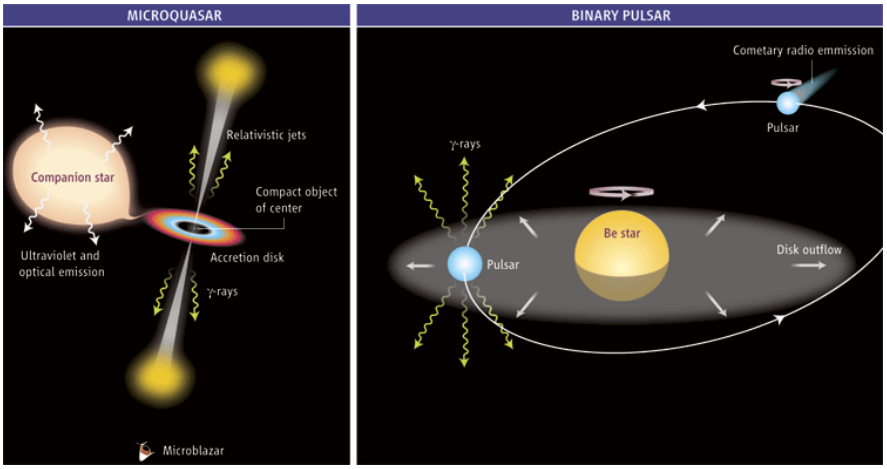

Figure 1.8: Shown are the two widely-theorized mechanisms of gamma-ray production in gamma-ray binaries. From [3].

Other Galactic Sources

The source classes presented in the preceding sections represent the great majority of identified Galactic VHE sources, however other types of VHE emission have been observed in the Galaxy. These include novae [81], colliding wind binaries [82], star forming regions [83], and globular clusters [84]. The Galactic center exhibits diffuse VHE emission as well as a number of unidentified sources in the Galactic plane[85].

1.4.2 Extragalactic sources

Active Galactic Nuclei

By far the most numerous source of extragalactic VHE emission is active galactic nuclei (AGNs). An active galactic nucleus occurs when a supermassive black hole (SMBH) at the center of a galaxy accretes matter from its surroundings. Non-thermal emission from AGN likely originates from shocks forming within relativistic jets which flow out from the SMBH [86]. Particles are accelerated at the shock via diffusive shock

acceleration and radiate non-thermally via synchrotron and inverse Compton radiation [87]. In some cases, relativistic electrons in the jet can upscatter synchrotron photons to even higher energies in a process known as synchrotron self-Compton (SSC) radiation. Hadronic and "lepto-hadronic" models have also been proposed to explain the observed emission from AGN [88]. As of the time of writing, 89 AGN have been observed in the VHE band. An image of the AGN in the galaxy Centaurus A is shown in Figure 1.9.

AGN are classified based on the viewing angle of the relativistic jet with the line of sight [89]. AGN in which the jet is aimed very near to the line of sight are called *blazars*, as opposed to *radio galaxies* whose jets are directed at large angles to the line of sight. Blazars can be further subdivided on the basis of their emission lines. Flat spectrum radio quasars (FSRQs) exhibit strong optical emission lines, whereas BL Lacertae (BL Lac) objects do not.

Gamma-ray Bursts

Gamma-ray bursts (GRBs) are likely the result of either a core-collapse or compact-merger supernova and when they occur are briefly the brightest objects in the observable Universe. Unlike supernova remnants, which remain visible for thousands of years after the initial explosion, the luminosity of GRBs is concentrated within $\sim$ minutes to $\sim$ hours after the initial event[2]. This is followed by an "afterglow" lasting for several days during which the luminosity diminishes. The relativistic outflow from the energetic explosion shocks the medium into which it expands, resulting in particle acceleration and radiation. Non-thermal radiation from GRBs is likely due to synchrotron and inverse Compton radiation [90], and SSC radiation may also play a role [91]. VHE emission was first observed from a GRB in 2019 ([4], Figure 1.10), and has since been observed from a total of 5 GRBs [92, 93, 94, 95].

[2] Some GRBs are caused by core-collapse supernovae and therefore leave behind supernova remnants. Here we distinguish between the emission related to the initial explosion (the GRB) and the emission associated with the expanding supernova shell (SNRs).

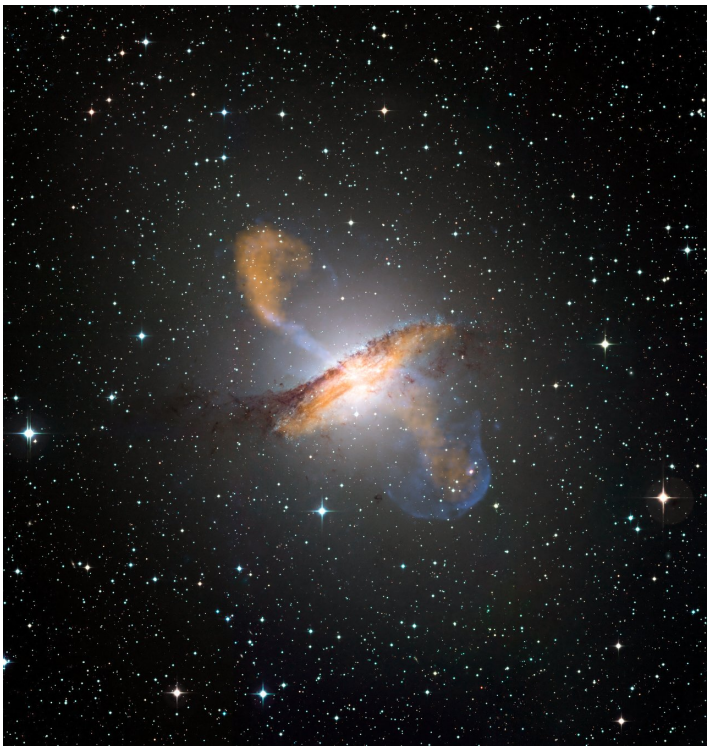

Figure 1.9: A false color composite image shows the jets emanating from the central black hole of the Centaurus A galaxy. The image combines infrared data from the APEX telescope, X-ray data from the Chandra X-ray observatory, and visible light data from the MPG/ESO 2.2 m telescope located at La Silla, Chile.
Image credit: ESO/WFI (Optical); MPIfR/ESO/APEX/A.Weiss et al. (Submillimetre); NASA/CXC/CfA/R.Kraft et al. (X-ray)

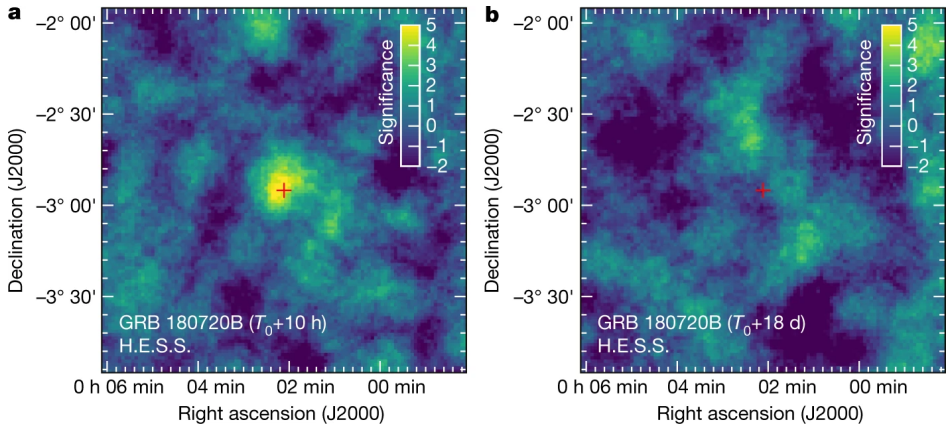

Figure 1.10: A significance skymap shows the first detection of a gamma-ray burst in the VHE regime. Reproduced from [4].

Other Extragalactic Sources

In addition to the sources mentioned above, a few other types of extragalactic sources have been observed as sources of VHE emission. VHE emission has been observed in two starburst galaxies [96, 97], likely resulting from the higher density of supernovae and cosmic rays in these objects. The Large Magellanic cloud is a source of large-scale diffuse emission, as well as a few identified individual sources [98].

1.5 Current Status of VHE Astronomy

The detection of VHE photons is typically accomplished by causing incoming photons to interact with some medium via pair production and observing the secondary products. Because a large amount of matter is required to cause VHE photons to interact, astronomical observations conducted in this energy band are typically done via ground-based instruments, using the atmosphere as a calorimeter. Ground-based VHE observatories fall into two categories: Imaging Atmospheric Cherenkov Telescopes

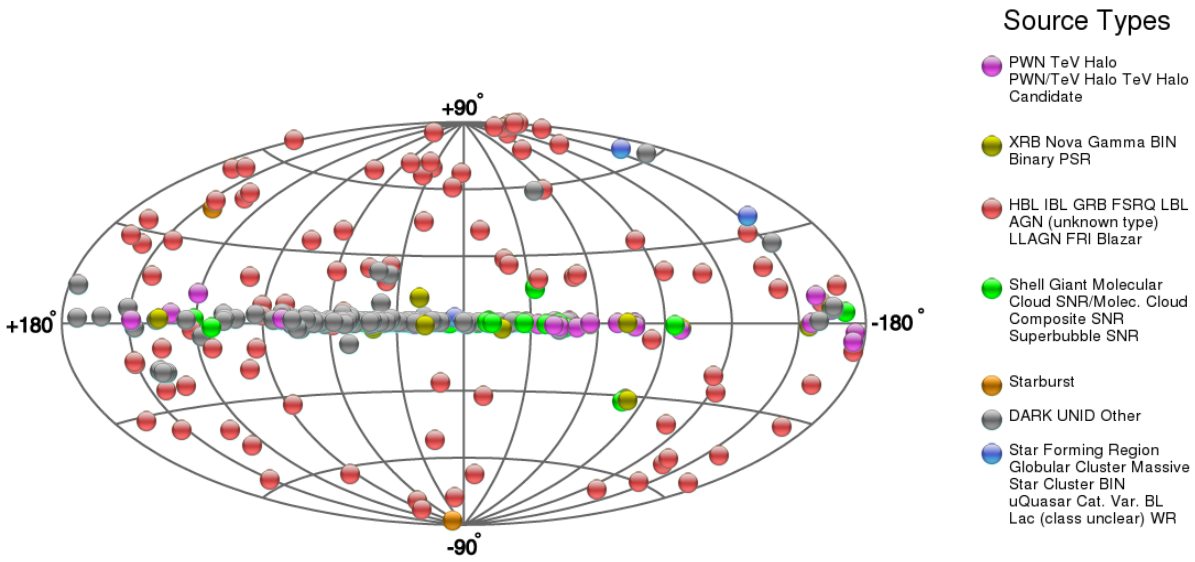

Figure 1.11: The all-sky map of VHE gamma-ray sources as of Fall 2024, from TeVCat.

(IACTs), which use the atmosphere as a gamma-ray calorimeter, and Extensive Air Shower arrays, which which observe interactions in ground-based water tanks. The specifics of these processes are described in Chapter 2. Here we briefly summarize the historical development of VHE astronomy.

The method of using Cherenkov light as a means to detect gamma rays was first demonstrated by Galbraith and Jelley in 1953 [99]. The light is emitted as a gamma-ray photon interacts with nuclei in the air, leading to the production of an electron/positron pair. Repeated cycles of Bremsstrahlung radiation and pair production produce a large shower of particles which radiate Cherenkov light as they move superluminally in the atmosphere. This process is described in detail in Chapter 2. VHE emission from an astrophysical source was first observed by the Whipple telescope at the Fred Lawrence Whipple Observatory in 1989 [80] with the detection of the Crab Nebula. Aside from the Crab Nebula, Whipple also detected VHE gamma rays from several AGNs, including Markarian 421 and Markarian 501 [100, 101]. The HEGRA observatory in La Palma, which saw first light in 1997, was the first IACT to successfully implement stereoscopic observations with multiple Cherenkov telescopes

[102]. This resulted in improved sensitivity, angular resolution, and energy reconstruction [103]. Among HEGRA's chief discoveries were the SNR Cassiopeia A [104], the PWN TeV J2032+4130 [105], and the radio galaxy M87 [106]. The current generation of IACTs comprises H.E.S.S in Namibia [107], MAGIC in La Palma [108], and VERITAS in Arizona [109]. These instruments are able to detect sources of similar flux of the Crab Nebula in under a minute and boast $\sim$ arcminute scale angular resolution. They are shown in Figure 1.12.

The High Energy Stereoscopic System (H.E.S.S.) is an array of five IACTs located in Namibia. H.E.S.S. is sensitive to gamma-rays in the range from $\sim$ 30 GeV to up to 100 TeV [107] and has a 5° field of view. Four of the telescopes are 13 meters in diameter and have been operating since 2003. In 2012, a fifth telescope,with a diameter of 28 meters, was added to the array. This significantly reduced the energy threshold of the array [110].

The Major Atmospheric Gamma Imaging Telescope (MAGIC) is an array of two IACTs located in La Palma, Spain. The first telescope began operations in 2004, and was joined by the second in 2009. Each telescope is 17 meters in diameter, and the array has a field of view of 3.5°. MAGIC is sensitive to gamma rays in the $\sim$ 50 GeV to $\sim$50 TeV range [108].

The Very Energetic Radiation Imaging Telescope Array System (VERITAS) is an array of four IACTs located near Tucson, Arizona. Each telescope is 12 meters in diameter. The array has a field of view of 3.5° and is sensitive to gamma rays in the range of $\sim$ 85 GeV to $\sim$ 30 TeV. VERITAS is described in detail in Chapter 3.

Air shower arrays are an alternative to IACTs for the detection of gamma-rays. Air shower arrays typically consist of a large number of ground-based water tanks within which secondary particles from the photon-induced atmospheric particle shower emit Cherenkov radiation. Light sensors within the tanks capture this radiation and use it to reconstruct the properties of the original gamma ray which caused the particle shower. Because only the highest energy gamma rays are capable of producing showers that reach the ground, the energy range over which air shower arrays are typically most

Figure 1.12: *Top*: The H.E.S.S. array. *Middle:* The MAGIC array. *Bottom:* The VERITAS array.

sensitive shifts to higher energy relative to IACTs, typically from ∼10s to ∼ 100s of TeV. In this way air shower arrays complement IACTs, which rapidly lose sensitivity above $\sim 10 - 30$ TeV.

The High Altitude Water Cherenkov Observatory (HAWC, [111]) is an air shower array located in Sierra Negra, Mexico. The array comprises 300 water tanks covering an area of approximately 22,000 m^2. HAWC has a larger field of view than any IACT (2 steradians) and is most sensitive to gamma rays in the energy range of $\sim$ 100 GeV - $\sim$ 100 TeV.

The Large High Altitude Air Shower Observatory (LHAASO, [71]) is another active air shower array located in Daocheng County, Sichuan Province, China. LHAASO consists of three interconnected arrays: a 1.3 km^2 array (KM2A), a 78,000 m^2 Water Cherenkov Detector Array (WCDA), and a Wide Field-of-view Cherenkov Telescopes Array (WFCTA). The KM2A and WCDA are designed for gamma ray detection while the WFCTA is designed to observe cosmic rays. Like HAWC, LHAASO has a large ($\sim$ 2 sr) field of view. It is most sensitive to gamma rays in the energy range from $\sim$ hundreds of GeV to $\sim$ a few PeV.

The number of known VHE sources ballooned rapidly with the onset of these observatories: as of the time of writing, more than 300 astrophysical sources have been detected in the VHE regime, according to TeVCat.

Chapter 2

VERY HIGH ENERGY GAMMA-RAY ASTRONOMY WITH IMAGING ATMOSPHERIC CHERENKOV TELESCOPES

Gamma-ray astronomy is fundamentally different from astronomy at other wavelengths. Radio, optical, X-ray, and other telescopes rely on the basic principle of reflecting or refracting incoming photons onto a photosensitive detector. This process is ineffective for photons with energies greater than a few MeV. At these energies, photons are best observed via their forced interaction with matter, usually pair production. The design of gamma-ray telescopes thus differs dramatically from instruments at other wavelengths. Furthermore, the analysis of data collected by these instruments is greatly complicated by the fact that photons themselves are not directly observed, and the properties of the original photon must be reconstructed by observing the products of the initial photon interaction. In this chapter, we describe the basic mechanisms of photon interactions at gamma-ray energies which drive the design of these telescopes, with a focus on ground-based gamma-ray detectors.

2.1 Basic principles

Broadly speaking, a gamma-ray detector must accomplish two things: 1) allow the incoming gamma-ray photon to interact within some material, and 2) observe the products of this interaction in order to reconstruct the properties (i.e. direction, energy) of the original photon. The latter is a more complex task than the former, and the design of a gamma-ray instrument is dictated by simultaneously optimizing these two tasks within the desired energy range (and budgetary constraints). For photon energies above $\sim$ tens of MeV, pair production ($\gamma \rightarrow e^+ + e^-$) is the dominant interaction with matter. Most gamma-ray detectors are thus designed around letting a photon

interact and then tracking the resulting pairs. At lower gamma-ray energies, Compton scattering can also be an important mechanism which drives the detector design (see e.g. COMPTEL [112] and the planned AMEGO [113]). In this discussion we focus on the high-energy (HE; $\sim 10^8 - 10^{11}$ eV) and very high-energy (VHE; $\sim 10^{11} - 5 \times 10^{13}$ eV), and therefore only consider pair production processes.

Pair production cannot occur in a vacuum (in order to ensure momentum conservation before and after the interaction), so some amount of matter is required in order for the interaction to take place. The characteristic distance traversed by a gamma-ray photon within a given material before pair production is related to the radiation length X_0 of the material:

$$\lambda_{pp} = \frac{9}{7} X_0 \tag{2.1}$$

The radiation length is a characteristic of the material and is related to the atomic number Z and the density ρ. X_0 is defined as the characteristic amount of matter traversed by an electron before losing all but $1/e$ of its initial energy in the Bremsstrahlung process. If an electron travels a physical distance z_0 in a material of density ρ before decaying to $E = \frac{1}{e} E_0$, then the radiation length is related to the travel distance as:

$$X_0 = \int_0^{z_0} \rho(z') dz' \tag{2.2}$$

X_0 thus has dimensions of $mass/area$, and is typically expressed in units of g cm^{-2}.

Measurement of the direction and energy of the pairs can be used to infer the direction and energy of the primary photon. This is complicated by the fact that the resulting pairs will be scattered, degrading the information they contain about the initial photon. This Coulomb scattering also scales with distance traversed through the material [114]. Space-based gamma-ray telescopes mitigate this by breaking the pair converter into several relatively thin layers, each accompanied with particle tracking

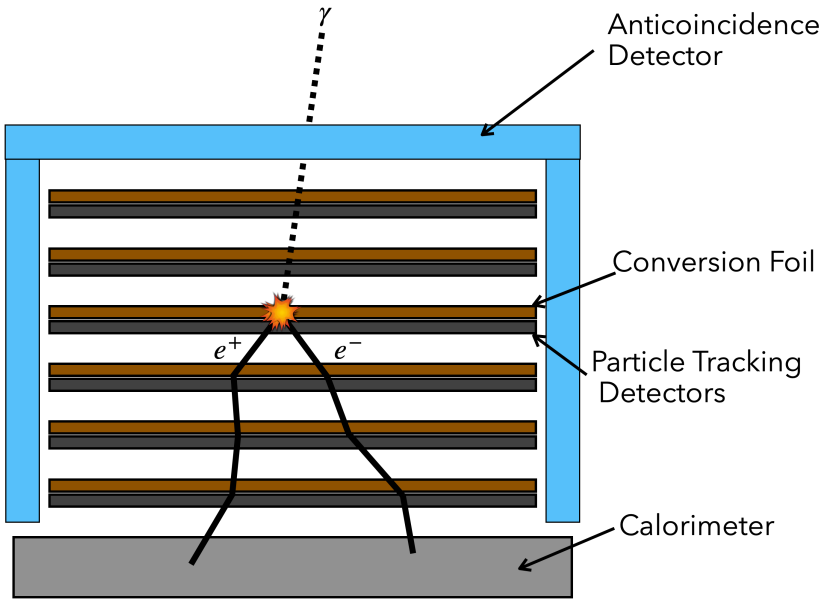

Figure 2.1: A schematic showing the basic design of a space-based gamma-ray detector. A gamma ray enters the telescope through the anticoincidence detector and converts into an electron/positron pair within a layer of Tungsten foil. The resulting pairs are tracked as they pass through subsequent layers containing silicon strip detectors before finally depositing their energy into the calorimeter.

detectors. This allows the photon to traverse several radiation lengths while simultaneously ensuring the $e\pm$ pairs cannot travel far before being tracked by the detector. A general schematic of this design is shown in Figure 2.1.

2.2 *Fermi*-LAT

The Large Area Telescope (LAT) onboard the Fermi Gamma-ray Space Telescope is a modern example of a space-based gamma-ray telescope [115]. The LAT makes use of the general design described above. It consists of 16 planes of high Z material (tungsten) to facilitate pair conversion. These planes range in thickness from 95 μm for the first 12 planes and 720 μm for the final four. This corresponds to 0.027 and 0.18 radiation lengths, respectively. Each plane is accompanied by two layers of 400 μm-thick silicon strip detectors which detect the charged pair particles and can be used to measure the tracks of charged particles. The energy of the pairs is measured by a calorimeter comprised of CsI crystals at the back of the detector. An anticoincidence

detector (a layer of scintillating tiles which is sensitive to charged particles) is utilized to detect charged particles entering the detector with the aim of vetoing cosmic-ray events. A detailed description of the instrument is given in [115].

The LAT is sensitive to gamma-ray photons with energies ranging from $\sim$ 20 MeV to hundreds of GeV. At lower energies, the detector is limited by Coulomb scattering of converted pairs, which degrades the direction reconstruction, as well as the increasing importance of Compton scattering close to the 1 MeV threshold for pair production. Instruments targeting this energy range require a different design ([112, 113]).

At high energies, the LAT is primarily limited by statistical uncertainties due to the low number of photons able to be collected by the $\sim$ 9500 cm^2 detector. As was discussed in the previous chapter, flux from gamma-ray sources typically exhibits some form of a power law relationship with energy ($\frac{dN}{dE} \propto E^{-\Gamma}$) so that the flux rapidly decreases with energy. With a collection area of 9500 cm^2 this corresponds to about $\sim$ 7 photons per year above 1 TeV from a Crab-like source. The *Fermi* telescope has been operating since 2008 and therefore now has sufficiently large exposure times to observe dozens of sources above 500 GeV up to 2 TeV [116][1]. Much larger collection areas are required to effectively characterize the nature of sources at these energies with relatively short ($\sim$ tens of hours) exposure times. Such telescopes are impractical for space-based missions due to the cost and size constraints of getting the instrument into orbit. Observations of very high-energy gamma rays is thus only practical via ground-based instruments.

2.3 The atmosphere as a gamma-ray detector

Fundamentally, ground-based gamma-ray detectors make use of the same basic principles as do space-based detectors: allow the primary photon to interact and produce pairs and then use the pairs to reconstruct the properties of the initial photon.

[1] The cited catalog shows 41 sources with $\sqrt{TS} \geq 3$ in the 500 GeV - 2 TeV range. Given that this catalog is now (at the time of writing) seven years old, the current number of detected in this energy range is likely significantly higher.

For ground-based instruments, the atmosphere itself provides the material necessary to initiate pair production. Radiation from the secondary particles then provides the means of detection by optical telescopes on the ground.

2.3.1 Extensive Air Showers

The typical radiation length in air is ≈37.1 g cm^{-2}, and the total thickness of the atmosphere above sea level (a.s.l) is ≈1030 g cm^{-2}; the atmosphere is therefore ≈ 28 radiation lengths thick and very opaque to gamma rays [117]. Upon entering the atmosphere, a gamma ray will pair produce after traversing a thickness $\lambda_{pp} = \frac{9}{7}X_0$. The resulting electron and positron traverse a thickness X_0 before interacting with an air molecule and radiating via the Bremsstrahlung process. If the resulting photon is sufficiently energetic, it will pair produce after traversing another λ_{pp}, and the process will repeat itself. The emission angle for both processes is inversely proportional to energy: $\theta \propto m_e c^2/E_0$ and the products will therefore be tightly beamed along the direction of the initial photon [117].

This process can be examined within a simple model first developed by Heitler [118]. In this framework, we make the approximation that the characteristic length scales for pair production ($\frac{9}{7}X_0$) and Bremsstrahlung radiation (X_0) are equal ($\lambda_{pp} \approx X_0$). A gamma ray incident upon the atmosphere will create a cascade of particles and photons via recurring pair production and Bremsstrahlung radiation, known as an extensive air shower (EAS). At each "level" of the shower (each integer multiple of radiation length nX_0), the number of particles (photons and $e\pm$) increases as $N = 2^n$. This is illustrated in the top panel of Figure 2.2. The energy E_0 of the initial photon is shared equally among shower constituents with energy E:

$$E = \frac{E_0}{2^n} \tag{2.3}$$

The cascade will continue to develop in this way until the average particle energy reaches a critical energy, E_c, at which ionization becomes the dominant loss mechanism for energetic electrons. This defines the maximum number of radiation lengths n:

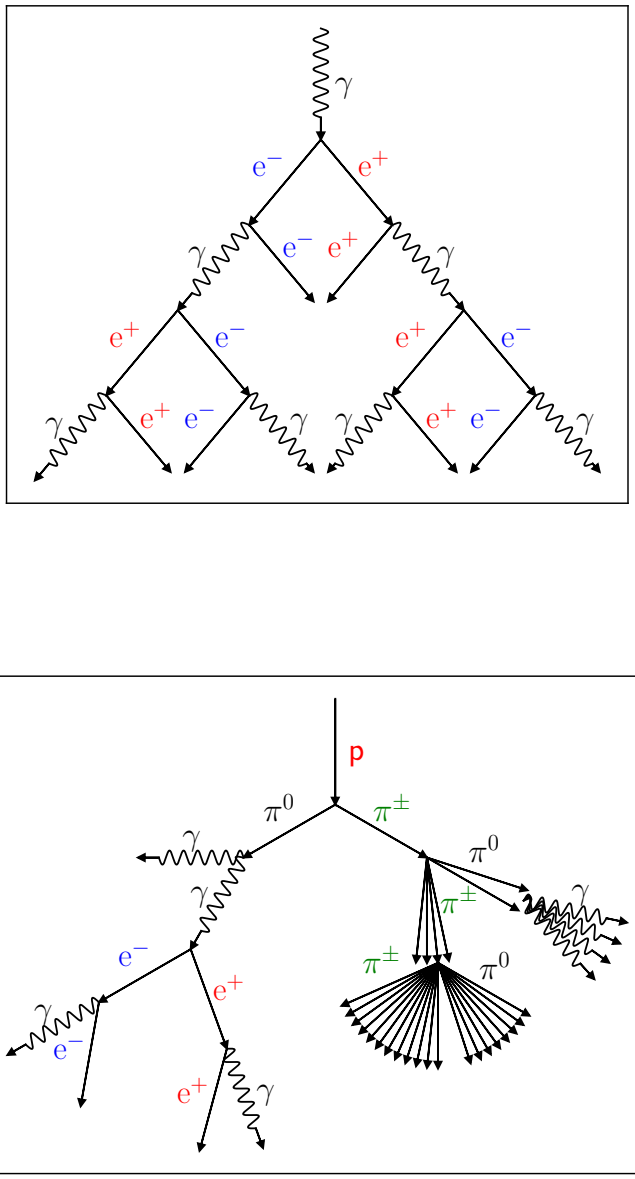

Figure 2.2: The top figure shows a simplified model of the development of a gamma-ray initiated air shower. The bottom figure shows a simplified model of the development of a hadron initiated air shower.

$$E = E_c = \frac{E_0}{2^{n_{max}}} \tag{2.4}$$

Which implies

$$n_{max} = \frac{1}{\ln 2} \ln \frac{E_0}{E_c} \tag{2.5}$$

From which we can find the maximum number of particles:

$$N_{max} = \frac{E_0}{E_c} \tag{2.6}$$

In air, $E_c \approx 85$ MeV. This model, though simplistic, nonetheless accurately reproduces the linear dependence between the maximum number of shower particles and E_0, as well as the logarithmic dependence upon E_0 of the maximum shower depth.

2.3.2 Cherenkov Radiation

The charged particles produced in the shower cause the atmosphere to radiate in a process called Cherenkov radiation. Predicted by Heaviside [119] and named for Cherenkov [120] who discovered it, this radiation is the result of polarization within a dielectric medium caused by a fast-moving charged particle. A charged particle moving through a dielectric will briefly polarize the molecules in the vicinity of the charge. For a slow-moving charge, this results in polarization which is symmetric in every direction, and thus no net electric field at large distances is observed. If the charge is moving faster than c/n (the speed of light in the medium, where n is the refractive index), then the polarization becomes asymmetric about the particle's trajectory, resulting in a net, transient dipole field moving along the trajectory of the particle. These cases are illustrated in the left panels of Figure 2.3. The latter case results in brief pulses of radiation tracking the particle trajectory. These pulses will interfere destructively unless the particle motion is sufficiently fast. Figure 2.3 (right panels) shows the spherical wavefront of each pulse along the particle trajectory. For particle velocity $v < c/n$, the wavelets are not able to form a coherent front, and no radiation is observed. Conversely, if $v \geq c/n$, the particle is able to produce pulses

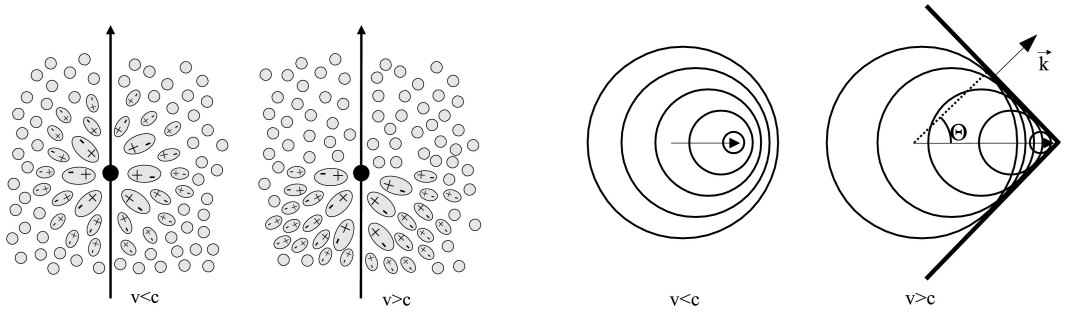

Figure 2.3: *Left*: Superluminal motion within a dielectric medium induces an asymmetric polarization with respect to the direction of motion. *Right*: Light emitted in the vicinity of the traveling particle constructively interferes to form a wavefront if $v > c/n$. Reproduced from [5]. Reprinted with permission from Elsevier Masson SAS.

which constructively interfere to form a wavefront traveling at an angle θ relative to the particle trajectory. The angle of the wave motion can be found by examining the wavelets using Huygen's principle:

$$\cos\theta = \frac{c/n}{v} \tag{2.7}$$

Clearly, no coherent radiation will be seen unless the particle velocity v equals or exceeds the speed of light in air c/n. At sea level, $n \approx (1 + 2.9 \times 10^{-4})$ [9], and an electron with velocity c results in a Cherenkov angle of $\sim 1.4°$. Cherenkov radiation is most prominent in the blue/UV wavelength regime; the spectrum is given by [121]:

$$\frac{\mathrm{d}^2 N_{\mathrm{ph}}}{\mathrm{d}x\mathrm{d}\lambda} = \frac{2\pi\alpha}{\lambda^2}\sin^2\theta_c \tag{2.8}$$

where θ_c is the Cherenkov angle and α is the fine-structure constant. The observed spectrum peaks near 340 nm, with shorter-wavelength emission suffering significant atmospheric absorption [122].

The distribution of the changing Cherenkov photons reaching the ground is determined by the longitudinal and lateral development of the particle shower, as well as the altitudinally-varying Cherenkov angle (left panel of Figure 2.4). The altitudinal variation is introduced in Equation 2.7 because the index of refraction decreases with altitude. The effect of the Cherenkov emission angle is to focus the light around ~ 120

m from the shower axis at sea level. The particle shower, in principle strongly beamed along the photon direction, obtains a significant lateral extent due to multiple Coulomb scattering of the charged particles. The shower particles are scattered at a typical angle of $\sim 5^\circ$ [122, 9, 36]. This results in a significant blurring of the Cherenkov ring; leading to a near uniform "pool" of light on the ground out to a radius of ~ 120 m followed by a slow decay for several hundred meters (Figure 2.5). For a 1 TeV gamma ray, the photon density within this pool will be ~ 100 photons m^{-2}. The origin of Cherenkov emission (superluminal particle velocities) also gives rise to peculiarities in the relative arrival times of photons generated through the shower [123]. If the horizontal distance from the shower axis to the observer is sufficiently small ($\lesssim 100$ m), photons emitted at the end of the shower will arrive before the photons that were emitted earlier from the beginning of the shower. This is a consequence of the shower front moving faster than the photons it radiates (and is also what allows for the radiation to be coherent, as explained above). For greater horizontal distances, or larger viewing angles (larger ratio of horizontal to vertical distance), this effect is overcome by the large distances the photons must travel, as well as the increasing index of refraction at lower altitudes (which slows the light speed c/n), and the photon arrival time increases approximately linearly with shower longitude/viewing angle. This phenomenon is depicted in the right panel of Figure 2.4.

Therein lies the basic principles that allow for ground-based gamma-ray astronomy. An energetic photon induces a cascade of charged particles and photons, which in turn cause the atmosphere to coherently radiate optical photons that reach the ground in detectable quantities. The number of shower particles (and thus the light yield) scales linearly with the energy of the primary photon, and the shower axis traces its direction. There remains an (unfortunate) caveat (for the gamma-ray astronomer): such particle showers and the resultant Cherenkov light also arise from high-energy cosmic rays entering the atmosphere, and the flux of these particles is in general much ($\sim 10^5$ times) greater. Here we briefly discuss air showers which result from hadronic primaries, an immense background confronting the relatively few gamma-ray induced

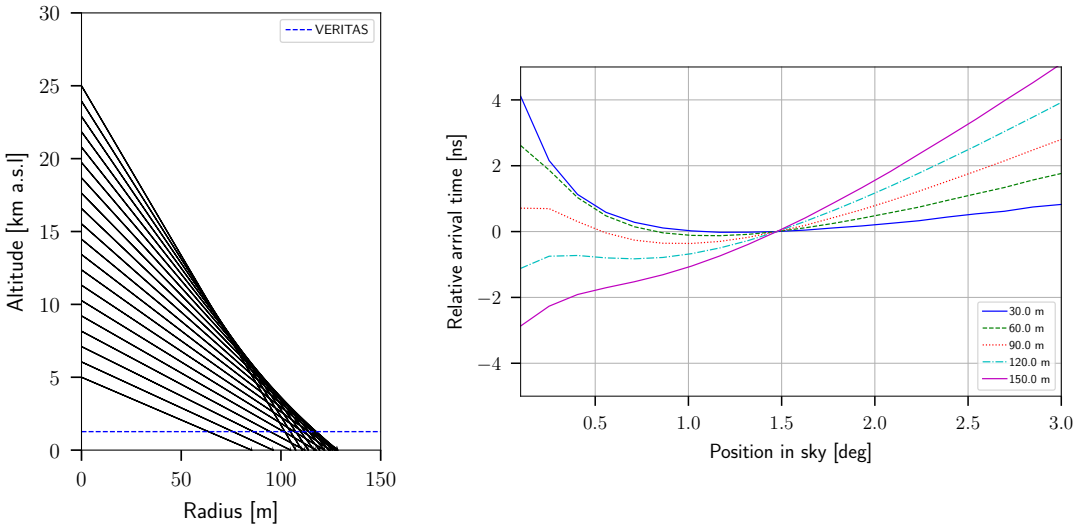

Figure 2.4: *Left:* The Cherenkov opening angle increasing with decreasing altitude. *Right:* The relative arrival time of photons emitted along the shower longitude (measured in degrees). The different curves show different horizontal distances between observer and shower axis.

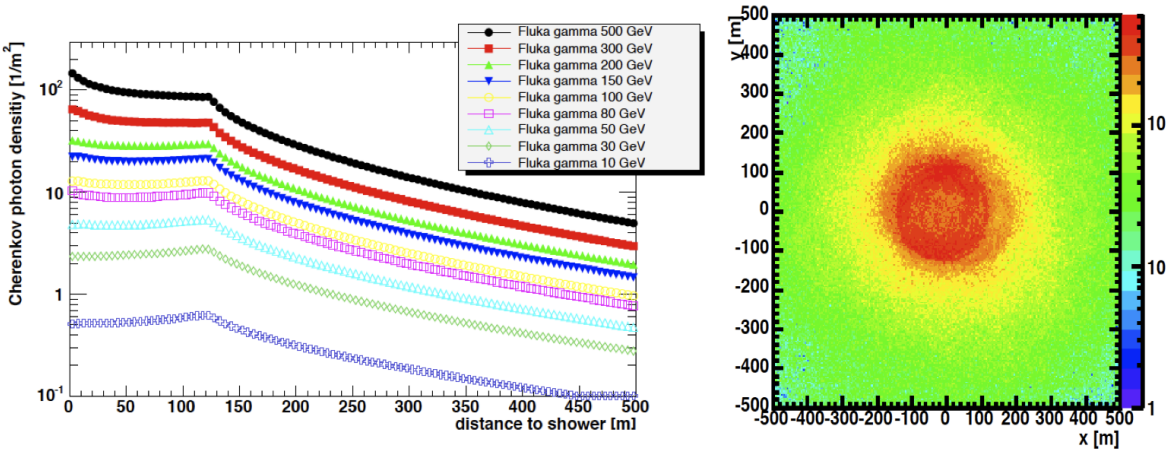

Figure 2.5: The 1D (*left*) and 2D (*right*) distribution of Cherenkov photons on the ground. Figure 1 from [6], Figure 4 from [7].

showers.

2.3.3 Hadronic Air Showers

A proton entering the atmosphere will eventually collide with a nucleus within an air molecule, converting some of its energy to charged and neutral pions, among small amounts of other particles. [124, 125, 126]. The former rapidly ($t \sim 10^{-16}$ s) decay into gamma rays ($\pi^0 \rightarrow \gamma + \gamma$), which initiate an electromagnetic sub-shower which develops in the same manner as described previously in the Chapter (pair production and Bremsstrahlung). The charged pions will either interact with air molecules to produce more pions, or decay into muons and neutrinos ($\pi^{\pm} \rightarrow \mu^{\pm} + \nu_{\mu}$). The relative probability of these two processes is dependent upon particle energy and altitude (air density) [125]. If the pions have sufficient energy (typically $\sim$ 10s of GeV and dependent upon the energy of the primary) they will traverse the necessary depth ≈ 120 g $\cdot$ cm^{-2} and interact with another nucleus before they are able to decay into muons and/or neutrinos. This interaction spawns a new generation of pions with slightly less energy than the previous one. Once the average energy of pions falls below this threshold energy, decay into muons and neutrinos becomes dominant over interactions with nuclei in the air. Many of these muons can penetrate to ground level and be observed before decaying, due to the relativistic time dilation of their 2.2 μs decay time.

Thus the initial proton interaction yields an electromagnetic cascade and a cascade of more hadrons. The number of hadrons produced at each interaction changes slowly with energy, and for a first-order approximation akin to the Heitler model [126] can be taken as a constant such that the number of particles at each level n of the shower is $\sim 10^n$. At each interaction, 1/3 of the primary energy is carried away by neutral pions into a subsequent electromagnetic cascade; the remainder takes the form of charged pions. Thus at the nth level of the shower, the energy per charged pion will be:

$$E_{\pi} = \frac{E_0}{\left(\frac{3}{2}10^n\right)} \tag{2.9}$$

The pions will continue interacting in this fashion until the average energy E_π falls below the critical energy E_c, at which point the pions will decay before interacting. This simplified model is depicted in the right panel of Figure 2.2. E_c is determined by the balance between the decay length scale (the distance traversed by the hadron before decaying in the lab frame) and the interaction length scale (determined by the air density). Because the former depends upon the energy of the primary E_0 while the latter does not, E_c decreases slowly with E_0, with $E_c \approx 30$ GeV for a 100 TeV primary, and $E_c \approx 10$ GeV for a 100 PeV primary [126]. Each charged particle will cause Cherenkov radiation as long as $v > c/n$ (Equation 2.7). Due mostly to the differing nature of the interactions in hadronic vs photonic showers (strong vs electromagnetic, respectively), the secondary particles produced in the hadron-initiated shower tend to have greater transverse momentum than those in the photon-induced shower [127]. The irregular development of the hadron-initiated shower, along with the larger transverse momentum of the hadronic secondaries, results in a broad and highly non-uniform distribution of light on the ground (Figure 2.7). Figure 2.6 shows a comparison of the lateral and longitudinal development of a gamma-ray vs proton induced particle shower.

The shower development of heavier cosmic rays is more complicated, but to a first approximation can be treated as a superposition of Z separate proton showers originating at the same position [126], where Z is the atomic number of the nucleus. Electrons entering the atmosphere will quickly radiate gamma rays via the Bremsstrahlung process and initiate an electromagnetic cascade nearly indistinguishable from a gamma-ray induced shower[2].

2.4 Imaging Atmospheric Cherenkov Telescopes

The goal of ground-based gamma-ray astronomy is to observe and characterize the gamma-ray induced particle shower in order to reconstruct the properties of the

[2] An electron-induced shower and a photon-induced shower will differ in size by one radiation length.

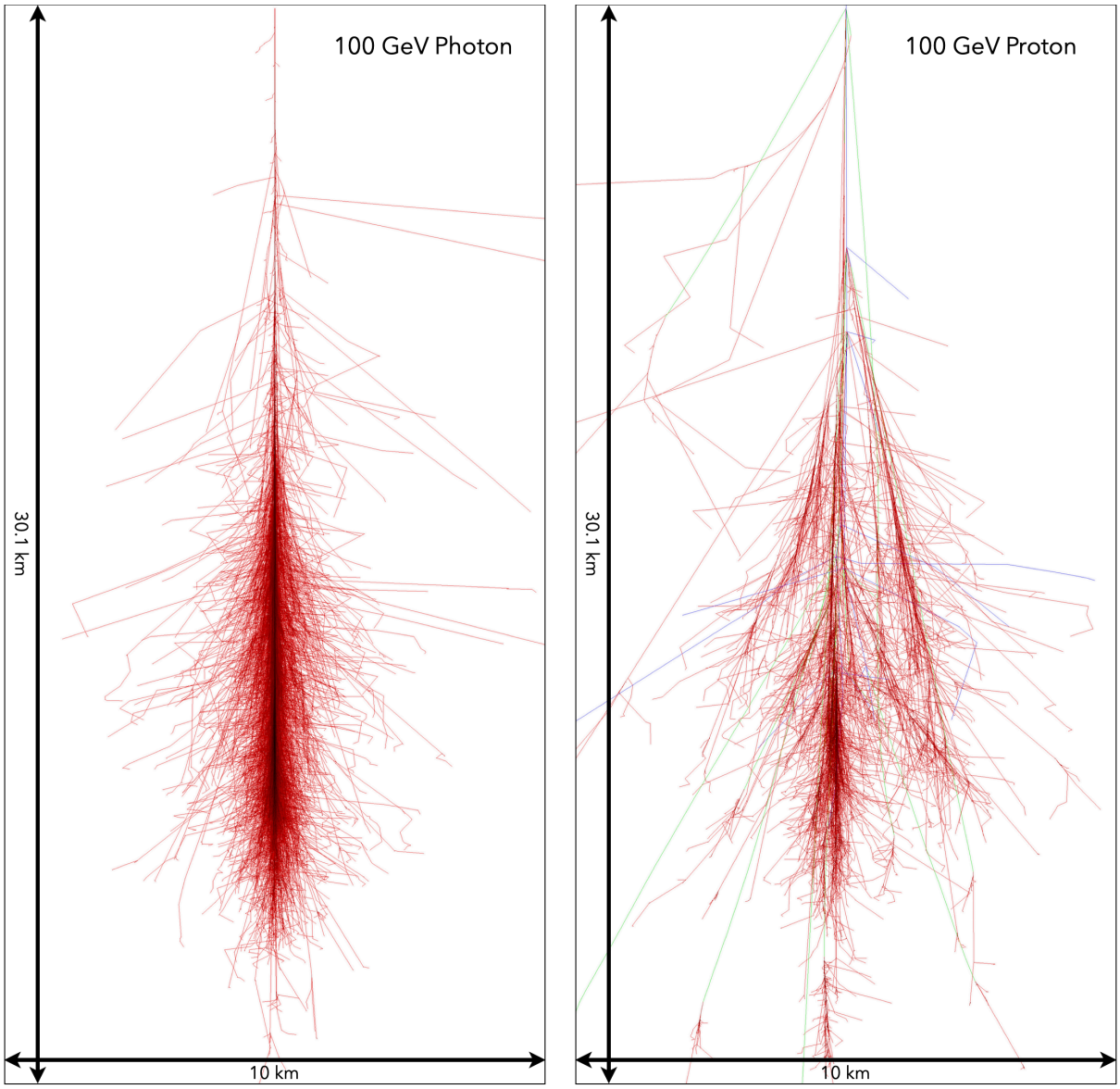

Figure 2.6: Monte Carlo simulations of the shower development of a 100 GeV gamma ray (left) and a 100 GeV proton (right) [8]. Red tracks show the path of electrons, positrons, and gamma rays. Green tracks show muons, blue tracks show hadrons.

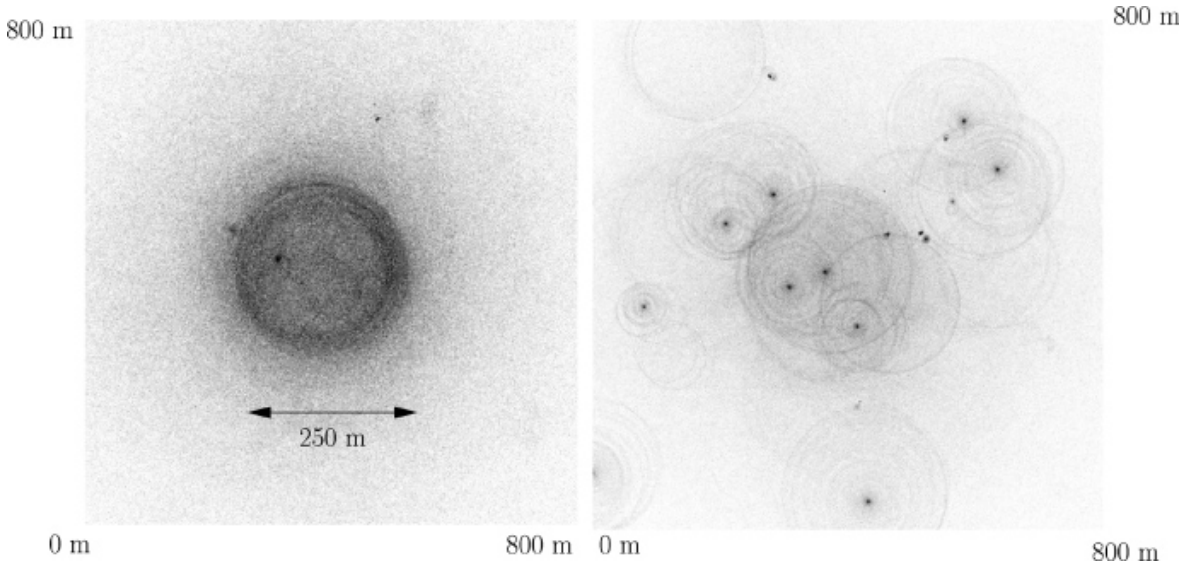

Figure 2.7: Figure 8 from [9], used with permission. The simulated light pool of a 300 GeV gamma ray (right), and a 1 TeV proton (left).

primary gamma-ray photon. Here we focus on gamma-ray instruments designed to observe the shower via the Cherenkov light produced in the atmosphere: Imaging Atmospheric Cherenkov Telescopes (IACTs), though it is also possible to observe the remnants of the particle shower that reach the ground, as is the case in Extensive Air Shower arrays such as MILAGRO [128], ARGO-YBJ [129], The Tibet Air Shower Array [130], HAWC [111], and LHAASO [71].

At the most basic level, the Imaging Atmospheric Cherenkov technique involves the use of a large mirror to focus Cherenkov photons onto a photon sensitive camera connected to an oscilloscope. This technique was first demonstrated by Galbraith and Jelley in 1953 [99], who used a 0.2 m^2 mirror and a single photomultiplier tube (PMT) to measure pulses from Cherenkov showers at a rate of ~ 1/minute. The design goals of IACTs are driven by the characteristics of Cherenkov light. The most basic requirement is the need to detect the signal from Cherenkov photons above the background light of the night sky (stars, airglow, artificial lighting, etc.). Following Weekes [117], the number of photoelectrons S collected by the telescope depends upon the observed Cherenkov photon density spectrum $C(\lambda)$ $(\frac{\text{photons}}{\text{area}\times\text{wavelength}})$, the wavelength-dependent

response of the PMT $\eta(\lambda)$, the mirror collection area A, and the mirror reflectivity $R(\lambda)$:

$$S = \int_{\lambda_1}^{\lambda_2} C(\lambda)\eta(\lambda)R(\lambda)A\mathrm{d}\lambda \tag{2.10}$$

Where $\lambda_{1,2}$ are the bounds of the PMT sensitivity. This signal is then superimposed on the background light from the night sky. If a temporally-steady night sky flux $W(\lambda)$ ($\frac{\text{photons}}{\text{area}\times\text{wavelength}\times\text{time}\times\text{solid angle}}$) is assumed, we can similarly write the number of night-sky photons collected during a period τ:

$$B = \int_{\lambda_1}^{\lambda_2} W(\lambda)\tau\eta(\lambda)R(\lambda)A\Omega\mathrm{d}\lambda \tag{2.11}$$

Unlike the Cherenkov signal, the night sky signal is isotropic and steady, and therefore depends on both solid angle Ω and time τ. The fluctuation (noise) due to the night sky background is $\sqrt{B}$. The signal-to-noise ratio $S/N = S/\sqrt{B}$ therefore increases with the square root of PMT response and mirror area, and decreases with the root of collection time and solid angle:

$$\frac{S}{N} \propto \left(\frac{RA\eta}{\tau\Omega}\right)^{\frac{1}{2}} \tag{2.12}$$

The flux of the weakest detectable pulse, and therefore the energy threshold of the telescope, is inversely proportional to S/N. The inverse proportionality between signal-to-noise and collection time τ assumes that τ is at least large enough to contain the Cherenkov pulse. The typical time of the pulse is only $\sim 3-5$ ns; very fast charge collectors/digitizers are therefore desirable to keep τ as small as possible while still being large enough to contain the pulse. The first IACTs utilized charge integration instruments with fixed integration windows; the current generation of instruments utilize rapid signal digitizers capable of sampling the light pulse at GHz frequencies, leaving the charge integration to be performed computationally. Increased mirror area results in a higher signal-to-noise ratio as well as a lower energy threshold. Large mirror areas are therefore desirable; modern IACTs have mirror areas as high as ~ 600 m^2.

Because the Cherenkov shower has a characteristic size of up to a few degrees, and the smallest meaningful structures are still on arcminute scales, the requirements for the reflector are significantly relaxed compared to instruments used for optical astronomy. A simple tessellated array of $\sim$ hundreds of small mirror segments suffices to effectively image the shower at significantly lower cost than a completely smooth reflector. The efficiency of the mirror must also be taken into account; the best mirrors will reflect 90% of the incident light, but will significantly degrade with age [131]. Lower mirror reflectivity effectively reduces the size A of the mirror.

Multiple PMTs are also required in order to image the shower. The camera must at least be large enough to completely image Cherenkov showers, which may subtend $\sim$ a degree, and will be offset from the camera center by another $\sim$ degree, depending on horizontal distance from the shower. The camera should therefore be at least $\sim 2^\circ$ in diameter. A larger field of view will enable the imaging of more distant showers, which increases the effective area for high-energy showers. In addition, it allows for imaging of more extended gamma-ray sources, which may subtend several degrees. The PMTs should be small enough to sample the details of the shower, not more than a few arcminutes. Smaller pixel sizes result in higher resolution shower images, which increases angular resolution and cosmic-ray background rejection, but may also lower the signal-to-noise ratio. The PMT response η is primarily characterized by the quantum efficiency of the tube, which is typically $\sim 30\%$ [132].

When imaged in such a camera, the Cherenkov light will resemble an ellipse. The major axis of the ellipse is determined by the longitude of the shower; the width of the ellipse reflects the lateral development. The minor axis corresponds to the point of maximum shower development. Because the longitudinal axis of the shower is the same as the initial trajectory of the photon, the major axis of the ellipse indicates the direction of origin of the primary photon. A single telescope can then constrain the origin of the gamma ray to a single dimension (i.e. somewhere along the line defined by the major axis of the ellipse). In contrast to the relatively compact gamma-ray initiated showers, showers of hadronic origin are significantly longer and more broad

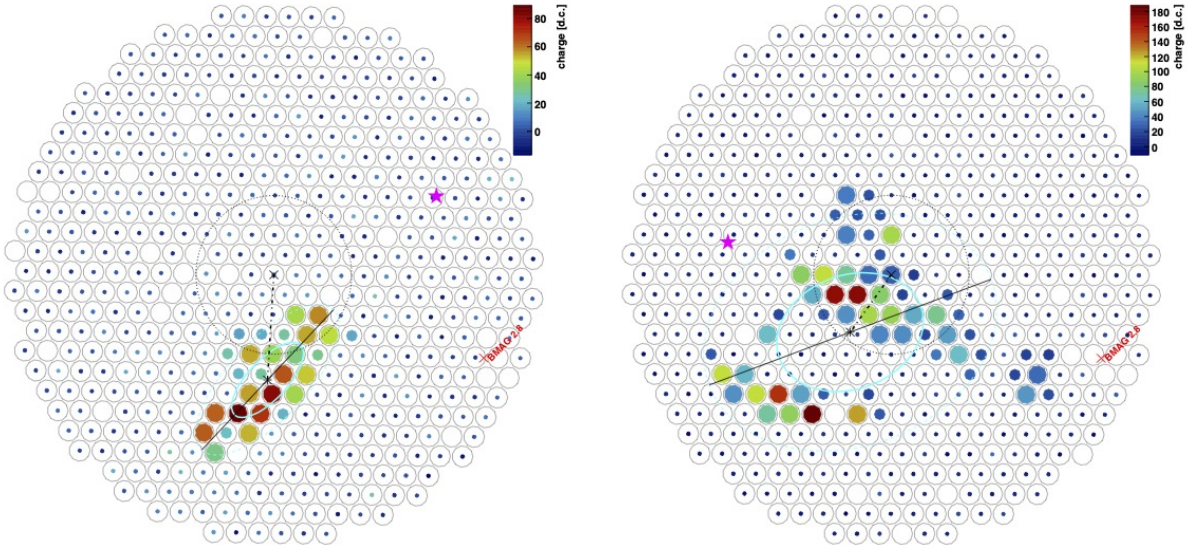

Figure 2.8: A gamma-ray initiated Cherenkov shower (left) compared to a cosmic-ray initiated shower (right) as imaged in the camera of an IACT. The light blue circles show an attempted elliptical parameterization of each image.

(Figure 2.6). This dramatic difference in the morphology (see Figure 2.8) allows for extremely efficient discrimination between gamma-ray and hadron initiated showers (e.g. [133]), which can overcome the otherwise overwhelming background of cosmic rays.

The unique nature of the Cherenkov light pool (steady emission over a ~ 120 m radius) has the important consequence that the effective collection area of the detector far exceeds the mirror surface area. A detector placed anywhere within the lightpool will be able to observe the light pulse, resulting in an effective area of $\sim 5 \times 10^4$ m^2. This exceeds the effective area of space-based instruments by nearly five orders of magnitude, and allows for the observation of gamma-ray sources above $\sim$ hundreds of GeV despite the very weak fluxes at such high energies.

The performance of an IACT observatory can improve dramatically if more than one telescope is used to image the light pulses. As long as the telescope spacing is not too sparse (distance between telescopes $\lesssim 120$ m), the effective area scales with the geometric size of the telescope array rather than the size of the light pool, which can more than double the effective area, compared to that of a single telescope. In addition, the use of multiple telescopes enables effective reconstruction of the original photon direction by intersecting the major axes of the images, as illustrated in Figure 2.9. The precision of this technique improves with the number of telescope images. With the large effective areas and precise event reconstruction offered by IACT arrays, modern IACT instruments are able to detect Crab-strength sources in under a minute, reconstruct photon energies to within $\sim 15\%$, and resolve gamma-ray sources down to $\sim$ arcminute scales [109]. The coming Cherenkov Telescope Array Observatory (CTAO) represents the next generation of IACTs. It will utilize innovative design and modern technology to greatly improve upon the performance of current IACTs. This is briefly discussed in Chapter 8.

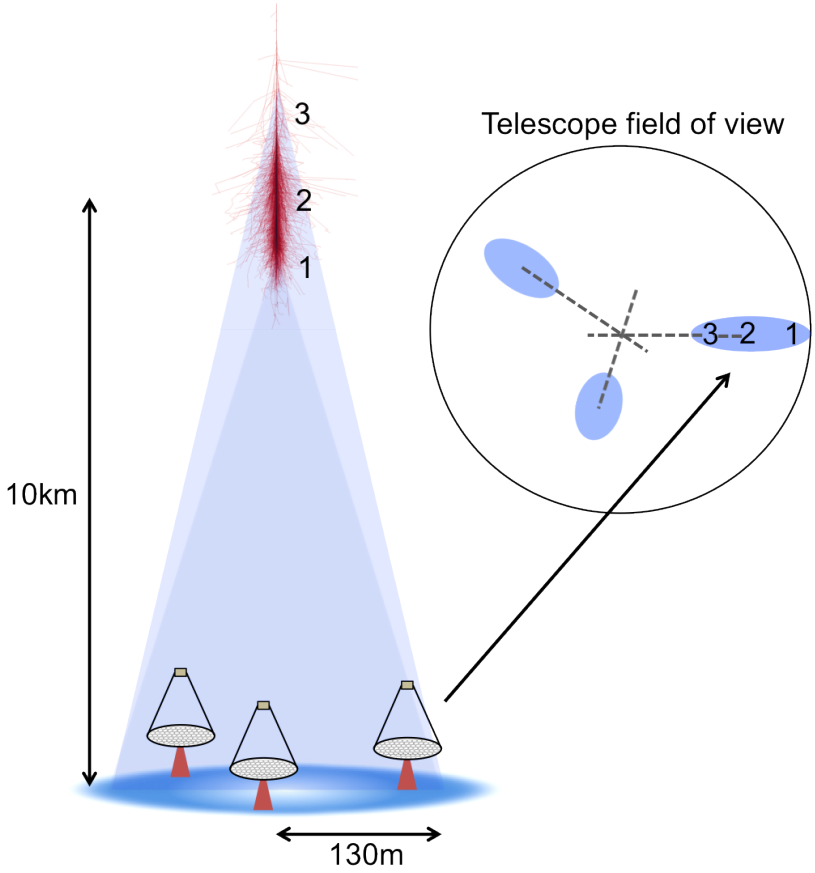

Figure 2.9: Figure 5 from [7]. Three telescopes within the lightpool capture images of the gamma-ray shower. The intersection of the major axes of the images indicates the initial direction of the photon.

Chapter 3

THE VERITAS OBSERVATORY

VERITAS (the Very Energetic Radiation Imaging Telescope Array System) is an array of Imaging Atmospheric Cherenkov Telescopes (IACTs) located in southern Arizona. The array, pictured in Figure 3.1, consists of four individual telescopes and is designed for observations of VHE gamma rays within the $\sim$ 85 GeV - $\sim$ 30 TeV energy range. VERITAS is located at the Fred Lawrence Whipple Observatory near Tucson, Arizona at 31° 40′ 30.21″ N, 110° 57′ 07.8″ W and sits at an altitude of 1268 meters. Here we review the design and specifications of the VERITAS array including the optics, camera and electronics, and data acquisition.

Figure 3.1: The VERITAS array in southern Arizona.

3.1 Optics

Each VERITAS reflector comprises a 12-meter aperture reflector with a 12-meter focal length making it an $f/1$ system. The reflector follows a Davies-Cotton design [134], which makes use of many identical, spherical mirror facets. The mirror consists of 350 hexagonal facets measuring 60.96 cm in width [131], giving the mirror a total area of ≈ 110 m^2. Each facet has an identical 12-meter focal length and has its axis facing the point $2f = 24$ meters from the telescope center (see figure 3.3). Each facet is fixed to a triangular frame with adjustable screws, enabling manual alignment. Precise alignment of the facets is necessary to minimize the point spread function (PSF) of the reflecting surface. The alignment of individual facets can be determined following the procedure outlined by McCann et al [11]: a digital camera placed at the focus of the telescope images the reflecting surface as the telescope scans a grid of points in the vicinity of a bright star. Facets which are aligned correctly are brightest when the telescope points directly at the star; misaligned facets are brightest when the telescope points away from the star by an angle equal to twice the misalignment angle. In this way, the optimal pointing angle for each individual facet can be determined; the facets pointing can be adjusted using the three screws on the triangular frame on which it is mounted. This alignment results in an optical PSF of $\sim 0.05^\circ$ at an elevation of $\sim 70^\circ$(figure 3.4, left). The PSF varies slightly with elevation due to flexure of the optical support structure (figure 3.4, right). The facets are coated with ~ 180 nm of aluminum and anodized to increase mirror longevity. The mirror reflectivity is determined by comparing the image of a star with its focal-plane reflection in the same field of view [135], with typical values of $\sim 70 - 80\%$. The mirrors are continuously exposed to the Arizona desert, which makes frequent re-coating necessary. The VERITAS mirror facets are cleaned and re-coated every few years, typically resulting in a $\sim 5-10\%$ increase in reflectivity.

The simplicity of the Davies-Cotton design is its primary advantage (identical mirror facets are easier and less expensive to produce), along with the small off-axis aberration compared to similar designs (i.e. parabolic) [136, 137]. A drawback of the design is a significant time spread in the arrival times of photons in the focal plane from

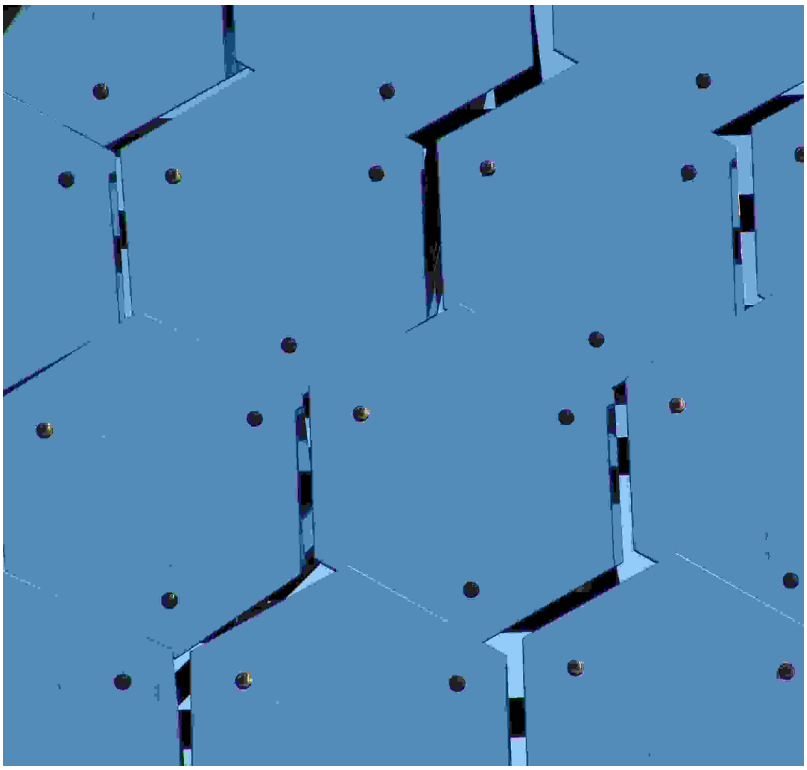

Figure 3.2: Close up view of VERITAS mirror facets.

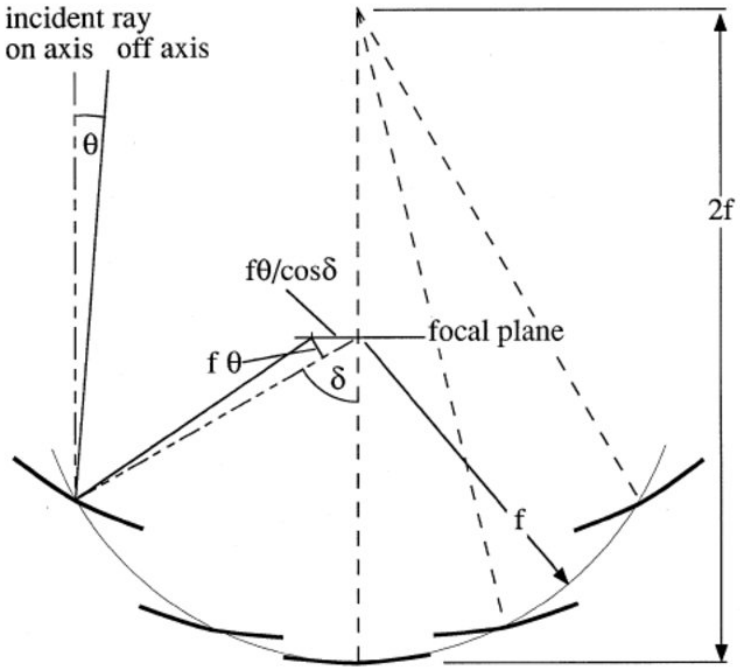

Figure 3.3: Figure 1 from [10]. A schematic of the Davies-Cotton design.

different areas of the mirror, which can be on the order of the timescale of Cherenkov pulses (a few ns) for large mirror diameters ($\gtrsim$ 15 m) [10].

The mirror facets are affixed to a tubular steel optical support structure (OSS) to form the mirror of the telescope. A quadrapod fixed to the OSS holds the camera, whose weight is balanced by counterweights extending behind the OSS. A single telescope is pictured in Figure 3.5.

The telescope pointing is handled by an altitude-over-azimuth positioner which is capable of $\sim 1^{\circ}$/s slew speeds. Telescope pointing measurements, as determined by an encoder coupled to the positioner, are recorded at a rate of 4 Hz and written to a database. Data from the encoder are supplemented by the VERITAS Pointing Monitor (VPM), which consists of CCD cameras at the base of each reflector. These cameras image the sky in the direction of the telescope pointing, and use the positions of observed stars to determine the actual pointing of the telescope. Pointing measurements recorded by the VPM are recorded at a rate of 0.5 Hz, and can determine the absolute

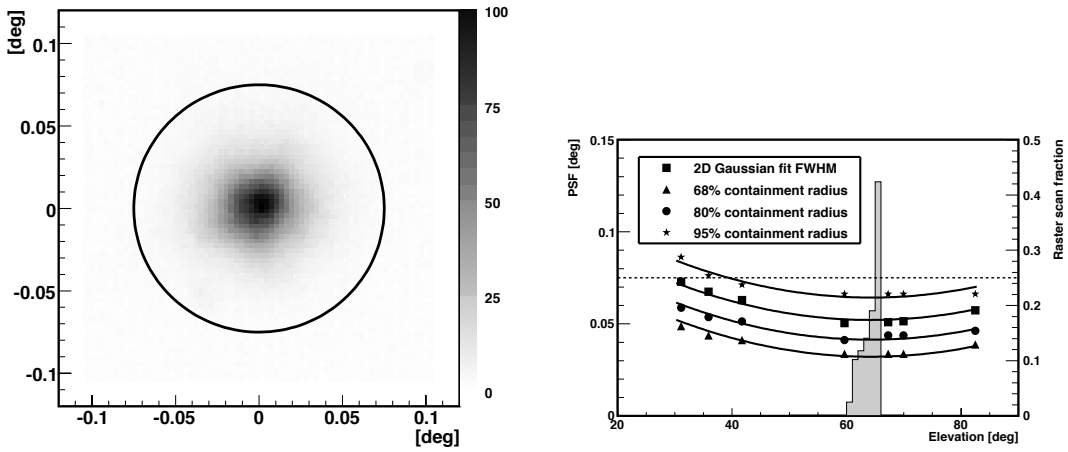

Figure 3.4: Figures 6,7 from [11]. *Left:* The optical PSF at 70°. The solid circle denotes the size of the PMT. *Right:* The optical PSF as a function of elevation. The dashed line denotes the PMT radius. The histogram shows the distribution of elevations at which the facet alignment was optimized.

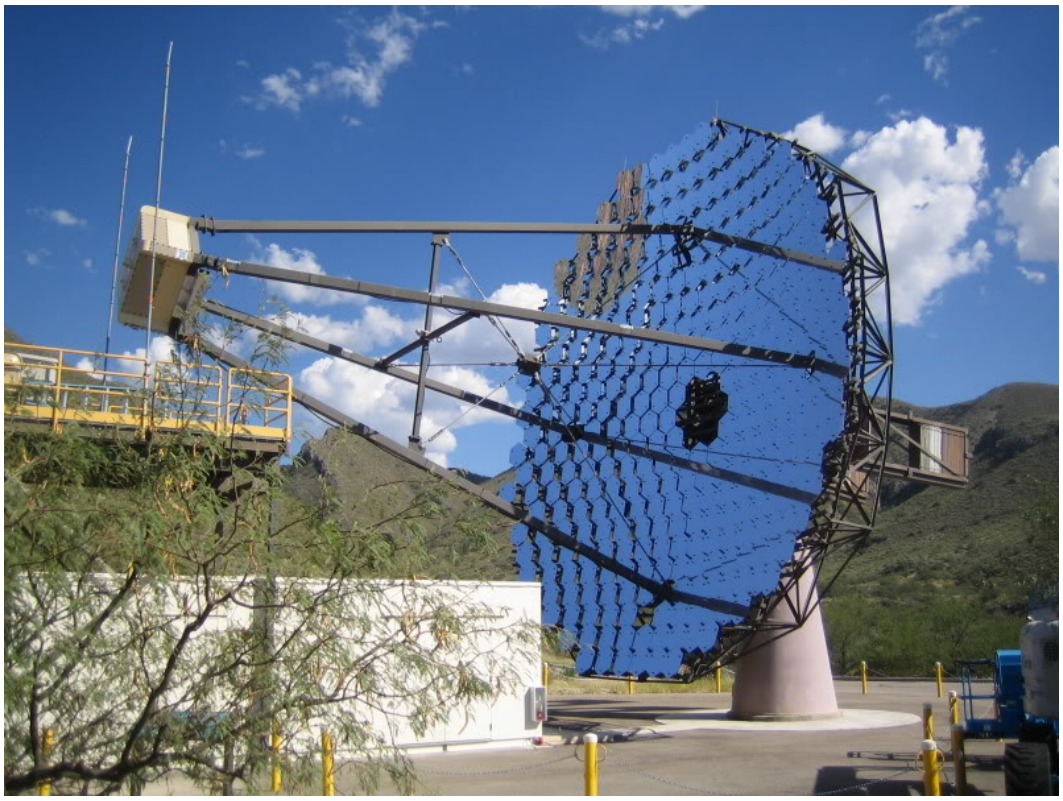

Figure 3.5: A single VERITAS telescope.

pointing of the telescopes with an accuracy of $\lesssim 20''$ [138].

3.2 Cameras

Each telescope is equipped with a 1.8-m camera box which lies in the focal plane of the telescope. The camera consists of 499 2.86-cm pixels arranged in a hexagonal grid with 0.15° spacing, resulting in a 3.5° overall field of view (FOV). A picture of a VERITAS camera is shown in Figure 3.6. A single pixel consists of a photomultiplier tube (PMT) which is coupled at its base to a preamplifier. Each pixel is equipped with a Winston cone light concentrator, which reduces the dead space between pixels and also shields off-axis background light. The cones increase the light-collection efficiency of the camera from $\sim 55\%$ to $\sim 75\%$ [139].

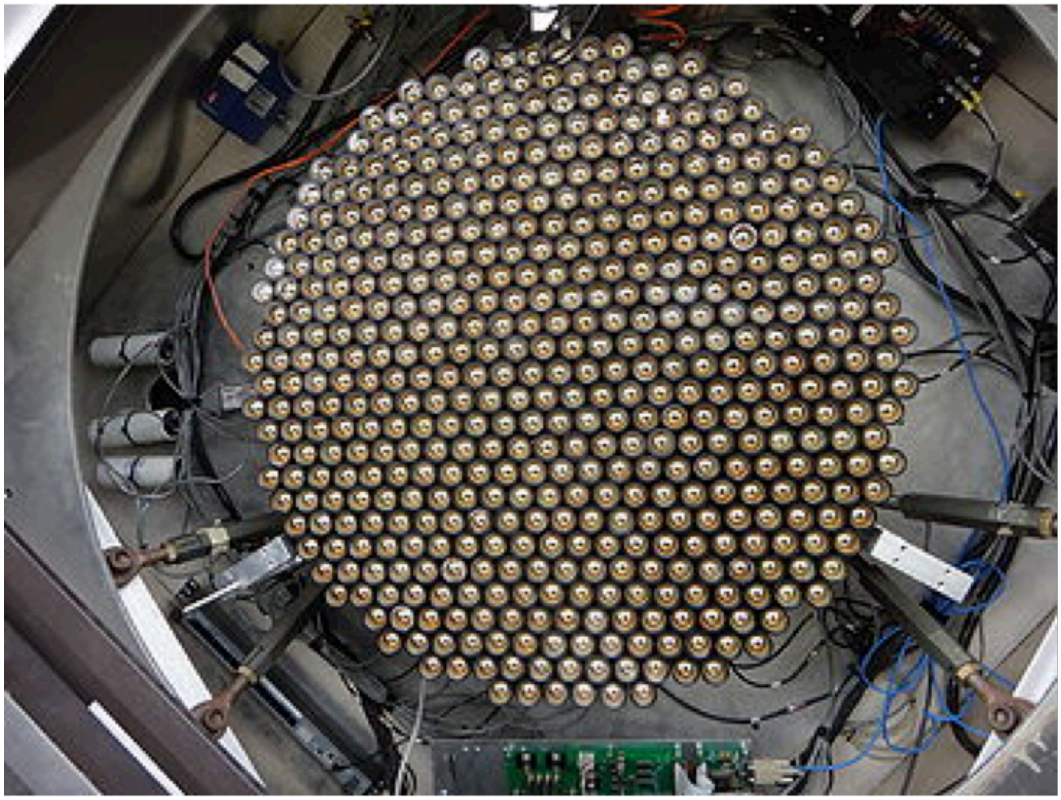

Figure 3.6: A VERITAS camera, consisting of 499 individual photomultiplier tubes. Image from [12].

3.2.1 Photomultiplier tubes

Photomultiplier tubes are sensitive light detectors which use electric fields and dynodes to multiply the electrons emitted by incoming photons via the photoelectric effect. These detectors are characterized by low noise, high gain, and fast response. PMTs consist of photocathode, a series of dynodes, and an anode. A photon incident on the photocathode will cause an electron to be ejected. A ~ 100 V potential difference between the cathode and first dynode directs the electron toward the dynode, where it collides and releases several more electrons. Each of these electrons is again accelerated toward the next dynode in the chain via a similar potential difference where they each eject several more electrons. The result is an exponentially growing number of electrons corresponding to the initial photon. This process is sketched in the top panel of figure 3.7. If a PMT has M identical dynodes, and each dynode emits α electrons per incident electron, then the number of electrons leaving the anode N (the *gain* of the PMT) is:

$$N = \alpha^M \tag{3.1}$$

Typical PMTs have $\alpha \sim 4$, $M \sim 10$, resulting in gains of $\sim 10^6$. An incident photon will therefore result in a short pulse of current. The electron emission ratio α, and therefore the PMT gain, depends on the dynode potential difference. Typically α is proportional to some power of the potential difference ΔV [13]:

$$\alpha \propto \Delta V^{\rho} \tag{3.2}$$

With $\rho \sim 0.7 - 0.8$. The overall gain therefore depends on applied voltage:

$$N = \alpha^M \propto \Delta V^{\rho M} \tag{3.3}$$

Typically $\Delta V \sim 100$ V, and so ~ 1 kV is required to power the entire dynode chain. The strong dependence of gain upon potential difference ($N \propto \Delta V^{6-10}$) necessitates a stable voltage supply. Electronic noise within the PMT (dark currents)

mostly arises from thermionic emission and is unavoidable. For IACTs, this noise is subdominant to the noise of the night-sky background light.

The finite transit time of electrons through the PMT, along with the dispersion of these transit times, forms a distinct pulse shape, typically characterized by the shape of the leading edge (the rise time, usually defined as the time over which the pulse increases from 10% to 90%), the width of the pulse (usually the full width at half maximum), and the fall time (the time, on the falling edge, over which the pulse decreases from 90% to 10% of the maximum value). Thus even a delta function input will result in a finite pulse shape (figure 3.7, bottom). The characteristic time for all of these features is typically on the order of a few nanoseconds, with faster rise times than fall times.

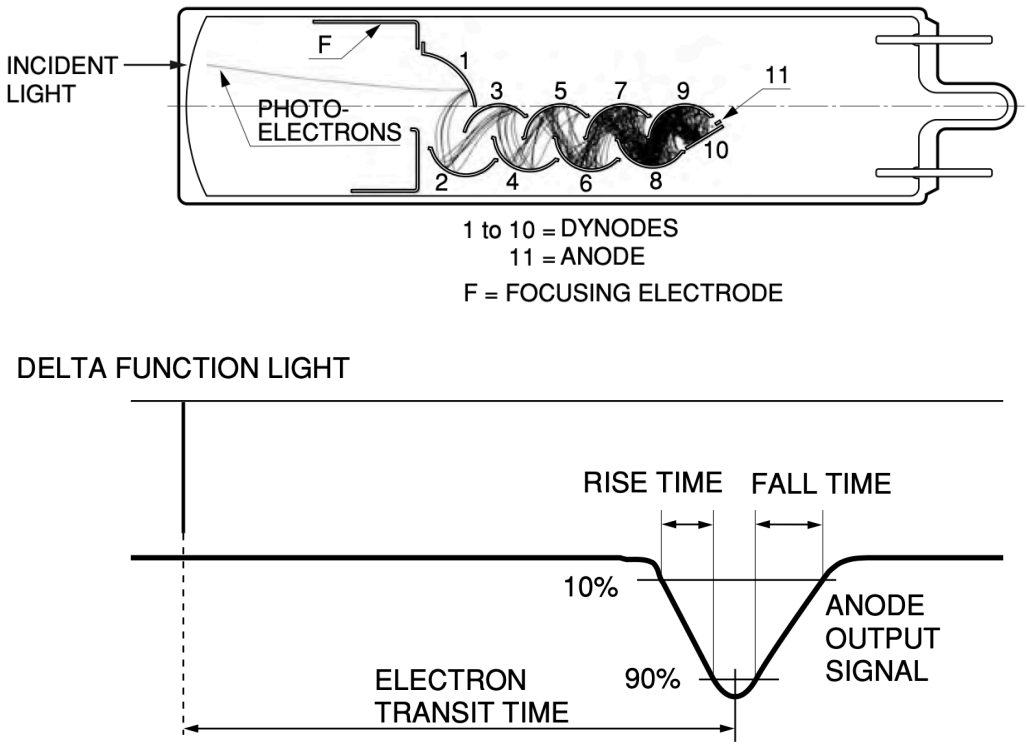

Figure 3.7: *Top:* Figure 2-5 from [13]. A schematic of the signal amplification of an incident photon. *Bottom:* Figure 4-16 from [13]. A delta function incident on the PMT is dispersed to form a finite pulse.

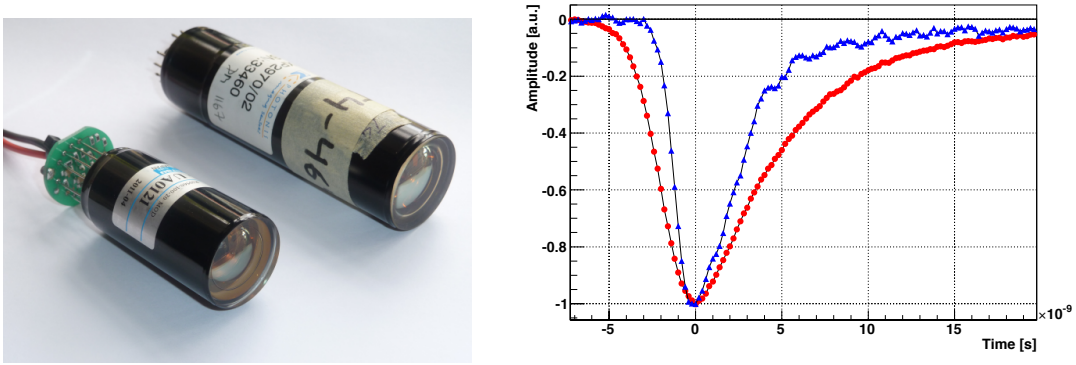

Figure 3.8: *Left:* Figure 1 from [14]. A photograph of the old XP2970 PMT (back) and the new R10560 PMT (front). *Right:* Figure 2 from [14]. The single-photon pulse shape of the old (XP2970) tube (red circles) compared to the new R10560 (blue, triangles). The pulses are normalized to the same amplitude.

The sensitivity of a PMT is expressed as the photon detection efficiency (PDE, the probability of detection of an incident photon). This quantity primarily depends on the quantum efficiency (QE) of the photocathode (i.e. the probability of a photon producing a photoelectron) and the collection efficiency of the PMT (i.e. the probability that a photoelectron successfully enters the dynode chain). Typical values are QE$\sim 20-40\%$, collection efficiency $\sim 70-90\%$, leading to PDE $\sim 20-30\%$. The QE, and thus the PDE, is variable with wavelength, peaking around ~ 400 nm.

The VERITAS cameras are operated at a gain of 2×10^5. The voltage necessary to achieve this gain (typically $\sim$ 1 kV) can be determined by observing the pixel response to a single photon at different voltages. From first light until 2012, the pixels utilized the Photonis XP2970/02 PMT, with 10 dynodes, QE$\sim$ 25%, and a pulse width of 6.8 ns [139, 14]. These were replaced in 2012 with Hamamatsu R10560-100-20 MOD PMTs (Figure 3.8, left), with 8 dynodes, QE$\sim$ 35%, and a pulse width of 4.2 ns [14]. The increase in light yield allows for the detection of fainter (and thus lower energy) showers. The smaller pulse width (Figure 3.8, right) allows for shorter integration times, which decreases the overall contribution of the night-sky background. Both of these improvements lowered the energy threshold of the array from $\sim$ 100 GeV to $\sim$ 70 GeV [14].

The signal from the PMT anode is amplified before traversing $\sim$ 180 feet of coaxial cable. This is accomplished via custom made preamplifiers at the base of the PMT, which amplify the current by a factor of 6.6. It is important that this amplification take place near the PMT, to avoid amplifying electronic noise in the cable. The preamplifier also provides a direct DC output to allow for monitoring of the anode currents. This is primarily necessary to ensure the safety of the highly-sensitive PMTs. Anode currents typically range from $\sim 4 - 8$ μA. The camera is housed within a camera box attached to the OSS which is equipped with a remotely operated shutter to protect the tubes during the day. Temperature and humidity monitors are also kept within the box to ensure the operating conditions are safe, as well as fans to cool the camera if the ambient temperature is too high. The PMT voltage is supplied by a commercial power supply which is capable of individually controlling each of the 499 pixels.

3.3 Trigger

The PMT outputs are transmitted along $\sim$ 180 foot coaxial cables threaded through the quadrapod arm and telescope pedestal into a trailer which houses the data acquisition electronics. Continuous $\sim$GHz frequency data collection is not feasible; the array is therefore designed to be self-triggering in order to preferentially select Cherenkov images and to maintain sustainable deadtime from the data acquisition system.

3.3.1 Level 1 Trigger

The Level 1 (L1) trigger acts at the single pixel level. It requires that the PMT pulse height exceed some pre-determined (and programmable) threshold voltage. This is determined by a custom made constant fraction discriminator (CFD), for which the trigger time is independent of pulse height [140]. A pulse $V(t)$ entering the CFD is split into three pulses. One pulse is delayed by a time τ and inverted, another is scaled

down by f where $|f| < 1$. The mechanism triggers when the sum of these pulses, called the zero crossing discriminator (ZCD) is zero:

$$V_{\mathrm{ZCD}} = f \cdot V(t) - V(t - \tau) = 0 \tag{3.4}$$

A small offset voltage V_0 is added to V_{ZCD} in order to reduce jitter in the trigger time. The VERITAS CFD is equipped with a separate circuit, known as the rate feedback loop, which serves to couple V_0 to the ZCD trigger rate, adjusting V_0 and reducing trigger time jitter for different night-sky background intensities.

The L1 trigger pulse is sent if the threshold discriminator, which requires that the pulse height exceed some pre-determined voltage (typically $\sim$ 45 mV), and the zero crossing discriminator both trigger. The output pulse is sent as a 4-25 ns length pulse (programmable in 12 steps). The trigger pulse can be delayed by up to 6 ns to compensate for differences in pulse transit times between PMTs, caused by differences in voltages and cable lengths.

3.3.2 Level 2 Trigger

The Level 2 (L2) trigger employs pattern recognition logic to require L1 triggers in multiple adjacent pixels. This reduces the rate of accidental triggers due to fluctuations in the night-sky background by several orders of magnitude. The original VERITAS L2 trigger followed the design of the Whipple telescope [141]. Pixels were organized into overlapping groups of 19 pixels each, in order to recognize adjacency patterns of up to four pixels within a hexagonal arrangement. The L1 output from several groups of pixels was routed to one of 19 pattern selection triggers (PST) [15]. The PST compared the observed pattern of triggered pixels against a store of adjacency patterns in its memory, and triggered if the observed pattern matched a predetermined trigger adjacency pattern within a given coincidence window, usually $\sim 8 - 10$ ns.

The L2 trigger was upgraded in 2011 to decrease the size of the coincidence window [142]. The new system utilizes three overlapping groups of pixels which are grouped into cells of up to six pixels each (a central pixel and up to six neighbors).

The coincidence logic is handled by a field-programmable gate array (FPGA) which determines the trigger status of each cell by comparing the trigger pattern to the patterns stored in memory. The FPGAs allow for the L1 signal from individual pixels to be delayed by a programmable amount (up to $\sim$ 10 ns with a resolution of 72 ps) to account for the finite transit time of the PMT pulse and L1 signal [142]. The delay for each pixel can be estimated by measuring the arrival time of the L1 trigger using a controlled light source, usually a flashing LED [143]. When properly calibrated, the dispersion in L1 pulse arrival times is reduced from $\gtrsim$ 1 ns to $\lesssim$ 200 ps [142]. The optimal coincidence window for the pattern recognition is correspondingly reduced to 5 ns.

3.3.3 Level 3 Trigger

The level 3 (L3) trigger operates at the array level, and requires that multiple telescope L2 triggers occur within a predetermined coincidence window. The L2 triggers for each of the four telescopes are sent to the centrally-located L3 subsystem via optical fiber using custom-made Digital Asynchronous Transceiver modules (DATs) [144].

Variation in the L2 arrival time is introduced by differing cable lengths as well as the differences in arrival time of Cherenkov photons between telescopes. The former can be dealt with precisely, the latter is approximated based on the current pointing position of the telescopes every $\sim$ 5 seconds. Based on these calculations, the L2 pulses are delayed by a custom-built 32-channel VME Pulse Delay Module (PDM), capable of delaying incoming signals by 100 ns - 16μs with a 2 ns resolution. The time-aligned pulses are routed to the SubArray Trigger board (SAT). The SAT assigns a digital time stamp to each incoming trigger with 1.25 ns resolution and then compares the pattern of L2 triggers to pre-programmed configurations. The system is triggered if the patterns match and are contained within a pre-programmed coincidence window. During normal operations, VERITAS requires a minimum of two telescope triggers within a 50 ns window, resulting in a L3 trigger rate of $\sim$ 400 Hz.

3.4 Data acquisition

The PMT pulses from each telescope are continuously digitized with 8-bit resolution by 500 MHz Flash Analog to Digital Converters (FADCs) housed in the electronics trailer [145]. Ten channels feed into an FADC module; 50 modules spread among four VME crates process the 499 channels of a single telescope. Typically, the number of "digital counts" output by the FADCs is ≈ 5.4 per incoming photon. By default, the PMT pulse follows a high-gain path to the digitizer; an analog switch is thrown if the signal exceeds a pre-determined threshold which sends the signal along a low-gain path where the gain is reduced by a factor of 6. This increases the dynamic range of the system, effectively increasing the maximum observable gamma-ray energy.

The signal from each PMT is digitized and stored, in 2-ns samples, with a memory depth of 64 μs. When the entire array is triggered (an L3 trigger is generated), a signal is sent by the L3 subsytem to each telescope. Upon receipt of the L3 signal, the crates select a portion of the digitized PMT signal, typically 16 samples (32 ns) and store it. The incoming L3 signal is intentionally delayed so that the signal is received a fixed amount of time after the L2 trigger was produced by the telescope. The data acquisition system then looks back within the 64 μs memory depth by this amount of time, typically ~ 3 μs, to find the start of the desired PMT signal [15]. The FADCs are unable to process new L3 triggers during the readout process, resulting in ~ 400 μs of "deadtime" after each trigger.

The data from each channel are stored in their respective crates and buffered; the buffers from all crates are asynchronously sent to a telescope-level computer, called the "Event Builder", when they reach a size of 8 MB [146]. The Event Builder combines data from every PMT according to the L3 trigger that generated it; i.e: a telescope "event" consists of the 16 sample window from all 499 PMTs following an array level trigger. Telescope events are gathered in a FIFO buffer which is asynchronously polled by a central, array-level process known as the "Harvester".

As the Event Builders are the telescope-level data acquisition processes, the Harvester is the array-level process. The Harvester runs on a single centralized machine

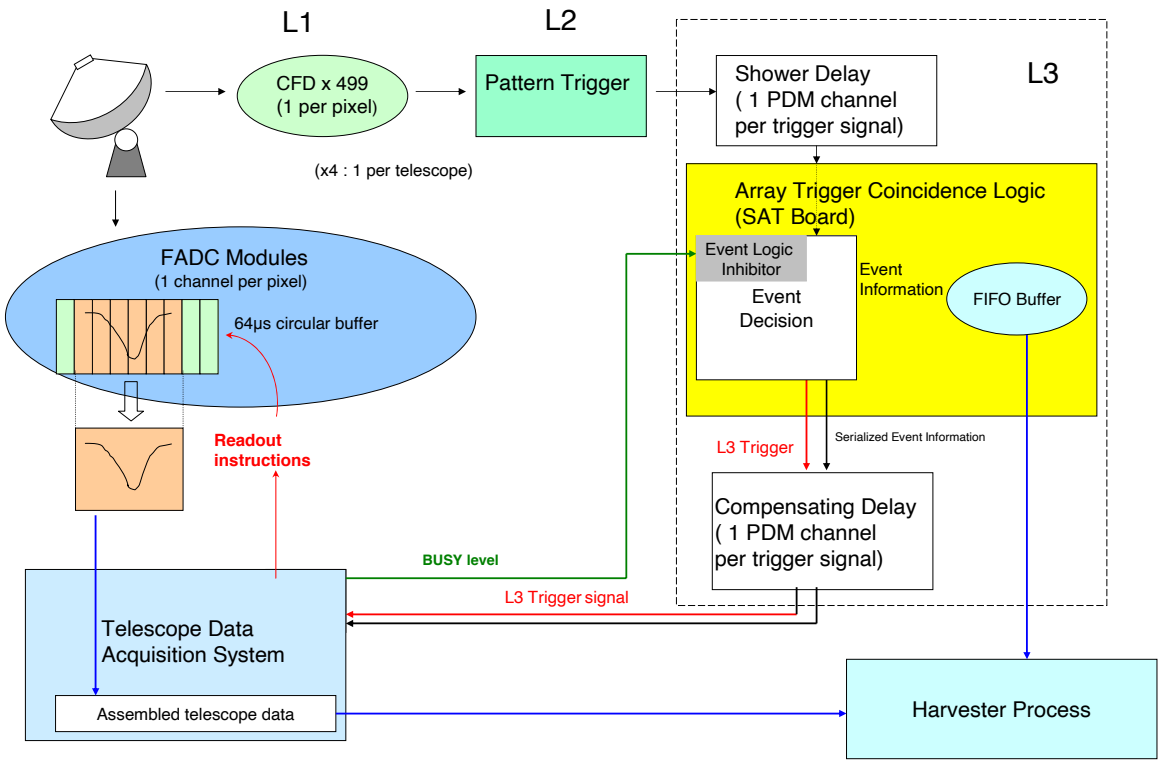

Figure 3.9: A schematic detailing the VERITAS trigger and data acquisition system. From [15]

and is responsible for combining events from each telescope into a single array-level event; each L3 trigger corresponds to an event. These data are combined by matching the unique event numbers assigned to each telescope event by the L3 trigger. The entire process of data acquisition, including the different triggers, is sketched in Figure 3.9. Data are saved to an archive in a custom file format called the VERITAS Bank Format (VBF). VBF is written in C++ and is designed for high-performance reading and writing, as well as efficient compression of the FADC traces. Data are typically taken in 20-30 minutes exposures, or runs: a typical VBF file for a 30-minute run is $\sim 8 - 10$ GB in size. The raw data in the form of VBF files is analyzed by standard VERITAS software; this process is described in chapter 4.

3.5 Major Changes

Since the VERITAS array was first commissioned in 2007, it has undergone two major upgrades: the relocation one of the four telescopes in 2009, and the upgrade of all four cameras in 2012. These upgrades define three basic time periods in the history of the experiment: the period before the movement of the first telescope (2007/09/01-2009/08/31), the period after the telescope relocation but before the camera upgrades (2009/09/01-2012/08/31), and the period after the camera upgrade up to and including the present.

3.5.1 Telescope Relocation

The VERITAS array consists of four individual telescopes, labeled T1-T4. During the first two years of operation, for historical reasons, the four telescopes within the VERITAS array were located in such a way that two of the telescopes, T1 and T4, were only separated by $\sim$ 35 meters, much less than the optimal $\sim$ 100 meters. This resulted in a semi-redundancy between those two telescopes, reducing the stereoscopic potential of the array, as well as the effective collection area. This was addressed during the summer of 2009, when T1 was moved $\sim$ 150 meters east of its original position (see Figure 3.10).

This relocation, together with a separate upgrade to the mirror alignment procedure [11], resulted in a 30% increase in the overall sensitivity of the array [147].

3.5.2 Camera Upgrade

In 2012, all 499 PMTs in each telescope were replaced in with Hamamatsu R10560-100-20 MOD PMTs (Figure 3.8). The new PMTs have a higher quantum efficiency and a narrower pulse width, which reduces the energy threshold of the array while increasing the effective collection area. The upgrade resulted in a 30% reduction in energy threshold and a 20-30% increase in effective area [12].

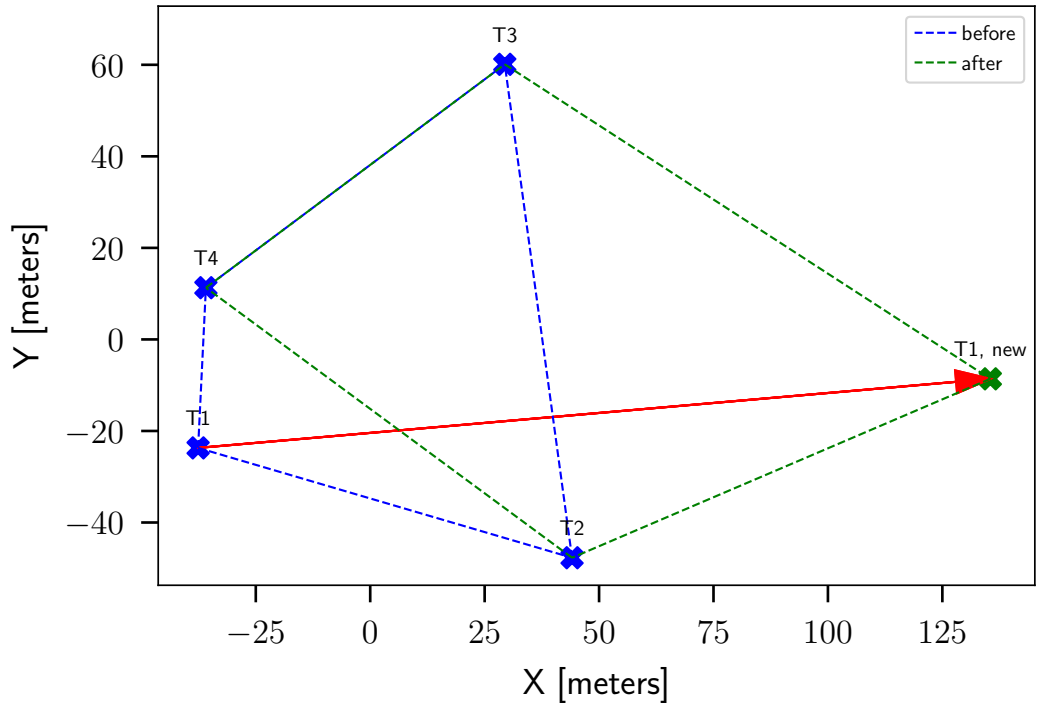

Figure 3.10: The picture illustrates the positions of the telescopes before and after the relocation of T1. The original array configuration is shown in blue, the configuration afterward is shown in green.

3.6 Summary

The full VERITAS array has been operating since 2007, collecting data on a nightly basis except when prevented by bright moonlight or inclement weather[1]. As of the time of writing, the array has been in operation for 17 years. During this time over 15,000 hours of data have been collected, leading to the discovery of 26 new gamma-ray sources and over 100 scientific publications. VERITAS is currently fully funded until 2025 and is planning to submit to another funding cycle. Plans beyond 2028 will depend upon progress of CTAO.

[1] Data collection ceases during the summer months of July-August due to the local monsoon season

Chapter 4

VERITAS DATA ANALYSIS

Data collected by the VERITAS instrument must be processed and carefully analyzed in order to produce meaningful results useful for physical interpretation. VERITAS typically collects data 20-30 minutes at a time in segments known as "runs". The raw data for each run consists of a sequence of "events": instances which caused the entire array to trigger and record data for each telescope. Each event consists of the data from each individual telescope, read out over (usually) a 32-ns time interval. The data from each individual telescope consists of the digitized signal from each individual pixel over the duration of the readout window; the signal is digitized in 2-ns intervals, resulting in a signal vs time series, called a "trace". Recall that the photons collected by the telescope are not gamma-ray photons directly collected from the region of interest; rather they are optical/UV photons created when either a gamma ray or cosmic ray primary generates Cherenkov radiation in the upper atmosphere[1]. The tasks of any analysis chain seeking to make meaning of data collected by an IACT are therefore manifold: the Cherenkov photon data in each pixel must be used to reconstruct the properties (location, brightness and dimensions) of the Cherenkov light which triggered the event; the properties of the reconstructed Cherenkov light are used to determine the energy and identity (gamma ray or cosmic ray) of the primary particle which caused the Cherenkov light; the distributions of the gamma-ray originated events in space, energy, and time are then used to reconstruct the intrinsic properties of the astrophysical source from which they originated. We discuss each step of the process in this chapter.

[1] See chapter 2 for a more detailed discussion of this process

4.1 Calibration

The raw data collected by the telescope consists of FADC traces for every pixel for each event that triggered the telescope. This information can be used to reconstruct the properties of the Cherenkov light which triggered the event, provided that the response of the instrument throughout the process of converting Cherenkov photons to digital FADC counts is precisely known. In order to accomplish this, the response of each pixel to a known amount of light must be measured to obtain a conversion factor from incident photons to digital counts, this is the *absolute* calibration of the instrument. This conversion factor will vary from one pixel to the next, and therefore these non-uniformities in the response of each pixel must also be measured and corrected for. This is part of the *relative* calibration of the instrument, which must also characterize the difference in response time of the pixels across the camera.

4.1.1 Absolute Calibration

Absolute calibration of a pixel yields a conversion factor between the number of digital counts observed in the FADC trace and the number of incident Cherenkov photons. This calibration is necessary in order to determine the energy of the primary particle (or photon) which generated the Cherenkov light, since Cherenkov light yield scales with energy of the primary.

The calibration procedure involves characterizing the response of a pixel to a known amount of light. For the light source, a custom-made assembly of blue light-emitting diodes (LEDs) is used [148]. This assembly, known as the "flasher", is mounted in a box along the axis of the telescope, approximately 4 meters from the camera. The flasher repeatedly illuminates the camera pixels with short ($\sim$ ns long) pulses which are diffused so as to arrive with uniform intensity across the face of the camera. For the calibration, the telescope cameras are flashed at a very low intensity, such that on average the number of photoelectrons produced by each pulse is less than 1 [16]. Extraneous light, including photons from the night-sky background (NSB), is mostly filtered by affixing an aluminum cover over the camera with a 3-mm hole drilled at the

Telescope	Ratio (d.c./p.e.)
T1	5.20 ± 0.18
T2	5.12 ± 0.18
T3	5.12 ± 0.24
T4	5.54 ± 0.17

Table 4.1: The estimated number of digital counts (d.c.) produced by a single photoelectron (p.e.), averaged over all pixels in the camera.

location of each pixel. The resulting spectrum (number of recorded events producing a given number of digital counts) can be used to estimate the single-photoelectron response. The spectrum is assumed to consist of a series of peaks caused by events with 1, 2, 3, or more individual photoelectrons. Events with a greater number of photoelectrons cause a higher number of digital counts, but also occur less frequently, leading to the general shape observed in Figure 4.1. This spectrum can be fit to estimate the single-photoelectron response, assuming the distribution obeys Poission statistics. Recent results from this calibration are shown in Table 4.1.

4.1.2 Relative Calibration

The absolute calibration characterizes the *average* response of a pixel to a known amount of light, but important differences remain between individual pixels which must be corrected for in the analysis. Two different pixels will, in general, respond differently to the same light source. These differences include both the amount of charge generated within the PMT as well the timing of the response. Both effects must be accounted for to properly reconstruct the Cherenkov light.

Relative Gains

The *gain* of a photomultiplier tube characterizes the amount of charge produced within the dynode, as discussed in a previous chapter. The absolute calibration summarized in the previous section determines the average gain of all pixels across the

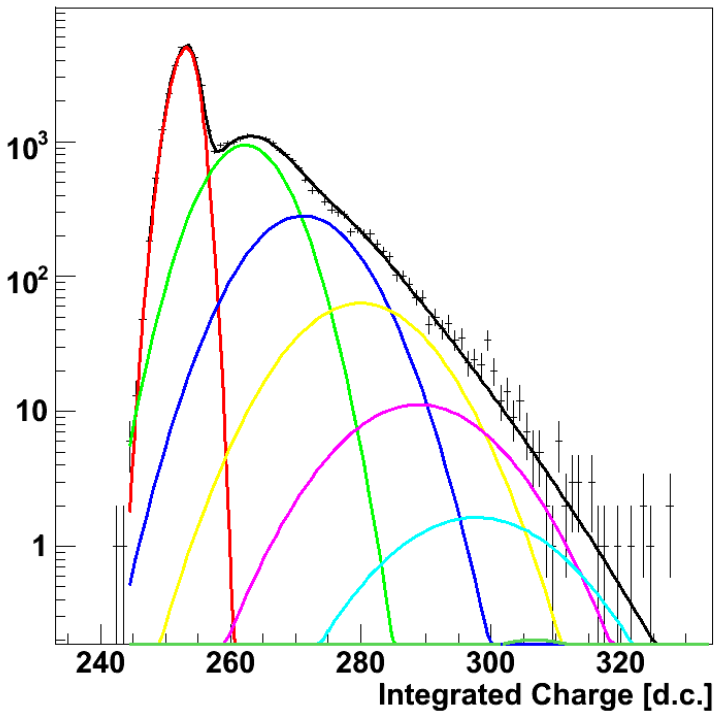

Figure 4.1: A histogram of events binned by number of digital counts, taken from a single-photoelectron calibration run (reproduced from [16]). Different colors show the contributions of different components to the model. The green curve is the contribution from single-photoelectron events, the blue comprises events with two photoelectrons, and so on. The red curve shows the contribution of so called "pedestal events" which will be discussed in an upcoming section.

camera. Because the pixel response is not uniform, flatfielding is necessary. This procedure characterizes the *relative* gain of each pixel, which can then be corrected for in the analysis.

The relative gain of each pixel is estimated using the flasher mechanism discussed in the previous section. This LED flasher repeatedly illuminates every pixel with an approximately uniform intensity of light. For each pixel, the total integrated charge in response to each flasher event is calculated. A histogram is constructed to characterize the distribution of events as a function of charge, which can then be normalized relative to the mean charge across the entire camera. In this way, a multiplicative factor is estimated which can be used to flatfield the camera.

Timing Calibration

The response of a pixel to incident light consists of a time-varying FADC "trace". The relative gain calibration compensates for differences in the size of this trace in response to the same amount of light; yet differences in arrival times of this signal will also generally exist between pixels, due to differences in cable lengths and voltages applied to each PMT. The FADC trace typically consists of 32-ns interval, which is much longer than the duration of a typical Cherenkov event. In order to maximize the signal-to-noise ratio in each pixel, it is therefore desirable to extract only the small subset of the full trace which contains the response to the Cherenkov light. In order to do this it is necessary to calibrate the pixels by characterizing their temporal response to a known light source.

This calibration is also accomplished by analyzing the camera response to events from the LED flasher. For each event and for each pixel, a singular "arrival time" can be calculated by analyzing the FADC trace (typically this time is defined to be the time at which the trace falls to half of its minimum value). A distribution of arrival times can be examined for each pixel, relative to the average arrival time across the camera. An example of such a distribution is shown in Figure 4.2. The mean and width of this

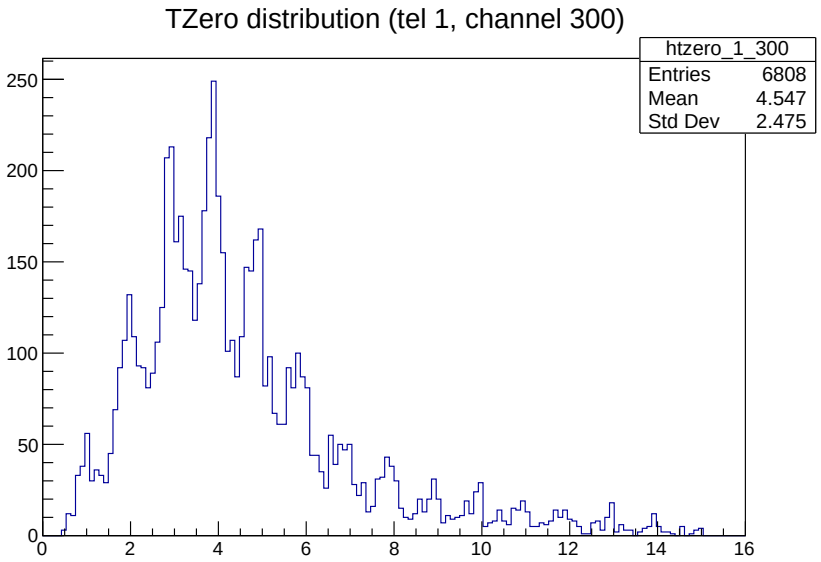

Figure 4.2: A histogram showing the frequency of event arrival time as a function of FADC sample for a single pixel.

distribution can then be used to "temporally flatfield" the camera to correct for this nonuniform response.

4.2 Image cleaning and parameterization

Once the raw data has been calibrated, it is then used to reconstruct the properties of the Cherenkov light from which the event originated. The first phase of this procedure involves estimating and removing background noise from each event; the final phase calculates the geometrical properties of the camera image and uses this information to reconstruct the direction, size, and intensity of the Cherenkov light.

4.2.1 Trace Integration

We seek to associate with each event a single "image", which consists of the distribution of charge (digital counts produced by incident photons) in space (discretized by individual pixels). The data for each pixel (for each event) consists not of a raw amount of charge, but of a time-varying signal which describes charge as a function of time, usually called a *trace*. An example of an FADC trace for a Cherenkov light pulse

event is depicted in Figure 4.3. In order to construct an image, the charge for each pixel for each event is found by integrating the total amount of charge under the FADC trace. This is not as straightforward as directly integrating the entire time series for each pixel; recall that minimizing the integration window (beyond the time period containing the Cherenkov pulse) maximizes the attainable signal-to-noise ratio between photons from the Cherenkov light and photons from the NSB. Care must therefore be taken in how the charge is totaled.

A simple way of accomplishing this is to use the average arrival time of traces in the camera to determine the event arrival time, and then integrate charge within a fixed window (at least $\sim 8-10$ ns) around this time. The results shown throughout this work make use of a slightly more sophisticated method of trace integration: the "double pass" or "two pass" method [17]. As the name suggests, this construction estimates the charge in each pixel twice: the first estimate is an initial approximation which then informs the more precise second estimate. The initial estimate is constructed by using the same integration window for every pixel: a (relatively wide) 20 ns window is used, the start time of which is determined by the average arrival time of pulses in the camera. The resulting image is roughly elliptical, as is characteristic of Cherenkov light. Once the image has been constructed in this manner, the orientation of the longitudinal axis is calculated. Recall from Chapter 2 that the Cherenkov light develops temporally along the longitudinal axis, resulting in a slight gradient in the arrival times of photons along this axis of the shower. Therefore, once the image orientation has been determined, the time gradient along the image axis can be measured (Figure 4.4). This gradient is estimated via a linear fit to pulse arrival times along the longitudinal axis of the image. The second stage of the "double pass" integration then utilizes this timing information to deploy a sliding integration window, whereby a a more narrow (12 ns) window is used for each pixel, with the start time of the integration determined by the pixel's position along the longitudinal axis of the preliminary image.

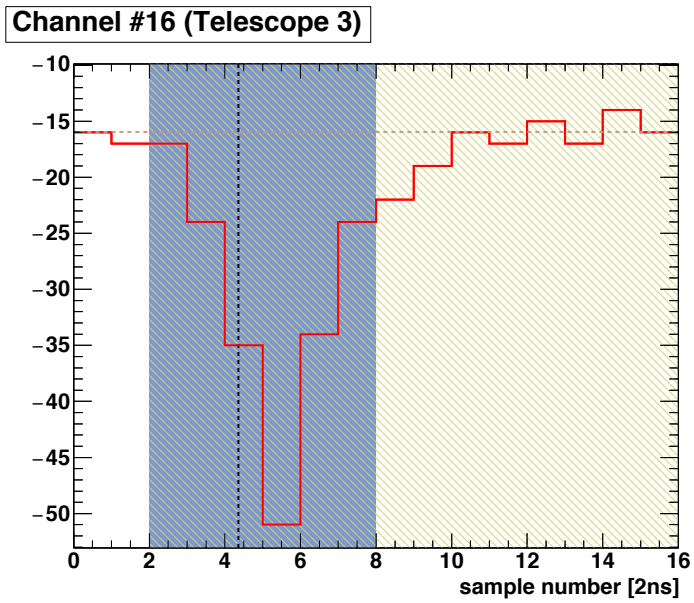

Figure 4.3: The red line shows a time series of digital counts from a particular FADC channel during a Cherenkov event. The horizontal brown line indicates the negative pedestal value, the vertical dashed black line indicates the "arrival time" of the trace in this channel, and the blue shaded region indicates the integration window around the pulse.

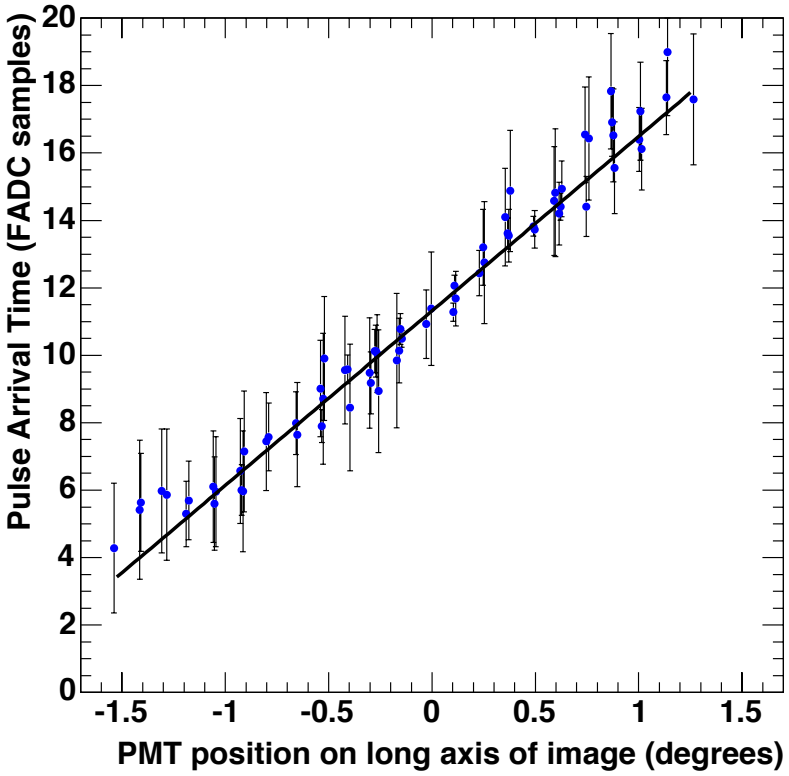

Figure 4.4: The arrival time of pulses (in units of FADC samples, 1 sample=2ns) as a function of position along the longitudinal axis of the image. Reproduced from [17].

4.2.2 Noise Estimation

While minimization of the charge integration window does much to improve the signal-to-noise ratio, contamination from the night-sky background (NSB) is inescapable and must be quantified and accounted for in the final analysis. The signal from each pixel is AC-coupled, which effectively filters the steady component of the NSB. What remains in the data are fluctuations in this background noise. These fluctuations are characterized by examining the FADC traces taken when no Cherenkov light is present. To accomplish this, the telescopes are manually triggered at a rate of 1 Hz; analysis of the resulting FADC traces can provide useful estimates for fluctuations in the NSB.

Removal of the steady-state component of the NSB effectively sets the baseline voltage from the PMTs to 0 V. Fluctuations in the NSB can be positive or negative; yet the FADCs are designed to digitize only negative signals. Therefore an artificial negative offset referred to as the "pedestal" is added to the PMT signal, so that positive fluctuations can be adequately characterized. The set of force-triggered "pedestal events", FADC traces recorded in the absence of known Cherenkov light, can then be used to measure fluctuations in the NSB for each pixel.

4.2.3 Image Construction and Parameterization

Once the charge for each pixel has been integrated and the noise level has been estimated, a full image can be constructed for each event. Pixels are included in the final image if:

1. The charge is greater than or equal to 5 pedestal standard deviations beyond the pedestal mean, or

2. The charge is greater than or equal to 2.5 pedestal standard deviations beyond the pedestal mean, and the pixel borders another pixel which satisfies the first criterion

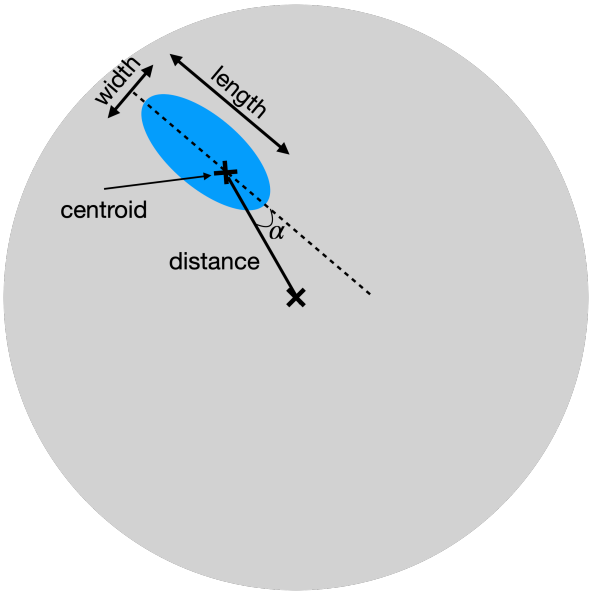

Figure 4.5: A summary of of some important parameters for a single-telescope image.

It has been noted (Chapter 2) that the image of a Cherenkov event caused by a gamma-ray photon will tend to be elliptical in shape. It was Hillas ([133]) who first noticed that a simple parameterization of the image can be useful to discriminate between showers of gamma-ray and cosmic-ray origins. Specifically, it is useful to describe the camera image in terms of its moments: the "zeroth" order moment (known as the *size* of the image) is simply the sum of the charge (in digital counts) from all pixels in the image; the first order moment (the *centroid*) is the mean or "center of mass" of the image, and the second order moment is the variance which describes the extent of the major and minor axes of the ellipse, known respectively as the image *length* and *width*. These and some other important image parameters are depicted in Figure 4.5.

4.3 Event reconstruction

An image is constructed in the manner described above for each telescope. At this point, the task of the data analysis is to use the images from each telescope to reconstruct the salient properties of the Cherenkov light in the images. Of particular interest are: the identity of the primary particle (was the Cherenkov light created by a

photon or a hadron?), the point of origin of the event (from where on the sky did the primary particle originate?), and the energy of the primary particle. In this section, we temporarily set aside the issue of determining the identity of the primary (we return to this question in the next section) and focus on reconstruction of the direction and energy of the primary particle.

4.3.1 Event direction

Reconstruction of the direction of the Cherenkov light is necessary in order to associate the primary particle with astrophysical sources in the sky. By using data from multiple telescopes, it is possible to associate with each event a corresponding right ascension and declination, describing the region of the sky from which the event originated.

For a single telescope, the axis of the image describes a line defined by the orientation of the major axis of the ellipse. Recall that this axis corresponds to the longitudinal development of the shower, and hence the arrival direction of the primary particle is constrained to lie somewhere along this line. By adding more telescope images to the analysis, the direction of the primary can be further constrained by finding the intersection point between the shower axes of multiple telescope images. This stereoscopic method of determining the image direction was first developed by the HEGRA telescope array [149]. The basic idea is to superimpose the images from multiple telescopes onto the same camera plane and then locate the intersection point of their major axes. This is depicted in Figure 4.6. When three or more images are used, the intersection point is not guaranteed to lie along every image's axis and is then defined by finding the average of every intersection point from any two telescopes. This average is weighted by the *size* of the images and the intersection angle between their axes, with near-perpendicular intersections being preferred. A similar technique can be used to reconstruct the "core location" of the shower: the intersection of the projected shower axis with the ground plane. This information is eventually useful in estimating the gamma-ray flux of the astrophysical source of photons.

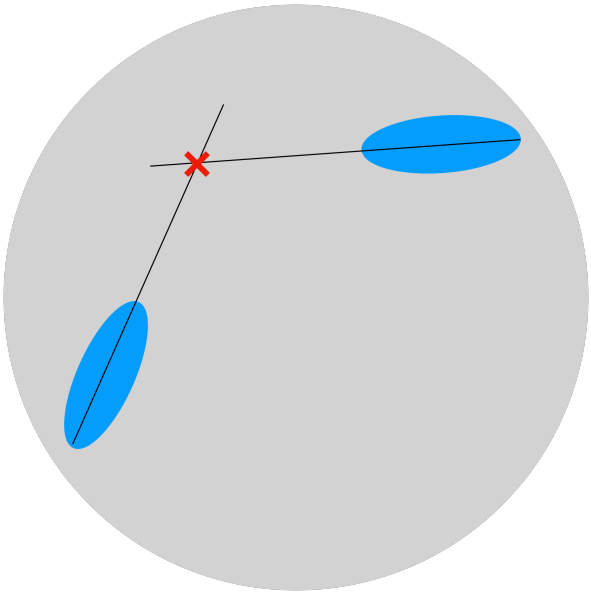

Figure 4.6: The intersection of the axes of separate images indicates the original direction of the primary.

4.3.2 Event energy

Reconstruction of the arrival direction of the primary allows for association of the event with astrophysical sources; reconstruction of the energy of the primary is necessary in order to construct energy spectra. In principle, the energy of the primary particle is proportional to the light yield of the Cherenkov light. This simple relationship ignores the fact that photons from Cherenkov light reach the telescope from different distances. And, of course, fewer photons reach from more distant events.

Fortunately, the physical interactions governing the origin and development of the Cherenkov event are well understood; this allows for the generation of simulated Cherenkov events which can then be compared to observations to reconstruct their intrinsic properties.

Simulations

The process of simulating a Cherenkov event is two-fold: first the interaction of the primary particle with the atmosphere must be simulated, the end result of which is a collection of photons generated by the Cherenkov light in the upper atmosphere.

These photons must then be propagated through a full model of the telescope in order to produce a simulated camera image as a final result. Comparison of this simulated image, with known primary energy, to data with unknown primary energy, can then be used to estimate the energy of observed Cherenkov events. Simulated gamma-ray events are also of critical importance in determining which Cherenkov events are caused by gamma rays rather than particles.

The first step in the simulation chain uses a Monte-Carlo technique to generate the chain reaction of particles in the atmosphere from a given primary. This involves recreating the electron-positron cascade caused by an electromagnetic primary particle, or the charged/neutral pion cascade caused by hadronic primaries. For most VERITAS simulations, the CORSIKA program [150] is used to generate the particle shower caused by a primary particle of known type and energy. This interaction depends on the identity of the primary, the energy of the primary, the zenith angle, and the properties of the atmosphere. Once the particle cascade has been simulated, a separate program, called GrISUDet [151], is used to generate the resulting Cherenkov photons. The creation and propagation of Cherenkov photons also depends heavily on the properties of the local atmosphere. In particular, air density and index of refraction as a function of altitude is a necessary input parameter for simulated Cherenkov emission. For VERITAS these data are primarily drawn from atmospheric sounding data collected in the nearby city of Tucson, and supplemented by data from a 1996 study of atmospheric profiles at different latitudes [152]. The final step of the simulation chain is to propagate the Cherenkov photons through a model of the entire telescope, a process which is also handled by the GrISUDet package. This involves reflection of the incoming photons off of the mirror facets and into the camera. This process takes into account the alignment and reflectivity of each mirror facet, as well as the shadow cast by the quadrapod and camera box. Each simulated photon that is reflected into the camera plane is then processed through the telescope electronics. At this point, photons from the night-sky background (NSB) are also generated and injected atop the Cherenkov photons (this noise level is an input parameter for the simulations). The PMT response is simulated

based on laboratory testing and includes the gain and quantum efficiency of each PMT. The temporal structure is also modeled based off of observations so that a realistic pulse is generated. The signal from each PMT is digitized by a model of the data acquisition hardware (the FADCs) and the full event is written to a data file which is identical in format to that of a "real" data file. These simulated events can then be processed by the same analysis chain used for actual data to create images of the Cherenkov light generated by each event. An image of a simulated gamma-ray event is shown in Figure 4.7.

Lookup Tables

Dedicated analysis of simulated events can then be used to allow for energy estimation of real events. This is done by creating tables to characterize the relationship between the energy of the primary, the *size*[2] of the image, and the distance from the telescope to the shower core. The latter two properties can be estimated from data, the former is an unknown. Simulated events are binned by size and core distance to create a 2D histogram which contains the average energy for each size/distance bin (Figure 4.8). Separate histograms are constructed for different combinations of zenith angle, night-sky background, and atmospheric model. These tables are then made available to the standard analysis chain, which uses image parameterization and stereoscopic reconstruction to estimate the image size and core distance, and then reads the energy from the appropriate bin of the simulation-generated tables in order to estimate the energy of the primary particle. Energy reconstruction of simulated events shows a typical energy resolution $\frac{E_{\text{rec}}-E_{\text{true}}}{E_{\text{true}}} \sim 15-20\%$ [109].

4.3.3 Identity of the Primary

The overwhelming majority of events captured by IACTs are caused by cosmic rays (particles) rather than gamma rays. In order to conduct gamma-ray astronomy, it

[2] Recall that size in this context refers not to the geometric area of the image but rather the integrated charge contained within.

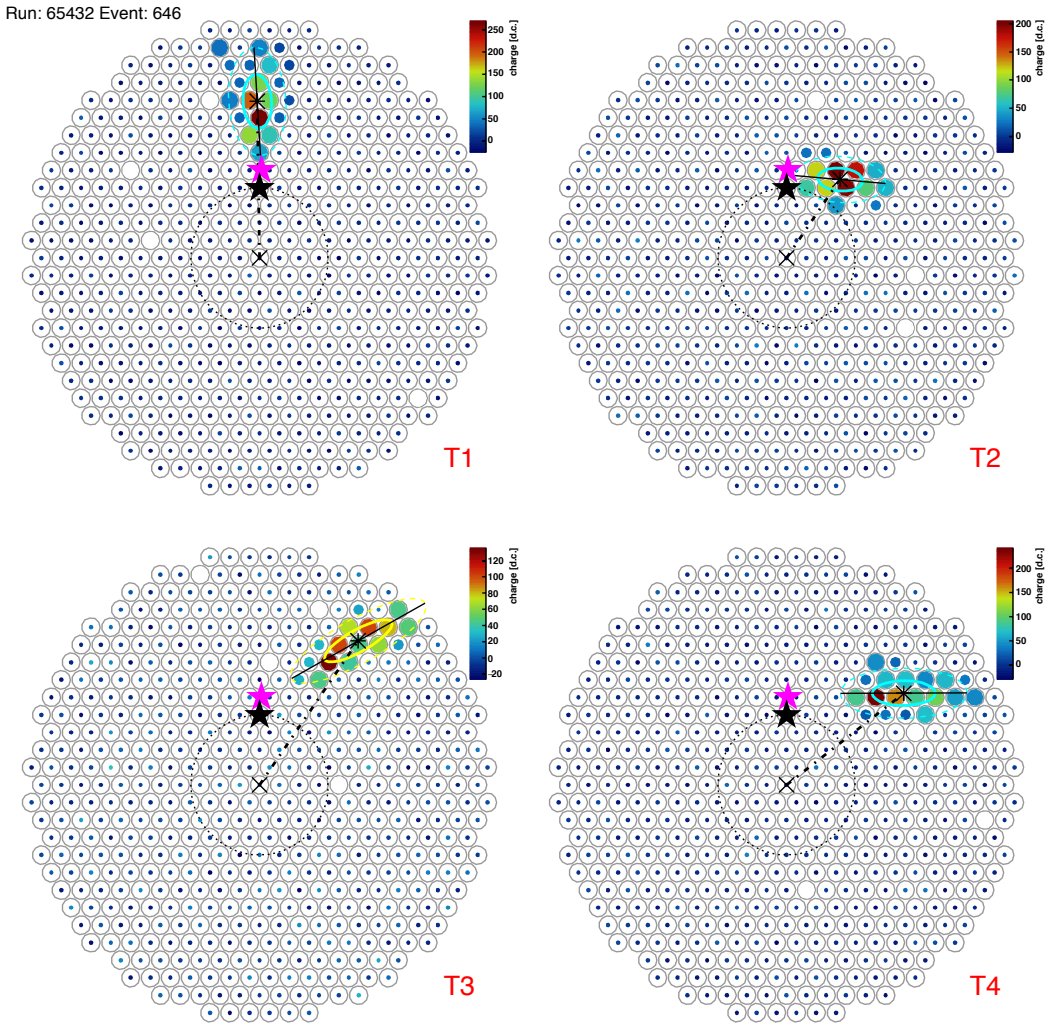

Figure 4.7: A simulated gamma-ray event as "seen" in the cameras of each of the four cameras.

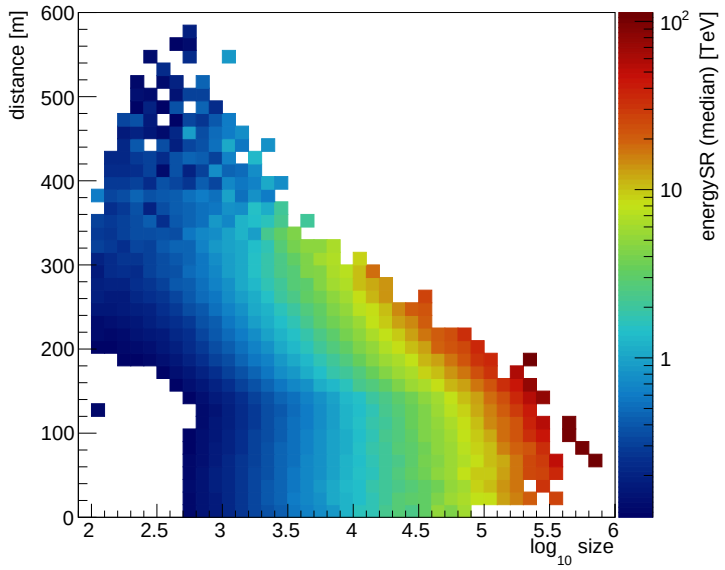

Figure 4.8: Shown is a typical table which records the median energy of simulated gamma-ray events as a function of event "size" (integrated charge in camera image) and core distance (the distance away from the telescope where the shower axis intersects the ground plane.)

is therefore necessary to efficiently separate gamma-ray produced Cherenkov light from hadronic (protons and larger atomic nuclei) light. As was discussed in Chapter 2, the development of proton-induced showers and gamma-ray-induced showers is fundamentally different. In particular, proton-induced showers tend to carry a larger transverse momentum, which results in a more broad and less uniform distribution of light on the ground. This translates into differences in the shapes of the images produced by the camera.

Following the method of Hillas [133], Monte-Carlo simulations can be used to characterize the difference in image properties between gamma-ray and hadron induced showers. Image parameters such as width and length are therefore potentially useful discriminators. Image shapes also depend on several other factors, most importantly: energy, core distance, and zenith angle. Therefore a straightforward analysis based on width and/or length is insufficient. Instead, a similar method as described in the previous section is employed. Simulated events are placed in bins according to their

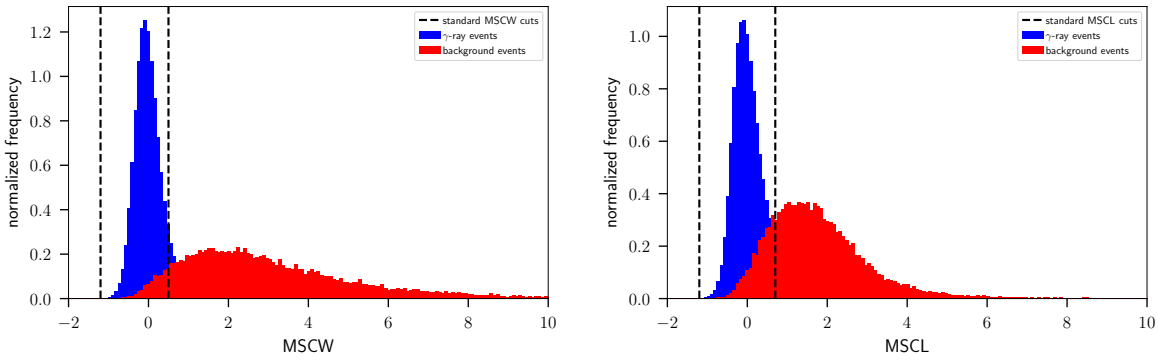

Figure 4.9: The distribution of the MSCW (right) and MSCL (left) parameters for simulated gamma-ray events (blue) and background events derived from real data (red).

image size and core distance, and each bin is filled with the average length and width in that bin. Separate tables are constructed for different zenith angles and noise levels (values of the NSB). A candidate gamma-ray event with a known (reconstructed) size and core distance can then have its shape (the *width* and *length* parameters) compared with the expected values of those same parameters derived from simulations. In this way, following the method described in [153], we use data from all telescopes to calculate the "mean scaled width" (MSCW) and "mean scaled length" (MSCL) parameters:

$$\mathrm{MSCW} = \frac{1}{N_{\mathrm{tel}}} \sum_{i=1}^{N_{\mathrm{tel}}} \frac{w_i - w_{\mathrm{sim}}}{\sigma_w}$$

$$\mathrm{MSCL} = \frac{1}{N_{\mathrm{tel}}} \sum_{i=1}^{N_{\mathrm{tel}}} \frac{\ell_i - \ell_{\mathrm{sim}}}{\sigma_\ell}$$

Where w_i/ℓ_i is the *width*/*length* of the image produced by the ith telescope, $w_{\mathrm{sim}}/\ell_{\mathrm{sim}}$ is the median *width*/*length* of images generated by simulations in the appropriate *size*-*distance* bin, and σ_w/σ_ℓ is the 90% *width* of the distribution of simulated *widths*/*lengths* in this bin.

As shown in Figure 4.9, the MSCW/MSCL parameter differs significantly between gamma-ray and cosmic-ray background events. Selection criteria can be developed on the basis of the MSCW/MSCL parameters which are capable of significant rejection of non-electromagnetic Cherenkov events. A standard analysis excludes or

"cuts" events if their shapes differ significantly from those expected based upon simulations. Specifically, events are cut whose mean scaled width is is greater than 0.5 or less than -1.2 or whose mean scaled length is greater than 0.7 or less than -1.2. Cuts based upon these criteria alone are capable of achieving *quality factors* of $Q = \epsilon_\gamma / \sqrt{\epsilon_{CR}} \sim 4$ [154], where $\epsilon_{\gamma/CR}$ is the fraction of gamma-ray/cosmic-ray background events which survive these cuts.

In recent years, the growth of computing power has allowed for the implementation of more sophisticated algorithms for this purpose. Modern analyses of VERITAS data, including prominent results cited in this dissertation, make use of multivariate regression in the form of boosted decision trees to determine the identity of the primary particle [155]. This method has been shown to increase the sensitivity of the instrument in comparison to the standard shape cuts.

4.4 High-level analysis

After the camera images for each event have been constructed, cleaned, and parameterized, what remains is a list of events with associated energies, directions, shape parameters, and other important parameters. The remaining task of the data analysis chain is to use this information to reconstruct the properties of the (potential) astrophysical source being studied. Most fundamentally this consists of source *detection* (determining whether a candidate source can be confidently said to emit gamma rays at a detectable level). If the source is detected, then from the existing data the distributions of gamma-ray photons from the source in energy, space, and time are sought. The first of these is the energy spectrum of the source, the second is an image, and the third is known as the light curve. Before any of this can be completed, significant reduction of the data is required to ensure that only gamma-ray events of sufficient quality are used in the analysis.

4.4.1 Data reduction

Of the $\sim 10^5$ events recorded in a typical 30-minute data file, the vast majority are not usable for high-level analysis. To be considered in a high-level analysis, an event must (1) be identified as a gamma ray and (2) consist of a sufficiently high-quality image for energy reconstruction. In order to accomplish this, events are considered on an individual basis and are removed from the analysis if they fail certain criteria which indicate insufficient data quality. Images from telescopes are not considered if they contain too few pixels (5, by default, after the removal of those with too little charge as described in Section 4.2.3), and event reconstruction does not proceed if too few telescopes produce images (at least 2, by default).

4.4.2 Source Detection

The gamma-hadron cuts are remarkably efficient at removing proton-nuclei initiated events, but background noise is inevitably present in the final dataset. Putative detection of photons from the direction of the candidate source field therefore does not represent a confirmed detection of the existence of a gamma-ray source. Rather, confirmation of source detection requires that the gamma-ray signal from the candidate source region sufficiently exceed the estimated level of spurious or "background" events occurring in that same region.

Background Estimation

The number of events detected from the source region generally comprise both gamma-ray events due to an astrophysical interaction and spurious "background events" due mostly to the isotropic flux of cosmic rays incident on the Earth. In order to confidently claim detection of a gamma-ray source, it is necessary to prove that the number of events from the source region is significantly greater than would be expected from the cosmic-ray background. This requires an independent estimation of the level of background events expected from the source region. In practice, this is accomplished by observing a region of the sky nearby to but not including the candidate source, and

where no other known source exists. The number of events recorded in this observation can then be used to estimate the number of background events originating from the candidate source region.

ON/OFF Observations

Perhaps the simplest method of background estimation is to dedicate observation time solely to study regions where no source is expected. In this scenario, the instrument dedicates an amount of time T_{ON} pointing at the candidate source region (the "ON" region) and a time T_{OFF} pointing at a previously chosen background region, (the "OFF" region). Under the assumptions that no source exists in the OFF region, and that the OFF region is sufficiently similar to the ON region, then one can estimate that the number of background events originating from the ON region during the time interval T_{ON} is $N_{\mathrm{BG}} = \frac{T_{\mathrm{ON}}}{T_{\mathrm{OFF}}} N_{\mathrm{OFF}}$, where N_{OFF} is the number of events observed from the background region during the time T_{OFF}. This method, described in [156], was used with great success to initially detect the Crab Nebula in 1989 [80]. While the simplicity of this method is an obvious advantage, the inefficient use of scarce observing time is such a significant drawback that this method is no longer frequently used by modern ground-based gamma-ray telescopes.

Reflected Regions

An alternative to the ON/OFF method of background estimation is the use of reflected regions. In this scenario, based on ideas first proposed by Fomin et al [157], the telescope camera is centered not on the candidate source region, but rather is offset by some fixed distance (often $\sim 0.5^{\circ}$). Events with a reconstructed direction that lies within the candidate source region are the "ON" events. The number of background events originating from the candidate source region can then be estimated by designating one or many OFF regions, which subtend the same solid angle as the ON region and which are offset from the camera center by the same angular distance (Figure 4.10). Although the sensitivity of the camera to Cherenkov events varies across

its face, with regions closer to the center being the most sensitive, this variation is generally radially symmetric. This implies that any two camera regions which are the same angular distance from the camera center will have the same sensitivity; therefore dedicated OFF regions which are equidistant from the camera center as the ON region are reliable estimators for the number of background events originating from the ON region. The obvious advantage is that the background can be estimated simultaneously with the candidate source region. If a number n of background regions are used, from which a collective number of events N_{OFF} are observed, then the estimated number of background events originating from the ON region is simply $N_{BG} = \frac{N_{OFF}}{n}$.

Ring Background

If the sensitivity of the camera across the field of view is known, then in principle the background can be estimated from any region and the difference in sensitivity between the OFF and ON regions can be corrected for using the independently measured camera sensitivity. A common method, known as the "ring background" method [158], is to estimate the background using events which originate from within a ring which surrounds the candidate source region (Figure 4.10). Unless the source is located at the camera center (which it usually is not), then the camera sensitivity will generally vary within different parts of the ring as well as between the ring and the ON region. A map of the camera's sensitivity across the field of view (an *acceptance* map), is therefore necessary in order to correct for the different exposures between the ON and OFF regions. Such a map can be produced from measurements of a region where no strong source is present. In this case, the rate of events across the field of view should be uniform; any non-uniformities observed in the concentration of reconstructed events across the camera will therefore be instrumental. An acceptance map is constructed simply by measuring the event rate across the face of the camera and normalizing every bin to the maximum observed event rate. This acceptance map can then be used to correct for differing exposures both within the OFF region and between the OFF and

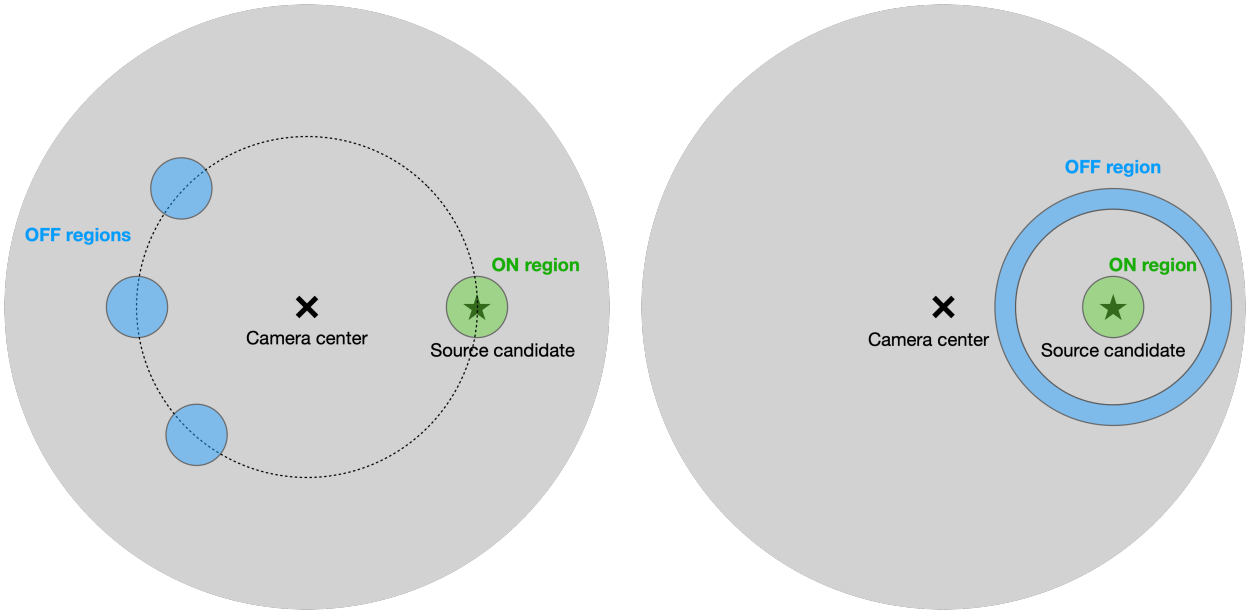

Figure 4.10: Two popular methods for estimating background events are depicted. *Left:* The reflected regions method records gamma-ray events from regions equidistant from the camera center as the source location. *Right:* The ring background method records gamma-ray events from a ring of pre-determined width centered on the source location.

ON regions. In this construction, the estimated number of background events originating from within the source region is $N_{\mathrm{BG}} = \alpha N_{\mathrm{OFF}}$, where as usual N_{OFF} is the total number of events originating from the ring and, following [158]:

$$\alpha = \frac{\int_{\mathrm{ON}} Acc(x,y)dxdydt}{\int_{\mathrm{OFF}} Acc(x,y)dxdydt} \tag{4.1}$$

That is, if $Acc(x,y)$ is the relative acceptance of the camera as a function of camera coordinates x, y, then the parameter α is a normalization factor which results from integrating the acceptance within the ON region and again within the OFF region, and then taking the ratio.

Hypothesis Testing

Regardless of the methodology used for background estimation, the question of confidence in a source detection remains. Note that the definition of α in Equation 4.1 reduces in such a way that for any background estimation technique, it can be

stated that the estimated number of background counts present in the source region is $N_{\mathrm{BG}} = \alpha N_{\mathrm{OFF}}$. We can then state that the number of events due to a real gamma-ray source (the excess events above the background noise) is $N_{\mathrm{src}} = N_{\mathrm{ON}} - \alpha N_{\mathrm{OFF}}$. A gamma-ray source can be confidently claimed if N_{src} is significantly greater than 0. Following Li and Ma (1983) [156], we model both N_{ON} and N_{OFF} using Poisson distributions and use the maximum likelihood framework put forward by Wilks [159] to define the statistical significance of N_{src} to be simply:

$$S = \sqrt{2}\left\{ N_{\mathrm{ON}} \ln\left[\frac{1+\alpha}{\alpha}\left(\frac{N_{\mathrm{ON}}}{N_{\mathrm{ON}}+N_{\mathrm{OFF}}}\right)\right] + N_{\mathrm{OFF}} \ln\left[(1+\alpha)\left(\frac{N_{\mathrm{OFF}}}{N_{\mathrm{ON}}+N_{\mathrm{OFF}}}\right)\right]\right\}^{1/2} \tag{4.2}$$

The value S is understood to be the "number of standard deviations" that N_{src} is above 0. Typically, a candidate source is generally accepted as a detected gamma-ray source upon an observation with $S \geq 5$, corresponding to a 99.9999997% probability that the observed signal can not be explained by statistical fluctuations.

4.4.3 Energy Spectrum

Once a candidate source is confirmed to exist, its intrinsic properties can be examined by studying the distribution of photon flux as a function of energy, the energy spectrum. The energy spectrum in particular is often useful for identifying the emission mechanism in the astrophysical source that produced the gamma rays.

The task is to transform the raw data, consisting essentially of a list of gamma-ray photons with associated energies, into a distribution of source flux as a function of energy. In order to do this, the energy-dependent sensitivity and collection area of the telescope array must be accounted and compensated for in order to produce an instrument-independent measurement.

To start, the gamma ray photons are binned according to energy to form a histogram depicting number of events vs energy. The distribution of this histogram is greatly biased by the energy-dependent response of the instrument. In order to transform this information into an instrument-independent flux measurement, it is necessary

to estimate the the energy-dependent "effective collection area" of the instrument. This accomplished by using simulations.

Effective Area

Recall that light from Cherenkov photons has the unique property that brightness on the ground is approximately steady over an area within 120 meters from the center of the shower axis (this area is known as the "light pool"). As a consequence, a detector placed directly underneath the shower axis and a detector placed 120 m away from the shower axis have approximately the same chance of recording the Cherenkov event. This means that the collection area of a single instrument scales not with the size of the mirror, but with the much larger size of the light pool.

For a single telescope, the effective collection area will be approximately $\pi\,(120\text{ m})^2 \approx 5 \times 10^4\text{ m}^2$. This does not represent the maximum collection area, however. Though the light intensity diminishes beyond the light pool, it does so gradually with distance ($\propto 1/r^2$). If a Cherenkov event is especially bright, it may be detected from distances even beyond 120 meters. Because the brightness of the Cherenkov event depends directly on the energy of the primary particle which caused the shower, this effectively means that gamma-ray photons of higher energy are detectable from greater distances. The effective collection area of the instrument therefore increases with energy. An example of this effect is shown for the stand-alone Whipple telescope in Figure 4.11.

When several telescopes are configured into an array, as is the case for the VERITAS instrument, the effective area scales with the geometric surface area spanned by the telescopes in the array. Simulated gamma-ray photons can be used to estimate the effective area as a function of energy. This is accomplished using the same simulation chain which was described previously. Gamma-ray photons with energies drawn from a power-law distribution are randomly generated along over a large area A which greatly exceeds the geometric area of the array. These simulated gamma-ray events are then processed through the telescope model and standard analysis chain and the fraction of events surviving quality and gamma/hadron discrimination cuts is recorded as a

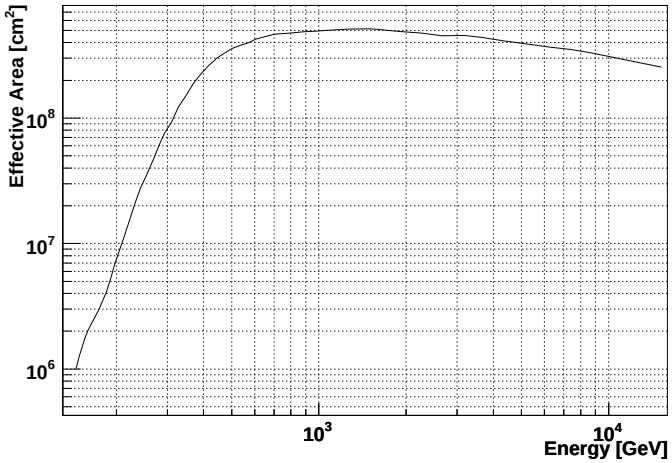

Figure 4.11: An example of effective collection area vs energy for the Whipple Telescope, from [18].

function of energy. The effective area is then defined as the product of the area A over which the photons were simulated and the fraction of reconstructed events as a function of energy. Two examples of estimated effective area values for the VERITAS array are shown in Figure 4.12.

Flux Calculation

The effective area curve, together with the exposure time of the data selection, can be used to transform the counts vs energy histogram into a flux vs energy curve. This simply entails dividing the number of events in each energy bin by the average effective area in that same energy bin, together with the total exposure time. This yields a curve which depicts "differential flux" (with dimensions of $[\text{area} \cdot \text{time} \cdot \text{energy}]^{-1}$). This product is considered to be the intrinsic energy spectrum of the source and can be modeled to investigate the properties of the astrophysical source of the gamma-ray emission. Figure 4.13 shows an example of such an energy spectrum, created using data from the Crab Nebula.

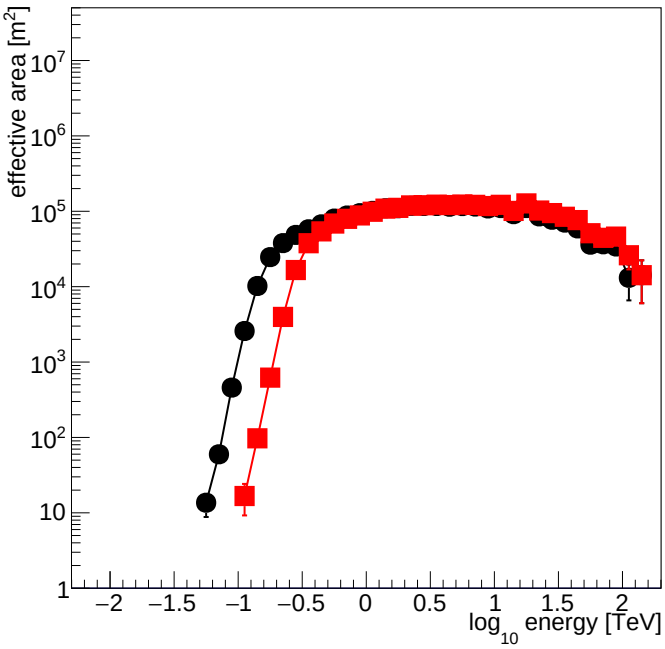

Figure 4.12: Effective area vs energy for the VERITAS array. Black circles depict data for *moderate* size cuts, red boxes show the same data after applying a more stringent *hard* size cut.

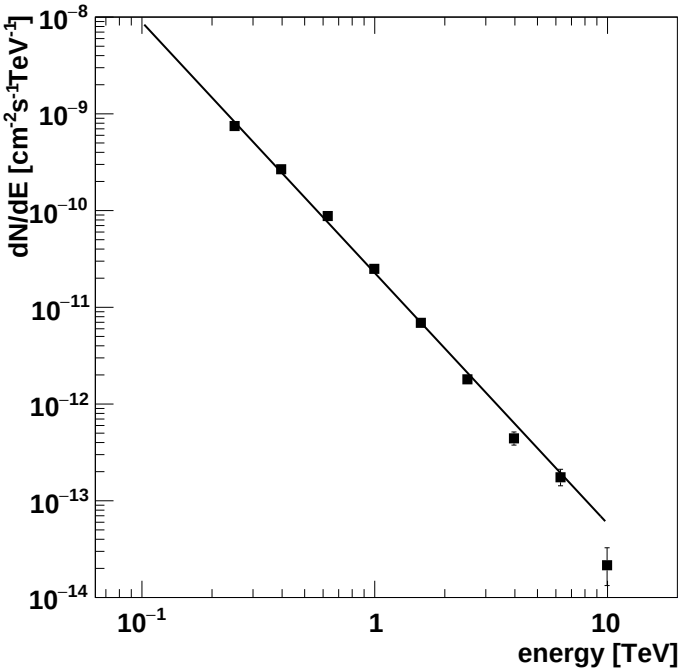

Figure 4.13: The energy spectrum of the Crab Nebula, produced by eventDisplay.

4.4.4 Morphology

Of additional interest in the study of astrophysical sources is the spatial distribution of the gamma-ray emission on the sky: the source *morphology*. The study of a source's morphology is enabled by the reconstruction of the incident direction of each gamma-ray event, a process which was described earlier. Starting from a list of gamma-ray photons, each with associated right ascension and declination, a 2D "sky map" can be constructed by binning these gamma-ray events by their RA and Dec into a 2D histogram. This raw histogram suffers from biases in the instrument response. In particular, it is generally true that the instrument is most sensitive to events directed toward the center of the camera and is less sensitive as angular distance from the camera center increases.

This difficulty can be overcome by estimating and subtracting the background counts from each bin in the histogram, leaving only the number of excess counts. The background events in each bin can be estimating using either of the "ring background"

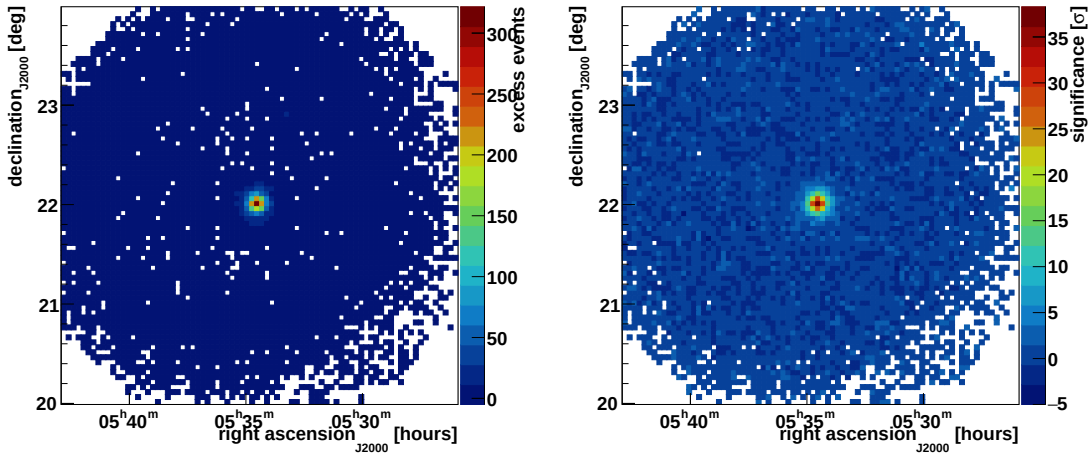

Figure 4.14: Two representations of the morphology of the Crab Nebula, produced by eventDisplay. The plot on the left shows a map of excess counts vs RA and Dec, the plot on the right shows the statistical significance in each bin, computing using Equation 4.2. The emission is consistent with that expected from an unresolved point source.

or "reflected regions" methods described previously. Because the acceptance of background events varies across the camera in the same way as the acceptance of gamma-ray events, the excess counts $N_{\mathrm{ON}} - \alpha N_{\mathrm{OFF}}$ removes the camera gradient entirely and reveals the intrinsic source morphology[3]. Examples of such plots are shown in Figure 4.14.

Angular Resolution

The ability of the instrument to resolve fine structure in the morphology of an astrophysical source is limited by the angular resolution of the instrument. The stereoscopic reconstruction process described in the previous section performs well but is of course not perfect. The performance of the instrument can be studied by examining its response to a perfect "point source", a gamma-ray source with no spatial extent. Due to uncertainties and limitations in the reconstruction of the direction of

[3] Actually, this plot is not completely independent of instrument response, as the point-spread function and off-axis gamma-ray sensitivity have not been accounted for (see next section).

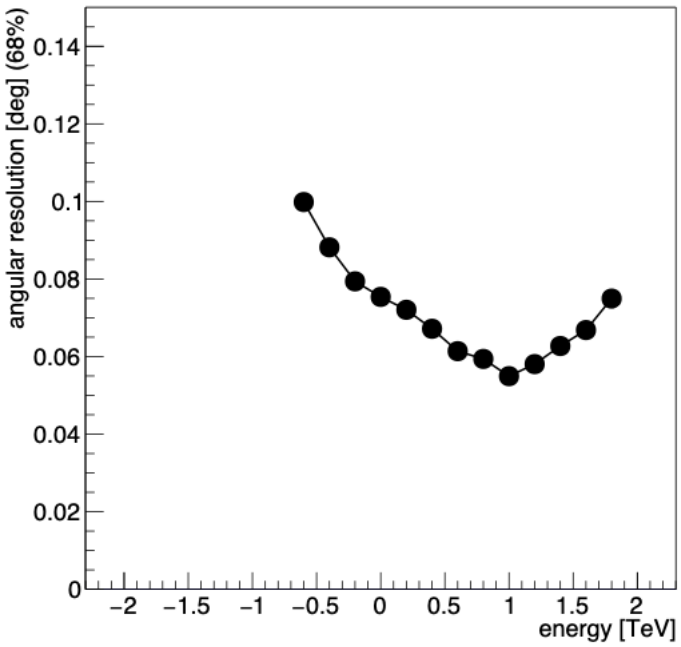

Figure 4.15: The angular resolution of the VERITAS array vs $\log_{10}\left(\frac{E}{1\ \text{TeV}}\right)$, constructed from analysis of simulated data. The angular resolution here is defined as the 68% containment radius of an imaged point source.

the gamma ray, a number of gamma-ray photons which in actuality originate from the same location will naturally have their reconstructed directions spread across a finite angular extent. Thus the spatial sky map of even a perfect point source of light will have a non-zero spatial extent. The characteristic width of an image taken of a point source used to quantify the angular resolution of the telescope is referred to as the "point spread function", or "PSF"; this width generally decreases with energy, reaching a minimum in the $\sim 1-10$ TeV range. The PSF vs energy for the VERITAS array, based on simulations, is depicted in Figure 4.15.

The finite PSF of the instrument necessarily means that adjacent spatial bins on a 2D sky map are likely to be correlated with one another, if the angular size of the spatial bin is significantly smaller than the PSF. This correlation can be represented by producing a new set of sky maps whereby each spatial bin contains the sum of

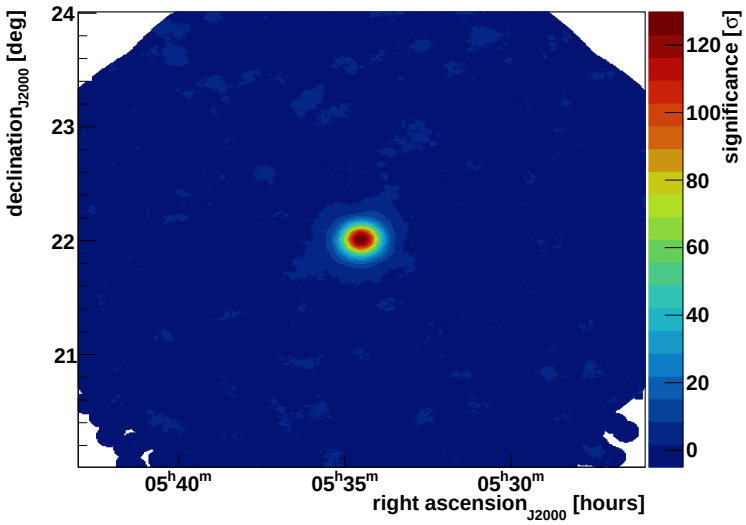

Figure 4.16: A correlated significance sky map of the Crab Nebula.

all counts within a given radius from the bin's center.[4] New sky maps containing gamma-ray counts, excess, and statistical significance can thus be constructed from these "correlated" maps. An example of such a sky map is shown in Figure 4.16.

4.5 Summary

Data analysis techniques are a crucial component to obtaining meaningful results with any IACT. Software optimizations and the implementation of new algorithms can improve the performance of the instrument just as significantly, if not more so, than hardware upgrades. The overall performance of the instrument is best characterized in terms of: 1) how faint of a source it can confidently detect, and 2) how precisely can it reconstruct the salient properties of a given source.

The former is quantified in the form of the instrument's "sensitivity", which specifies the minimum flux detectable by the array in a given amount of time. VERITAS is able to detect a source as faint as 1% of the flux of the Crab Nebula in only 25 hours of observing time [109].

[4] When modeling a point source, this radius is usually $\approx 0.09°$, for a source with larger spatial extent a larger radius of $\approx 0.23°$ is used.

As has already been discussed, the instrument's ability to faithfully reconstruct the morphology of a gamma-ray source is limited by the point spread function, an example of which is illustrated in Figure 4.15. At high energies, VERITAS is able to resolve structures on scales of a few arcminutes.

Finally, the distribution of energies of the gamma-ray photons is of great interest. Just as there is an angular resolution which introduces angular spread in spatial reconstruction of photons, there exists a finite energy resolution which introduces spread in the energies of reconstructed photons. This resolution itself is energy-dependent, but is relatively constant at $\approx 15-20\%$ over much of the energy range for which VERITAS is most sensitive. This means that the 68% containment radius for the reconstructed photon energy is typically smaller than 20% of the true photon energy.

Chapter 5

GAMMA-RAY BINARIES

Gamma-ray binaries are rare astrophysical systems comprised of a compact object (either a neutron star or a black hole) orbiting with a massive star. Although they are thought to represent a short-lived phase in the evolution of high-mass X-ray binaries [160] (HMXB), gamma-ray binaries share a number of distinct characteristics which set them apart from this larger class of objects. Unlike HMXBs, gamma-ray binaries exhibit bright gamma-ray luminosities, with a distinct VHE component, as well as modest non-thermal X-ray and radio emission. These systems take their name from the defining characteristic that most of their radiated power is emitted above 1 MeV (in the gamma-ray regime). Observations of gamma-ray binary systems provide a unique opportunity to study particle acceleration and emission mechanisms in a continuously and periodically changing physical environment.

As of the time of writing, nine gamma-ray binary systems have been discovered. While the growing population of this relatively new source class shares a broad set of general characteristics, the mechanisms that drive the emission from these systems are still subject to debate. Here we summarize the known population of gamma-ray binaries, generalize some common characteristics, and discuss different physical scenarios proposed to explain these observations.

5.1 The population of gamma-ray binaries

Overview

Gamma-ray binaries have been a subject of interest for a half century. In many ways, the development of the modern field of high-energy astrophysics can be traced to the search for gamma rays from binary systems such as Cygnus X-3 [161]. The late

Name	P_{orb} [days]	ϵ	distance [kpc]
PSR B1259-63[165]	1236.724526	0.86987970	2.6
LS 5039 [166]	3.90603	0.35	2.5
LS I +61° 303[167, 168]	26.496	0.537	2.0
HESS J0632+057[169, 170]	308-321[1]	0.66-0.83	1.1-1.7
1FGL J1018.6-5856[171, 172]	16.544	0.31	5.4
LMC P3[173]	10.301	0.4	50
PSR J2032+4127[174]	17000	0.961	1.33
HESS J1832-093	86.28	-	-
4 FGL J1405.1 - 6119	14	-	-

Table 5.1: Orbital period P_{orb}, eccentricity ϵ and distances of the confirmed gamma-ray binaries.

1970s and 1980s saw a number of claims of gamma-ray emission from known X-ray binaries, including Cygnus X-3 and Hercules X-1 [162], however most of these claims were eventually found to be spurious [163, 164].

The first VHE detection of binaries came in the 2000's with the advent of a new generation of Imaging Atmospheric Cherenkov Telescopes (IACTs). PSR B1259-63, the first such source to be detected, was detected by the H.E.S.S. collaboration in 2004. It was followed swiftly by LS 5039 discovered by H.E.S.S. in 2005, and LS I +61° 303 discovered by MAGIC in 2006.

There are now nine known gamma-ray binary systems (see Table 5.1). In this section we review each system and summarize the salient multi-wavelength details.

5.1.1 PSR B1259-63/LS 2883

PSR B1259-63 is a radio pulsar discovered in 1992 as a result of a radio pulsar search conducted by the Parkes radio telescope [175]. The pulsar has a pulse period of 47 ms and a measured spin-down luminosity of 8.3×10^{35} erg s^{-1}. PSR B1259-63 is in a binary orbit with the 20 $M_\odot$ Be star LS 2883 which features a large ($\sim$ 10 stellar radii) equatorial disk [176, 175, 177]. The orbit of the system is characterized by a 1237 day period and an eccentricity of 0.87 [178, 165], and the system lies at a distance of 2.6 kpc [165].

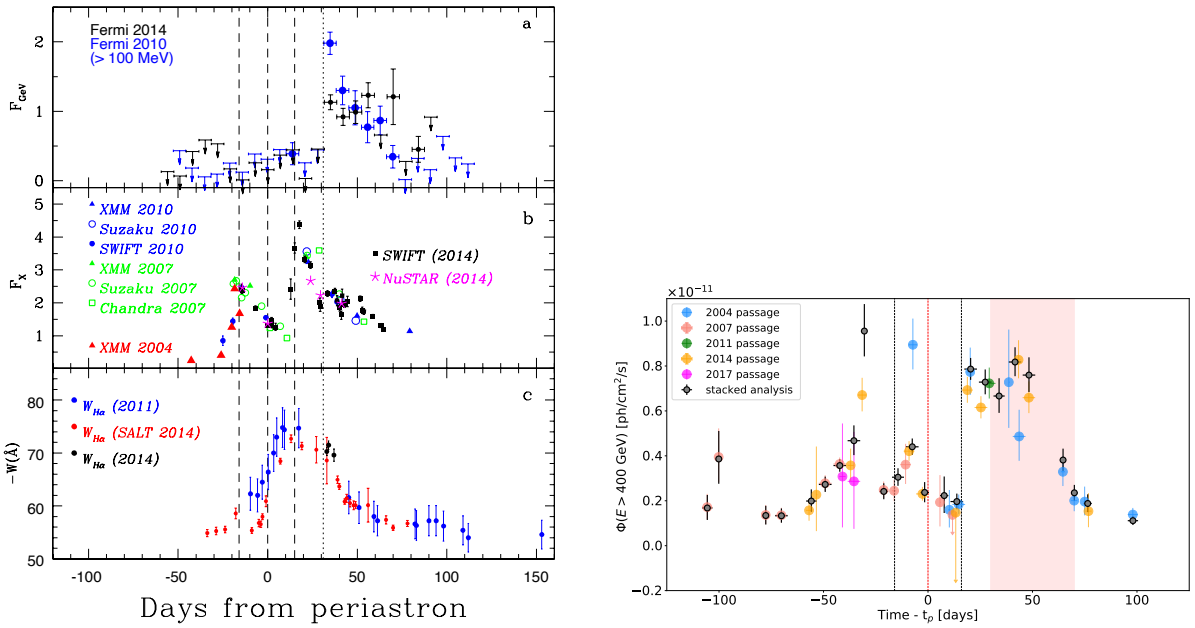

Figure 5.1: *Left*: The light curves of PSR B1259-63 in (from top to bottom) high energy, X-ray, and optical. From [19]. *Right*: The VHE light curve of PSR B1259-63 as seen by H.E.S.S., from [20].

VHE gamma rays

PSR B1259-63/LS 2883 was initially discovered in VHE gamma rays by the H.E.S.S. collaboration in 2005 [179]. The VHE emission is characterized by a time-variable light curve which displays an asymmetric, double-peaked structure around the periastron passage, with a flux minimum corresponding to the periastron passage [179, 180, 181]. The two peaks, each lasting only a few days, likely correspond to the times at which the neutron star crosses the circumstellar disk of the companion [20]. The VHE spectrum is well-fit by a simple power law with $\Gamma \approx 2.7$, with no evidence of spectral variability [20]. The average luminosity is $\sim 1 \times 10^{34}$ erg s^{-1}, which is approximately 1.3% of the pulsar's spin-down power.

HE gamma rays

High-energy emission associated with the binary system was first discovered by *Fermi*-LAT in 2011 [182]. The HE emission is relatively faint before, during, and up

to several weeks following the periastron passage. The most prominent feature of the HE emission is a powerful flare which typically occurs $\sim$ 30 days after periastron and fades after $\sim$ 60 days [182, 183, 184, 185]. The flux observed during this flare can be $\sim$ 30 times that of the pre-periastron flux, and the power emitted is comparable to the spin-down power of PSR B1259-63, and may even exceed it [186]. The spectrum during this time is well-described by a power law with an exponential cutoff. The spectrum has been shown to be variable, with a general "softer-when-brighter" correlation with the flux [183].

X-rays

X-ray emission from PSR B1259-63/LS 2883 was first seen by *ROSAT* in 1994 [187]. The X-ray light curve is characterized by an asymmetric, double-peaked structure about periastron, with a local minimum occurring several days after periastron [188, 189, 19, 190]. The two peaks correspond to the times at which the pulsar crosses the circumstellar disk of LS 2883. These peaks are accompanied by an increase in hydrogen column density by a factor of ~ 2 and a hardening of the spectral index from $\Gamma \approx 1.8$ to $\Gamma \approx 1.2$ with the onset of the first peak [188]. The 0.3-10 keV luminosity is $\sim 2 \times 10^{34}$ erg s^{-1} ($\sim 2\%$ of the pulsar's spin-down power).

Not long after periastron, a $\sim 4''$ clump of X-ray-emitting matter is observed moving away from the star at a projected speed of about $0.15c$ [191, 192, 193, 194]. The clump is thought to be a piece of the disk around the Be star broken away and launched at high speeds by the pulsar wind.

Radio

Pulsed radio emission from PSR B1259-63 was discovered in 1992 [175]. As the pulsar moves into the dense environment near the massive star, the pulsed emission disappears for $\sim$ 30 days, beginning approximately two weeks prior to periastron. This is replaced by a transient unpulsed component which displays a double-peaked structure about the periastron, with a local minimum occurring approximately 10 days

after periastron [175, 195]. As is the case with the X-ray emission, the peaks in unpulsed radio emission likely correspond to the times of disk-crossing events. The radio emission is well-described by a power law with index $\alpha \approx 0.5$, indicative of synchrotron emission [196]. The radio luminosity is $\sim 6 \times 10^{29}$ erg s^{-1} [27]. The radio emission is able to be resolved, and consists of a 50 mas structure which peaks 10 to 20 mas away from the system [197].

5.1.2 LS 5039

LS 5039 is a gamma-ray binary system consisting of the massive ($\sim$ 23 M$_\odot$) O7 star of the same name and an unidentified compact companion. The system has a relatively short (3.9 day) orbit with an eccentricity of 0.35, and lies at a distance of 2.5 kpc [166].

VHE gamma rays

VHE emission was initially seen from the LS 5039 system by H.E.S.S. in 2005 [198]. Periodicity was subsequently established in the gamma-ray light curve in 2006. The flux is highly variable over the course of the orbit, with a maximum occurring near the inferior conjunction of the system and a minimum not long after the superior conjunction [21]. The energy spectrum varies with orbital phase. For observations closer to inferior conjunction, the spectrum exhibits a hard power law ($\Gamma = 1.85$) with an exponential cutoff after $E \approx 8.7$ TeV. Observations from the other half of the orbit (closer to superior conjunction, when the source is fainter) are consistent with a simple power law model with a relatively soft ($\Gamma = 2.53$) spectral index [21]. The average luminosity of the source above 200 GeV is $\sim 8 \times 10^{33}$ erg s^{-1}.

HE gamma rays

LS 5039 was definitively detected in the HE energy regime by *Fermi*-LAT in 2009 [199]. The flux is highly variable over the orbit and is in anti-phase with the TeV flux: reaching a maximum at superior conjunction and a minimum at inferior conjunction. The shape of the energy spectrum is variable with orbital phase and

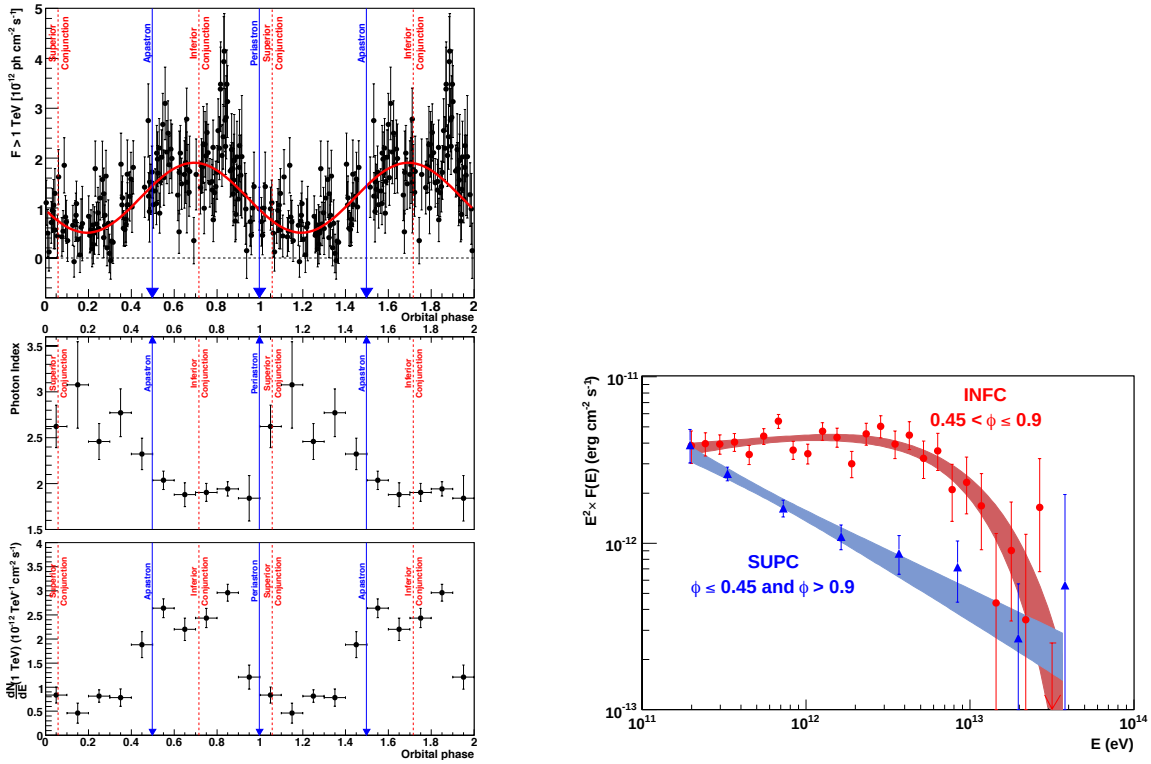

Figure 5.2: *Left*: The phase-folded light curve and spectral evolution of LS 5039, as seen by H.E.S.S.. The top figure shows the integral flux above 1 TeV, the middle figure shows the spectral index for a power law fit, the bottom figure shows the flux normalization for a power law fit. *Right*: TeV spectra taken of LS 5039 during two different periods around its orbit (from H.E.S.S.). The spectrum shows a soft power law near superior conjunction, and exhibits a hard, cutoff spectrum near inferior conjunction. Both figures reproduced from [21]

displays a general "softer-when-brighter" correlation with the flux [199]. There is no evidence, however, for differing spectral shape between the superior and inferior conjunctions [200], as is the case for the VHE emission. The average spectrum is consistent with an exponentially cut power law with $\Gamma = 2.05$ and $E_{\rm cut} = 2.2$ GeV. The overall spectrum also contains evidence of an additional hard power law component above 10 GeV, with an index of $\Gamma = 1.6$ [200]. The average luminosity is $\sim 3 \times 10^{35}$ erg s^{-1} [27].

X-rays

LS 5039 was suggested as an X-ray binary following an analysis of *ROSAT* data in 1997 [201]. The X-ray light curve is variable by a factor of ~ 2.5, and the orbital modulations are in phases with the VHE light curve: maximum close to inferior conjunction, minimum close to superior conjunction [202, 203]. The spectral index is variable throughout the orbit with $\Gamma \approx 1.6$ near superior conjunction and $\Gamma \approx 1.4$ near apastron. The hydrogen column density is stable across the orbit at $N_H \approx 7 \times 10^{21}$ cm^{-2} [204, 202, 203]. The source is detected up to energies as high as 70 keV at all orbital phases [202] and is seen by *INTEGRAL* up to 200 keV near inferior conjunction with a slightly steeper index of $\Gamma \approx 2.0$ [205]. Collmar and Zhang (2014, [206]) found that LS 5039 is associated with a previously unidentified COMPTEL source. The MeV source exhibits an orbital modulation which is in phase with the X-ray source with a spectral index of $\Gamma \approx 1.6$. Durant et al (2011,[207]) found evidence using *Chandra* of X-ray emission extending up to $2'$, however this was not confirmed in a similar study by [208]. The average X-ray luminosity is $\sim 10^{34}$ erg s^{-1} [27].

Radio

A weakly-variable radio source associated with LS 5039 was first reported by [209], who found a hard spectral index consistent with a non-thermal emission mechanism. While periodicity has not been observed in the radio flux [209, 210], the morphology has been observed to evolve periodically [211]. The spectrum is described by

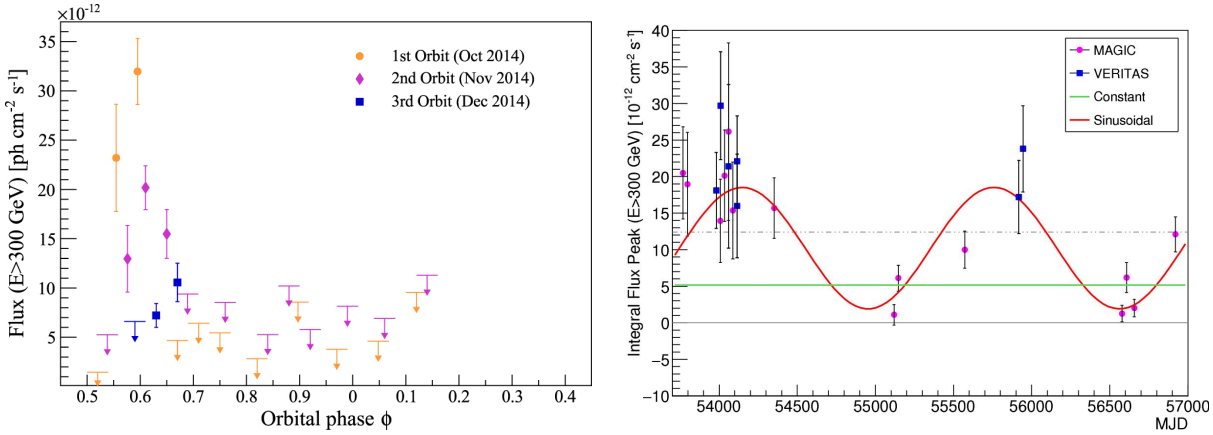

Figure 5.3: *Left*: VERITAS light curve of LS I +61° 303 during a major flaring episode in 2014 [22] *Right*: Evidence for periodicity beyond the 26.5 day orbital period of the system as seen by MAGIC [23].

a pure power law with $\alpha = -0.43$ down to ~ 1 GHz, below which it breaks to $\alpha = 0.75$ [212, 213]. The average radio luminosity is $\sim 6 \times 10^{29}$ erg s^{-1} [27].

5.1.3 LS I +61° 303

The LS I +61° 303 gamma-ray binary system consists of the 10-15 $M_\odot$ Be star of the same name orbiting with a compact object[214]. The two objects share a 26.5 day orbit with an eccentricity of 0.54 [167], although super-orbital modulations with a period of $\sim$ 1667 days is evident at all wavelengths [215]. The system lies at a distance of 2.0 kpc [168]. The recent detection of radio pulsations with a period of 269 ms from within LS I +61° 303 [216] firmly identifies the nature of the compact object as a pulsar, making this one of only three gamma-ray binary systems where the compact object is identified (PSR B1259-63, PSR J2032+4127).

VHE gamma rays

VHE gamma rays from LS I +61° 303 were first reported by MAGIC in 2006 [217]. Subsequent observations showed the emission to be periodic, peaking near apastron [218, 219]. The source is now detected in VHE gamma rays around the entire orbit, with bright flares consistently around apastron ranging from 15-30% of the Crab

Nebula flux [220]. Evidence for super-orbital periodicity was found in VHE wavelengths with a period of ~ 1610 days [23]. This periodicity is also seen in X-ray and radio wavelengths.

The spectrum appears to be stable on both orbital and super-orbital timescales and is characterized by a power law with $\Gamma = 2.4 - 2.6$ [23]. The average luminosity in VHE gamma rays is $\sim 10^{34}$ erg s^{-1} [27].

HE gamma rays

HE emission was seen by *Fermi*-LAT in 2009 [221]. The light curve is variable about the orbit, with a maximum soon after periastron and a minimum near apastron. The energy spectrum is consistent with a power law with an exponential cutoff throughout the orbit, and also displays significant variability: the spectrum is softest ($\Gamma \approx 2.1$) near periastron and hardest ($\Gamma \approx 1.9$) near apastron, and exhibits a "softer-when-brighter" correlation with the HE flux. The cutoff energy is maximal ($E_{\rm cut} \approx 6$ GeV) at apastron and minimal ($E_{\rm cut} \approx 3$ GeV) at periastron [200]. Unlike other gamma-ray binaries, the detection of flux points near ~ 90 GeV points to a potential connection between the HE and VHE spectra [222], though emission at these wavelengths are not correlated [220]. The average luminosity is $\sim 2 \times 10^{35}$ erg s^{-1} [27].

X-rays

An X-ray source associated with LS I $+61^\circ$ 303 was first identified by *EINSTEIN* in 1981 [223]. The X-ray flux is variable on the orbital timescale [224] and has shown variability on timescales as small as $\sim$ 40 minutes [225]. The X-ray and VHE flux appear to be correlated [220], indicating that the same population of electrons is responsible for emission at both wavelengths. The orbital phase of maximal X-ray emission varies on the superorbital timescale of the system, and has been shown to consistently lead the radio outbursts by $\sim$ 5 days [226]. The X-ray superorbital variability leads the radio variability by ~ 280 days [227]. The energy spectrum is well fit by an absorbed power law with $\Gamma \approx 1.5$ and $N_H \approx 5 \times 10^{21}$ cm^{-2}[224], and the

spectral index shows evidence for a "harder-when-brighter" correlation with the flux [228]. Although no break in the spectral index is apparent up to 300 keV [27], the existence of a COMPTEL source associated with LS I +61° 303 up to $\sim$ 30 MeV with a spectral index of $\Gamma \approx 2$ [229] suggests a spectral break at some point in the X-ray spectrum. The average X-ray luminosity is $\sim 10^{34}$ erg s^{-1} [27].

Radio

Variable radio emission from the region was first reported in 1978 [230]. Similar to the emission at other wavelengths, the radio light curve is unstable and has shown peaks of variable intensity at different orbital phases. This is presumably tied to the superorbital variability of the system [231, 232]. As was discussed in the previous section, the radio emission lags the X-ray emission by $\sim$ 5 days on the orbital timescale and $\sim$ 280 days on a super-orbital timescale. The spectral shape is variable during radio outbursts, transitioning from an optically thin state ($\alpha \approx -0.4$) near flux minimum to an optically thick state ($\alpha \approx 0.2$) around flux maximum [233]. The radio emission exhibits a cometary morphology on scales of $\sim$ 2 AU, and the morphology varies considerably near periastron [234]. The average radio luminosity is $\sim 3 \times 10^{30}$ erg s^{-1} [27].

5.1.4 HESS J0632+057

HESS J0632+057 consists of the 13-19 $M_\odot$ Be star MWC 148 [235] orbiting with an unidentified compact object. Estimates of the orbit differ: [169] find an orbital period of 321 days with an eccentricity of 0.83, while [170] prefer a slightly shorter (308-313 days), less eccentric (0.66-0.71) solution. The system lies at a distance of 1.1-1.7 kpc [169, 235].

VHE gamma rays

VHE emission was first seen from the direction of HESS J0632+057 by H.E.S.S. in 2007 [236]. Subsequent observations by VERITAS failed to detect the source [237],

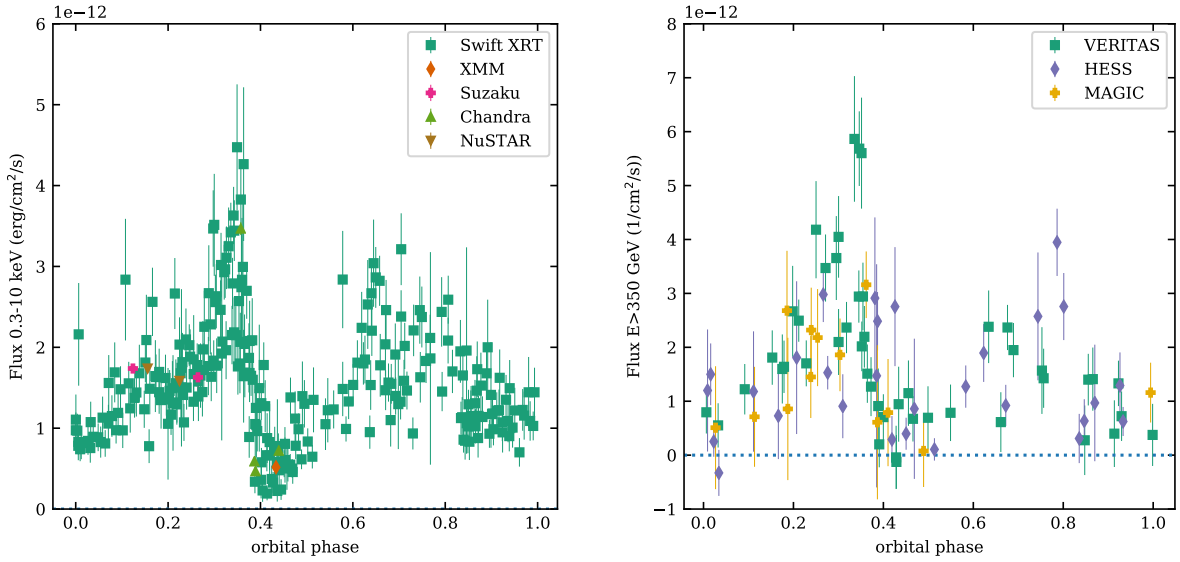

Figure 5.4: *Left*: Phase-folded X-ray light curve (0.3-10 keV) *Right*: Phase-folded gamma-ray light curve ($>$ 350 GeV). Reproduced from [24].

indicating variability. Periodicity was later found by *Swift*-XRT [238], confirming the source as a gamma-ray binary.

The emission is variable throughout the orbit and displays a double-peak structure with an initial, higher peak at orbital phase $\phi \approx 0.3$ followed by a broader, fainter peak near $\phi \approx 0.6$ [239]. These outbursts occur near apastron and periastron (respectively) in the orbital solution presented by [170], while no such association is present in [169]. The energy spectrum is consistent with a power law with spectral index $\Gamma = 2.67$, and shows no signs of orbital variability [240]. The average luminosity is $\sim 7 \times 10^{32}$ erg s^{-1}.

HE gamma rays

A GeV counterpart to HESS J0632+057 was identified by *Fermi*-LAT in 2017 [241]. The flux is variable, although a high-precision light curve is not yet possible due to limited statistics. The spectrum is consistent with a power law with index varying from $\Gamma \approx 2.1 - 2.6$ across the orbit. The average luminosity is $\sim 2 \times 10^{33}$ erg s^{-1}.

X-rays

An X-ray source associated with HESS J0632+057 was identified by *XMM-Newton* in 2009 [242]. The X-ray light curve displays a similar behavior to the VHE light curve: a sharp peak near $\phi \approx 0.3$ followed by a fainter, broader peak near $\phi \approx 0.7$, with significant spectral hardening (from $\Gamma \approx 1.4$ to $\Gamma \approx 1.0$) observed during the dip in between peaks [243, 244]. The X-ray peaks are also accompanied by an increase in hydrogen column density [244]. The average luminosity in X-rays is $\sim 7 \times 10^{33}$ erg s^{-1} [27].

Radio

A radio counterpart was identified in 2009 which showed variability on a timescale of months [245]. The spectrum is consistent with a power law with $\alpha \approx -0.6$. Extended emission with a characteristic size of ≈20-50 AU and displaced by ≈20 AU has been observed during the X-ray and VHE dip between peaks [246]. The average radio luminosity is $\sim 4 \times 10^{27}$ erg s^{-1} [27].

5.1.5 1FGL J1018.6-5856

The gamma-ray binary system 1FGL J1018.6-5856 comprises the 31 $M_\odot$ O star 2MASS 10185560–5856459 and an unidentified compact object [172]. The orbital period of system is 16.6 days, with an eccentricity of ≈0.31 [247, 171]. The distance to the system is measured to be approximately 5.4 kpc [172].

VHE gamma rays

VHE emission was discovered near 1FGL J1018.6-5856 in 2012 by H.E.S.S.[248]. The emission consists of a point source spatially consistent with the location of 1FGL J1018.6-5856 in addition to a diffuse extension nearby to PSR J1016-5857. The gamma-ray light curve is variable about the 16 day orbit, peaking near phase $\phi \approx 0$ [25]. The energy spectrum is consistent with a pure power law up to $\sim$ 20 TeV with an index of $\Gamma \approx 2.20$, without evidence of spectral variability. The average VHE luminosity is $\sim 10^{34}$ erg s^{-1}.

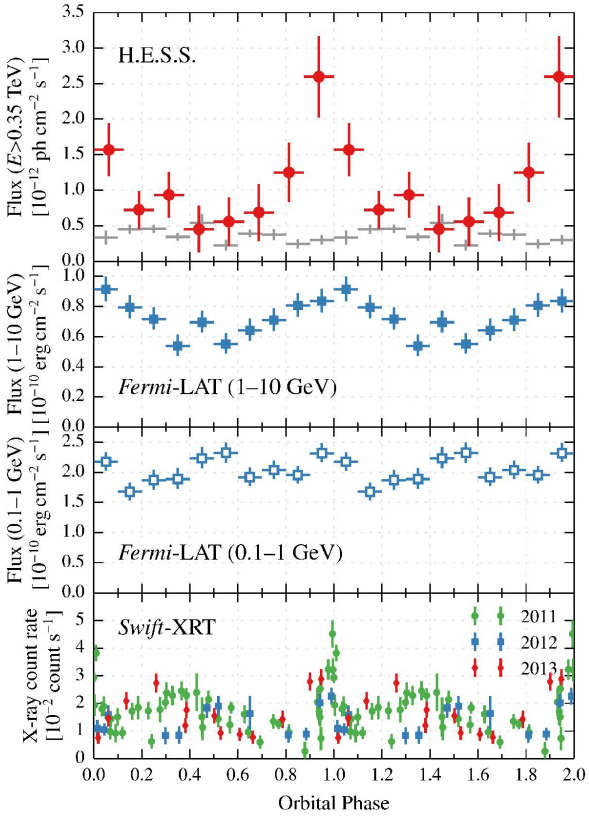

Figure 5.5: Multiwavelength light curve of 1FGL J1018.6-5856. From [25].

HE gamma rays

Variable HE emission modulated with a 16.6-day period was discovered by *Fermi*-LAT in 2012 [247]. The light curve is characterized by a single peak near $\phi \approx 0$. The energy spectrum is described by an exponentially cut power law with an index of $\Gamma \approx 1.9$ and cutoff energy of $E \approx 2.5$ GeV. The spectral curvature varies significantly about the orbit, and the average luminosity is $\sim 10^{36}$ erg s^{-1} [27].

X-rays

An X-ray counterpart was identified by *Swift*-XRT in 2012 [247]. The light curve is characterized by a sharp peak near orbital $\phi \approx 0$ in addition to a broad sinusoidal peak near $\phi \approx 0.4$ [249]. The spectral index varies significantly about an average of $\Gamma \approx 1.4$ throughout the orbit, and exhibits a "softer-when-brighter" correlation with the flux. Variability of the hydrogen column density has not been determined, with an average value of $N_H \approx 7.7 \times 10^{21}$ cm^{-2}. The average luminosity is $\sim 2 \times 10^{34}$ erg s^{-1} [27].

Radio

A faint radio source associated with 1FGL J1018.6-5856 was discovered in 2012 [247]. The light curve shares the sinusoidal peak of the X-ray light curve, although the sharp peak at $\phi \approx 0$ is absent. The spectral index is significantly variable about $\alpha = 0$ throughout the orbit. The average radio luminosity is $\sim 4 \times 10^{29}$ erg s^{-1} [27].

5.1.6 LMC P3

LMC P3 is the only known extra-galactic gamma-ray binary. The system consists of a ~ 34 M$_\odot$ O star which orbits with an unidentified compact object. LMC P3, located in the Large Magellanic Cloud, is variable on a period of 10.3 days with a moderate eccentricity of 0.4 [173].

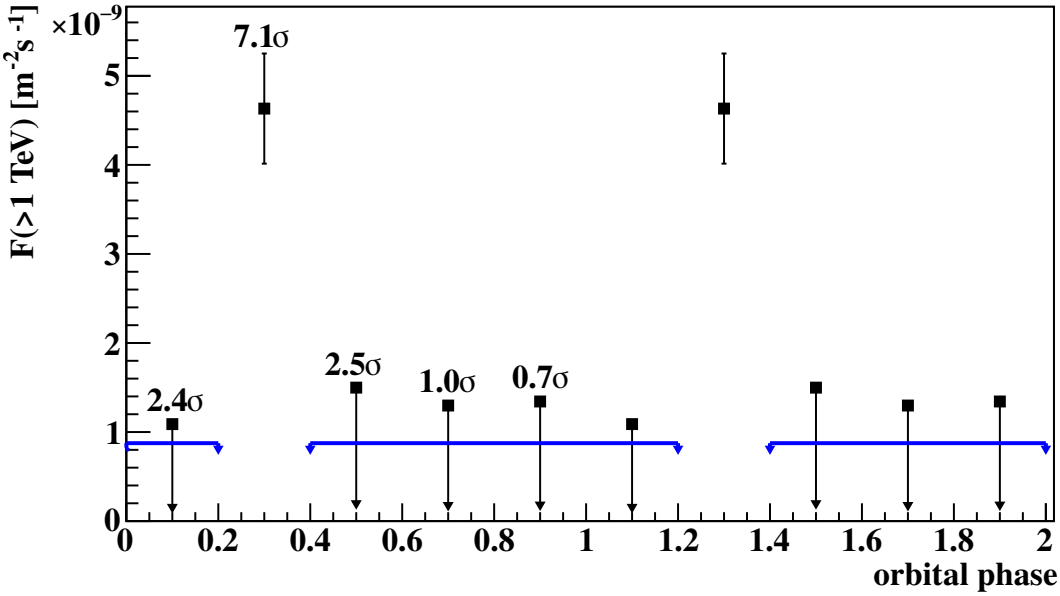

Figure 5.6: The light curve of LMC P3 as seen by H.E.S.S.. The source is only detected near orbital phase $\phi = 0.3$ [26].

VHE gamma rays

Variable VHE emission from LMC P3 was announced by H.E.S.S. in 2017 [26, 250]. The emission exhibits a peak near $\phi \approx 0.3$ and is otherwise undetected. The energy spectrum is consistent with a power law with $\Gamma \approx 2.5$, with no evidence for spectral variability [250]. The average VHE luminosity is $\sim 5 \times 10^{35}$ erg s^{-1}.

HE gamma rays

HE emission was noticed from the direction of LMC P3 by *Fermi*-LAT in 2016 [251]. The variable gamma-ray emission apparently leads the VHE emission, peaking soon after $\phi \approx 0$ [252]. Spectral variability has not been investigated. The average HE luminosity is $\sim 4 \times 10^{36}$ erg s^{-1}.

X-rays

An X-ray counterpart was identified in 2016 by *Swift*-XRT[252]. The emission is variable around the orbit, peaking near orbital phase $\phi \approx 0.5$ and thus seemingly anti-correlated with the HE flux. The energy spectrum is well fit by an absorbed power

law with $\Gamma \approx 1.3$, while the hydrogen column density could not be constrained [252]. The average X-ray luminosity is $\sim 3 \times 10^{35}$ erg s^{-1}.

Radio

Radio emission associated with LMC P3 was discovered in 2016 [252]. The emission is modulated with the 10.3 day orbital period, and displays similar behavior as the X-ray: peaking near $\phi \approx 0.5$ and hence out of phase with the HE gamma ray emission.

5.1.7 PSR J2032+4127/MT91 213

PSR J2032+4127/MT91 213 is known to contain a pulsar as the compact object. The system consists of the $\sim 15 M_\odot$ Be star MT91 213 orbiting with the pulsar PSR J2032+4127[253, 174]. The system exhibits an extreme ($\sim$ 50 year) period with a high eccentricity ($\epsilon \approx 0.94$). The system lies at a distance of $\approx$ 1.3 kpc [254]. The identification of PSR J2032+4127 as a gamma-ray binary is the result of this work and [30]. We briefly describe its multi-wavelength properties here; see chapter 6 for detailed results and discussion.

VHE gamma rays

VHE emission from PSR J2032+4127/MT91 213 was detected by VERITAS and MAGIC in 2017 [30]. The light curve exhibits a double-peaked structure around periastron, with an initial peak right at the periastron date, and a second peak $\sim$ 10 days later. The energy spectrum is well described by an exponentially cut power law with $\Gamma \approx 1.3$ and $E_{\rm cut} \approx 0.6$ TeV. The average luminosity of the source above 200 GeV is $\sim 7 \times 10^{32}$ erg s^{-1} (0.4% of the pulsar's spin-down power). There is no evidence of spectral variability throughout the orbit.

HE gamma rays

Unpulsed HE emission associated with the binary interaction has not been observed [28, 29]. This could be due to the dominance of the pulsed emission originating

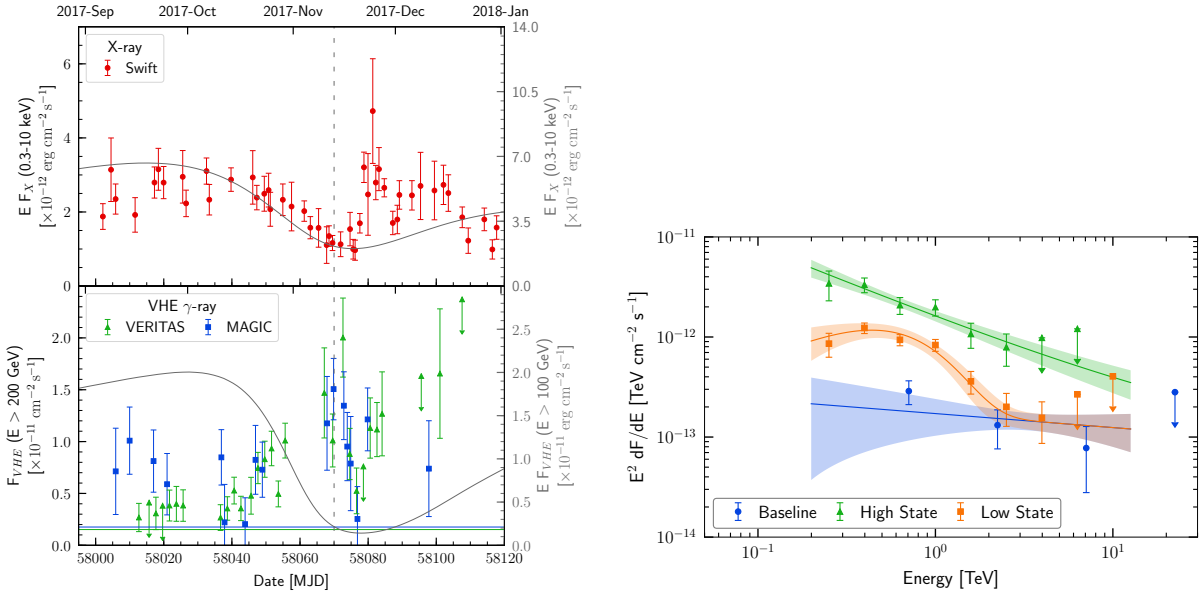

Figure 5.7: *Left*: The X-ray (top) and VHE (bottom) light curve of PSR J2032+4127 around periastron. *Right*: Spectra of PSR J2032+4127 from different portions of the orbit. The green curve shows the spectrum during the high flux state closer to periastron, the orange curve shows the spectrum during the low flux state prior to periastron. The blue curve is the baseline emission from TeV J2032+4130. See chapter 6 for details.

from the pulsar's magnetosphere. Using the pulsed emission from [29] as an upper limit to the binary emission, the HE luminosity can be constrained to be $\lesssim 3 \times 10^{34}$ erg s^{-1} ($\sim 20\%$ of the pulsar spin-down power).

X-rays

Enhanced X-ray emission from the region was first reported in 2016 [174]. The X-ray light curve also displays a double-peaked structure, reaching a minimum around periastron bracketed by maxima days before and after [30]. The average X-ray luminosity (0.3-10 keV) is $\sim 4 \times 10^{32}$ erg s^{-1} (0.25% of the pulsar's spin-down power) [32]. The X-ray spectrum is variable, becoming harder close to periastron [255], with possible rapid softening coincident with the post-periastron flare [256]. The X-ray spectrum is consistent with a broken power law with the break occurring between $\sim 4 - 8$ keV [255, 256].

Radio

Radio emission associated with the binary interaction was reported in 2019 [255]. The radio emission mirrors the X-ray emission, with a sharp dip near periastron and a bright flare a few days later. The pulsed radio component disappeared during this time, fading away near periastron, and not returning for ~ 20 days. During the brightest radio flares, the spectrum can be described by a power law with $\alpha \sim -0.7$. The spectrum is more complex at other epochs [255].

5.1.8 Recent Discoveries

A number of gamma-ray binaries were discovered during the time of writing this work, they are briefly summarized here.

HESS J1832-093

HESS J1832-093 was first discovered at VHE energies by H.E.S.S. in 2015 [257]. Although the VHE flux was not found to be variable, variability was subsequently observed in the X-ray light curve, providing evidence that the source is a gamma-ray binary [258]. Further multiwavelength studies established that the source is likely in the vicinity of a massive O or B type star, and that it exhibits a non-thermal spectrum in the radio, X-ray, and GeV bands which is very similar to other known gamma-ray binaries [259, 260]. Taken together, the evidence points overwhelmingly toward an interpretation of HESS J1832-093 as a gamma-ray binary. The orbital period of the binary is 86.28 ± 3.77 days.

4FGL J1405.1-6119

4FGL J1405.1-6119 was first discovered as a source of GeV gamma-rays by *Fermi*-LAT in 2010 [261]. Corbet et al (2019) subsequently discovered a ~ 14 day periodicity in the GeV, X-ray, and radio light curves and identified an O-type star as its stellar counterpart [262]. This firmly establishes 4FGL J1405.1-6119 as a gamma-ray binary.

5.1.9 Summary

Gamma-ray binary systems share a number of common characteristics which distinguish them as a population from similar systems. All systems exhibit modest X-ray luminosities with hard spectra and no curvature. The X-ray and VHE luminosities are comparable in every system. The HE gamma-ray spectrum is typically curved and similar in shape to most HE gamma-ray pulsars, and does not connect smoothly with the VHE spectrum. The typical HE luminosity is much greater than the VHE luminosity. Non-thermal radio emission is observed in all systems.

These characteristics differ from other HMXB systems, which typically exhibit brighter, curved X-ray spectra with pulsations, and almost always lack radio emission. Gamma-ray binaries are most luminous in the gamma-ray band of the spectrum (above 1 MeV), which sets them apart from other famous binary systems such as Cygnus X-3 or Centaurus X-3 [27].

5.2 Non-thermal emission

The observed non-thermal emission from gamma-ray binary systems is thought to be caused by a population of accelerated electrons radiating their energy via synchrotron and inverse Compton cooling. Because the nature of the compact object is unknown in the majority of systems, the origin of this emission is still an open question in the study of gamma-ray binaries. If the compact object is an energetic pulsar, as it is for PSR B1259-63, PSR J2032+4127, and LS I +61° 303, then the emission likely originates at the shock formed by the interaction between the pulsar and stellar wind (see Figure 5.9). If the compact object is instead a stellar-mass black hole (or an accreting neutron star), then the system probably behaves like a microquasar (an accreting stellar-mass black hole with relativistic jets which mimics a scaled down quasar) where the emission likely originates within a relativistic jet. As will be discussed later, the evidence supports the pulsar-driven scenario in known gamma-ray binary systems.

Regardless of the location of the accelerator, the non-thermal emission is likely dominated by synchrotron cooling in the local magnetic field and inverse Compton

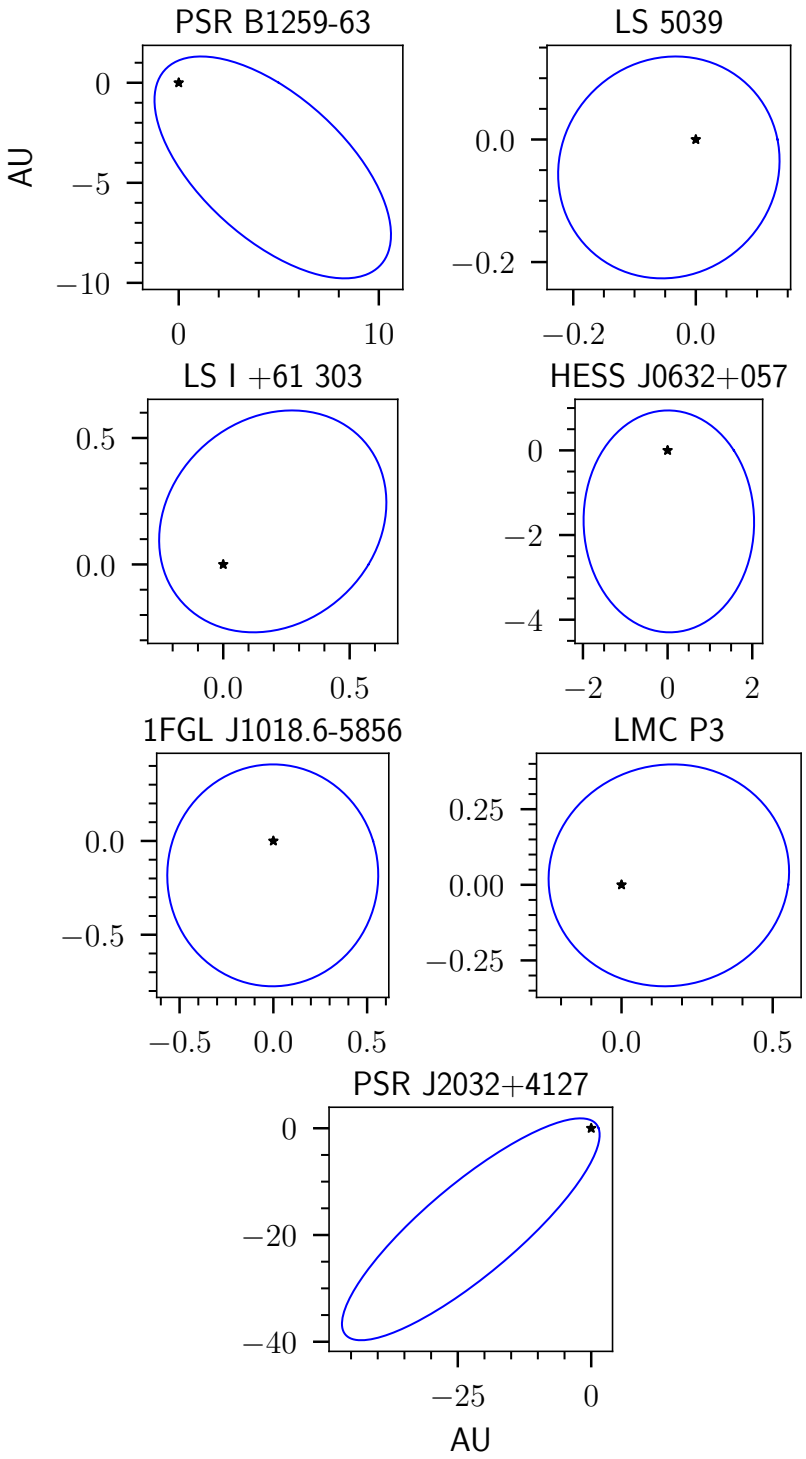

Figure 5.8: The orbit of each system, seen looking down onto the orbital plane. *Note: large uncertainties exist in the orbital solution in several of these sources, the plots are constructed using the mean values.*

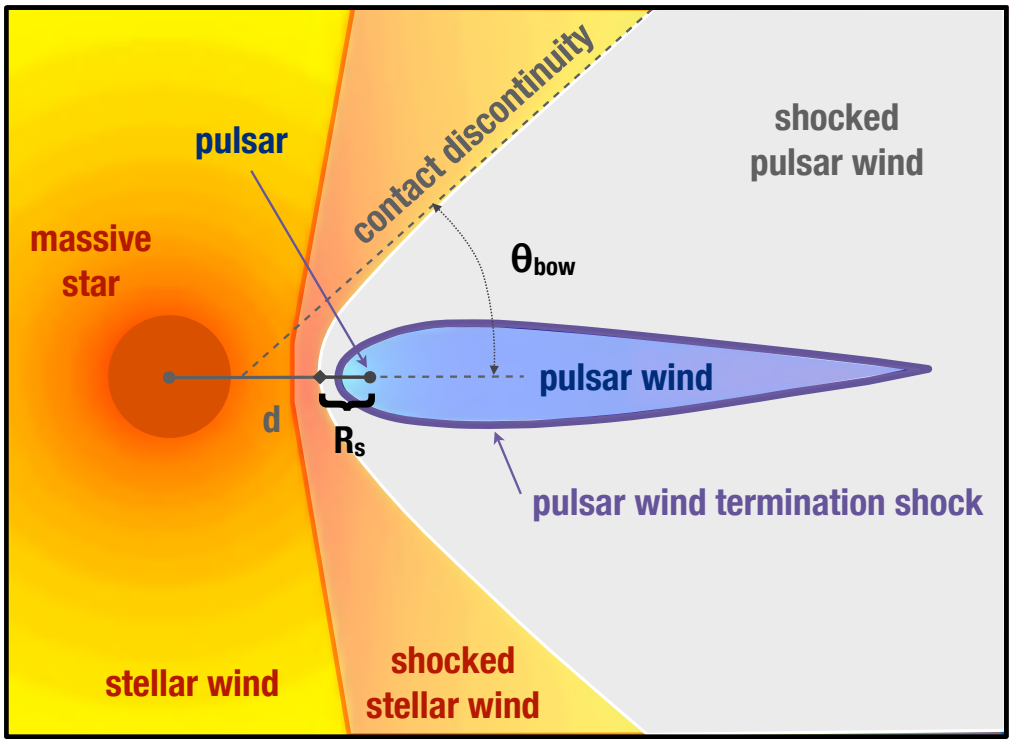

Figure 5.9: The geometry of the intra-binary shock. Reproduced with permission from [27].

cooling by upscattering photons from the massive star.

For diffusive shock acceleration, we assume the shock creates a population of electrons distributed as a power law in energy (see chapter 1):

$$N(E) \propto E^{-\alpha} \tag{5.1}$$

The maximum energy of accelerated electrons is the energy at which the electrons cool faster than they are accelerated. The highest energy electrons cool via synchrotron radiation, which has a characteristic cooling time of [59]:

$$\tau_{\text{sync}} = \frac{3}{4}\frac{m_e^2 c^3}{\sigma_T}\frac{8\pi}{B^2}\frac{1}{E} \tag{5.2}$$

Where σ_T is the Thomson cross-section. With $E = 1$ TeV and $B = 1$ G, $\tau_{\text{sync}} \approx 400$ s. The timescale for acceleration of electrons at the shock is at least the

timescale of gyration in the magnetic field:

$$\tau_{\rm acc} \geq \eta \frac{R_L}{c} = \eta \frac{E}{eBc} \tag{5.3}$$

Where R_L is the electron's Larmor radius and $\eta > 1$ is a parameter characterizing the efficiency of the accelerator (typically $\eta \gg 1$). $\tau_{\rm acc} \approx 0.1$ s in the conditions stated above. $\tau_{\rm sync}$ decreases with energy while $\tau_{\rm acc}$ increases; electrons will be accelerated up to a maximum energy determined by $\tau_{\rm acc}$=$\tau_{\rm sync}$:

$$E_{\rm max} = \left(\frac{3}{4} \frac{m_e^2 c^4 e}{\sigma_T} \frac{8\pi}{B} \right)^{\frac{1}{2}} \tag{5.4}$$

Which results in a maximum electron energy of $E_{\rm max} \approx 60$ TeV. At these energies, the typical Larmor radius ($R_L \approx 10^{11}$ cm) is smaller than the emission region by at least an order of magnitude, thus cooling, and not escape, is the dominant factor determining the maximum energy.

Gamma-ray binary systems are typically radiation dominated for much of the orbit: the radiation energy density $u_{\rm rad}$ dominates the magnetic energy density $u_{\rm B}$. This means that inverse Compton cooling dominates over synchrotron cooling, since $\frac{\tau_{\rm IC}}{\tau_{\rm sync}} = \frac{u_{\rm B}}{u_{\rm rad}}$. This is true as long as $E_{\rm photon} \ll m_e c^2$ in the rest frame of the electron. Since the typical photon energy is $E_{\rm photon} \approx 7$ eV, the Thomson cross-section σ_T is no longer valid for electrons above ~ 25 GeV. This scattering takes place in the Klein-Nishina regime, where the cooling time is [263]:

$$\tau_{\rm IC} \approx \frac{64\pi^2 (k_b T)^2 E^2 + 45 (mc^2)^4}{240 (mc^2)^2 \sigma_T \sigma_{sb} T^4 E} \left(\frac{d}{R_\star} \right)^2 \tag{5.5}$$

$\tau_{\rm IC} \approx 20$ s for $E = 1$ TeV, $T = 3 \times 10^4$ K. In the Klein-Nishina regime, the inverse Compton cooling time now increases with energy and is eventually overtaken by synchrotron cooling when $\tau_{\rm KN} = \tau_{\rm sync}$, at around $E \sim 5$ TeV for the conditions used here. This results in a steep break in the inverse Compton spectrum at around $\sim 0.1 - 10$ TeV, accompanied by a break in the synchrotron spectrum near $\sim 0.1 - 10$

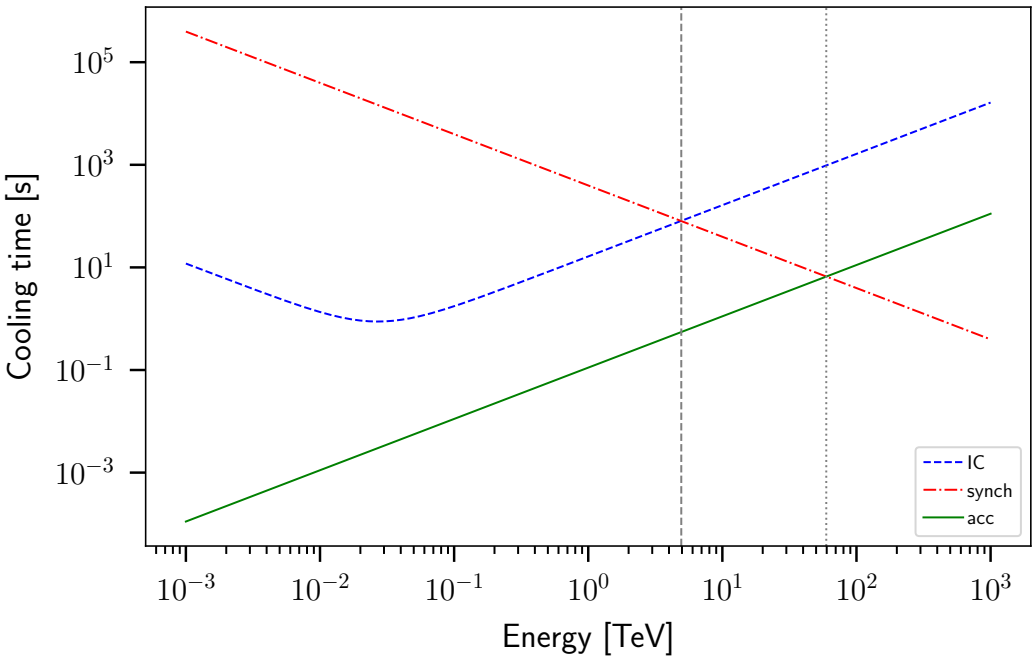

Figure 5.10: Cooling time vs energy for synchrotron and inverse Compton radiation. $\tau_{\rm acc}$ is also plotted. The first (dashed) vertical gray line denotes $\tau_{\rm IC} = \tau_{\rm sync}$. The second (dotted) gray line shows where $\tau_{\rm sync} = \tau_{\rm acc}$. To the left of the first vertical line, IC cooling dominates, even after it enters the Klein-Nishina regime and becomes less efficient. Between the gray lines, synchrotron cooling dominates. At the second vertical line, electrons cannot be effectively accelerated before cooling, and the electron spectrum cuts off. Values are shown for $B = 1$ G, $T_\star = 3 \times 10^4$ K, shock distance $d = 0.1$ AU.

MeV [264, 27]. An example of the cooling time evolution for relevant processes and typical physical conditions is shown in figure 5.10.

The location of the break is dependent upon the magnetic field at the shock: $E_{\rm brk} \propto \frac{1}{B}$. The magnetic field can vary with orbital phase as the location of the shock with respect to the compact object changes. This introduces variability in the break energy throughout the orbit, which will modulate the observed flux as well as the shape of the energy spectrum. Such a spectral cutoff has been observed in two gamma-ray binary systems. LS 5039 shows a cutoff in the high-state spectrum (near inferior conjunction) at $E_{\rm brk} \approx 9$ TeV, while the low-state spectrum (between inferior conjunction and periastron) of PSR J2032+4127 cuts off near $E_{\rm brk} \approx 0.3$ TeV. Since the stellar companion of LS 5039 is hotter than that of PSR J2032+4127 ($\sim$40,000 K

vs 30,000 K), electrons in the LS 5039 system should enter the Klein-Nishina regime at a lower energy than those in PSR J2032+4127. All else being equal, this should result a lower energy cutoff in LS 5039 than PSR J2032+4127, contrary to observations. This might imply a higher shock magnetic field in PSR J2032+4127 than in LS 5039, which would tend to lower the break energy. Many other factors influence the energy spectrum, however, and detailed simulations are the best way to investigate the physical environment in these systems.

The high-energy gamma-ray spectrum is thought to be formed by a different electron population than the X-ray/VHE spectrum. The HE spectrum in gamma-ray binary systems is characterized by a cutoff at low energy which is incompatible with the VHE spectrum. The typical energy of this cutoff ($\sim 1 - 10$ GeV) is lower than the expected pair production threshold, and is characteristic of the high-energy spectrum observed in most gamma-ray pulsars. This similarity has led a number of authors to invoke a pulsar as the compact object; the HE emission then originates in the pulsar magnetosphere, or as a result of inverse Compton scattering of stellar photons by the pre-shock pulsar wind [27]. The former scenario would result in pulsed emission, though this would be difficult to recognize without knowledge of the pulsar's period. HE emission from PSR B1259-63 is not pulsed, which indicates that it originates well outside the pulsar's light cylinder [182]. The emission will then vary with orbital separation and inverse Compton scattering angle. A consistent explanation which accounts for HE emission in all systems has yet to emerge, and the nature of the HE emission remains a topic of debate.

As the massive star and compact orbit each other, the physical conditions in the vicinity of the emission region change continuously. This results in significant variability in the observed emission. The energy spectrum of the observed emission is influenced by a number of factors, many of which vary with the orbital phase of the system. These factors include absorption of VHE photons by the stellar photon field, the anisotropy of the inverse Compton process, and relativistic doppler boosting of the post-shock flow. Additionally, the emission region may encounter changing

magnetic and radiation fields at different orbital phases, which will significantly affect the relative importance of synchrotron and inverse Compton cooling in these different environments. These factors create competing effects across the orbit, resulting in highly complex variability in the observed emission.

Many gamma-ray binary systems comprise highly eccentric orbits such that the separation distance between the two objects is highly variable (in PSR B1259-63, for example $\frac{d_{\text{apastron}}}{d_{\text{periastron}}} \sim 15$). The emission region is thus much closer to both the compact object and the stellar companion at periastron, leading to an increase in radiation energy density and magnetic energy density that will increase the intrinsic inverse Compton and synchrotron luminosities close to periastron. These luminosities are then modulated by a number of other effects, mostly dictated by the geometry of the orbit.

Absorption of VHE photons in the proximity of the intense photon field of the stellar companion is perhaps the most significant effect introducing variability. This "absorption" actually takes the form of pair production, in which a VHE photon interacts with a stellar photon (typically in the UV range) to create an electron-positron pair. The energy threshold for pair production upon an interaction between two photons is given by [265]:

$$E_\star E_\gamma \geq \frac{2m_e^2c^4}{1-\hat{e}_\gamma \cdot \hat{e}_\star} \tag{5.6}$$

Where $E_{\star/\gamma}$ is the energy of the stellar/gamma-ray photon, m_e is the electron rest mass, c is the speed of light, and $\hat{e}_{\star/\gamma}$ is the unit vector describing the direction of propagation of the stellar/gamma-ray photon ($\hat{e}_\star \cdot \hat{e}_\gamma = \theta$ in Figure 5.11). The cross section of the interaction (see [265]) is maximal near the threshold energy. For a typical Be star, $T_\star \approx 3 \times 10^4$ K and so a typical photon will have energy $E_\star = 2.7kT \approx 7$ eV. Hence an incident gamma ray may pair-produce (during a head on collision) for energies above $E_\gamma \approx 40$ GeV. The total absorption effect as seen by the observer is a result of integrating the product of this cross-section and the stellar radiation density along the line of sight, resulting in heavier absorption in orbital phases where the shock

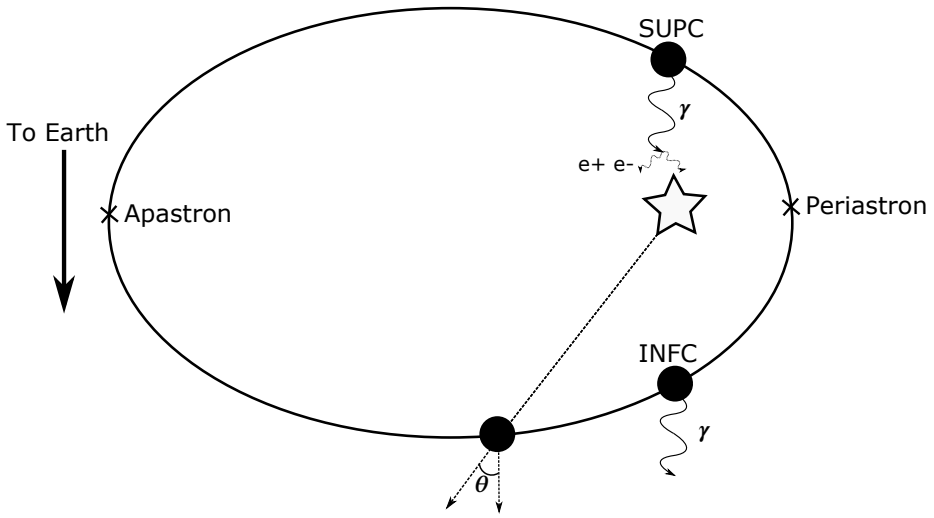

Figure 5.11: The geometry of the gamma-ray binary. The star shape represents the massive star, the block dot represents the position of the compact object at different points around the orbit. Apastron and periastron are labeled, as are inferior and superior conjunction (INFC/SUPC).

is closer to the star (higher radiation density) and/or the shock moves behind the star relative to the observer, where VHE photons must travel the greatest distance through the photon field. This absorption has been invoked to at least partially explain the drop in flux observed in many gamma-ray binary systems close to periastron [30, 266, 267].

At inferior conjunction, VHE photons are moving away from stellar photons and $\hat{e_\gamma} \cdot \hat{e_\star}$ is maximal, resulting in minimal absorption. Absorption of VHE photons will create a trough feature in the gamma-ray spectrum, the location, depth, and width of which depends highly on the viewing geometry of the system [268, 269]. This feature likely spans several decades in energy ($\sim$ 30 GeV - 30 TeV [269]), making it difficult to detect with any single instrument. This picture is modified by the radiation of the $e\pm$ pairs created by the absorption of the VHE photon. These secondary pairs can cool via synchrotron or inverse Compton radiation, depending upon the environment in the vicinity of the stellar companion. If they cool via inverse Compton scattering, the corresponding VHE photon can again be absorbed, and the process is repeated, resulting in a cascade until the VHE photon is below the threshold energy. The chief

effect of this process is to re-emit absorbed flux farther away from the star, making it less opaque at otherwise highly-absorbed orbital phases. Modeling of this process is complex, and must account for the orbital geometry of the system relative to the observer, the ambient magnetic field in the vicinity of the stellar companion, and the diffusion of electrons in this region [270, 271, 272].

The observed VHE emission also reflects the variable importance of inverse Compton cooling at different orbital phases. The power radiated by an electron up-scattering photons from a point source is [27]:

$$P = \sigma_T c U_\star (1 - \beta\mu) \left[(1 - \beta\mu)\gamma^2 - 1\right] \tag{5.7}$$

Where σ_T is again the Thomson cross-section, $U_\star$ is the radiation density from the star, γ is the electron lorentz factor, $\beta = v/c$, and $\mu = \hat{e}_\star \cdot \hat{e}_\gamma$, the cosine of the angle between the incoming photon and electron. The inverse Compton radiation will thus tend to be maximal (given constant $U_\star$) during orbital phases where the collision between photon and electron is head-on ($\mu = -1$). This means that, ignoring absorption effects, a maximum in the VHE light curve might be expected near superior conjunction, when the star is between the emission region and the observer. In practice, however, this maximum is often overpowered by the intense absorption effects at that same orbital phase. This is most clearly observed in the case of LS 5039, where the maximum and minimum VHE flux correspond approximately to inferior and superior conjunction, respectively [267]. The high energy threshold for absorption might also explain why the HE light curve is in anti-phase with the VHE in several gamma-ray binary systems: if absorption is unimportant in the HE regime, the peaks should follow the un-absorbed inverse Compton profile, peaking at superior conjunction and fading at inferior conjunction.

Because the velocity of the post-shock flow can be mildly relativistic, ($\beta \approx 1/3$ [273]), the radiation emitted in this region can be significantly beamed in the direction of motion. In the case of a pulsar-powered binary, a bow shock is expected to wrap around the pulsar, with the flow directed away from the stellar companion (see Figure

5.9). For synchrotron radiation, this has the effect of amplifying the observed flux at inferior conjunction and suppressing it near superior conjunction. This effect can be significant, with a maximum flux ~ 8 times that of the minimum flux [274], and has been invoked to explain the X-ray variability in LS 5039 and PSR J2032+4127 [274, 28]. For inverse Compton emission, the effect is to reduce the amplitude of modulations, as electrons at superior conjunction are deboosted and see a lower photon flux, and vice-versa for inferior conjunction. These effects can become more complex and arise at different orbital phases in the case that the direction of the post-shock flow is not purely radial [274]. For microquasar systems, Doppler beaming is not expected to contribute to variability, as the angle of the jet with respect to the line of sight of the observer is expected to be steady.

5.3 Summary

The origin of emission in the majority of gamma-ray binary systems remains a key question. The non-thermal emission in these systems is probably powered either by the rotational energy of a pulsar or the accretion energy of a black hole. Distinguishing between these two scenarios remains an important goal in the study of gamma-ray binaries. Only in three systems, PSR B1259-63, PSR J2032+4127, and LS I +61° 303, is the nature of the compact object, and thus the probable origin of high-energy emission, certain. The detection of pulsations from other gamma-ray binary systems would provide direct evidence of a pulsar as the compact object, however the absence of pulsations does not preclude a pulsar. A precise measurement of the mass of the compact object can be used to rule out the presence of a pulsar if $M \gtrapprox 2.1$ M$_\odot$ [275]. In the case of LS 5039, $M_{\rm CO} = 3.7^{+1.3}_{-1.0}M_\odot$, if the orbital inclination $i \approx 30°$, however the inclination in this system is not well constrained [166]. Similarly with HESS J0632+057, differing orbital solutions have been proposed which lead to different conclusions about the compact object: Moritani et al (2018,[170]) suggest a mass compatible with a neutron star for most orbital inclinations, while Casares et al (2012, [169]) favor a black hole. Similar analyses of other systems have also been inconclusive.

In the absence of any direct evidence for either a pulsar or a black hole, indirect evidence implies that the pulsar scenario may be more likely. The general spectral characteristics shared by gamma-ray binary systems mirror those observed in other pulsar-related systems. The X-ray and radio spectra are similar to those observed in pulsar wind nebulae, and and the X-ray spectra do not show a cutoff or turnover characteristic of accretion-driven systems [27]. The high-energy spectra, with an exponential cutoff at a few GeV, resemble those of gamma-ray pulsars, though orbital variability originating in the pulsar magnetosphere is difficult to explain. The cometary radio morphology observed in several of these systems is indicative of a pulsar wind scenario. Although the extended radio structure can also be attributed to microquasar jets, the periodic variability of the position angle in these systems is more suggestive of a pulsar [276, 27, 211]. Observations of gamma-ray binary systems have nonetheless been explained in the context of both microquasar and pulsar wind scenarios, and despite moderate indirect evidence favoring the presence of pulsars, the question remains unresolved for the majority of systems.

In the discussion throughout this chapter, leptonic processes have been assumed to be responsible for the non-thermal emission. Hadronic emission mechanisms have also been invoked to explain the emission in both microquasar (e.g. [277]) and pulsar wind scenarios ([224]). These models generally invoke proton-proton interactions between protons originating in either the pulsar wind or in the relativistic jet and protons in the stellar wind and/or disk. Such models face several challenges. The long cooling timescale and large Larmor radii of high-energy protons imply that only a small fraction of particle energy can be radiated before escaping the emission region, while observations suggest that a significant fraction of available is energy converted to radiation. The presence of a hot massive star in every system makes inverse Compton scattering an efficient and therefore quite likely mechanism which also explains the orbital variability. Conversely, the orbital variability is more difficult to explain using hadronic models. Finally, the pulsar wind is likely to be dominated by electrons and positrons, rather than nuclei. Thus, the majority of recent gamma-ray binary models,

of both the microquasar and pulsar wind variety, have opted for leptonic mechanisms. Even so, hadronic emission formally remains a possibility.

While gamma-ray binaries still comprise a relatively rare source class, recent estimates suggest there may be as many as $\sim$ 200 systems within our galaxy [160]. The currently known systems likely represent the most luminous of all systems, due to the sensitivity of current instruments. Further exploration of *Fermi*-LAT data, and surveys with future instruments, namely CTA, may more than double the size of the current population. The addition of new sources to examine and model, together with increased precision of measurements of current systems, is critical to developing a consistent theoretical framework for these important particle acceleration laboratories.

Chapter 6

NON-THERMAL EMISSION FROM THE BINARY PSR J2032+4127/MT91 213

PSR J2032+4127/MT91 213 is a newly discovered gamma-ray binary system which comprises the young, energetic pulsar PSR J2032+4127 in a long-period, eccentric orbit with the massive Be star MT91 213. Detailed observations of the system during its periastron passage revealed dramatic variability across the electromagnetic spectrum. As only the second gamma-ray binary system known to be powered by a pulsar, observations of PSR J2032+4127/MT91 213 can help to shed light on the acceleration and emission mechanisms at work in gamma-ray binary systems. The discovery of TeV gamma-ray emission from PSR J2032+4127/MT91 213 and its subsequent identification as a pulsar-powered gamma-ray binary is the primary result of this thesis. These results have been published in an Astrophysical Journal Letter [30][1], and are presented and discussed in further detail within this Chapter.

6.1 PSR J2032+4127/MT91 213

PSR J2032+4127 is a relatively energetic ($\dot{E} = 1.7 \times 10^{35}$ ergs s^{-1}) pulsar with a period of 143 ms and a characteristic age of 180 kyr. The pulsar was first discovered at gamma-ray energies in a blind search of *Fermi*-LAT data in 2009 [278], and subsequently detected in radio by the Green Bank Telescope [279]. MT91 213 is a ~ 15 M$_\odot$ star of spectral type B0Ve with a large circumstellar disk varying in size from 0.2-0.5 AU [253, 174]. MT91 213 is spatially coincident (to within 4″) with the position of PSR J2032+4127.

[1] The author of this dissertation is a corresponding author for this publication

Timing analyses of radio and gamma-ray photons from PSR J2032+4127 indicate a significant evolution in the pulse period of PSR J2032+4127, which is best explained by Doppler shifting of the period arising from a significant radial velocity. This points to a binary connection between PSR J2032+4127 and MT91 213 [280, 174]. The most likely orbital solution places the pulsar in a long period (45-50 years) and highly elliptical ($\epsilon \approx 0.94 - 0.99$) orbit with its massive companion. The system is located in the Cyg OB2 stellar association at a distance of ≈ 1.3 kpc [254]. It is nearby in the sky to the famous microquasar Cygnus X-3, and lies only about 0.1° away from the center of the unidentified TeV gamma-ray source TeV J2032+4130[2], whose extended emission overlaps the location of PSR J2032+4127/MT91 213.

The binary system reached periastron on November 13, 2017. The periastron passage was the subject of an extensive, months-long multiwavelength observing campaign, focusing on X-ray and VHE emission from the region ([30], this work).

6.2 X-ray observations

X-ray photons are expected to be produced in gamma-ray binaries as electrons accelerated at the intra-binary shock cool via synchrotron radiation in the local magnetic field (see Chapter 5). X-ray observations were secured from *Swift*-XRT via proposals submitted to the observatory's guest investigator program, for one of which the author of this thesis was a co-investigator. *Swift*-XRT conducted (approximately) bi-weekly observations of the region for several months prior to and following the periastron passage, with more frequent observations covering the periastron passage itself. Detailed variability from these observations are described in [30] and are discussed in more detail below.

6.2.1 *Swift*-XRT

Swift-XRT is a grazing incidence X-ray telescope on board the Neil Gehrels Swift Observatory, which was launched in 2004 and remains active [281, 282]. The

[2] See Chapter 7 for a more detailed discussion of TeV J2032+4130.

XRT instrument consists of a 600 x 600 pixel CCD camera with a 23.6′ x 23.6′ field of view, and is sensitive to photons ranging from 0.2-10 keV. The instrument is most sensitive at ∼1.5 keV, where the effective area peaks at approximately 120 cm^2 and the angular resolution is 18″.

6.2.2 Data analysis

Data selection

Publicly available *Swift*-XRT data from June 16 2008 to December 10 2018, consisting of 210 individual observations, were selected for analysis. This time span covers the baseline state of the system, before enhanced flaring activity was noted, and includes the latest available data, collected several months after the periastron passage. The exposure of the dataset is concentrated around the periastron passage during the fall of 2017. All observations were taken in photon-counting mode, during which the instrument reads out the entire field of view every 2.5 seconds.

The data analysis described in this work and in [30] made use of the standard HEAsoft tools [283] from version 6.24. The `xrtpipeline` script was utilized for bias subtraction and identification and removal of hot or flickering pixels. Photons from the source were extracted from a 20 pixel (47.2″) radius circle centered on the location of PSR J2032+4127. Background events were taken from five regions of the same size and with the same offset from the camera center as PSR J2032+4127.

Energy spectrum

The number of counts from the pre-defined source (ON) region and background (OFF) regions were extracted in each energy bin (of width 10 eV) from 0.3 - 10 keV. The excess counts in each energy bin were then determined following:

$$N_{\rm ex} = N_{\rm on} - \alpha N_{\rm off} \tag{6.1}$$

Where α is the normalization factor used to correct the differing exposures of the two spectra:

$$\alpha = \frac{\sum_{i,j \in \mathrm{ON}} E(i,j)}{\sum_{i,j \in \mathrm{OFF}} E(i,j)} \tag{6.2}$$

With E being the exposure, in seconds, across the entire instrument field of view. Instrument response functions, including the effective area table and energy dispersion matrix, were copied from the HEASARC Calibration Database (CALDB). Spectra from the source and background region, along with the relevant instrument response files, were then analyzed using the spectral fitting software XSPEC [284]. The spectra were rebinned to ensure a minimum of three counts per energy bin. The background-subtracted spectrum was then fit (via χ^2 minimization) to an absorbed power law model (`phabs*powerlaw` in XSPEC):

$$\frac{dN}{dE} = e^{-n_H \sigma(E)} K \left(\frac{E}{1 \text{ keV}} \right)^{-\alpha} \tag{6.3}$$

Where $\sigma(E)$ is the photo-electric cross section, n_H is the hydrogen column density in units of 10^{22} cm^{-2}, α is the spectral index, and K is a normalization constant, in units of keV^{-1}cm^{-2}s^{-1} A flux was calculated by integrating the best-fit energy spectrum; 1 σ uncertainties on the flux measurement were estimated by sampling from the distribution defined by the best fit parameters and their uncertainties 1000 times. The overall energy spectrum is well-fit with the parameters $\alpha = 1.76 \pm 0.04$, $n_H = (9.1 \pm 0.3) \times 10^{21}$ cm^{-2}, consistent with other spectral studies from this source.

Light curve

The X-ray light curve was constructed by calculating the flux in the manner described above for every observation in the dataset. Due to the dense sampling rate across the periastron passage, multiple light curves were constructed with different binning. The rebinning was accomplished by reading multiple observations into the `xselect` tool and merging them into a single event list. Spectra were then constructed following the procedure outlined earlier. Three different light curves were generated: an unbinned curve, a curve with a one-day bin size, and a curve with a one-week bin size. This allows for study of the temporal behavior of the system on multiple time

scales with minimal statistical uncertainties. The resulting curves for the one-week bins (a) and one-day bins (b) are shown in the top panel of Figure 6.1.

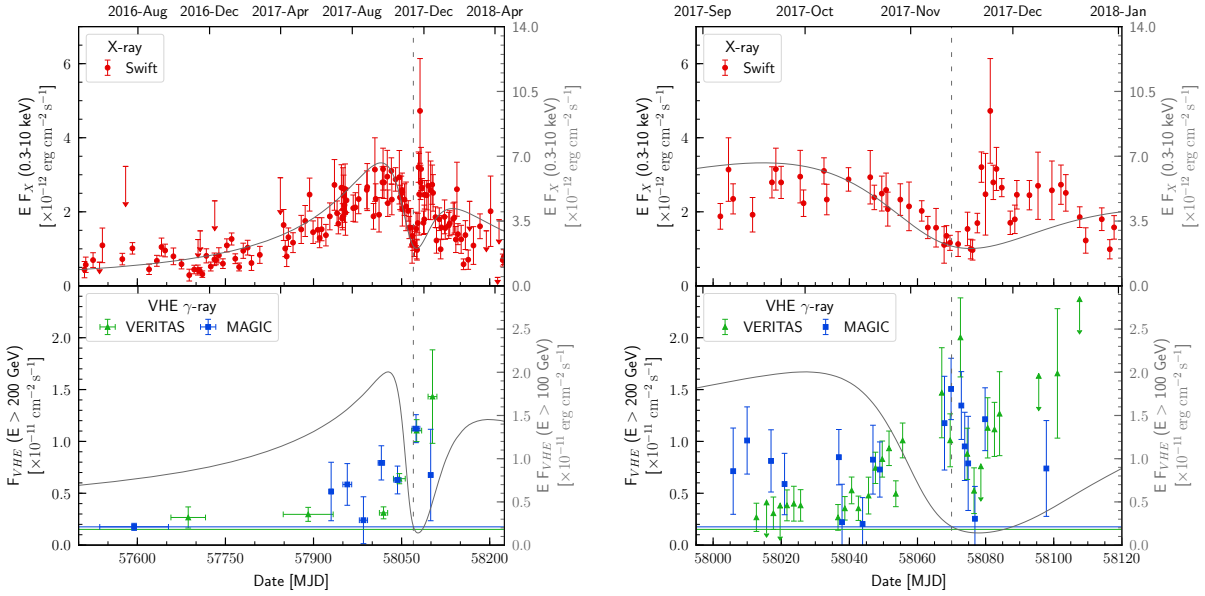

(a) Long-term light curve

(b) Light curve across periastron

Figure 6.1: X-ray (top panels) and VHE light curves. Figure (a) shows the long-term light curve starting in early 2016, with week-long bins for the X-ray flux. Figure (b) shows the light curve with finer bins and zoomed to show detailed variability around periastron. Shown in gray, and corresponding to the scale on the right-hand side, are the predicted X-ray and VHE light curves from [28] and [29]. Periastron is indicated by the vertical dashed line. Figure produced by author and shared from [30].

6.3 VHE Observations

VHE observations were conducted jointly by VERITAS[3] and MAGIC. VERITAS is described in detail in Chapter 3; MAGIC is an array of two 17-m diameter Imaging Atmospheric Cherenkov telescopes located on the island of La Palma in Spain. MAGIC is further described in [285]. This joint campaign allowed for more dense and reliable coverage of the source. Since VERITAS does not operate for most of July and August, MAGIC observations were critical to study the behavior of the source several months before periastron. The use of multiple instruments at different locations also

[3] The author of this dissertation is affiliated with the VERITAS collaboration

introduces a redundancy to increase the chances of data collection in the case of poor observing conditions at one site. The results for both VERITAS and MAGIC are presented in [30]; this work will focus on the VERITAS results, which were produced by the author of this dissertation.

6.3.1 Data Selection and Analysis

A total of 181.3 hours of VHE data from VERITAS, taken over a 9 year period from November 2008 to December 2017, were used for the analysis. This included 51.6 hours of archival data taken before 2016 (targeting the nearby source TeV J2032+4130), 30.1 hours taken over the fall of 2016 through the spring of 2017, and 99.6 hours covering the immediate periastron passage (September through December of 2017). This dataset consisted of 6 observations, or "runs", taken in the original VERITAS configuration (prior to the movement of telescope 1 to its current location, designated "V4"), 149 runs taken in the current array configuration but prior to the upgrade of all VERITAS cameras in 2012 ("V5"), and 316 runs taken after the camera upgrade ("V6") [4]. The exposures and time spans of the total dataset and its sub-datasets are described in Table 6.1. All data were collected in *wobble* mode, where the source is offset by $\sim 0.5^{\circ}$ to allow for simultaneous background estimation in the field of view [157]. The distribution of observing time about the orbit of the system is plotted in Figure 6.2.

All data were analyzed using the EventDisplay analysis package [286]. Several selection criteria, optimized *a priori* for a point-like gamma-ray source with a spectral index similar to that of the Crab Nebula, were employed for data reduction [5,6]. These

[4] See Chapter 3 for a detailed description of the VERITAS array and its different configurations

[5] See Chapter 4 for a detailed description of the data reduction process

[6] The size of the expected emission region ($\lesssim 1$ AU) and distance from Earth (~ 1.3 kpc) imply an emission region of $\lesssim 2$ mas, much smaller than the point spread function of VERITAS. Hence a point source is assumed *a priori*.

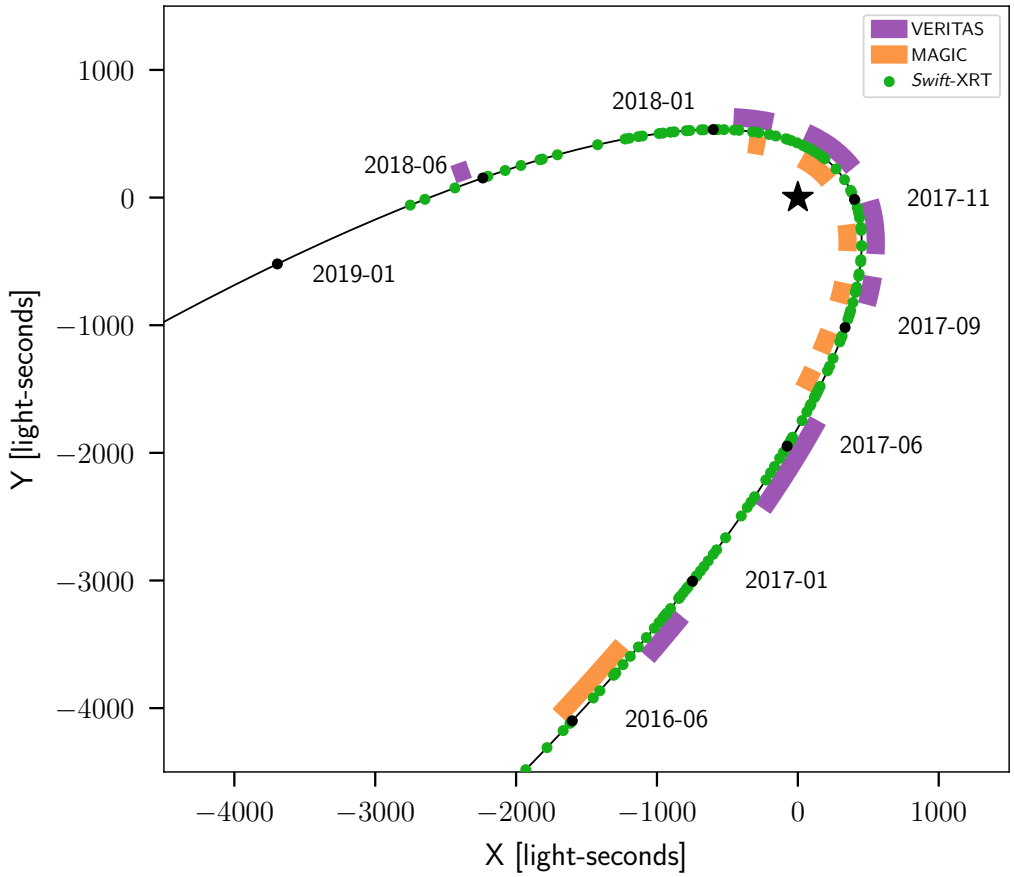

Figure 6.2: The orbit of PSR J2032+4127 (solid line) around MT91 213 ($\star$), as projected onto the plane containing the line-of-sight and the major axis of the orbit. VERITAS, MAGIC, and *Swift*-XRT observing windows are also plotted along the orbit.

Name	Exposure [hrs]	Time Span
Archival	51.6	2008–2015
Fall 2017	99.6	September–December 2017
Other	30.1	September 2016–June 2017
Total	181.3	2008-2017

Table 6.1: Summary of VERITAS data. Archival data, targeting TeV J2032+4130, were collected prior to the detection of the binary emission. Fall 2017 data cover the binary periastron passage and contain the peak of the binary emission. Other data were taken before the detection of the binary, but too close to the periastron for a robust analysis of TeV J2032+4130.

Cut	Value
size	400 d.c (V4-5), 600 d.c (V6)
# Tels	≥ 2
θ^2	< 0.008 $(^\circ)^2$
mean scaled width	$-1.2 <$ msw < 0.5
mean scaled length	$-1.2 <$ msl < 0.7

Table 6.2: Selection criteria used in the VHE analysis. "size" = the total signal accumulated in the image, in units of digital counts (d.c). θ^2=the square of the radius of the source region. Mean scaled width/length are parameters pertaining to the shape of the image, used to discriminate between gamma-ray and cosmic-ray events. See Chapter 4 for a full description of these parameters.

cuts are summarized in Table 6.2.

Source detection

While observations of the region over the fall of 2016 and spring of 2017 showed insufficient evidence for a gamma-ray source associated with the binary [287], a highly significant signal of 21.5 standard deviations (σ) was observed from the region during the periastron passage of fall of 2017, resulting in the confirmation of the system as a newly discovered gamma-ray binary. According to the right ascension and declination of the maximum VHE emission, the new gamma-ray source was given the name VER J2032+414.

Light curve

Two different light curves, one with $\sim$ month-long bins, and one with 2-day bins, were constructed. Events from the source and background region were summed for each bin, and significances and fluxes were calculated following the procedure detailed in Chapter 4. If the statistical significance of the signal from a bin is below 2 standard deviations, a 95% confidence upper limit, calculated following Helene [288] is used instead. Both light curves are shown in Figure 6.1.

6.3.2 Morphology and energy spectrum

TeV J2032+4130

TeV J2032+4130 is an unidentified, extended VHE gamma-ray source centered $\sim 0.1^{\circ}$ away from the location of PSR J2032+4127 and partially overlapping it (see Chapter 7 for a more detailed study of TeV J2032+4130). It was first detected by HEGRA in 2005 [105], and has been seen by a number of VHE instruments since. Most recently, VERITAS reported in 2014 that the extended emission is asymmetrical, and that the VHE emission coincides with a rare gap in emission at other wavelengths [31]. While the nature of TeV J2032+4130 is still unconfirmed, a pulsar wind nebula relationship with PSR J2032+4127 appears likely [31]. For this analysis, TeV J2032+4130 was dealt with primarily as a complicating source of background, or "baseline", gamma-ray emission which must be accounted for in order to properly understand the emission from the intra-binary shock.

Because of the overlap between TeV J2032+4130 with PSR J2032+4127/MT91 213, the emission from the region is best understood as a sum of the separate emission from each individual source. A more complicated model is therefore required to accurately fit the spectrum and morphology of the emission originating from the binary interaction.

Energy Spectrum

The observed gamma-ray spectrum from the region comprises both the steady "baseline" emission, associated with TeV J2032+4130, and the transient "binary" emission, associated with the intra-binary shock (see the schematic in the top panel of Figure 6.4). The gamma ray emission from the binary interaction was determined by modeling the observed emission as a superposition of flux from the binary interaction in addition to the steady, extended emission from TeV J2032+4130. The gamma-ray spectrum of TeV J2032+4130 was modeled as a power law (Equation 6.4) with a spectral index bounded by the 1 σ range reported in [31]. For the binary interaction component of the emission, both an ordinary power law (Equation 6.4) and a power law with an exponential cutoff (Equation 6.5) were used.

$$\frac{dN}{dE} = N_0 \left(\frac{E}{E_0}\right)^{-\Gamma} \tag{6.4}$$

$$\frac{dN}{dE} = N_0 \left(\frac{E}{E_0}\right)^{-\Gamma} e^{-\frac{E}{E_{\text{cut}}}} \tag{6.5}$$

The gamma-ray spectrum of TeV J2032+4130 has been well-studied (see, for example: [31] and [1]) and is known to exhibit a hard power-law shape with an index near ~ 2. Initially, one might assume that the spectrum of the binary emission could be examined simply by subtracting the known spectrum of TeV J2032+4130 from the observed spectrum of the Fall 2017 dataset. The observed spectrum from Fall 2017, however, was extracted from a relatively small (0.09° radius) region which is offset from the center of TeV J2032+4130 by $\sim 0.1°$. The emission from TeV J2032+4130 in this region is significantly weaker and, due to the relatively small statistical sample, a precise measurement of the spectrum could not be obtained from the available archival data (data collected before the appearance of the binary emission). Such a measurement is nonetheless necessary in order to study the spectrum of the binary component of the emission. In order to more precisely estimate the contribution of this baseline emission from TeV J2032+4130, a joint fit was conducted with the archival and newly

collected data. The two-component model was fit to the dataset from fall 2017, while the baseline power law component of the model was simultaneously fit to the archival dataset of TeV J2032+4130 (see Figure 6.4). Simultaneous, in this context, means that the χ^2 statistic that was minimized was constructed by summing the individual χ^2 values from the residuals of each model-dataset pairing:

$$\chi^2 = \chi^2_{\text{baseline}} + \chi^2_{\text{baseline+binary}}$$

Such a joint fit mechanism enables the otherwise poorly-measured spectrum of the baseline to be informed by the newly collected data containing the binary emission. The archival data used for the fit were re-analyzed with the same source region and data reduction cuts as the analysis of the binary interaction. The results of this fit are given in Table 6.3 and plotted in Figure 6.5. For the binary component, both a power law and a power law with an exponential cutoff were tested. The spectrum of the intra-binary interaction strongly favored (as determined by an F test comparing the two χ^2 values) an exponentially cutoff power law model with a cutoff between 0.4–0.8 TeV.

To search for spectral variability, the data were divided according to flux level. To ensure sufficient statistics in each of these datasets, only two are defined: one "high state" containing data with a measured flux $\geq 1 \times 10^{-11}$ cm^{-2} s^{-1} and one "low state" comprising the remaining data, and limited to data taken prior to the periastron passage. This allows the spectral variability to be assessed as a function of either flux or time (the low state data are lower in flux and were collected entirely prior to the high state data). The same joint fit mechanism as described above was used to determine the spectral parameters, except with three model-dataset pairs instead of two. A baseline-only model was fit to the archival dataset, a baseline + low state model was fit to the low state dataset, and a baseline + high state model was fit to the high state dataset. The χ^2 statistic was constructed in the same manner as described above:

$$\chi^2 = \chi^2_{\text{baseline}} + \chi^2_{\text{baseline+low}} + \chi^2_{\text{baseline+high}}$$

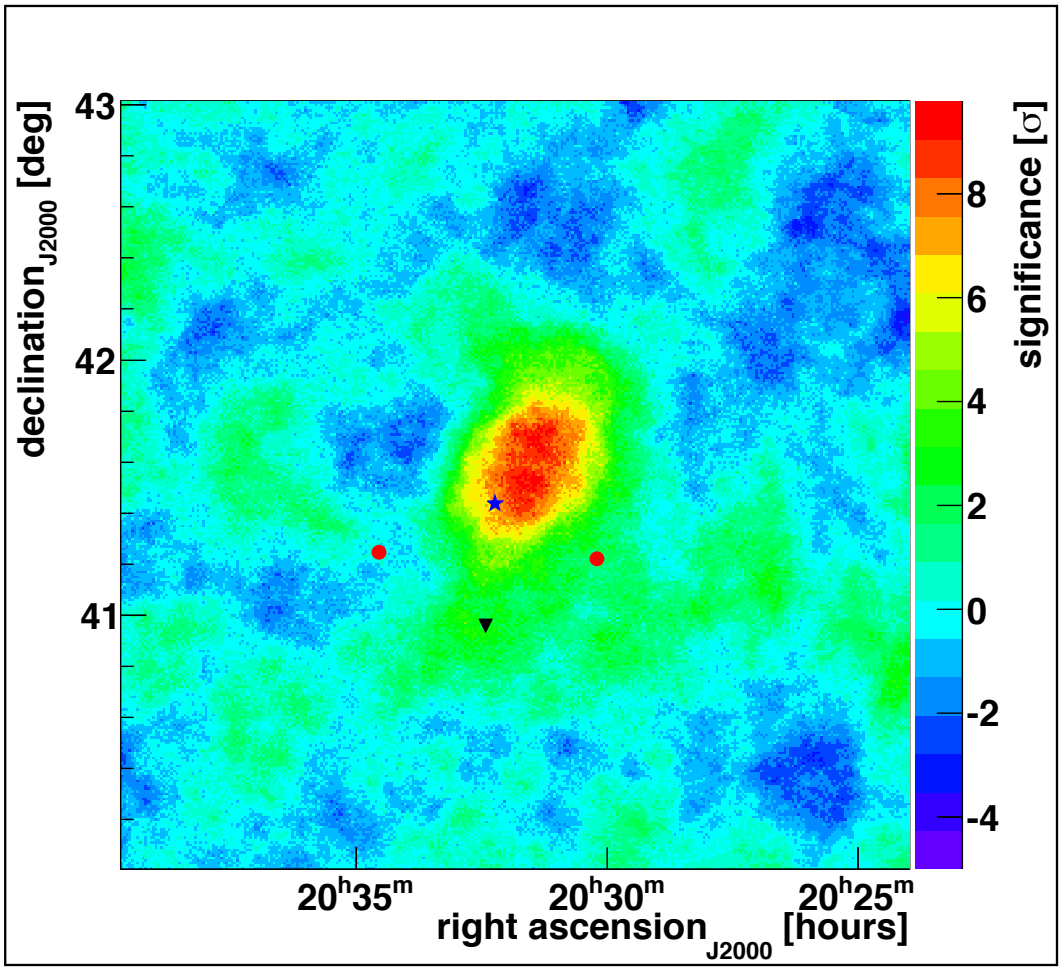

Figure 6.3: The VERITAS skymap of TeV J2032+4130 from [31]. The position of PSR J2032+4127 is indicated by the blue star while the black triangle indicates Cygnus X-3. The red circles show the telescope pointing position, which was equidistant from both TeV J2032+4130 and Cygnus X-3. Figure produced by author and shared from [30].

The results of this fit are shown in Table 6.3 and plotted in Figure 6.5. The low state spectrum, similar to the average spectrum, strongly favored a cutoff, this time ranging from 0.2–0.5 TeV. The high-state spectral fit was not significantly improved by the addition of a cutoff, so the simpler power law model was assumed. It is important to note that this result does not exclude the possibility of a spectral cutoff in the high state, it only indicates that there is insufficient evidence in support of one.

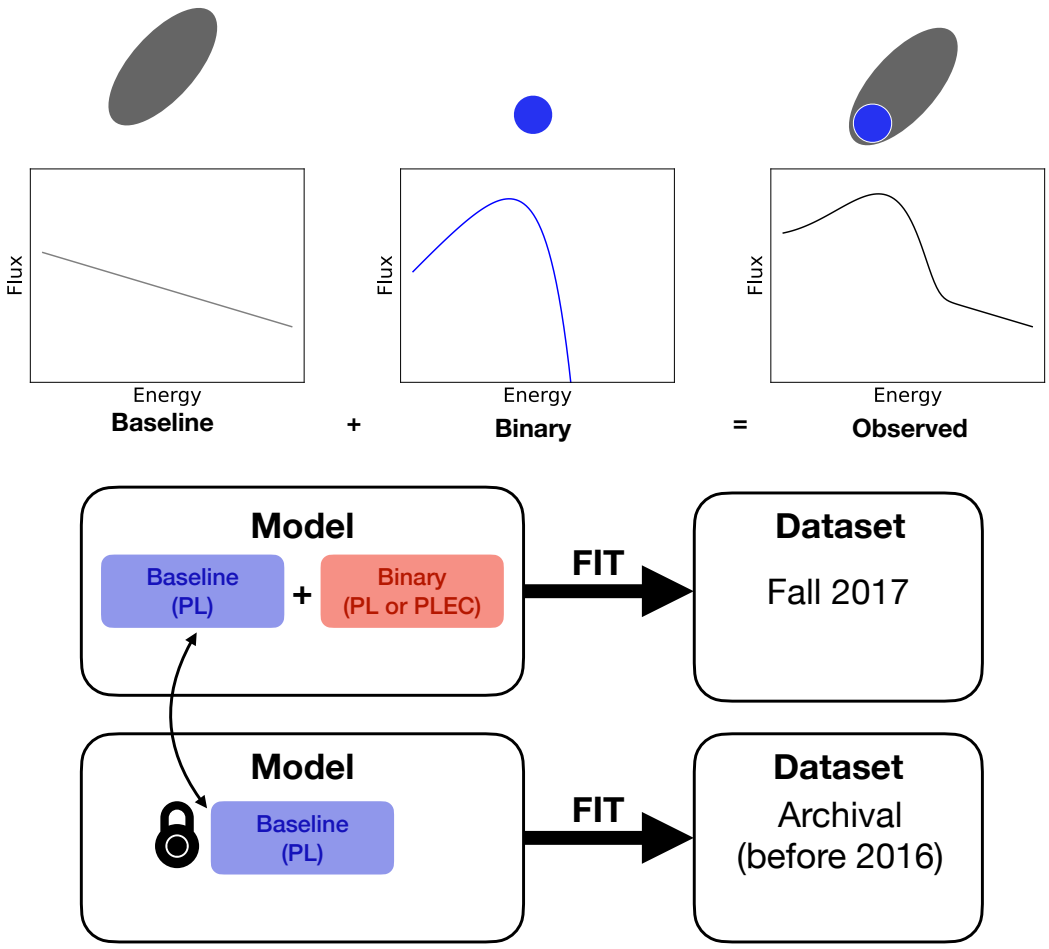

Figure 6.4: *Top*: A schematic illustrating the total observed spectral and individual spectral components described in the text. The observed emission is the sum of the "basline" emission (from TeV J2032+4130) and the transient binary emission (VER J2032+414).
Bottom: A schematic illustrating the joint fit process described in the text. Two different models were simultaneously fit to two different datasets. One model was used to describe the Fall 2017 dataset, during which the binary emission was significantly detected. A second model was used to describe the archival, pre-2016 dataset. The first model consisted of a power-law baseline component together with a binary component, for which both a power law (PL) and power law with an exponential cutoff (PLEC) were tested. The same baseline component used in this model was simultaneously used in the second model and fit to the archival (pre-2016) dataset. The best fit was determined by minimizing the χ^2 statistic across both model-dataset pairs.

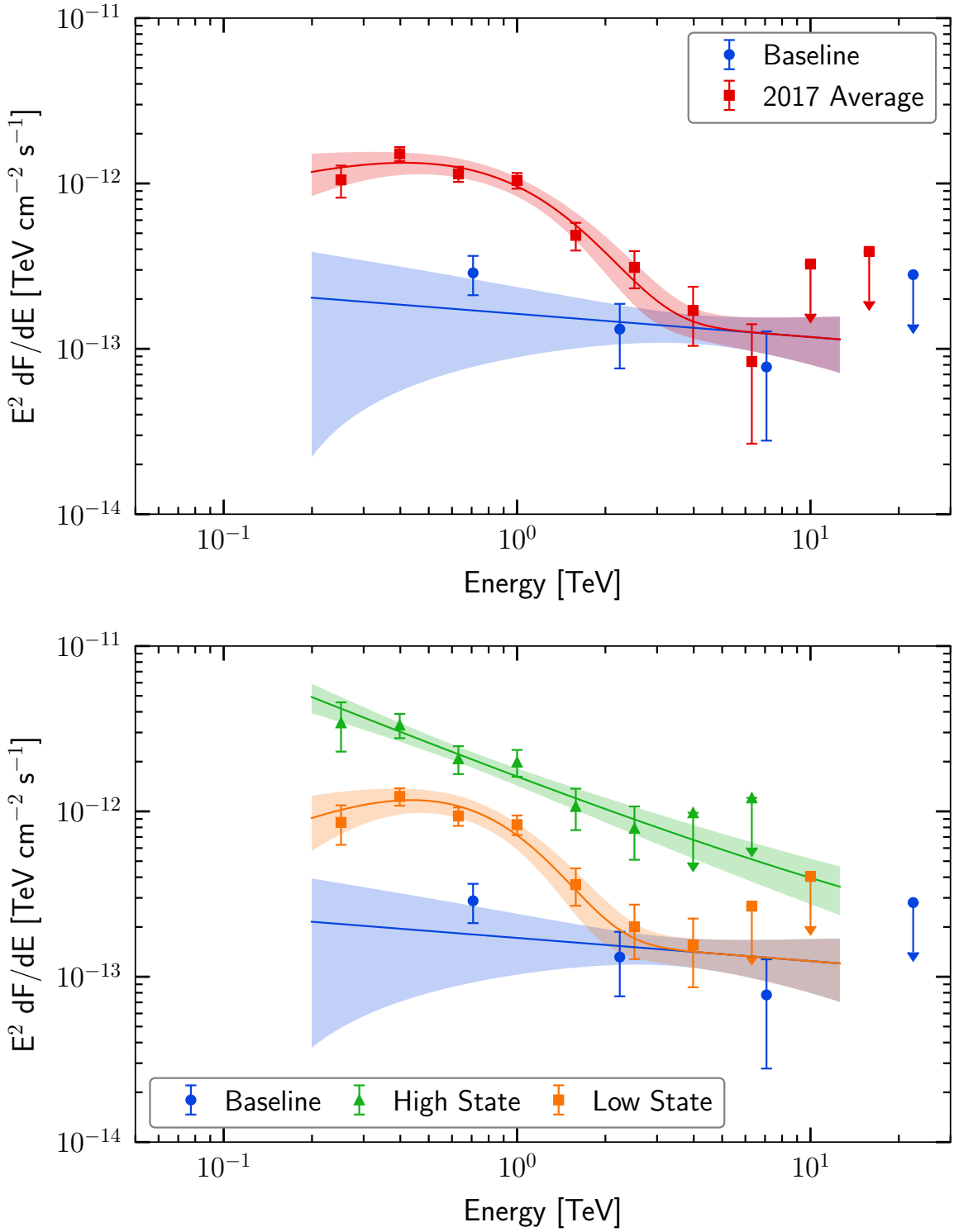

Figure 6.5: Spectral energy distribution and fits for the 2017-averaged dataset (top panel) and the dataset separated by flux state (bottom panel). Figure produced by author and shared from [30].

Period	Model	N_0 [cm^{-2} s^{-1} TeV^{-1}]	E_0 [TeV]	Γ	E_C [TeV]	χ^2/dof
Archival	$\mathbf{PL}_{\text{baseline}}$	$(8.78 \pm 2.56) \times 10^{-15}$	3.47	2.14 ± 0.53	-	40.6/7
Fall 2017	$\text{PL}_{\text{baseline}}$ + $\mathbf{PL}_{\text{binary}}$	$(1.53 \pm 0.14) \times 10^{-12}$	0.70	2.81 ± 0.09	-	
Archival	$\mathbf{PL}_{\text{baseline}}$	$(7.62 \pm 1.51) \times 10^{-15}$	4.18	2.14 ± 0.29	-	8.6/6
Fall 2017	$\text{PL}_{\text{baseline}}$ + $\mathbf{PLEC}_{\text{binary}}$	$(8.04 \pm 3.37) \times 10^{-12}$	0.64	1.26 ± 0.45	0.57 ± 0.20	
Archival	$\mathbf{PL}_{\text{baseline}}$	$(4.65 \pm 1.18) \times 10^{-15}$	4.98	2.14 ± 0.85	-	
Low State	$\text{PL}_{\text{baseline}}$ + $\mathbf{PL}_{\text{binary}}$	$(8.12 \pm 3.77) \times 10^{-14}$	1.76	2.86 ± 0.11	-	26.8/10
High State	$\text{PL}_{\text{baseline}}$ + $\mathbf{PL}_{\text{binary}}$	$(9.69 \pm 1.75) \times 10^{-13}$	1.17	2.72 ± 0.15	-	
Archival	$\mathbf{PL}_{\text{baseline}}$	$(1.23 \pm 0.24) \times 10^{-14}$	3.43	2.14 ± 0.28	-	
Low State	$\text{PL}_{\text{baseline}}$ + $\mathbf{PLEC}_{\text{binary}}$	$(1.63 \pm 1.12) \times 10^{-11}$	0.56	0.65 ± 0.75	0.33 ± 0.13	7.9/9
High State	$\text{PL}_{\text{baseline}}$ + $\mathbf{PL}_{\text{binary}}$	$(1.45 \pm 0.18) \times 10^{-12}$	1.00	2.73 ± 0.15	-	
Archival	$\mathbf{PL}_{\text{baseline}}$	$(1.26 \pm 0.25) \times 10^{-14}$	3.39	2.14 ± 0.28	-	
Low State	$\text{PL}_{\text{baseline}}$ + $\mathbf{PLEC}_{\text{binary}}$	$(1.64 \pm 1.12) \times 10^{-11}$	0.56	0.65 ± 0.75	0.33 ± 0.13	7.2/8
High State	$\text{PL}_{\text{baseline}}$ + $\mathbf{PLEC}_{\text{binary}}$	$(1.20 \pm 0.41) \times 10^{-11}$	0.51	2.37 ± 0.50	2.39 ± 3.23	

Table 6.3: Best-fit spectral parameters for the intra-binary shock component for the data periods described in the text. Each cell shows the results of a joint fit performed across 2 or 3 model-dataset pairs. For each row within a cell, the best fit parameters shown correspond to the boldface model component. Fits are shown for both power law (PL) and power law with an exponential cutoff (PLEC) models. Parameters shown are the flux normalization N_0 (which is calculated at the decorrelation energy E_0), spectral index Γ, cutoff energy E_c (for PLEC models), and the χ^2 for the joint fit (as described in the text).

Morphology

Much like the energy spectrum, the spatial morphology of the region results from a combination of both baseline emission from TeV J2032+4130 in addition to a binary emission component. A two component model was therefore also required to study the morphology of the region. An asymmetric, bivariate Gaussian model was used to model TeV J2032+4130, while a symmetrical Gaussian was used to model PSR J2032+4127/MT91 213. The emission from the region was assumed to be a combination of these two models. Because a morphological analysis utilizes information from the entire field of view, the limitation of low statistics from a small, offset extraction region that applied to the spectral analysis is not applicable in this analysis. The complex joint-fit mechanism is therefore unnecessary, and the morphological analysis can rely upon a precise estimate of TeV J2032+4130 using archival data alone. This analysis was carried out in [1], whose parameters are copied in Table 6.4.

The two-component model, with the bivariate Gaussian component's parameters

Name	RA (J2000)	Dec (J2000)	σ_1	σ_2	θ
TeV J2032+4130	$20^{\rm h}31^{\rm m}33^{\rm s} \pm 2^{\rm s}$	$41°34'38'' \pm 36''$	$(0.19 \pm 0.02)°$	$(0.08 \pm 0.01)°$	$(41 \pm 4)°$
VER J2032+414	$20^{\rm h}32^{\rm m}10^{\rm s} \pm 2^{\rm s}$	$41°26'34'' \pm 16''$	-	-	-

Table 6.4: Best-fit morphology parameters for TeV J2032+4130 and VER J2032+414.

fixed to those in [1], was fit to the fall 2017 dataset. The results of this fit are given in Table 6.4 and plotted in Figure 6.6. The emission from the binary interaction is unresolved (the 1σ radius of the source is smaller than the VERITAS point spread function) and the position is consistent with the location of PSR J2032+4127.

6.4 Discussion

Non-thermal emission from pulsar-powered gamma-ray binaries is driven by the synchrotron and inverse Compton cooling of electrons which have been accelerated at a shock formed between the pulsar and the massive star. The variable emission from PSR J2032+4127/MT91 213 can be studied to better understand the physical environment at the location of the shock. Here we offer a brief summary of wind-collision shocks and investigate the key observational results of PSR J2032+4127/MT91 213 in this context.

6.4.1 The intra-binary shock

The most likely mechanism for particle acceleration in pulsar-powered gamma-ray binaries is an MHD shock formed at the interface between the relativistic pulsar wind and the stellar wind of the massive companion [289, 290, 27]. In this scenario, a shock forms between the pulsar and the massive star at a distance R_s from the pulsar where the pulsar wind pressure is balanced by the pressure of the stellar wind:

$$P_{pw} = \frac{\dot{E}}{4\pi R_s^2 c} = P_w = \rho_w v_w^2 = \frac{\dot{M} v_w}{4\pi (d - R_s)^2} \tag{6.6}$$

Where d is the instantaneous distance between the pulsar and the star and v_w is the escape velocity of the stellar wind. R_s is thus determined by the ratio of the pulsar wind momentum and the stellar wind momentum $\eta = \frac{\dot{E}/c}{\dot{M} v_w}$ as:

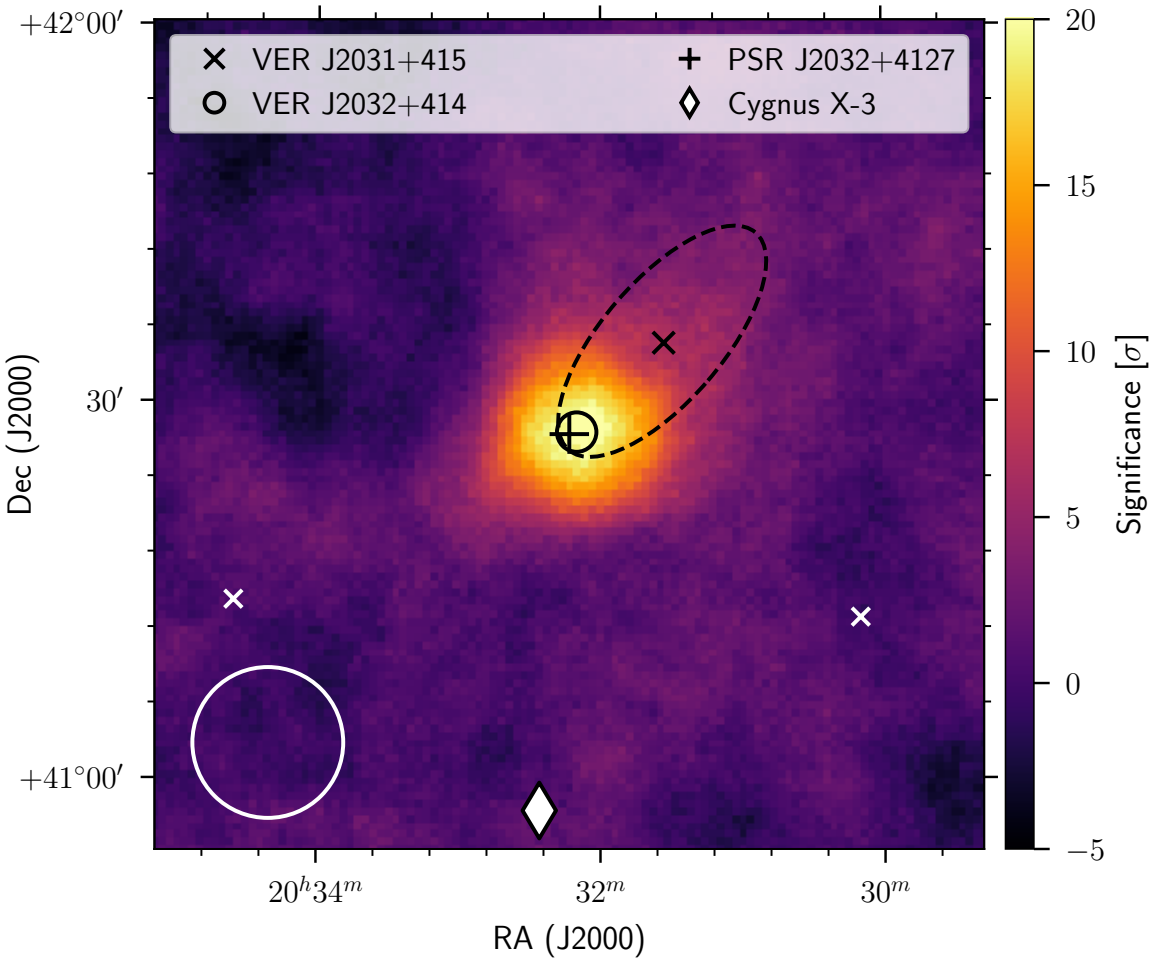

Figure 6.6: Significance sky map for VERITAS. The morphology of TeV J2032+4130 (VER J2031+415) is indicated with the dashed ellipse. The centroid of the binary source (VER J2032+414) is indicated by the black circle. The black cross denotes the location of the pulsar PSR J2032+4127, as well as the massive companion MT91 213. The white circle indicates the gamma-ray point spread function for VERITAS. The white x's indicate telescope pointing positions. Figure produced by author and shared from [30].

$$R_s = \frac{\eta^{\frac{1}{2}}}{1+\eta^{\frac{1}{2}}} d \tag{6.7}$$

In most gamma-ray binaries, $\eta \ll 1$ and the shock is located close to the pulsar. Assuming an escape velocity $v_w \approx \sqrt{\frac{2GM_\star}{R_\star}} \approx 8 \times 10^7$ cm s^{-1}, a typical Be star mass loss rate ($\sim 10^{-9} - 10^{-7}$ M$_\odot$ yr $^{-1}$), and $\dot{E} \approx 1.7 \times 10^{35}$ erg s^{-1}, $\eta \approx 0.1$ and $R_s \approx 0.25d$. If $\eta < 1$, the bow shock will wrap around the pulsar, causing the post-shock flow to move away from the star at $v \sim c/3$ [273]. This scenario is illustrated in Figure 6.7. The post-shock magnetic field is sourced by the magnetized pulsar wind [273]:

$$B = 3(1-4\sigma)\left(\frac{\dot{E}/c}{R_s^2}\frac{\sigma}{1+\sigma}\right)^{\frac{1}{2}} \tag{6.8}$$

Where σ is the ratio of magnetic energy to kinetic energy in the pulsar wind:

$$\sigma = \frac{B^2}{4\pi\Gamma n_e m_e c^2} \tag{6.9}$$

Where Γ and n_e are the lorentz factor and number density of the pulsar wind. Far from the pulsar, $\sigma \ll 1$ [273]. Assuming $\sigma = 10^{-3}$ (e.g. [273]), $R_s \approx 10^{12}$ cm, and $\dot{E} = 1.7 \times 10^{35}$ erg s^{-1}, $B \sim 0.1$ G. Electrons from the pulsar wind are accelerated at the shock via the first-order Fermi mechanism, and radiate in the presence of the orbitally-modulated magnetic and radiation fields, as described in Chapter 5.

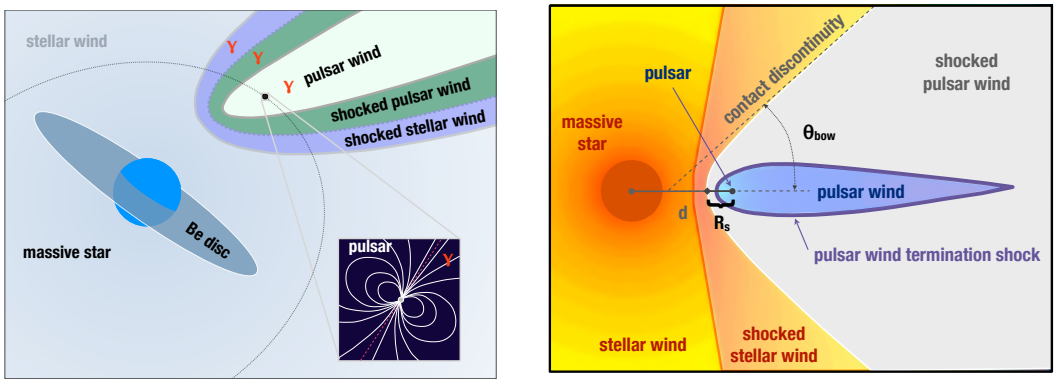

Figure 6.7: The geometry of the intra-binary shock. Reproduced with permission from [27].

6.4.2 Light Curve

The orbital modulation of the light curve and energy spectrum of PSR J2032+4127/MT91 213 reflect both the changing environment at the location of the shock and the changing geometry of the system as seen by the observer. The steady increase in X-ray and TeV emission from the system leading up to periastron is the result of the shock location moving closer to both the pulsar and the massive star (and therefore into more intense magnetic and radiation fields). This increases the synchrotron and inverse Compton luminosity, respectively.

The X-ray flux attains a maximum approximately 30 days before the periastron passage, after which it steadily decays until the periastron passage. In the model presented in [28], this feature can be understood by examining the evolution of the magnetization in the pulsar wind together with the diminished doppler boost as the system moves past inferior conjunction and the post-shock flow angles away from the observer. This model investigates a radial dependence to the magnetization parameter $\sigma(r) \propto r^{-\alpha}$. The synchrotron luminosity is maximal when σ is large enough for a strong magnetic field, yet small enough to deliver enough kinetic energy to particles in the downstream flow. $\sigma \approx 0.1$ is optimal for maximum synchrotron luminosity; this has the somewhat unintuitive effect of suppressing the synchrotron luminosity if the shock moves closer to the pulsar such that $\sigma > 0.1$ [28]. Doppler boosting of the post-shock flow will also affect the variability of the observed emission. At inferior conjunction ($\sim$ 5 months before periastron) the X-ray photons are being emitted from a frame that is moving rapidly ($\sim c/3$) toward the observer, boosting the observed flux. This effect diminishes after inferior conjunction when the post-shock flow angles away from the line of sight. The maximum and subsequent decay in the X-ray flux is therefore understood as the interplay between the orbitally modulated σ together with the doppler boosting of the post-shock flow. Model light curves produced using this formulation are drawn along with the data points in Figure 6.1.

Conversely, the maximum and decay of the X-ray flux can be explained if the disk of the Be star is inclined relative to the orbital plane [32, 33], as is the case for

PSR B1259-63. This has the effect of shadowing some of the stellar wind over certain segments of the orbit, which increases η and moves the shock away from the pulsar toward the stellar companion (Equation 6.7). This decreases the magnetic field while simultaneously increasing the radiation field at the shock location, decreasing the X-ray flux while increasing the VHE flux. The inclined-disk scenario is supported by an observed radio eclipse of the pulsar near periastron which has been attributed to free-free absorption by the dense circumstellar disk [32]. A similar effect is seen when a complex model of the stellar wind is considered. Petropoulou (2017,[291]) investigated the effect of an anisotropic stellar wind with varying dependencies on distance and polar angle relative to the star. This variable wind density introduces complex variability in η which will modulate the X-ray and TeV flux and could contribute to the observed features in the light curves. It should be noted that while each of the effects described here and in the previous paragraph (varying σ in the pulsar wind, varying η via shadowing and wind anisotropy) were investigated separately, they are not mutually exclusive and may all contribute to the observed emission.

The most prominent feature of the VHE light curve is a sharp drop in flux beginning a few days after the periastron passage and lasting for about one week. The coincidence of this feature with the superior conjunction of the system ($\sim$ 10 days after periastron) points to photon-photon absorption (pair production) in the stellar radiation field as the likely cause (see Chapter 5 for a detailed discussion of this effect). A similar dip feature is observed in both LS 5039 and PSR B1259-63. Photon-photon absorption has been invoked to explain this feature in both systems [267, 266], although enhanced non-radiative losses (i.e adiabatic cooling, particle escape from the acceleration site) might also play a significant role [292].

The X-ray light curve exhibits a short flare feature approximately one week after the periastron passage, lasting for $\sim$ 20 days. This flare is not anticipated by the quantitative model generated by [28, 29]. A natural explanation could be an interaction between the pulsar and the disk of the Be star. Similar X-ray flares before and periastron in PSR B1259-63 have been attributed to the pulsar crossing the inclined

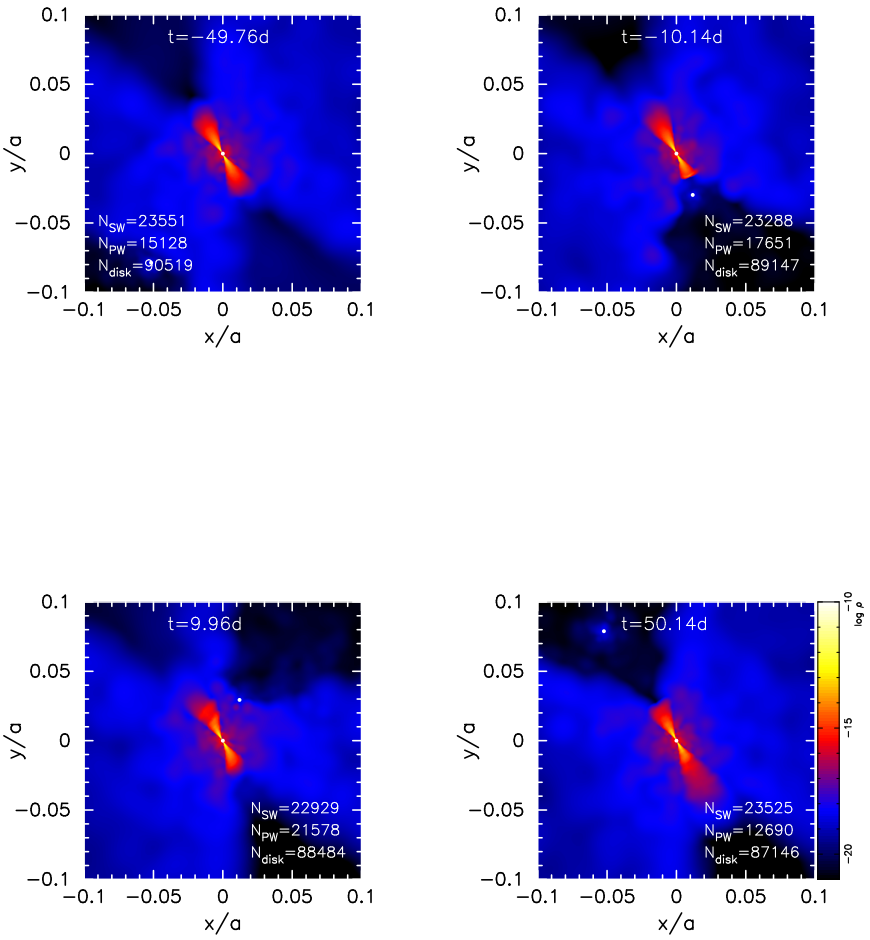

Figure 6.8: A hydrodynamic simulation of an inclined disk model. The Be star is at the center of each image, the pulsar is indicated by the bright point. Images show snapshots in time relative to periastron, which is annotated on the image. The scale shows relative density in the vicinity of the star. The disk creates a wind "shadow": a less dense region which moves the binary shock closer to the star. Reproduced from [32].

disk of the Be star (e.g. [190]). In this scenario, the pulsar penetrates the disk of its massive companion, and the pulsar wind is completely confined by disk matter. This results in a far greater conversion of pulsar spin-down energy to particle acceleration,

increasing the non-thermal luminosity. Takata et al (2017,[28]) expect this increase to be most apparent in the X-ray regime, as the cooling is synchrotron dominated in this scenario. This penetration can only happen if the disk is dense enough to withstand truncation by the pulsar wind [293, 28]. Takata et al (2017,[28]) find that if the base density of the disk is below $\rho_0 \approx 10^{-10}$ g cm^{-3}, the disk will be truncated by the pulsar wind at a radius smaller than the pulsar orbit, and the pulsar will not cross the disk. Significant truncation of the disk before periastron has indeed been reported [32, 33]. Li et al (2018,[29]) note that the time scale of the flare is significantly longer than the time required for the pulsar to traverse the disk. This can be explained if a significant amount of disk matter piled up ahead of the pulsar and influenced the geometry of the shock on a longer time scale. Accretion of stellar material onto the pulsar is also possible if the pulsar enters the dense disk. If the disk is sufficiently dense, and the relative velocity of the pulsar and disk rotation is sufficiently low, the disk matter will be stopped by the pulsar wind inside the Bondi radius $r_B \approx \frac{2GM_{\rm psr}}{v^2}$. This could result in the formation of an accretion disk around the pulsar which radiates UV photons that are subsequently upscattered by the pulsar wind. Such an effect may be observable in the HE or VHE regime [28]. While the observed VHE light curve does not show evidence of this, the VHE flux is neither precisely measured nor frequently sampled after recovering from the post-periastron dip, and such a feature may have been missed. Accretion of the stellar wind onto the pulsar is not likely, as the pulsar wind will stop the more tenuous stellar wind far beyond the Bondi radius [255].

As was discussed previously, the time-dependent emission from this system has been modeled quantitatively by [28], and subsequently revised with the addition of more X-ray data by [29]. It is worthwhile to compare the predictions of this model with the observations. The data and model predictions are plotted together in Figure 6.1. The model corresponds to a radial evolution of σ such that $\sigma \propto r^{-2}$, an orbital inclination $i = 60°$, and a pulsar wind lorentz factor $\Gamma = 10^4$. The X-ray light curve is well described by the model prior to periastron. The post-periastron flare is not predicted by the model, which did not account for the disk interaction described above.

The model clearly fails to explain the VHE variability across the periastron, missing both the location of the maximum and the short time scale of the flux variability. It must be noted that the model parameters have been optimized in the absence of any VHE data, and it may be possible to explain both the X-ray and VHE light curve within the framework of this model. Even so, it is useful to discuss possible reasons for this rather significant discrepancy. An imprecise knowledge of the orbital geometry of the system is likely at least partially responsible for this shortcoming. The inverse Compton luminosity is highly sensitive to the viewing angle of the observer, and alteration of the orbital inclination, for example, can significantly effect the rate of variability (see Figure 12 from [28]). Similarly, if the post-periastron flux dip is due to photon-photon absorption, then the location and time scale of the dip depends on the viewing angle of the observer as well as the orientation of the orbit within the orbital plane [266, 294]. Additionally, this model does not consider anisotropies in the stellar wind, which can arise intrinsically (i.e. [291]) or as a result of the inclined disk of the star ([32, 33]). Finally, while adiabatic losses were included in this model, a more sophisticated treatment of non-radiative losses, including orbitally-modulated adiabatic cooling and particle escape, may be necessary to characterize the observed variability [292, 295].

High-energy (MeV-GeV) emission is observed in every gamma-ray binary system. Emission from PSR J2032+4127/MT91 213 in this energy range has been the subject of several analyses [28, 29, 33]. No evidence has been found for emission beyond the pulsed emission originating in the pulsar magnetosphere. We can set a crude upper limit to the intra-binary emission using the pulsed flux to find the luminosity $L_{HE} \leq 2 \times 10^{34}$ erg s^{-1}. This corresponds to $\approx 10\%$ of the pulsar's spin-down power and implies $L_{HE} \leq 30 L_{VHE}$, which is not very constraining compared to other gamma-ray binary systems ($L_{HE} \sim 20 L_{VHE}$). The high-energy emission should be investigated further by employing a robust timing analysis to remove the pulsed emission.

6.4.3 Energy Spectrum

The non-thermal energy spectrum is formed as electrons accelerated at the shock cool via synchrotron radiation, inverse Compton scattering, or non-radiative processes such as adiabatic expansion or escape from the emission region. The intrinsic spectrum depends upon the physical conditions at the shock such as magnetic and radiation fields and orbital separation; the spectrum seen by the observer will also depend on the viewing geometry of the system. Examination of the spectrum can therefore provide insight into the physical conditions at the acceleration site.

As is thought to be the case in PSR B1259-63, adiabatic/escape losses may be dominant in PSR J2032+4127/MT91 213, particularly close to periastron [292, 295, 28, 33]. While difficult to formulate analytically, such losses typically exhibit a cooling time scale of $\tau \propto d/v$, where d can be as small as the characteristic size of the emission region and $v \approx c/3$ is the characteristic speed of the downstream flow. A key feature of the VHE energy spectrum is the break at $E_\gamma \approx 0.3 - 0.5$ TeV. This feature is observed both in the pre-periastron low state as well as the time-averaged dataset. Observations of the post-periastron high state show no evidence of such a break but cannot rule this feature out. This feature reflects a transition from one cooling mechanism to another. If non-radiative losses dominate, this will be a transition from non-radiative losses to synchrotron losses. Otherwise, it could be a transition from inverse Compton to either non-radiative processes or synchrotron cooling. Precise measurements of the indices of the power law before and after the break could distinguish between these scenarios, but this is impractical with the sensitivity of current instruments.

For inverse Compton cooling, a break in the low-state photon spectrum at $E_\gamma \approx 0.2 - 0.5$ TeV corresponds directly to a break in the electron spectrum at approximately the same energy. If the transition is from inverse Compton cooling to synchrotron cooling, then the magnetic field at the shock can be approximated by equating the cooling time scales for the two processes (see Chapter 5):

$$\tau_{\rm sync} = \frac{3}{4}\frac{m_e^2 c^3}{\sigma_T}\frac{8\pi}{B^2}\frac{1}{E} = \tau_{\rm IC} \approx \frac{64\pi^2 (k_b T)^2 E^2 + 45(mc^2)^4}{240 (mc^2)^2 \sigma_T \sigma_{sb} T^4 E}\left(\frac{d}{R_\star}\right)^2 \tag{6.10}$$

The inverse Compton cooling time is determined by the Be star temperature $T_\star = 30,000$ K and the distance from the star to the shock, which ranges from $d_\star \approx 1.5$ AU to $d_\star \approx 0.6$ AU over the dataset collection time. Under these conditions, a break at $E_\gamma \approx 0.2 - 0.5$ TeV implies a magnetic field of $B \approx 0.4 - 0.8$ G. This also results in a synchrotron break in the X-ray spectrum at $E_\gamma \approx \frac{3}{2}\left(\frac{E_e}{m_e c^2}\right)^2 \hbar \frac{eB}{m_e c} \approx 2 - 13$ keV, which is consistent with the X-ray break observed during this time period at $E_\gamma \approx 5$ keV [255, 256].

It is possible that the X-ray break arises from the minimum energy threshold of the accelerated electrons, which would be related to the bulk kinetic energy of the pulsar wind. This is the interpretation suggested by [256]. Uchiyama et al (2009,[296]) attributed a similar break in the X-ray spectrum of PSR B1259-63 to this phenomenon. That study found $E_{pw} \approx 0.2$ TeV ($\gamma_{pw} \approx 4 \times 10^5$). If the same value holds for PSR J2032+4127/MT91 213, then $B \approx 1 - 2$ G is required to reproduce the feature in the X-ray spectrum. Unless E_{pw} is higher, the corresponding break in the inverse Compton spectrum will be below the energy threshold of the observations, and the X-ray and TeV breaks will be unrelated. This scenario implies a second X-ray break $\sim 5 - 10$ keV after the first (corresponding to the inverse Compton break), which is either not observed or statistically indistinguishable from the first.

Pal et. al (2019,[256]) found evidence for an increase in the break energy close to periastron, from $E_{brk} \approx 5$ keV to $E_{brk} \approx 13$ keV. If this is caused by the low-energy threshold as discussed above, then this implies an increase in the magnetic field, from $B \approx 1-2$ G before periastron to $B \approx 4-5$ G at periastron, which is naturally explained by the movement of the shock closer to the pulsar as the system approaches periastron. Conversely, a quickening of non-radiative losses around the periastron could cause a similar shift in break energy. It should be noted that a similar analysis conducted by [255] does not confirm the variability in the break energy reported by [256].

Chernyakova et. al (2020,[33]) conducted SED modeling of data corresponding to the VERITAS/MAGIC high state (see Figure 6.9). This analysis considers escape-dominated cooling for most energies until synchrotron cooling takes over at ~ 5 TeV.

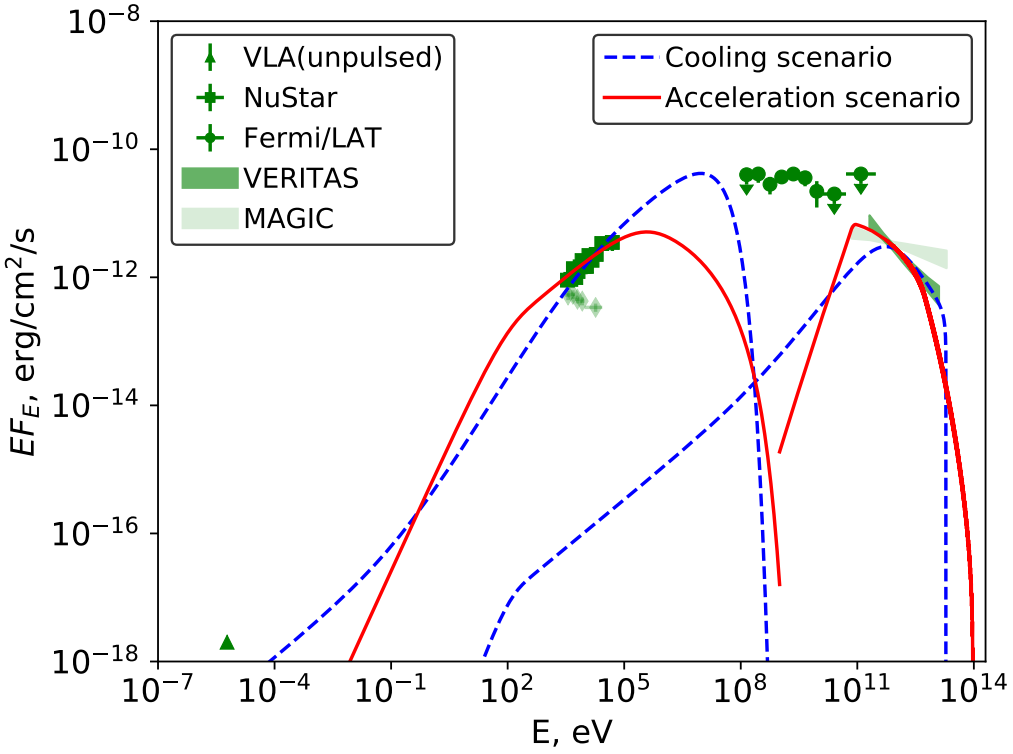

Figure 6.9: SED model of PSR J2032+4127/MT91 213 over the high state, reproduced from [33].

The resulting X-ray-TeV SED is best fit with a magnetic field of $B \approx 0.2$ G. This results in a break in the VHE spectrum at ~ 5 TeV, and a break in the synchrotron spectrum at ~ 300 keV. Because the X-ray break occurs in an unobserved region of the spectrum, and the VHE break cannot be ruled out for the high-state spectrum, these predictions are consistent with the observations. These authors do not confirm the spectral break reported by [255] and [256], possibly because the break location is near the low-energy threshold of the analysis.

As discussed in Chapter 5, at least one spectral break is expected in all gamma-ray binary systems due to the eventual transition to synchrotron cooling. PSR J2032+4127/MT91 213 is one of only two gamma-ray binaries to exhibit such a cutoff in the VHE spectrum. In the other system, LS 5039, the cutoff is present in the high state and is significantly higher, $E_{brk} \approx 8.7$ TeV. SED modeling of this feature yields a magnetic field of $B \approx 0.8$

G [267]. The absence of a cutoff when the system is farther from periastron is probably indicative of a lower magnetic field when the shock moves away from the pulsar. Comparisons between LS 5039 and PSR J2032+4127/MT91 213 are not straightforward since the periastron "high" state in the latter system neither confirms nor precludes the existence of a cutoff. The companion star in LS 5039 is significantly hotter than MT91 213, which should lower the energy at which inverse Compton scattering enters the Klein-Nishina regime as well as the inverse Compton cooling time. SED modeling of both systems at periastron suggests a higher magnetic field ($B \approx 0.8$ G) in LS 5039 than in PSR J2032+4127 ($B \approx 0.2$ G). The higher magnetic field, combined with the lower Klein-Nishina energy, should lower the cutoff energy in LS 5039 compared to PSR J2032+4127. This effect may compensated for by the lower overall cooling timescale for inverse Compton scattering in the more energetic radiation field of LS 5039. A more precise measurement of the periastron spectrum in PSR J2032+4127 is required for a robust comparison.

Recent observations of PSR B1259-63 show no evidence for a spectral break in the VHE spectrum between 0.2-40 TeV [20]. It is possible that the break due to the transition to synchrotron cooling occurs below 0.2 TeV and the spectrum observed by H.E.S.S. is the high-energy component of a broken power law. The detection of ~ 40 TeV photons indicates that electrons are being accelerated up to approximately this same energy. For a magnetic field of ~ 2 G, synchrotron cooling becomes faster than the minimum acceleration timescale for diffusive shock acceleration around this energy. The detection of higher energy photons therefore constrains the upper bound of the magnetic field, or implies a different acceleration mechanism.

While PSR B1259-63 and PSR J2032+4127 share similar X-ray light curves, they exhibit different spectral behavior. While the X-ray spectrum of PSR B1259-63 softens significantly (from $\Gamma \approx 1.5$ 20 days prior to periastron to $\Gamma \approx 2$ at periastron [190]), PSR J2032+4127 shows the opposite behavior, hardening from $\Gamma \approx 2$ hundreds

of days before periastron to $\Gamma \approx 1.5$ at periastron [255, 33].[7] Chernyakova et. al (2020,[33]) propose that this discrepancy is related to a higher-density environment in PSR B1259-63 compared to PSR J2032+4127 due to the more prominent Be star disk measured in the former. This could cause the electron cooling in PSR J2032+4127 to be escape-dominated throughout the periastron, resulting in a harder spectrum. Ng et. al (2019,[255]) also suggest that the hardening is due to increasing non-radiative losses near periastron. Pal et al. (2019,[256]) report a brief softening in the X-ray spectrum near the same time as the post-periastron flare. This supports the interpretation of an interaction with the stellar disk, which would dramatically increase the synchrotron cooling efficiency and soften the X-ray spectrum.

Near superior conjunction, the VHE emission is significantly suppressed by photon-photon absorption. The optical depth is likely maximal near $\sim$ 100 GeV [28, 297] and may be greater than unity over much of the high-energy spectrum. This likely results in a large trough feature in the energy spectrum beginning around this same energy. Although the primary VHE photons are significantly absorbed during this time, the pair production may initiate an $e\pm$ cascade which can re-radiate VHE photons and reduce the effective opacity of the system (see Chapter 5). Bednarek et al. (2017,[297]) considered the effect of secondary emission from cascades and found that this process may be dominant below $\sim$ 100 GeV. The overall effect on the VHE spectrum will be a suppression and hardening near the phase of maximal absorption. A similar hardening due to absorption is expected from PSR B1259-63 [266]. The sensitivity of current instruments is not sufficient to detect such a feature in either system.

[7] Note that the dramatic difference in timescale (tens of days in PSR B1259-63 vs hundreds of days in PSR J2032+4127) is due to the large difference in orbital period: ($\sim$ 1200 days vs $\sim$ 17000 days)

6.5 Conclusion

The detection of VHE emission from PSR J2032+4127/MT91 213 marks the discovery of only the second gamma-ray binary with a pulsar confirmed to be the compact companion. The VHE emission exhibits a peak luminosity of $L \approx 2 \times 10^{33}$ erg s^{-1} ($\sim 1.3\%$ $\dot{E}$) and is variable by a factor of 10 over the periastron passage. The X-ray emission peaks at $L \approx 8 \times 10^{32}$ erg s^{-1} ($\sim 0.4\%$ $\dot{E}$) and varies by a factor of ~ 5. The comparable X-ray and VHE luminosity observed in this system is similar to other gamma-ray binaries.

While the quantitative model developed by [28, 29] fails to reproduce the observed TeV emission, the assumption that the emission is of leptonic origin is not likely to blame. Hadronic models are disfavored in gamma-ray binaries for several reasons, see Chapter 5. Hadronic emission requires a mostly proton-loaded pulsar wind which interacts with protons in the dense circumstellar disk of the massive star [298]. In this scenario, non-thermal emission should peak when the pulsar is near the stellar disk. Even if the pulsar wind is proton-loaded (which is not likely), this model is unable to account for emission farther away from the disk, where the stellar wind is not nearly dense enough for effective proton-proton interactions. Furthermore, the proton energies required for $\sim$ TeV photons implies larmor radii comparable to or larger than the characteristic size of the emission region [27]. The anti-correlation between X-ray flux and VHE flux leading up to periastron is also not reproducible within this framework. Leptonic processes are thus far more favorable in models of binary systems.

One obvious limitation faced by modelers is a poorly constrained knowledge of the orbital geometry of the system. Many effects known to modulate the emission depend both on the pulsar's position relative to the massive star as well as the viewing angle of the observer. Orbital parameters in these systems are typically inferred from radial velocity measurements of the massive star. If pulsations are observed, the evolution of the pulse period about the orbit can also be used to constrain the orbit [178, 280, 174]. Parallax measurements can provide additional insight [165]. Constraints on orbital parameters are improved with increased coverage of the orbital phase, and estimates of

the orbital geometry using different parts of the orbit can differ dramatically. In the case of HESS J0632+057, an orbital solution resulting from an analysis over several orbits with full phase coverage results in an entirely different geometry from an earlier estimate using the same methodology and a smaller dataset [170, 169]. The addition of more phase coverage from the orbit of PSR J2032+4127/MT91 213 altered the geometry of the system and accurately predicted the date of periastron. Pulsations were first seen from PSR J2032+4127 in 2009, and thus (at the time of writing) a maximum of $\sim 20\%$ of the ~ 50 year orbit has been observed. Additionally, published estimates of the orbit are based solely on pulsar timing; optical spectroscopy and radio resolution of the orbit can further constrain the geometry of the orbital plane. This has been the case with PSR B1259-63, which was discovered much earlier than PSR J2032+4127 and has a much shorter orbital period (≈ 3.4 years). As a result, observations are available from every orbital phase and spanning many orbits, resulting in a more confident estimate of the geometry of the system. This reduces the number of uncertain parameters that emission models must account for, allowing for a more robust investigation of the parameters of interest. Though full orbital phase coverage of PSR J2032+4127/MT91 213 will not be possible for several more decades, increased phase coverage will result in better-constrained estimates of the orbital geometry.

Recent analyses have also investigated the possibility of using VHE data to constrain some of the orbital parameters. If the characteristic dip observed in most gamma-ray binary systems can be attributed to absorption by the photon field of the massive star, then the location of this dip can be used to constrain the orientation of the orbit. This has recently been demonstrated by Sushch et al. (2019,[294]), who use the TeV light curve of PSR J2032+4127 to jointly constrain the inclination angle and longitude of periastron. Such work is promising, but still allows for a broad range of parameters and must be used in conjunction with other method for determining the orbit.

In addition to a continued refinement of the orbit of PSR J2032+4127/MT91

213, observations and modeling of other gamma-ray binaries can inform the interpretation of data from this system. Any model of pulsar-powered gamma-ray binaries is highly dependent on the pulsar wind. Little is known for sure about this phenomenon. How much of the pulsar's spindown energy is carried away by the wind? How is this energy distributed between magnetic and kinetic forms (i.e., what is σ)? How does σ evolve with distance? If such properties are common among pulsars, then discovery and observation of new pulsar-powered gamma-ray binaries will refine the interpretation of emission from PSR J2032+4127/MT91 213. Other uncertainties can be resolved by observations of the massive star MT91 213. The momentum ratio η partially depends upon the mass-loss rate $\dot{M}$ of MT91 213, which is currently assumed in most models by the mass-loss rates reported in similar stars, which vary by several orders of magnitude.

Thus, in spite of the fact that periastron observations are impossible for several more decades, continued studies of PSR J2032+4127/MT91 213, along with observations of similar systems, can shed light on the mechanisms driving the emission in this system. Immediate revisions to models are already possible, since the quantitative model discussed in this Chapter ([28, 29]) was developed based solely on X-ray data, before the detection of the VHE source. A model within this framework which is able to simultaneously explain the X-ray and VHE emission therefore remains a possibility. Revisions to this framework, some of which were briefly suggested in the previous section, are also possible even in the absence of new X-ray and VHE data. Continued studies of this system will better constrain the basic emission mechanisms, and will inform the interpretation of new gamma-ray binary systems for years to come.

Chapter 7

DEVELOPMENT OF A MAXIMUM LIKELIHOOD ANALYSIS AND APPLICATION TO VER J2032+414 AND TeV J2032+4130

The previous chapter presented results of extended observations of the transient gamma-ray binary VER J2032+414. One particular challenge faced during this analysis was the fact that the pulsar system responsible for the gamma-ray binary lies in the immediate vicinity of another, previously-known gamma-ray source, TeV J2032+4130. TeV J2032+4130 is very likely associated with the energetic pulsar (as a pulsar wind nebula), but is steady source unrelated to the variable emission from the binary interaction which was the focus of the previous chapter. The photons seen by VERITAS therefore comprise a combination of those from both sources. Care must be taken in any analysis therefore to isolate, to the greatest extent possible, the signal from VER J2032+414. In the previous chapter, a "joint-fit" approach was described, whereby a spectral analysis of data taken before the appearance of VER J2032+414 was conducted simultaneously with data containing both TeV J2032+4130 and VER J2032+414 in attempt to separate the two sources. The results of that analysis showed consistency in the properties of TeV J2032+4130 across all time periods analyzed, inspiring confidence in the obtained results from VER J2032+414 presented in the previous chapter. The analysis also prompted discussion and development of a more robust framework capable of analyzing such situations (overlapping sources in the field of view) for other such systems. In particular, it was realized that the spectral analysis of VER J2032+414 and TeV J2032+4130 was only possible due to the existence of a sizable data set of the region from a time period before VER J2032+414 was significantly detected. In this chapter, we describe the development of a more sophisticated analysis tool which was specifically designed for the analysis of overlapping sources.

7.1 Maximum Likelihood Analysis

Motivation

In a standard analysis of VERITAS data[1], gamma-ray events are counted from within a predetermined source region and compared with the number of gamma-ray counts from within a region where there is no known source. Assuming the counts from each region obey a Poisson distribution, one can calculate the "statistical significance" of the signal from the source region, which can be interpreted as the number of standard deviations separating the source gamma-ray signal from the background signal. This calculation is detailed in [299]. Source detection is then determined on the basis of this statistical significance, where typically a signal of five standard deviations or greater is required to claim the detection of a new gamma-ray source. If a source is determined to exist, its physical characteristics can be further analyzed, with morphological information contained in two dimensional sky histograms and spectral information contained in one-dimensional energy histograms. The intrinsic properties of the gamma-ray source can then be estimated by "unfolding" the observed data through various systematic instrument responses.

In this chapter, we describe an alternative "Maximum Likelihood Method" (MLM) approach for simultaneous estimation of intrinsic source properties and detection significance. This work is especially motivated by the occasional need to disentangle multiple sources within a field of view, or to test for the presence of an additional source in the field of view that is not obvious from the standard analysis. The analysis framework described in this chapter was especially inspired by the *Fermi* Science Tools[2], which by necessity (due to the large field of view, high diffuse background, and relatively poor angular resolution at low energies) were designed to analyze and detect many potential sources simultaneously. Similar analysis packages include 3ML [300], gammapy [301], and CTOOLS [302].

---

[1] described in detail in Chapter 4

[2] https://fermi.gsfc.nasa.gov/ssc/data/analysis/documentation/Cicerone/

Concept

A primary goal of data analysis of a gamma-ray source is the reconstruction of the intrinsic properties of the source, chiefly the source energy spectrum and morphology. Typically these are reconstructed by separately considering a distribution of counts versus energy to examine the energy spectrum, and a distribution of counts versus sky coordinates to examine the morphology. It is possible to consider a more holistic approach, which simultaneously considers spectral and spatial information. At any given time, the luminous intensity of a gamma-ray source can vary as a function of angular coordinates in the field of view x and y, as well as energy E. In general, we consider a gamma-ray source whose intensity can be described as:

$$S(x, y, E) = \frac{dN}{dxdydEdAdt} = \phi(E)M(x, y) \tag{7.1}$$

S thus has dimensions of $\frac{\text{photons}}{\text{(solid angle)}\cdot\text{(energy)}\cdot\text{(area)}\cdot\text{(time)}}$. $\phi(E)$ can be considered the energy spectrum, while $M(x, y)$ describes the source morphology (how the intensity is distributed throughout the field of view). For example: if the energy spectrum follows a power-law distribution and the morphology is described by a point source model, then we would have:

$$S(x, y, E) = N_0 \left(\frac{E}{E_0}\right)^{-\Gamma} \delta(x - x_0)\delta(y - y_0) \tag{7.2}$$

Where δ denotes the Dirac delta function.

S represents the intrinsic distribution of source photons throughout angular space and energy. This distribution is not what is measured by the detector. Unavoidable noise and uncertainties in the photon reconstruction process results in an artificial spread in both the angular and energetic dimensions of these distributions. A photon with true (intrinsic) angular coordinates x_{true} and y_{true} will be observed as having angular coordinates x_{obs} and y_{obs}. The probability of a photon's direction being reconstructed to the point $(x_{\text{true}} + \Delta x, y_{\text{true}} + \Delta y)$ diminishes with distance in an

approximately Gaussian manner[3]:

$$P(\Delta x, \Delta y, E) = \frac{1}{2\pi\sigma^2} e^{-\frac{(\Delta x)^2+(\Delta y)^2}{2\sigma(E)^2}} \tag{7.3}$$

As a result, consecutive photons originating from the same point (x_{true}, y_{true}) will be reconstructed to different points scattered throughout angular space such that the resulting image, rather than being a perfect point with zero spatial extent, will be observed to have a characteristic width of σ. The function P can then be interpreted as the spatial morphology which would be recorded by the instrument upon observation of a perfect point source; P is referred to as the point spread function and σ can be thought of as the angular resolution of the instrument. Since the Cherenkov light yield is energy-dependent (higher energy events tend to be brighter), the quality of the event reconstruction varies with energy (both because the signal is stronger in individual telescope images and because brighter events are more likely to be observed by three or more telescopes); σ is therefore in general a function of energy.

A similar effect occurs during the reconstruction of photon energies. A gamma ray with true energy E_{true} observed as having the reconstructed energy E_{obs}. As is the case for the reconstructed direction, the probabilistic distribution of E_{obs} approximates a Gaussian of width σ_E which is centered around E_{true}. The characteristic width σ_E, which can be energy dependent, is referred to as the energy resolution of the instrument.

$$R(\Delta E, E) = \frac{1}{\sqrt{2\pi\sigma^2}} e^{-\frac{\Delta E^2}{2\sigma_E(E)^2}} \tag{7.4}$$

R can be thought of as an "energy point spread function", though this term is not widely used.

---

[3] Several authors ([303], [304]) argue convincingly that the "King" function better describes this instrument response. A simple Gaussian was used in this case, though the author acknowledges that adopting a King function might improve the analysis in the future.

Forward Folding

The function S (Equation 7.1) specifies the intrinsic flux due to the source at the location of the instrument but before being observed by the instrument. Upon observation, the intrinsic flux is convoluted in both energy and spatial dimensions, and this resulting flux is effectively binned into spectral and spatial histograms.

The process of transforming the intrinsic source flux into observed histograms proceeds as follows:

The instrument samples the intrinsic flux $S(x, y, E)$ of the source, which is the number of photons per surface area per solid angle per energy per time. The effective flux that is observed by the instrument is the convolution of the intrinsic flux with the instrument point spread function and energy response:

$$S_{\text{obs}}(x, y, E) = \int_0^\infty \int_{-\infty}^\infty \int_{-\infty}^\infty S(x', y', E') P(x - x', y - y', E') R(E - E', E) dx' dy' dE'$$

The instrument ultimately measures event counts and not flux. These counts are binned into 2D spatial histograms and 1D energy histograms. The effective collection area A_{eff} over which the instrument samples this flux is energy dependent: $A_{\text{eff}} = A_{\text{eff}}(E)$. This is because higher energy Cherenkov events are brighter, and thus can be detected from farther away. One must also take into account that the probability of observing identical gamma rays varies over the field of view, with events near the camera center being more likely to result in detection. Events farther from the camera center are more likely to suffer from truncation at the edge of the camera and therefore be poorly reconstructed. We therefore define the gamma-ray acceptance $\alpha(x, y, E)$ which specifies the relative probability of event detection across the field of view. Conventionally, α is normalized to a maximum value of 1. Therefore, if the instrument observes a source over a time duration Δt, then the expected number of counts per energy per spatial coordinate is:

$$\frac{dN}{dx dy dE} = S_{\text{obs}}(x, y, E) A_{\text{eff}}(E) \alpha(x, y, E) \Delta t$$

A standard VERITAS analysis bins this distribution separately into spatial and energy bins. If the energy histogram has bins of width ΔE and spans a range $E_{\rm min}$ to $E_{\rm max}$, then the expected number of counts in the $k^{\rm th}$ bin can be found by integrating over x and y:

$$N_k = \int_{x_{\rm min}}^{x_{\rm max}} \int_{y_{\rm min}}^{y_{\rm max}} \int_{E_{\rm min}+k\Delta E}^{E_{\rm min}+(k+1)\Delta E} S_{\rm obs}(x,y,E) A_{\rm eff}(E) \alpha(x,y,E) \Delta t dx dy dE$$

Similarly, the number of counts in bin (i,j) of the 2D spatial histogram is found by integrating over the energy:

$$N_{ij} = \int_{x_{\rm min}+i\Delta x}^{x_{\rm min}+(i+1)\Delta x} \int_{y_{\rm min}+j\Delta y}^{y_{\rm min}+(j+1)\Delta y} \int_{E_{\rm min}}^{E_{\rm max}} S_{\rm obs}(x,y,E) A_{\rm eff}(E) \alpha(x,y,E) \Delta t dx dy dE$$

Binning the counts in this way allows for the construction of separate spatial and spectral histograms which can be used to independently analyze the source's morphology and energy spectrum.

These histograms can then be fit assuming different source models in order to reconstruct the intrinsic properties of the source.

Another approach would be to contain the spatial and spectral information in a single 3D histogram. Within such a histogram, the expected number of counts in the $i^{\rm th}$ x coordinate bin, $j^{\rm th}$ y coordinate bin, and $k^{\rm th}$ energy bin would be:

$$N_{ijk} = \int_{x_{\rm min}+i\Delta x}^{x_{\rm min}+(i+1)\Delta x} \int_{y_{\rm min}+j\Delta y}^{y_{\rm min}+(j+1)\Delta y} \int_{E_{\rm min}+k\Delta E}^{E_{\rm min}+(k+1)\Delta E} S_{\rm obs}(x,y,E) A_{\rm eff}(E) \alpha(x,y,E) \Delta t dx dy dE \tag{7.5}$$

Maximum Likelihood Analysis

If the instrument response functions P, R, and $A_{\rm eff}$ are known (see the next section), one can construct a model of one or more sources, each with a specified functional form, and evaluate the likelihood with which the model explains the data.

We denote by $\vec{\theta}$ the set of parameters which describe the functional form of the source model. For example: if the intrinsic source model is:

$$S(x, y, E) = N_0 \left(\frac{E}{E_0}\right)^{-\Gamma} \delta(x - x_0)\delta(y - y_0)$$

Then the model is parameterized by N_0, Γ, x_0, y_0 and we have $\vec{\theta} = \{N_0, \Gamma, x_0, y_0\}$[4]. In other words, $\vec{\theta}$ contains the intrinsic properties of the source which we wish to estimate. We then define $N_{ijk}^{\rm exp}(\vec{\theta})$ as the number of counts one would observe in bin i, j, k (as calculated from Equation 7.5) if the intrinsic source model used the parameters $\vec{\theta}$.

In general, we allow the model to include multiple sources. We denote by $N_{ijk,n}^{\rm exp}(\vec{\theta_n})$ the expected number of counts in bin i, j, k due to the $n^{\rm th}$ source. If there are N many sources, then we can write:

$$N_{ijk}^{\rm exp}(\vec{\Theta}) = \sum_{n}^{N} N_{ijk,n}^{\rm exp}(\vec{\theta_n})$$

Where $\vec{\theta_n}$ is the set of parameters for each source model and $\vec{\Theta}$ is the entire set of all model parameters across all source models. In each bin we wish to compare the number of expected counts from the model $N_{ijk}^{\rm exp}(\vec{\Theta})$ to the number of observed counts from the data $N_{ijk}^{\rm obs}$. It should be noted that the expected counts $N_{ijk}^{\rm exp}(\vec{\Theta})$ represents the number of event counts *due only to the source*, whereas the actual observed counts include both source events and cosmic ray "background" events. For the remainder of this section, we modify our definition of $N_{ijk}^{\rm exp}(\vec{\Theta})$ to include an estimated number of background counts $N_{ijk}^{\rm bg}$ in each bin:

$$N_{ijk}^{\rm exp}(\vec{\Theta}) = \int_{x_{\rm min}+i\Delta x}^{x_{\rm min}+(i+1)\Delta x} \int_{y_{\rm min}+j\Delta y}^{y_{\rm min}+(j+1)\Delta y} \int_{E_{\rm min}+k\Delta E}^{E_{\rm min}+(k+1)\Delta E} S_{\rm obs}(x,y,E) A_{\rm eff}(E) \alpha(x,y,E) \Delta t dx dy dE + N_{ijk}^{\rm bg}$$

We will discuss how this estimate is derived in the next section.

[4] E_0 is not a unique parameter in this case and so is not included in $\vec{\theta}$

Let $p\left(N_{ijk}^{\text{obs}}|N_{ijk}^{\text{exp}}(\vec{\Theta})\right)$ be the probability of observing N_{ijk}^{obs} many counts, given the model prediction of $N_{ijk}^{\text{exp}}(\vec{\Theta})$. For event-counting experiments, the relevant probability distribution is the Poisson distribution, so that

$$p\left(N_{ijk}^{\text{obs}}|N_{ijk}^{\text{exp}}(\vec{\Theta})\right) = \frac{N_{ijk}^{\text{exp}}(\vec{\Theta})^{N_{ijk}^{\text{obs}}}}{N_{ijk}^{\text{obs}}!} e^{-N_{ijk}^{\text{exp}}(\vec{\Theta})}$$

We can then find the total probability of observing the recorded data given the current model predictions, known as the likelihood: $\mathcal{L}\left(N^{\text{obs}}|N^{\text{exp}}(\vec{\Theta})\right)$. This is found by taking the product of the probability in each bin over every bin in the data set:

$$\mathcal{L}\left(N^{\text{obs}}|N^{\text{exp}}(\vec{\Theta})\right) = \Pi_i \Pi_j \Pi_k p\left(N_{ijk}^{\text{obs}}|N_{ijk}^{\text{exp}}(\vec{\Theta})\right)$$

It is often more convenient to deal with the log-likelihood rather than the likelihood itself:

$$\ln\left[\mathcal{L}\left(N^{\text{obs}}|N^{\text{exp}}(\vec{\Theta})\right)\right] = \sum_i \sum_j \sum_k N_{ijk}^{\text{obs}} \ln\left(N_{ijk}^{\text{exp}}(\vec{\Theta})\right) - N_{ijk}^{\text{exp}}(\vec{\Theta}) - \ln\left(N_{ijk}^{\text{obs}}!\right) \quad (7.6)$$

Equation 7.6 can then be maximized for $\vec{\Theta}$ to obtain the most likely estimate, or the "maximum likelihood estimate" of $\vec{\Theta}$, denoted $\vec{\Theta}_{\text{MLE}}$.

Wilks' Theorem

In terms of evaluating how well the data are described by the model, the actual value of $\mathcal{L}$ is arbitrary. Wilks (1938) [159] presents a convenient result to use the likelihood values of different models to compare them. If one is considering two different source models and wishes to determine which model is the best descriptor of the data, then a "test statistic" can be computed:

$$TS = -2\ln\left(\frac{\mathcal{L}_{\text{null}}}{\mathcal{L}_{\text{test}}}\right) \quad (7.7)$$

Where $\mathcal{L}_{\text{null}}$ is the likelihood of a specific model, potentially the "null hypothesis" model, and $\mathcal{L}_{\text{test}}$ is the likelihood of the model being tested. In the case that the test model is able to reduce to the null model under suitable choice of parameters $\vec{\Theta}_{\text{test}}$, then

Wilks finds that test statistic should be distributed as a χ^2 with number of degrees of freedom equal to the difference in dimensionality between $\vec{\Theta}_{\text{test}}$ and $\vec{\Theta}_{\text{null}}$. The p value, or the probability that the differences between the test and the null models can be adequately explained by random fluctuations, can be calculated as:

$$p = \frac{1}{2} \int_{TS}^{\infty} \chi^2_d(x) dx$$

Where d is the number of degrees of freedom. The factor of $1/2$ in the integral (following Mattox et al. [305]) is due to the fact that the source flux is constrained to be ≥ 0 and thus negative fluctuations will effectively concentrate at $TS = 0$. It is common in gamma-ray astronomy to report detections with a significance value S, which is interpreted as an "S standard deviation result." Once one has computed the p value, a significance value can be numerically determined by finding ξ such that the CDF of a standard normal distribution at ξ is equal to p.

One can then use this framework to compare different hypotheses and models. To test for the existence of a source, one would first choose a source model and find $\vec{\Theta}_{\text{MLE}}$ which maximizes $\mathcal{L}_{\text{test}}$. A null model should then be constructed by choosing parameter values in $\vec{\Theta}_{\text{test}}$ which will result in an intrinsic source flux of 0. The test statistic can then be calculated from Equation 7.7, and then a probability value and significance can be found.

This framework can also be used to explore different models in the properties of known sources. For instance, one could construct a test model consisting of an energy spectrum with an exponential cutoff, and compare this to a null model in which the energy spectrum follows a straight power law distribution. Upon finding $\vec{\Theta}_{\text{MLE}}$ for each model, a test statistic can be computed, from which one can decide if the power-law model can be rejected.

A final example allows for one to test for the existence of a second source in a field of view where one is already known to exist. This requires construction of a test model, in which parameters of both sources are free to vary, and a null model in which the parameters of the first source can vary but the second are fixed to zero flux. In

the same way, the test statistic can be found by comparing $\mathcal{L}\left(\vec{\Theta}_{\rm MLE}\right)$ for each model following Equation 7.7. On the basis of this TS value, a significance can be computed which represents the degree of confidence in the two-source model over the one-source model.

7.2 Implementation

Background Estimation

The method described in the previous section relies upon comparing the number of gamma-ray counts in a given space-energy bin to the number of counts predicted by some model. The gamma-ray counts are not background subtracted, in order to ensure that the number of counts will be approximately Poisson distributed. Rather, an estimate of the background events is added to the model such that $N_{ijk}^{\rm exp}$ includes both the events associated only with the source (Equation 7.5) as well as counts associated with cosmic ray background events $N_{ijk}^{\rm bg}$. The background estimate is arrived at using the ring background method described in chapter 4. We briefly summarize the procedure here.

In order to estimate the the number of background counts $N_{ijk}^{\rm bg}$ in a given space-energy bin, a ring of specified width is constructed and centered on said bin. If the total number of gamma-ray events originating from within the ring is $N_{ijk}^{\rm ring}$, then the number of counts expected to originate from within the given space-energy bin is $N_{ijk}^{\rm bg} = \frac{\bar{\alpha}_{\rm bin}}{\bar{\alpha}_{\rm ring}} \frac{A_{\rm bin}}{A_{\rm ring}} N_{ijk}^{\rm ring}$, where $A_{\rm bin/ring}$ is the total solid angle of the bin and ring, and $\bar{\alpha}_{\rm bin/ring}$ is the average gamma-ray acceptance within the bin/ring (normalized to 1). The average acceptance is derived from the radial acceptance curve (described in chapter 4), which effectively flatfields the gamma-ray rate across the camera. It is important to note that while the background estimation is included in the model, it is a fixed parameter and is not itself being modeled. This approach should be valid as long as the field of view is not so crowded as to prevent a reliable background estimate. For crowded fields of view, the background must be modeled along with the source(s) (see [304]).

Instrument Response Functions

In order to convert a model source flux to a flux observed by the instrument and finally to a number of counts in a given space-energy bin, the intrinsic source flux must be propagated through the various instrument responses, such as the effective area $A_{\rm eff}(E)$, the point-spread function $P(x, y, E)$, and the energy response $R(\Delta E, E)$. Once these functions are known, they are utilized as described in the previous section to arrive at $N_{ijk}^{\rm exp}$.

Effective Area

The effective collection area describes the size of the physical region within which a gamma-ray event will be successfully detected by the telescope array. This function is estimated using simulations. The effective area is simulated by throwing gamma-ray showers uniformly over a constant area, and multiplying the area by the fraction of events which are properly reconstructed. Gamma-ray events of different energies are generated, resulting in an energy dependent effective area. This function is sensitive to, among other things: the level of night-sky background, the zenith angle of the simulated source, the energy spectrum of the simulated source, the atmospheric model used in the simulations, the data reduction cuts used in the analysis, and the angular size of the region from which source events are counted (the θ^2 cut). Therefore many simulations must be generated to span this parameter space. In a standard VERITAS analysis, a fixed-width region of diameter θ is used as the "source region": gamma-ray events drawn from this region are attributed to the source and then used for source detection and spectral analysis. Because the effective area is sensitive to the size of this region, and new simulations must be generated for each region size, standard VERITAS analyses are constrained to two basic source models: a "point source" model which uses a source region with a width of about 0.09°, and an "extended source" model which uses a width of 0.5°. Therefore simulations need only be generated for two θ values. These simulations are widely available for use in most VERITAS analyses.

In the analysis described here, we are interested not in one spatial bin of radius θ, but of several spatial bins of arbitrary size. We therefore wish to rid the effective area of any dependence on a predetermined source region, as this will be compensated for by integrating the point spread function. As we will show in the next section, the process of deriving the point spread function will simultaneously allow us to modify the effective area in the desired way.

Point Spread Function

The point spread function (PSF) describes the probability of mis-reconstruction of the direction of gamma-ray events as a function of space. If the flux from a source is distributed spatially as a delta function, then the distribution of counts as recorded by the instrument will be distributed exactly according to the PSF of the instrument. In general, the spatial distribution of source counts is given by the convolution of the source flux with the instrument PSF.

The PSF of the instrument can be estimated either from real data (using a source with an extent that is known to be much smaller than the angular resolution of the telescope) or from simulations (see [109]). In general, the PSF depends upon the same quantities as does the effective area: night-sky background, zenith angle, etc. Unlike the effective area function, however, the point spread function is not directly utilized in a standard VERITAS analysis. This is because the θ dependence of the effective area (as discussed earlier) effectively "bakes in" the effect of the instrument PSF. Therefore, in order to save disk space and computing time, mass simulations of the PSF over the relevant parameter space are not conducted. Such an undertaking is beyond the scope of this analysis; here we describe a simpler approach to obtaining the PSF.

As was mentioned previously, the effect of the PSF is present in the estimation of the effective area functions. The effective area function is derived by simulating gamma-ray events over a constant area A, and then recording the fraction of events which are reconstructed as gamma-rays and reconstructed from within the source region (within

a circle of radius θ of the source location). Let $f_\gamma(E)$ be the fraction of simulated events with energy E that are successfully determined by the analysis to be gamma rays, and let $f_\theta(E)$ be the fraction of those events which are reconstructed within the source region. We can then define the effective area as:

$$A_{\text{eff}}(E) = f_\gamma(E) f_\theta(E) A \tag{7.8}$$

The $f_\gamma(E)$ term depends on a host of factors, including the brightness and shape of the reconstructed image. The $f_\theta(E)$ term, however, depends only on the instrument's PSF. In fact, if the simulated events are drawn from a point-source model, then $f_\theta(E)$ simply represents the integral of the PSF within a radius of θ:

$$f_\theta(E) = \int_{x^2+y^2 \leq \theta^2} P(x, y, E) dx dy \tag{7.9}$$

Given that $P(x, y, E)$ is normalized such that the integral over all space is unity.

Because effective areas for at least two values of θ are widely available, the PSF can be estimated by comparing two effective areas which are otherwise identical accept for the size of the source region θ. In this case, the only difference between the two functions will be due to the different integration windows used in the above equation.

Given two effective area curves for which every parameter (zenith, noise, atmosphere, etc) is the same except for θ, we can take the ratio of the two curves in every energy bin:

$$\frac{A_{\text{eff},\theta_1}(E)}{A_{\text{eff},\theta_2}(E)} = \frac{f_\gamma(E) f_{\theta_1}(E) A}{f_\gamma(E) f_{\theta_2}(E) A} = \frac{\int_{x^2+y^2 \leq \theta_1^2} P(x, y, E) dx dy}{\int_{x^2+y^2 \leq \theta_2^2} P(x, y, E) dx dy} \tag{7.10}$$

If a single-parameter functional form for P is assumed, then this equation can be solved to determine the simulated energy-dependent point spread function. In this analysis we assume P is a radially symmetric Gaussian:

$$P(x, y, E) = \frac{1}{2\pi\sigma(E)^2} e^{-\frac{x^2+y^2}{2\sigma(E)^2}}$$

Equation 7.10 then becomes:

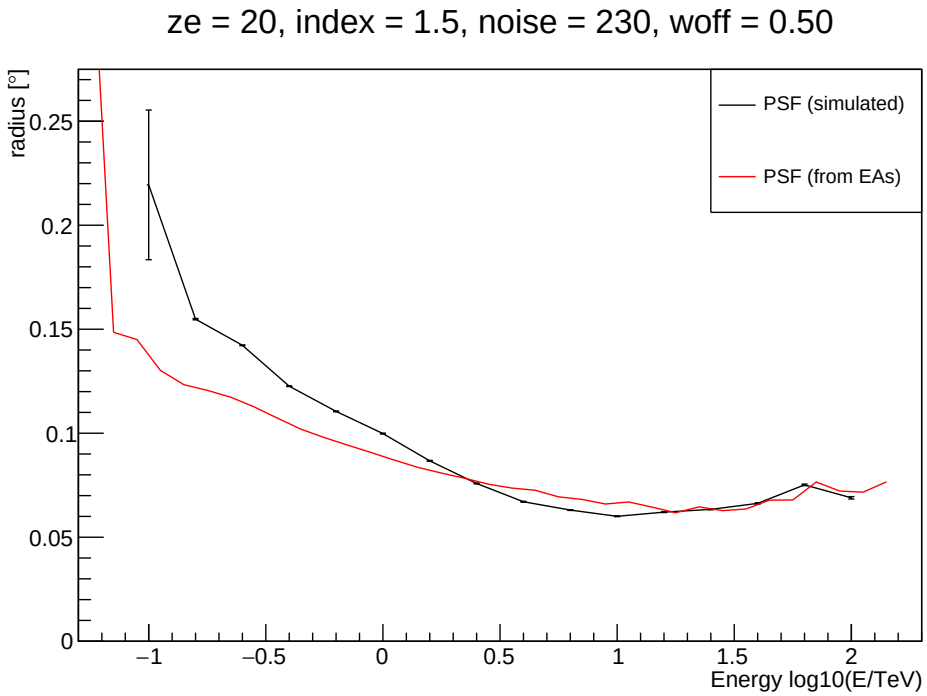

Figure 7.1: Instrument PSF derived from simulations (black) plotted together with PSF derived using the method described in the text (red). The energy threshold is $\log_{10}\left(\frac{0.15\ \text{TeV}}{TeV}\right) \approx -0.83$

$$\frac{A_{\text{eff},\theta_1}(E)}{A_{\text{eff},\theta_2}(E)} = \frac{1 - e^{-\frac{\theta_1^2}{2\sigma(E)^2}}}{1 - e^{-\frac{\theta_2^2}{2\sigma(E)^2}}} \tag{7.11}$$

Which can be solved numerically for $\sigma(E)$ at each energy bin for which $A_{\text{eff},\theta_1}(E)$ and $A_{\text{eff},\theta_2}(E)$ both exist. An example of a PSF derived in this manner is plotted in Figure 7.1, along with a PSF derived from simulations. In this example the PSF is slightly underestimated at low energies; these discrepancies are possibly due to the simplified single-parameter model used to estimate the PSF, while the simulated PSF is independent of functional form. A more complex PSF model would likely be a better fit to the data, but as can be seen from Equation 7.10, the method described here only works for a single-parameter PSF functional form. A subsequent iteration of this analysis could conduct mass simulations to acquire the PSF functions that span simulation parameter space, but this is considered beyond the scope of this work.

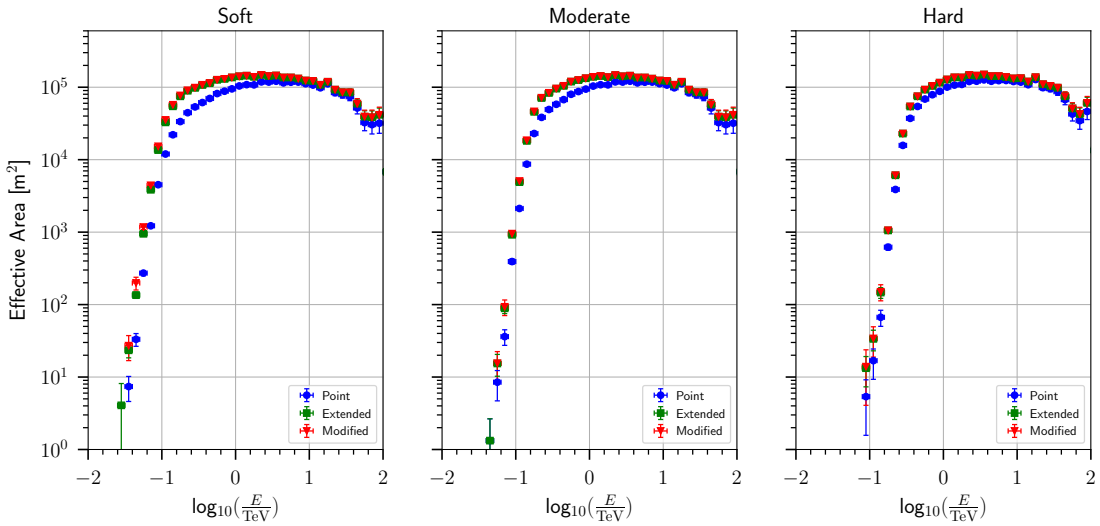

Figure 7.2: Effective areas are plotted for different sets of gamma-ray cuts. Blue boxes show the effective areas derived using $\theta = 0.09°$, green show $\theta = 0.5°$, and red show modified effective areas independent of source region.

With a working function for $P(x, y, E)$, it is now possible to calculate $f_\theta(E)$ and divide the effective area curve by this factor, ridding the effective area of dependence on the simulated θ^2 cut (Figure 7.2). We therefore see that be using a pair of otherwise identical effective area simulations with different source region sizes, one can derive the point spread function for those observing conditions and subsequently the PSF-modified effective area curves needed for this analysis. Modern analysis tools such as gammapy ([301]) include similar functionality in their instrument response function data structures.

Energy Response

Just as the point spread function characterizes the probability of a gamma-ray event being reconstructed with an erroneous direction; the energy response function characterizes the probability of a gamma-ray event being reconstructed with an erroneous energy. It can be considered the "point spread function" in energy space. Unlike the point spread function, the energy response function can only be estimated from simulations. While the point spread function could be derived from already-generated

Source	Exposure [hr]	Significance [σ] (ED)	Significance [σ] (MLM)
Crab	4.6	71.5	98.8
PKS 1424+240	16.0	6.5	6.1
TeV 2032+4130	63.6	8.6	14.6
SNR G106.3+2.7	47.5	3.7	9.1
Ursa Minor	103.6	1.2	0.2

Table 7.1: Detection significances for both analysis methods

and thus readily available effective area files, no such workaround is available for the energy response. It is therefore necessary to conduct mass simulations, which would need to be done for different zenith angles, night sky background levels, etc. Such an undertaking is considered to be beyond the scope of this work; and so henceforth the effect of the energy response is not included in the overall instrument response. Although this will result in some degree of unavoidable distortion of the intrinsic source spectrum, this is not expected to be a significant effect as long as the energy resolution is not too large ($\approx 10-20\%$). It should be noted that the standard VERITAS analyses also do not directly account for the energy response of the instrument.

7.3 Testing

The analysis described here was tested on five objects: the Crab Nebula (the standard candle of gamma-ray astronomy), Ursa Minor (a region where no gamma-ray source is known to exist, to test for false positives in the likelihood technique), PKS 1424+240 (a faint, soft-spectrum, high background extra-galactic source), TeV J2032+4130[5] and SNR G106.3+2.7 (both hard spectrum, extended galactic sources). In this section, we present basic results derived from each source and compare them with those from a standard VERITAS analysis.

Crab Nebula

The Crab Nebula is the brightest steady gamma-ray source and is the first source studied by any new analysis method. 4.6 hours of data were processed using

[5] Using a dataset from before the appearance of VER J2032+414

Eventdisplay (ED) [286]. The spectral properties of the source were then studied using both the standard Eventdisplay tools and the maximum likelihood method (MLM) described here.

The Crab Nebula was initially modeled using a point source spatial model and a standard power law spectral model:

$$S(x, y, E) = N_0 \left(\frac{E}{E_0} \right)^{-\Gamma} \delta(x - x_0)\delta(y - y_0)$$

The model parameters are N_0, Γ, x_0, and y_0, all of which are left free during the fit. The spatial morphology of the source, after convolution with the PSF, is shown in Figure 7.3. The x_0 and y_0 parameters were both consistent with 0, corresponding to the RA and DEC of the nebula. The spectral fit parameters are given in Table 7.2 and plotted in Figure 7.4. The spectral fit is consistent with the Eventdisplay fit.

Comparison of the best-fit model with the null model (equivalent to setting $N_0 = 0$ in the source model) yields a test statistic (TS, Equation 7.7) of $TS = 9768.1$. Since the source model has four free parameters, Wilks' Theorem states that the TS should be distributed according to a χ^2_4 distribution. From this a detection significance can be estimated as described in section 7.1. In this case the TS is so large that determination of the probability is limited by the numerical precision of the machine, which is to say that a numerical integration to find p yields a result that is computationally indistinguishable from 0. The resulting detection significance is then technically infinite. Instead, we make use of a handy result from Wilks [159] that the detection significance for a model with one additional degree of freedom over the null model can be approximated as $\sigma = \sqrt{TS}$. We therefore quote this as the detection significance of this source, with the notable caveat that the true significance is lower than this (since the source model has not one but four degrees of freedom).

The only notable feature in the morphological fit (Figure 7.3) is the appearance of a ring of negative excess surrounding the source region in the residuals map. This is likely due to the simplistic model used to construct the PSF resulting in over subtraction around the source model. A more sophisticated PSF model could alleviate this,

Model	**Method**	N_0 $[10^{-9}\text{cm}^{-2}\text{s}^{-1}\text{TeV}^{-1}]$	E_0 [TeV]	Γ	β
PL	ED	2.7 ± 0.1	0.15	2.41 ± 0.03	-
PL	MLM	2.7 ± 0.1	0.15	2.36 ± 0.03	-
LogPar	MLM	2.0 ± 0.2	0.15	1.90 ± 0.12	0.14 ± 0.04

Table 7.2: Spectral fit parameters for the Crab Nebula

however this effect is likely irrelevant for fainter sources.

It is widely observed that a straight power law is a poor description of the Crab Nebula's gamma-ray spectrum and that instead exhibits significant curvature [306, 110, 307, 308]. To test the MLM analysis framework's ability to detect this curvature, fitting was again conducted using a Log-Parabola model for the source spectrum rather than a simple power law:

$$S(x, y, E) = N_0 \left(\frac{E}{E_0}\right)^{-\left(\Gamma + \beta \ln \frac{E}{E_0}\right)} \delta(x - x_0)\delta(y - y_0)$$

The best fit values are given in Table 7.2 and plotted in Figure 7.4. No corresponding fit was conducted with Eventdisplay, since that software does not have a Log-Parabola model. The published values for Γ and β range from $\Gamma = 2.10 - 2.63$ and $\beta = 0.15 - 0.24$ [306, 110, 307, 308]. The best-fit values found here are generally similar to the published values, with the caveat that the best-fit index Γ is slightly harder than the hardest published value.

To determine whether the curved spectrum is favored, it is necessary to compare the two models (power law and log-parabola power law) and calculate a test statistic using Equation 7.7. In this case the "null" model is the standard power law and the "test" model is the log-parabola power law. This results in a test statistic of $TS = 15.0$. According to Wilks' Theorem, the test statistic should obey a χ^2_1 distribution, which we use to determine a significance of $\sigma = 3.7$. This means that the log-parabola model is favored over the standard power-law model at the 3.7σ level.

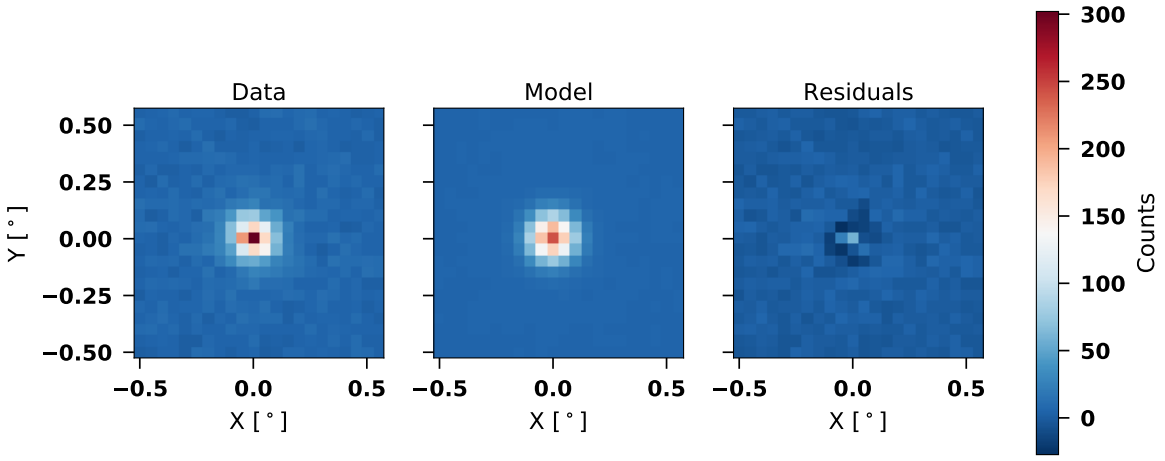

Figure 7.3: Observed counts (Data), model-predicted counts (Model), and residuals for the Crab Nebula.

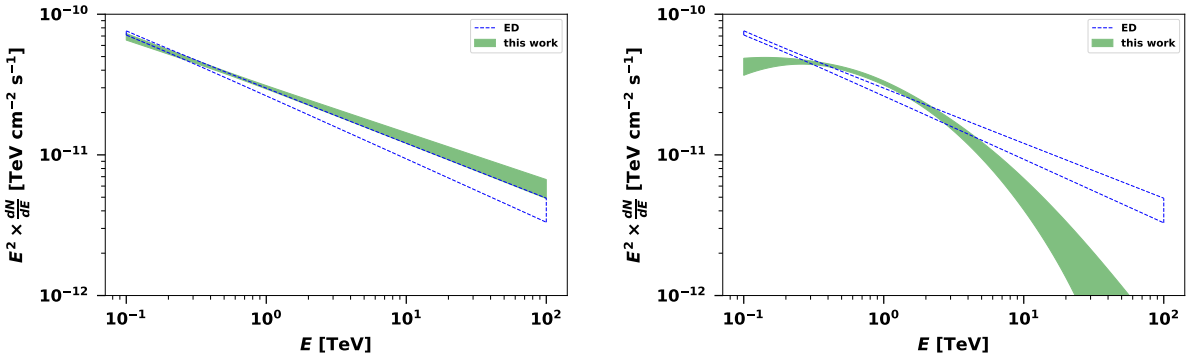

Figure 7.4: The best-fit spectrum is shown for both the simple power law model and the log-parabola model.

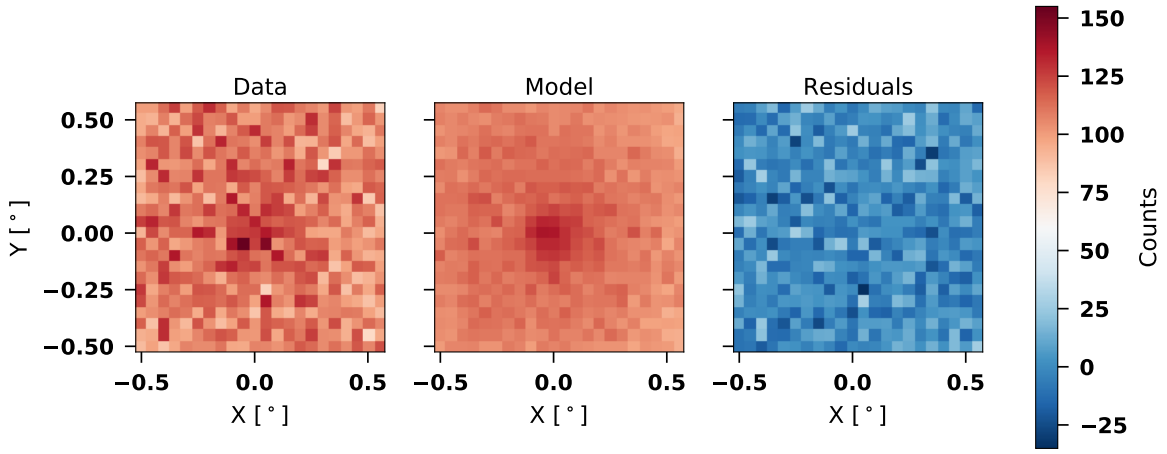

Figure 7.5: Data/Model/Residuals plot for PKS 1424+240.

Model	**Method**	N_0 $[10^{-9}\text{cm}^{-2}\text{s}^{-1}\text{TeV}^{-1}]$	E_0 [TeV]	Γ
PL	ED	1.3 ± 0.8	0.09	4.56 ± 1.01
PL	MLM	2.5 ± 1.1	0.09	5.67 ± 0.72

Table 7.3: Spectral fit parameters for PKS 1424+240

PKS 1424+240

PKS 1424+240 was selected due to its nature as a faint, extra-galactic source with a very soft spectrum. This ensures that the MLM analysis is equipped to deal with a variety of source types.

The source was modeled as a point source with a simple power law spectrum. The source was detected with a significance of 6.1σ. The fit is plotted in Figures 7.5 and 7.6; the spectral fit parameters are given in Table 7.3. The Eventdisplay spectrum, constructed from only two flux points, was included solely for comparison purposes and should not be taken seriously. This explains the erratic behavior of the butterfly plot in Figure 7.6

TeV J2032+4130

TeV J2032+4130 is a highly extended and asymmetric galactic source which makes it a good choice to test the morphological capabilities of the MLM analysis.

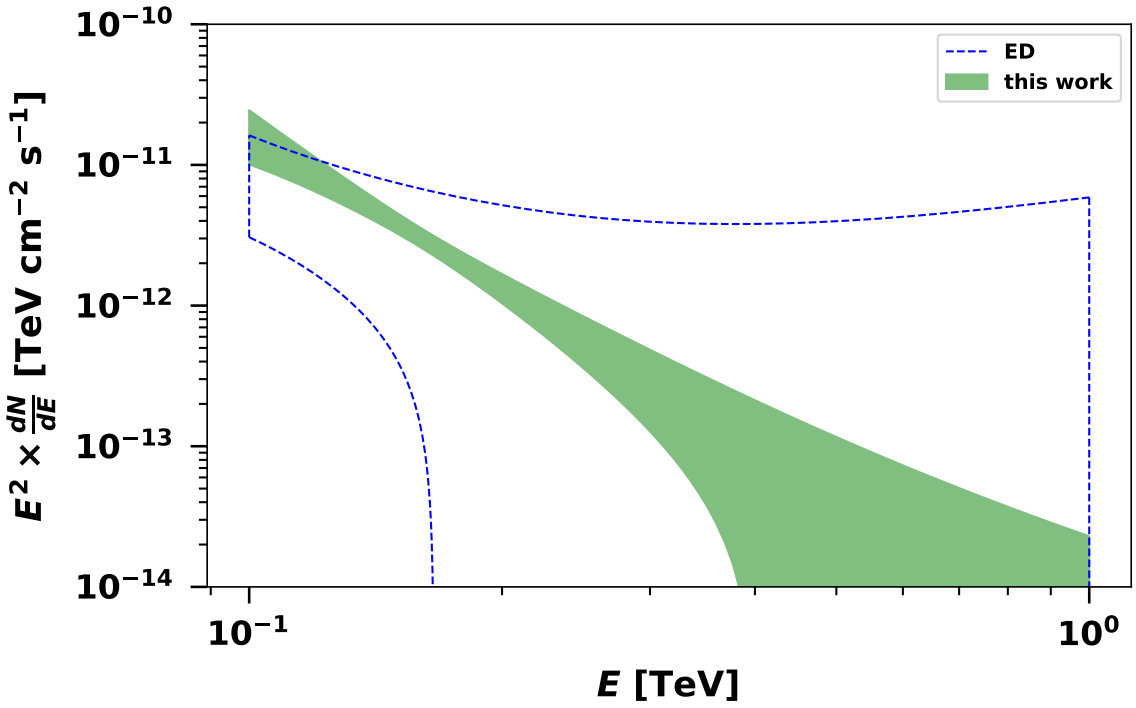

Figure 7.6: The best-fit spectrum is shown for PKS 1424+240.

The data examined here were collected well before the appearance of the gamma-ray binary VER J2032+414; a joint analysis of the two sources follows in the next section.

The spatial component of the source is modeled as a 2D Gaussian while the spectral component is modeled as a power law:

$$S(x, y, E) = N_0 \left(\frac{E}{E_0} \right)^{-\Gamma} e^{-a(x-x_0)^2 - b(x-x_0)(y-y_0) - c(y-y_0)^2}$$

Where:

$$a = \frac{\cos^2\theta}{2\sigma_x^2} + \frac{\sin^2\theta}{2\sigma_y^2}$$
$$b = \frac{\sin 2\theta}{2\sigma_x^2} - \frac{\sin 2\theta}{2\sigma_y^2}$$
$$c = \frac{\sin^2\theta}{2\sigma_x^2} + \frac{\cos^2\theta}{2\sigma_y^2}$$

The model parameters are: N_0, Γ, x_0, y_0, σ_x, σ_y, θ. All parameters are left free for the fit. The source is detected with a significance of 14.6σ; the results of the fit

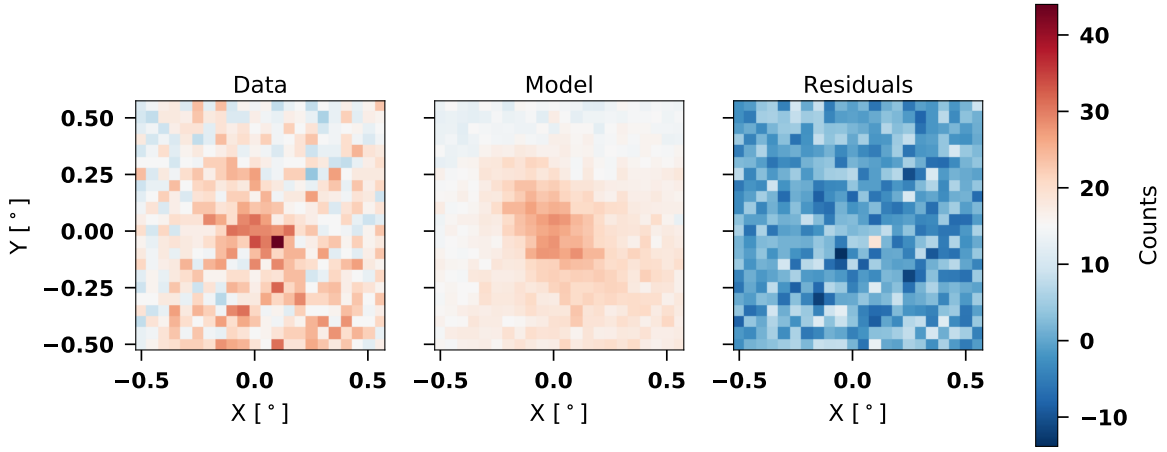

Figure 7.7: Data/Model/Residuals plot for TeV J2032+4130.

are given in Tables 7.4 and 7.5 and plotted in Figures 7.7 and 7.8. The morphological properties are consistent with recently published values [1].

The spectral indices estimated by Eventdisplay and the MLM analysis are consistent, however the normalization estimated by the MLM analysis exceeds the Eventdisplay analysis by more than a factor of three. It is likely that this is at least in part due to significant fraction of source counts falling beyond Eventdisplay's source integration region. Since Eventdisplay does not assume any spatial model for a source, there is no way to account for flux from the source originating from beyond the source region. Leakage due to the PSF is accounted for via the effective area curves, but for an extended source region ($\theta = 0.22°$) this is a negligible effect, since the PSF is typically less than 0.1°. The spatial model derived by the MLM analysis can be used to estimate the amount of flux lying outside of the source region (see Figure 7.9). This shows that the flux observed by Eventdisplay represents about 57% of the total flux. This does not completely account for the disparity between the analyses, but is certainly a large contributor. A similar scaling factor has been employed by HAWC to facilitate comparisons of VERITAS results (which are model-independent) with HAWC results (which are model-dependent), such as in [309].

The asymmetry of TeV J2032+4130 is well-documented [31]; it is worthwhile

Model	**Method**	N_0 $[10^{-11}\text{cm}^{-2}\text{s}^{-1}\text{TeV}^{-1}]$	E_0 [TeV]	Γ
PL	ED	0.8 ± 0.1	0.3	2.01 ± 0.14
PL	MLM	2.9 ± 1.2	0.3	2.21 ± 0.09

Table 7.4: Spectral fit parameters for TeV J2032+4130

Model	x_0	y_0	σ_x	σ_y	θ
2D Gaussian	-0.03 ± 0.02	0.04 ± 0.02	0.10 ± 0.02	0.21 ± 0.03	22.1 ± 6.0

Table 7.5: Spatial fit parameters for TeV J2032+4130. All parameters are expressed in degrees. $x_0, y_0 = (0, 0)$ corresponds to the RA/Dec of TeV J2032+4130 as reported in [1].

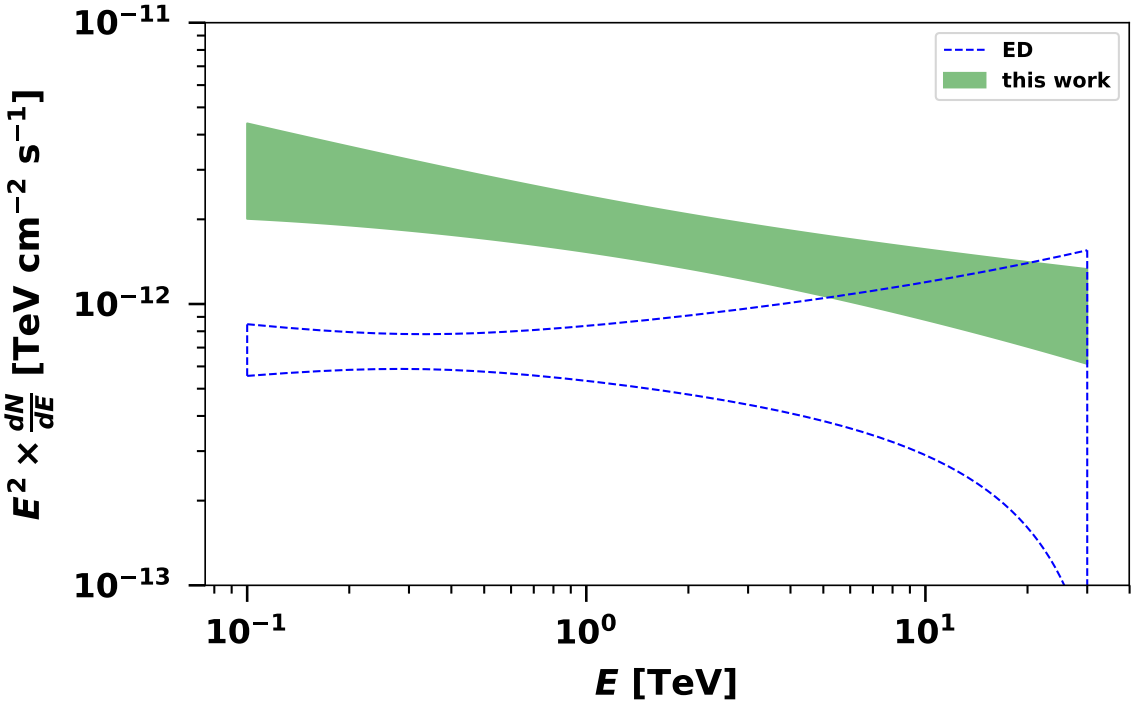

Figure 7.8: The best-fit spectrum is shown for TeV J2032+4130.

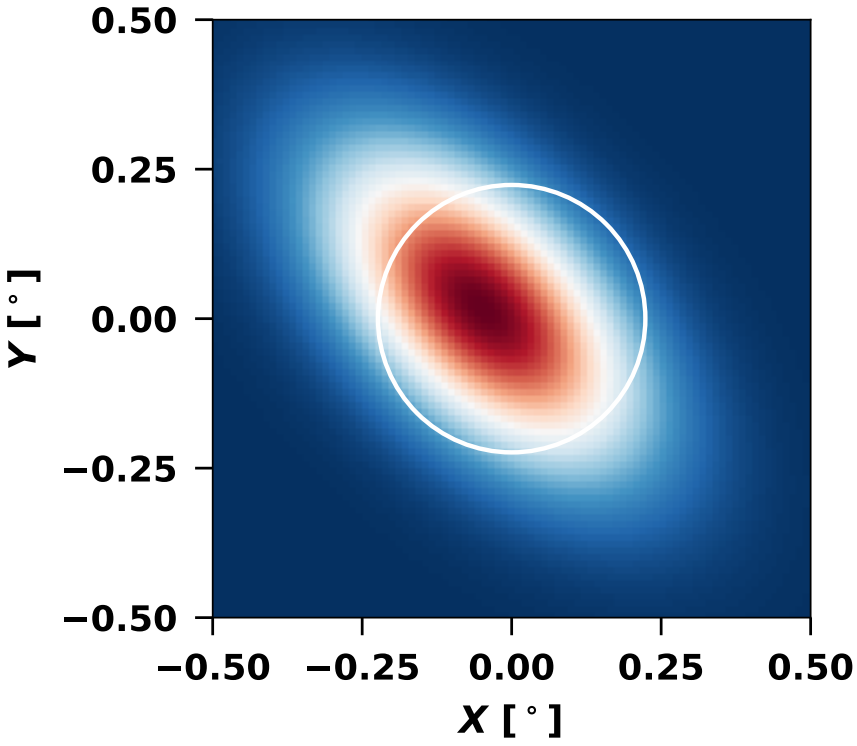

Figure 7.9: The PSF-convolved source model. The white circle shows the Eventdisplay integration window.

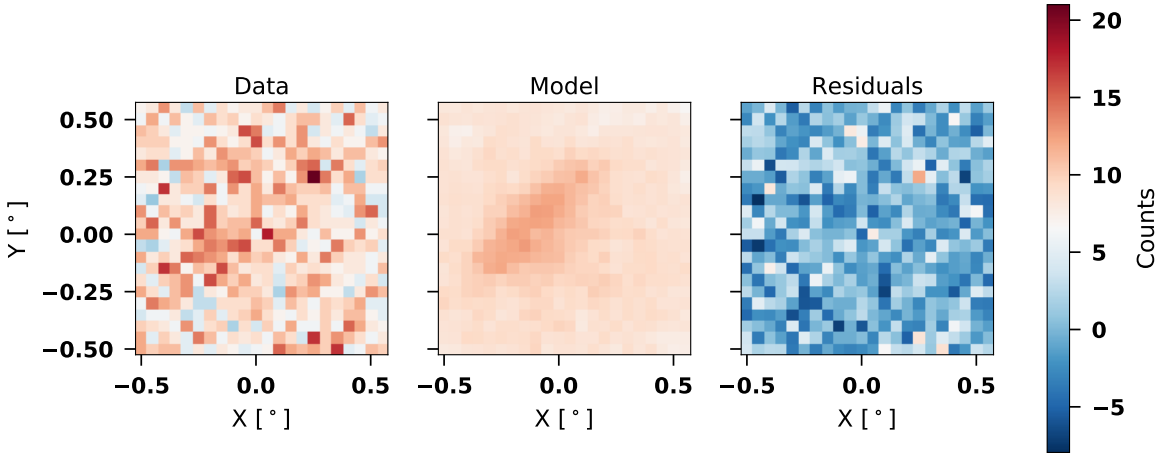

Figure 7.10: Data/Model/Residuals plot for SNR G106.3+2.7.

to see if the MLM analysis is capable of distinguishing between a radially symmetric model (a Gaussian disk) and a standard 2D Gaussian. To determine this, a second fit was performed with a simpler spatial model:

$$S(x, y, E) = N_0 \left(\frac{E}{E_0}\right)^{-\Gamma} e^{-\frac{(x-x_0)^2+(y-y_0)^2}{2\sigma^2}}$$

The 2D Gaussian model is favored over the symmetric Gaussian with a test statistic of 14.4. The significance is found in the usual way, by assuming that the TS obeys a χ^2_2 distribution, resulting in a significance of 3.2σ.

SNR G106.3+2.7

SNR G106.3+2.7 is a supernova remnant near the Boomerang Nebula. It is another hard-spectrum, asymmetrically extended galactic source to serve as a test subject for the MLM analysis. The spatial component of the source is modeled as a 2D Gaussian while the spectral component is modeled as a power law. The source was detected with a significance of 9.1σ. The fit is plotted in Figures 7.10 and 7.11; the spectral fit parameters are given in Table 7.6.

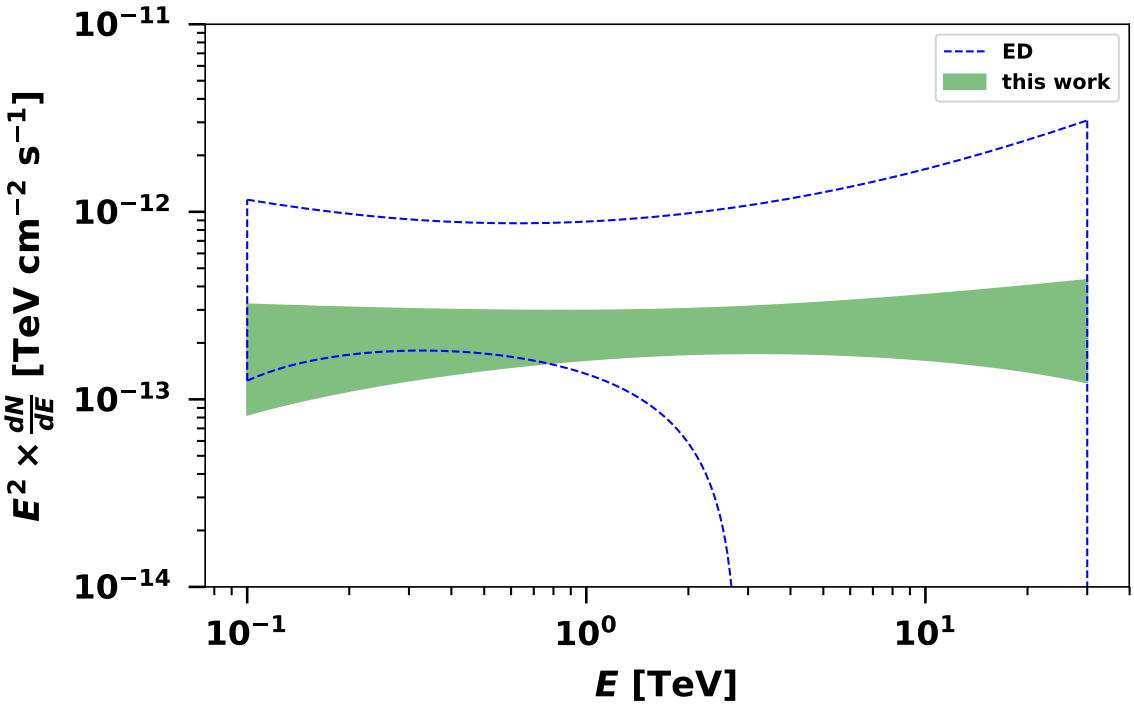

Figure 7.11: Data/Model/Residuals plot for SNR G106.3+2.7.

Ursa Minor

Ursa Minor is a galaxy which is not associated with any known gamma-ray source. It is included here to test the MLM analysis's ability to reject null sources. The source was modeled spatially as a point source and spectrally as a power law. The best fit model has a test statistic of 1.5, which corresponds to a significance of 0.2σ meaning the null hypothesis is not rejected. The fit is shown in Figure 7.12.

The Ursa Minor field was further utilized to test Wilks's Theorem. According to the theorem, the TS of a null model will be distributed as a χ^2_f, where f is the number of additional free parameters contained in the test model over the null model. To test this, successive fits were conducted over a grid throughout the Ursa Minor field while keeping the source position fixed. The test was conducted repeatedly while varying the number of free parameters, and histograms were constructed to examine the distribution of TS values. The results are shown in Figure 7.13. The figure shows the observed TS distributions along with the χ^2 distributions expected from Wilks's

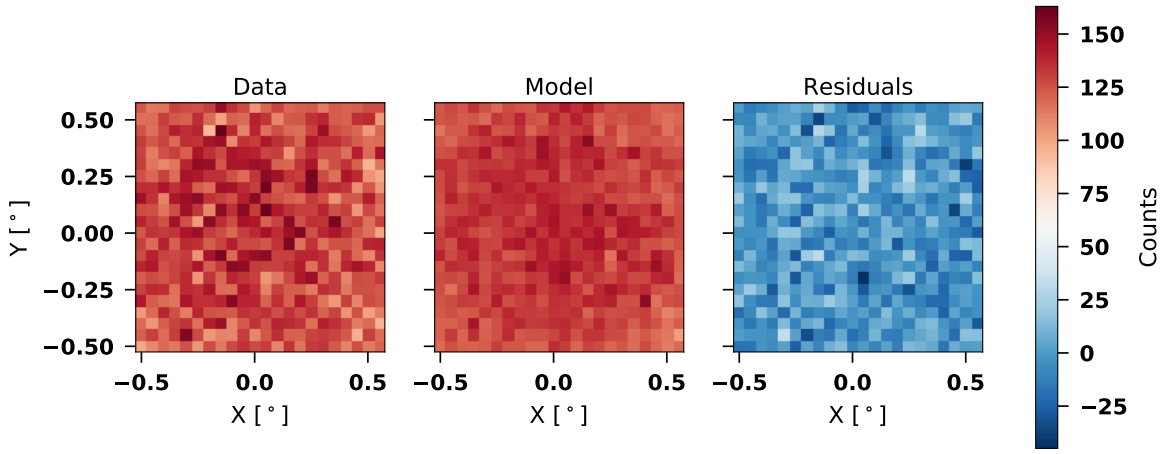

Figure 7.12: Data/Model/Residuals plot for Ursa Minor.

Theorem. The figure shows that the observed TS frequency drops off slower than the expected frequency. Based on this observation, the significance values estimated by the MLM analysis are likely overestimates. A significantly larger analysis utilizing both real and simulated null sources could help to quantify this effect; however the general similarity between the detection significances between Eventdisplay and this analysis suggest that the effect is likely small.

7.4 Results

VER J2032+414 and TeV J2032+4130

The gamma-ray binary VER J2032+414, present in the same field of view as the extended PWN TeV J2032+4130, serves as a useful test of this analysis method's ability to disentangle multiple sources in a single dataset. A detailed analysis and discussion of this region was presented in the previous chapter; the analysis presented here serves as a test of the functionality of the maximum likelihood analysis method.

The analysis presented in the previous chapter made use of the fact that a large dataset exists containing only TeV J2032+4130 and not VER J2032+414; a joint fit was therefore performed using data from before and after the appearance of the binary VER J2032+414. The analysis presented in this Chapter includes only data from the fall of 2017, when both the binary and the nebula were emitting a measurable

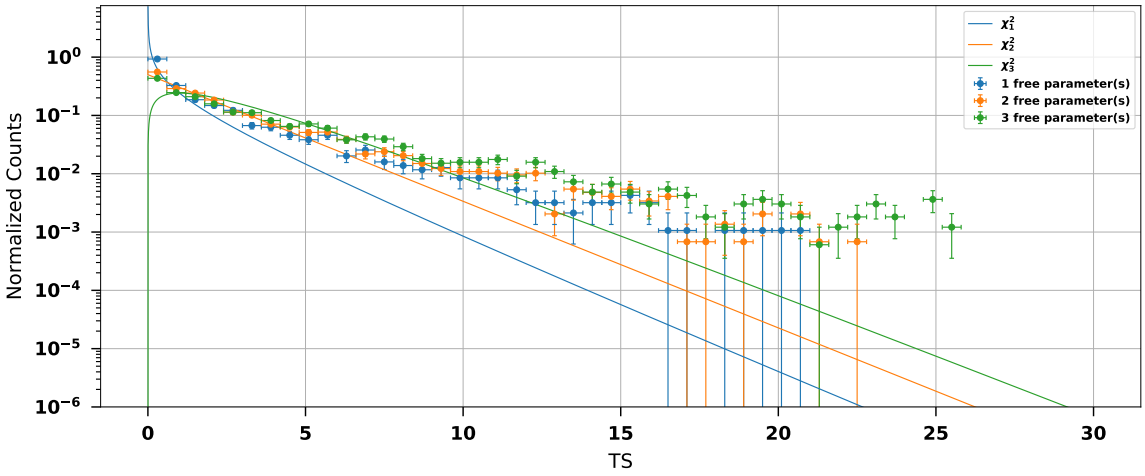

Figure 7.13: The figure shows the distribution of TS for many fits conducted from the Ursa Minor field. Distributions are shown for three different source models with 1 (cyan), 2(orange), and 3 (green) degrees of freedom. The lines show the probability density functions for χ^2_1 ,χ^2_2, and χ^2_3.

gamma-ray flux. By fitting different models with multiple sources to the dataset, the TS values of different models can be compared to determine the relative likelihood of a multi-source model as opposed to a single-source model. The goal of this analysis is to determine the effectiveness of the maximum likelihood tool at resolving multiple sources in the same field of view.

Three different models were fit to the dataset. The first model consisted of a single source, assuming a point source spatial model with a simple power law spectrum. The second model consisted of two sources: the first modeled as a point source with a power law spectrum; the second modeled as an extended source with a power law spectrum. The third model also consisted of two sources: the first modeled as a point source with a exponentially-cutoff power law spectrum; the second modeled as an extended source with a power law spectrum.

The presence of a second source in the field of view is demonstrated by constructing a test statistic from comparing the likelihoods of the single-source model to the two-source model (Equation 7.7). The model with two power law components is favored over the single-source model with a TS of 108.2. Factoring in the additional

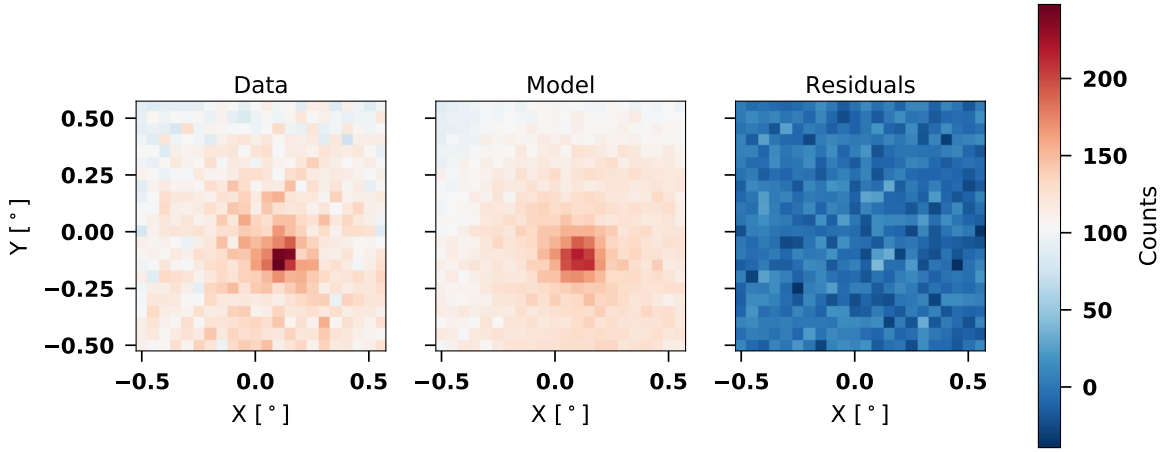

Figure 7.14: Data/Model/Residuals plot for the joint fit of VER J2032+414 and TeV J2032+4130.

8 degrees of freedom, this corresponds to a significance of approximately 9.0 σ. This result is interpreted as $\sim 9\sigma$ evidence of the presence of a second source in the field of view (this amounts to a detection of TeV J2032+4130 in addition to the bright binary emission).

The component modeling the binary in the previous analysis used a power law for the spectrum, whereas the analysis in the previous chapter preferred a power law with an exponential cutoff. The presence of this feature in the spectrum can be tested by comparing the likelihood of the second and third models, which differ only in the spectral form of the point source component. The third model is found to be preferred over the second model with a TS of 21.1. Since the models differ by 1 degree of freedom, this corresponds to a significance of 4.4σ. Therefore an exponential cutoff is favored in the spectrum of the binary component over a power law with a significance of 4.4σ. The results of the spectral fit are given in Table 7.7 and plotted in 7.15. It should be noted that these parameters are consistent with those presented in the previous Chapter.

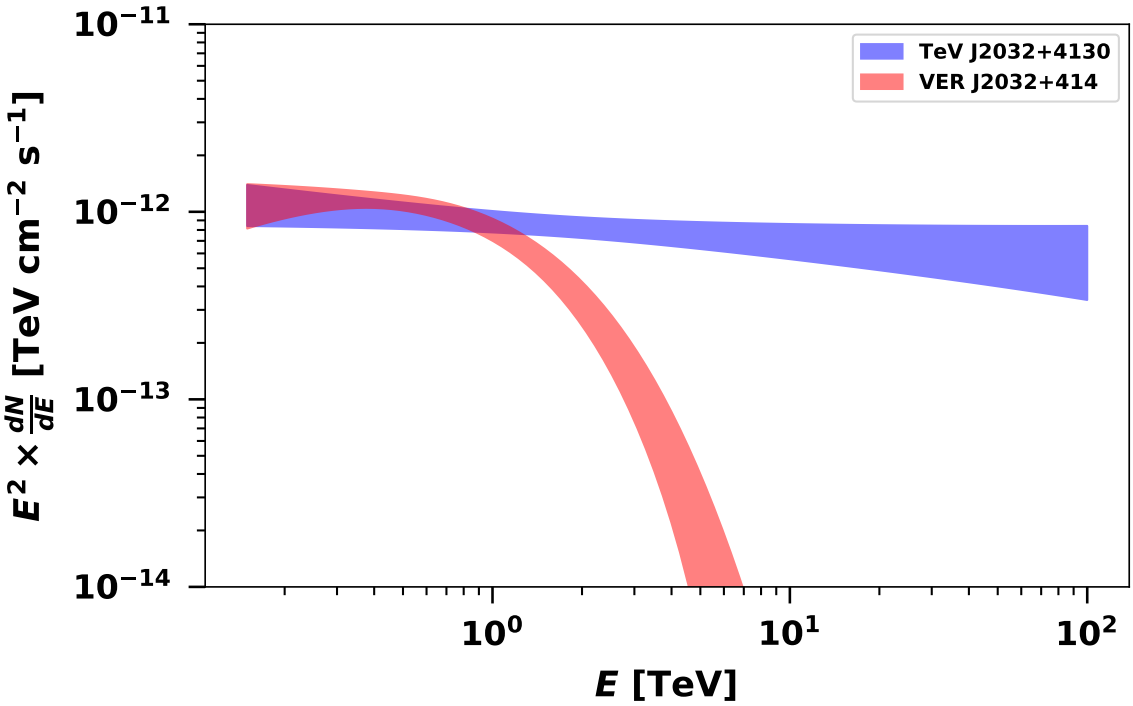

Figure 7.15: Spectral results of the joint fit of VER J2032+414 and TeV J2032+4130.

HESS J0632+057 & LS I +61 303

The existence of a PWN associated with PSR J2032+4127 indicates that the pulsar is the chief power source for both the gamma-ray binary and the larger PWN. This indicates that a significant amount of the pulsar wind escapes confinement from the stellar wind of MT91 213 and diffuses to the termination shock with the interstellar medium. PWNe associated with other gamma-ray binaries have not been reported, but if the majority of these systems are indeed pulsar-powered then the possibility remains that some of the pulsar wind could escape the massive star and form a larger nebula. Even though no such feature has been detected thus far, it is possible that PWNe are "hiding" in the same field of view as the gamma-ray binary system. If the binary emission greatly outshines the PWN emission then it may go unnoticed. In the case of PSR J2032+4127/MT91 213, the point-like binary emission dominates the PWN emission in orbital phases close to periastron (Figure 7.16). The discovery of TeV J2032+4130 was likely only possible due to the system's large orbit. Near periastron,

the pulsar and massive star are separated by less than 1 AU; at apastron this distance is $\sim 50 - 60$ AU. At large separation distances the intra-binary emission subsides, allowing the surrounding PWN to be seen. This dramatic difference is not present in the other gamma-ray binary systems, in which the compact object and massive star never separate by more than $\sim 15 - 20$ AU, and in many cases are constantly within just a few AU of each other. Were there PWN present in these systems in addition to the binary emission, it may well be outshone by the binary emission. On the other hand, the more compact orbit may prevent the pulsar wind from diffusing beyond the stellar wind, preventing the formation of a PWN in the first place. Given that the sample size of gamma-ray binaries is still relatively small, a search for possible PWN is merited. The analysis method described in this Chapter is well-suited for such a task. As was demonstrated in the previous section, an analysis of the PSR J2032+4127/MT91 213 field based only on data when the binary emission dominated the PWN emission was still able to significantly detect the presence of the PWN. Here, we apply this same technique on two other gamma-ray binary systems for which VERITAS has accumulated a large dataset: HESS J0632+057 and LS I +61 303.

HESS J0632+057

214 hours of data from HESS J0632+057 was analyzed, covering all phases of the binary orbit (but not necessarily evenly). The goal of this analysis is to search for an extended nebula. Two models were fit to the dataset. Model 1 consisted of a single point source with a power law spectrum. Model 2 consisted of a single source with a power law spectrum plus a radially symmetric Gaussian with a power law spectrum. Both models were fit to the data. The Model 1 fit results in an energy spectrum for HESS J0632+057 characterized by a normalization (at 1 TeV) of $(4.6 \pm 0.2) \times 10^{-13}$ cm^{-2}s^{-1}TeV^{-1} and a spectral index of 2.64 ± 0.05. The index is consistent with that reported in [240], the flux normalization is slightly greater because the source is variable and the time spans used in this analysis and [240] are not the same.

Model 2 is a better fit with a test statistic of 0.50. With five additional degrees of

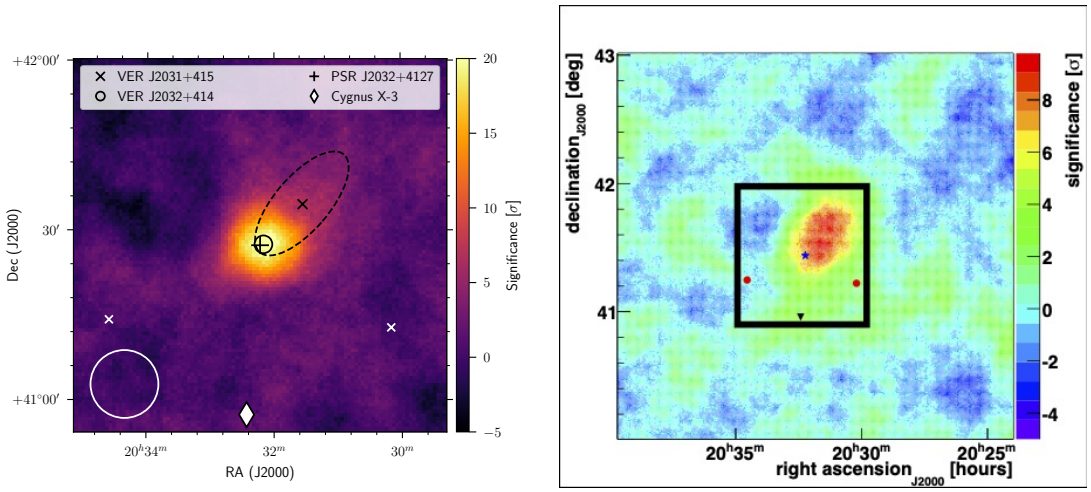

Figure 7.16: *Right:* Significance sky map for VERITASshowing the field of view containing PSR J2032+4127 and TeV J2032+4130 from September - December 2017 (close to periastron of the binary). The morphology of TeV J2032+4130 is indicated with the dashed ellipse. The centroid of the binary source (PSR J2032+4127/MT91 213) is indicated by the black circle. The black cross denotes the location of the pulsar PSR J2032+4127, as well as the massive companion MT91 213. The white circle indicates the gamma-ray point spread function for VERITAS. The white x's indicate telescope pointing positions. Figure presented in Chapter 6 and copied here for convenience. *Left:* The VERITAS skymap of TeV J2032+4130 from [31]. The position of PSR J2032+4127 is indicated by the blue star while the black triangle indicates Cyngus X-3. The red circles show the telescope pointing position, which was equidistant from both TeV J2032+4130 and Cygnus X-3. The two images do not show the same field of view. The box drawn on the right image approximately indicates the field of view displayed in the left.

freedom, this corresponds to a significance of approximately 0.01σ. There is therefore no evidence for a second source in the field of view containing HESS J0632+057. In the absence of a detection we can set an upper limit on the flux from a hypothetical second source in this field. This is done by constructing a likelihood profile for the flux and finding the upper flux limit enclosing 95% of the probability (see[310]). This yields an upper flux limit of $F(E > 200 \text{ GeV}) \leq 4.8 \times 10^{-12}$ cm^{-2}s^{-1}, which is comparable to the level seen from the binary at its peak.

LS I +61 303

The same analysis was run on 70 hours of data from LS I +61 303. A single-source model and a two-source model were constructed following the methodology of the previous section. The fit of the single-source model yielded a spectrum for the binary emission with a normalization (at 1 TeV) of $(1.1 \pm 0.5) \times 10^{-12}$ cm^{-2}s^{-1}TeV^{-1} and a spectral index of 2.55 ± 0.05. The index is consistent with the phase-averaged index reported in [23] while the normalization is greater. This again likely indicates that the data set used here is more biased towards periods of bright emission than the set used in [23].

Model 2 is only marginally preferred with a test statistic of 0.002, corresponding to a significance of approximately zero. The upper limit on the flux of a potential second source is $F(E > 200 \text{ GeV}) \leq 1.1 \times 10^{-11}$ cm^{-2}s^{-1}, again comparable to that of the binary at its peak.

Discussion

This analysis shows no evidence of a PWN associated with either HESS J0632+057 or LS I +61 303. There are many reasons why this could be the case. In the case of HESS J0632+057, the possibility remains that the source is powered by a black hole rather than a pulsar, in which case no PWN would be expected. The lack of a detected PWN in no way precludes the presence of a pulsar, however. In fact, LS I +61 303 is now known to be powered by a pulsar. The relatively compact orbit of both sources

could disrupt the formation of a PWN since the compact object is continually in an environment where the stellar wind is dense. The maximal separation of the compact object and massive star is only a few AU in the HESS J0632+057 system, and is less than an AU for LS I +61 303. Thus the stellar wind could confine most of the pulsar wind, directing much of the pulsar's energy into powering the intra-binary shock. It also remains possible that PWNe are indeed present in this fields but are too faint to be detected. This would also be a result of the intra-binary shock siphoning energy from the PWN.

7.5 Conclusion

In this chapter we present a new analysis tool which is useful for determining the spatial and spectral properties of astrophysical gamma-ray sources. A key feature of the method is its ability to simultaneously detect multiple sources in the same field of view, as was demonstrated by the analysis of VER J2032+414 and TeV J2032+4130. The method works well though has significant room for improvement. While Wilk's Theorem is useful for an initial approximation of the statistical significance of any result, a better estimate can be derived by detailed studies of the analysis method's response to null sources, as was briefly presented in the discussion of Ursa Minor. More detailed instrument response functions could also improve the analysis: for example an energy response matrix and a fully simulated point spread function. Finally, it should be noted that, while this analysis was developed for the purpose of analyzing multiple sources in the same field of view, it is constrained by the need to simultaneously estimate background counts from this same field of view. This means that if too great a fraction of the field of view is filled with potential gamma-ray sources, the analysis is not trustworthy. That problem is much more difficult to solve, and has been attempted elsewhere (see [304]).

The results presented in this Chapter serve as a promising proof of concept for a maximum likelihood framework to analyze VERITAS data. It has shown the ability to reconstruct source properties in agreement with the established and tested Eventdisplay

software, and reproduces the results on VER J2032+414 and TeV J2032+4130 from the previous Chapter based only on the dataset where both sources were present.

Model	**Method**	N_0 $[10^{-12}\mathrm{cm}^{-2}\mathrm{s}^{-1}\mathrm{TeV}^{-1}]$	E_0 [TeV]	Γ
PL	ED	3.8 ± 2.5	0.38	2.09 ± 0.29
PL	MLM	1.5 ± 0.6	0.38	1.94 ± 0.14

Table 7.6: Spectral fit parameters for SNR G106.3+2.7

Source	**Model**	N_0 $[10^{-11}\mathrm{cm}^{-2}\mathrm{s}^{-1}\mathrm{TeV}^{-1}]$	E_0 [TeV]	Γ	E_{cut} [TeV]
VER J2032+414	PLEC	5.7 ± 1.2	0.15	1.62 ± 0.32	0.91 ± 0.34
TeV J2032+4130	PL	4.8 ± 1.2	0.15	2.11 ± 0.09	-

Table 7.7: Spectral fit parameters for VER J2032+414 and TeV J2032+4130 using a two-source model.

Chapter 8

SUMMARY AND FUTURE WORK

In this work, we have reviewed the multi-wavelength properties of gamma-ray binaries and presented the detection of a new gamma-ray binary: PSR J2032+4127/MT91 213. In this Chapter, we briefly review gamma-ray binaries and reflect reflect on how the observations of PSR J2032+4127/MT91 213 contribute to our understanding of gamma-ray binaries as a population. We then discuss the prospects for future observations of gamma-ray binaries with the next generation of gamma-ray telescopes, in particular the Cherenkov Telescope Array Observatory (CTAO).

8.1 Gamma-ray binaries and PSR J2032+4127/MT91 213

Recall that a gamma-ray binary consists of a massive O or B type star orbiting with a compact object (either a neutron star or a black hole). Regardless of the nature of the compact object, gamma-ray binaries are distinct from the broader class of High Mass X-ray Binaries (HMXBs) in that they emit most of their energy as gamma rays (> 1 MeV) and their radio and X-ray emission is of non-thermal origin. Emission from HMXBs (which mostly takes the form of X-rays) typically originates from the accretion of stellar material onto the compact object, while emission from gamma-ray binaries originates in shocks far from the compact object. In the case of pulsar-powered gamma-ray binaries, the pulsar wind exerts enough pressure to prevent accretion and shocks the stellar wind at a point in between the pulsar and star, the "intra-binary shock". Charged particles then accelerate at the shock and radiate via synchrotron and inverse Compton radiation in the magnetized wind and stellar photon field. For gamma-ray binaries powered by a stellar-mass black hole, the particle acceleration likely happens

at shocks within the relativistic jets from the black hole rather than an intra-binary shock, though the radiation mechanisms will be the same.

Regardless of the identity of the compact object, significant orbital variability is expected and is observed in all gamma-ray binary systems. As the compact object and massive star progress through their orbit, the location of the shock relative to the massive star and compact object is subject to change. This will result in orbitally modulated changes in the local magnetic and radiation fields in the shock environment, which will vary the acceleration and radiation efficiency at the shock with time. Additional variability is introduced by the orientation of the binary system relative to the line of sight of the observer. This can result in absorption of gamma-rays and Doppler beaming of X-rays near inferior conjunction. The shape of the energy spectrum is determined by the balance between the rates of acceleration, synchrotron radiation, and inverse Compton radiation. These in turn depend upon the strength of the local magnetic and radiation fields. Since these fields vary as the shock location changes, this can introduce orbital variability in the energy spectrum of gamma-ray binary systems. See Chapter 5 for a full discussion of the emission mechanisms and orbital variability in these systems.

In most known gamma-ray binary systems, the identity of the compact object is unknown. The emission from a system with an unknown compact object could arise from either of the two primary scenarios outlined above: the *pulsar scenario* in which particle acceleration and radiation occurs at the intra-binary shock, or the *microquasar scenario* in which particle acceleration and radiation occurs in shocks within the relativistic jet of the black hole. The identity of the compact object can be unambiguously determined to be a pulsar if radio pulsations are detected from the area, however the absence of pulsations does not preclude the presence of a pulsar. While either scenario remains plausible, the balance of available evidence makes the pulsar scenario the more likely of the two. Of the nine known gamma-ray binaries, three are now known to contain pulsars. All gamma-ray binaries exhibit spectral features characteristic of pulsars, such as curved high-energy spectra and X-ray indices similar to

pulsar wind nebulae (PWNe) [27]. Radio emission, present in all gamma-ray binaries, is a hallmark of PWNe but is typically absent in accretion-driven systems like HMXBs. Additionally, the fact that all gamma-ray binaries exhibit broadly similar spectral and timing features, taken together with the fact that three of these systems are known to be powered by pulsars, points to a pulsar scenario being more likely in all systems. In the absence of direct evidence of a pulsar, however, the microquasar scenario remains plausible in those systems in which the compact object remains unidentified.

At the time of its discovery, PSR J2032+4127/MT91 213 was only the second gamma-ray binary known to contain a pulsar (after PSR B1259-63). Knowledge of the identity of the compact object greatly constrains the possible emission scenarios and allows for detailed study of the physical environment in the vicinity of the intra-binary shock. When a pulsar is known to be the power source of a gamma-ray binary this also clearly defines the energy available for the observed processes (the pulsar's spin-down power). PSR J2032+4127 is a moderately energetic $\left(\dot{E} \approx 2 \times 10^{35} \text{ erg s}^{-1}\right)$ gamma-ray and radio pulsar. Its large orbit (≈ 50 years) sets it apart from other gamma-ray binaries whose orbital periods range from ≈ 4 days to ≈ 3.4 years. The size of the orbit is advantageous for Imaging Atmospheric Cherenkov Telescopes (IACTs). Since IACTs typically require extended exposure times—on the order of several hours—to precisely characterize a source's gamma-ray flux, variability on shorter timescales than this can be difficult to observe. The unusually large orbit of PSR J2032+4127/MT91 213 ensures that IACT exposure times are a much smaller fraction of the orbital period than in other systems, allowing the orbital variability to be probed on finer timescales. The obvious drawback of the large orbit is that periastron observations happen infrequently. With the next periastron in this system likely to occur between $\sim$ 2062 and $\sim$ 2067, CTAO and any other next-generation IACTs will not be able to detect this system before then.

As with all pulsar-driven systems, the non-thermal emission from PSR J2032+4127/ MT91 213 originates from the intra-binary shock and is variable with time.
PSR J2032+4127/MT91 213 exhibits a steady increase in gamma-ray flux over the $\sim$

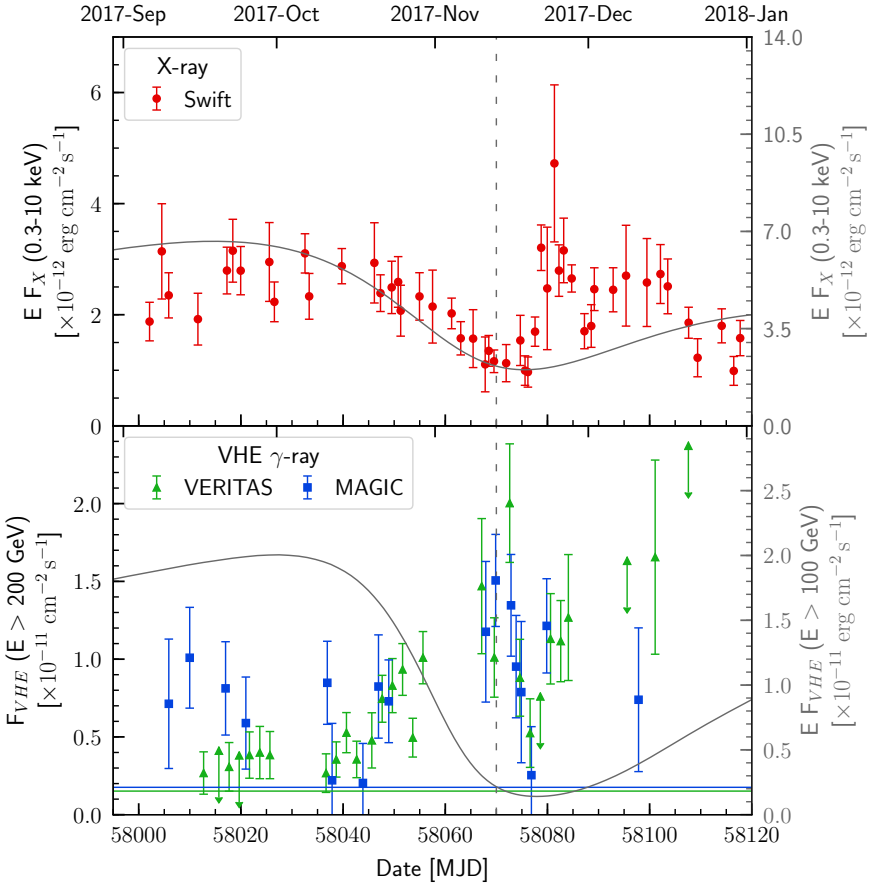

Figure 8.1: Figure 6.1 from Chapter 6, reproduced here for convenience.

month leading up to periastron, peaking just afterwards. The peak is followed by a sharp dip in flux for a few days before recovering. The light curve in the weeks after the flux recovered from the dip is poorly constrained.

The X-ray light curve reaches a maximum about a month prior to periastron before steadily decaying and reaching a minimum near the time of periastron. The X-ray flux then exhibits an abrupt flare about 10-15 days after periastron. The underlying causes for the variability in both the X-ray and VHE fluxes are complex and intertwined. A detailed discussion is given in Chapter 6. The increase in VHE flux leading up to periastron is likely due to the intra-binary shock moving closer to the massive star and thus into a more intense radiation field, increasing the inverse Compton luminosity. The dip after periastron is likely due to absorption of VHE gamma-rays as the shock moves behind the massive star, relative to the observer. Contrary to the VHE flux, the X-ray flux steadily decays leading up to periastron. This can naturally be explained if the pulsar wind magnetization parameter σ (the ratio of magnetic to kinetic energy in the wind) has a steep distance dependence at the shock front. Takata et al (2017, [28]) found that the synchrotron luminosity will be greatest for $\sigma \approx 0.1$: higher σ will yield a greater magnetic field but too little kinetic energy for particle acceleration at the shock, lower σ will result in sufficient particle kinetic energy but a weak magnetic field resulting in inefficient synchrotron cooling. Assuming that σ decreases with distance from the pulsar, the shock's movement toward the pulsar could increase σ beyond the optimal value of 0.1, causing diminished synchrotron emission. Doppler beaming of the X-ray emission could also play a role, although the magnitude of this effect is highly sensitive to the orbital inclination of the system, which is poorly constrained. Doppler beaming would enhance the X-ray emission the most at inferior conjunction, which occurs several months before periastron. On the contrary, Doppler beaming would be suppressive at superior conjunction, ~ 10 days after periastron.

Both light curves can also be explained if the disk of the massive star is sufficiently inclined. The inclined disk could create a "shadow" in the stellar wind: a region where the stellar wind is less dense. Upon entering this region, the intra-binary shock

would move away from the pulsar and toward the massive star. The resulting decrease in magnetic field and increase in radiation field would naturally result in a decaying X-ray flux and increasing VHE flux. The X-ray flare approximately 10 days after periastron is likely due to an interaction with the disk of the massive star. While the VHE light curve in the weeks leading up periastron and including the post-periastron dip is well-characterized by both instruments, the flux in the weeks after periastron is poorly constrained. This is due to the diminishing observable window for the source resulting in reduced exposure times from both instruments. Inclement weather also hampered post-periastron observations.

The discovery and detailed observation of the PSR J2032+4127/MT91 213 binary system represents a significant contribution to our broader understanding of gamma-ray binary systems. At the time of its discovery, PSR J2032+4127/MT91 213 was the seventh known gamma-ray binary system, and just the second such system known to be powered by a pulsar. Since the establishment of gamma-ray binaries as a unique source class, PSR J2032+4127/MT91 213 is the first system from which VHE emission was predicted before it was observed[1], it therefore represents a significant milestone in the growth of the population of these systems. Though subsequent periastron observations will not be possible for the current or (likely) next generation of IACTs, further observations and analysis can nonetheless contribute to our understanding of PSR J2032+4127/MT91 213 and of the population of gamma-ray binaries.

Modeling of this system is plagued by a large number of model parameters, many with large uncertainties. Parameters related to the massive star include the density and profile of the stellar wind, the extent, inclination, and density of the circumstellar disk, and the mass loss rate of the star. Parameters related to the pulsar include the magnetization parameter σ (including possible distance dependence), the density of the wind, and the distribution of particle energies in the wind. Finally the orbital geometry of the system relative to the viewer can greatly alter the observed emission from the

[1] In all other systems except for PSR B1259-63, the VHE source was initially unidentified and only determined to be a gamma-ray binary after subsequent analysis.

system. Effects such as Doppler beaming, absorption, and inverse Compton scattering efficiency are all geometry-dependent. Many orbital parameters of this system remain poorly constrained; orbital parameters are therefore essentially nuisance parameters in the modeling of these systems. While various models have included subsets of the aforementioned variables, a model has yet to emerge which investigates their combined effect and which simultaneously accounts for X-ray and VHE emission.

Continued radio observations of the pulsar can provide timing information over a larger fraction of its orbit and constrain parameters related to the orbital geometry. Extended VLBI observations could further constrain the distance and orbital parameters of PSR J2032+4127/MT91 213, as was done for PSR B1259-63 [165], though the great size of the orbit makes this more challenging. Ultimately, the discovery of similar sources and population studies of gamma-ray binaries will contribute to our understanding PSR J2032+4127MT91 213 and sources like it. There are currently only nine known gamma-ray binaries, several of which have been sparsely studied. Only three systems have a firmly identified compact object. The discovery and detailed study of a large population gamma-ray binaries is desirable to better understand how these systems work.

8.2 Gamma-ray Binaries: Future Prospects

Gamma-ray binaries are not likely to be ubiquitous throughout the Galaxy. They are formed from the rather rare combination of a pulsar (or a stellar-mass black hole) and a massive O or B star. Additionally, they are likely to be short-lived, transitioning into HMXBs once the pulsar's rotational energy can no longer hold off accretion of the stellar wind [311]. The current population of gamma-ray binaries likely represents the upper end of the luminosity distribution of these systems and reflects the sensitivity of the current generation of instruments. Dubus et al. (2017) constructed an approximate gamma-ray binary luminosity distribution and, based on simulated surveys conducted by several gamma-ray telescopes, concluded that the Galactic population of gamma-ray binaries likely contains between 49 - 190 systems [160]. They

conclude that many more systems of comparable luminosity to the known population are unlikely to be found: the discovery of more systems requires more sensitive instruments, namely CTAO.

The Cherenkov Telescope Array Observatory

As the current generation of IACTs near the end of their lifetimes, the future of ground-based gamma-ray astronomy is represented by the Cherenkov Telescope Array Observatory (CTAO) [312, 34]. By using a much larger number of telescopes equipped with modern cameras and data acquisition equipment as well as more sophisticated analysis methods, CTAO will achieve an order of magnitude increase in sensitivity relative to current instruments [313]. Additionally, it will approximately halve the angular resolution and energy resolution compared to H.E.S.S., VERITAS, and MAGIC. This will enable CTAO to both discover new gamma-ray binaries (early simulations suggest four new sources could be found by CTAO in its first two years [160]) and to study existing sources in much more detail.

CTAO will consist of two separate arrays: CTAO-North will be located at the Roque de los Muchachos Observatory on the island of La Palma in Spain; CTAO-South will be located at the Paranal Observatory in the Atacama Desert in Chile. The north-south division will allow CTAO to cover a broad range of source declinations, providing nearly full-sky coverage. Each observatory will consist of multiple telescope types: a Small-Sized Telescope (SST, [314]) with a mirror diameter of 4.3 meters and field of view of 8.8°, a Medium-Sized Telescope (MST, [315]) with a mirror diameter of 11.5 meters and a field of view ranging from $7.5° - 7.7°$, and a Large-Sized Telescope (LST, [316]) with a mirror diameter of 23.0 meters and a field of view of 4.3°. The LSTs and MSTs will be equipped with high quantum-efficiency ($\sim 40\%$) PMTs [317], and the SSTs will utilize silicon photomultipliers (SiPMs) [318].

CTAO will utilize mixed arrays which contain multiple types of telescopes, allowing it to achieve a high sensitivity across an unprecedented energy range ($\sim$ 20 GeV

- $\sim$ 300 TeV, Figure 8.2). Accomplishing this with a single telescope type is infeasible. Due to the general power law (flux $\propto E^{-\Gamma}$) nature of most astrophysical sources, gamma rays are relatively frequent at low energies and sparse at higher energies. Conversely, the Cherenkov light produced by low-energy gamma-ray initiated showers is faint and difficult to detect, while the Cherenkov light from high-energy showers is bright and can be detected from distances far beyond the light pool.[2]

The low-energy threshold of an array of IACTs therefore depends on the size of the individual telescopes. This threshold decreases with mirror diameter (see Chapter 2). The high-energy threshold is instead limited by the paucity of events. This can be mitigated by increasing the effective collection area of the array.

Thus for low-energy sensitivity, the size of the individual reflectors is more important than the size of the overall array; whereas this is reversed for high-energy sensitivity. For a fixed number of telescopes, effective collection area can be increased by increasing the inter-telescope spacing. At high energies, gamma-rays produce bright Cherenkov showers that are visible even at great distances. Increasing the inter-telescope distance will therefore increase the collection area of the array without diminishing its ability to detect high-energy events, out to hundreds of meters [319]. Increasing the inter-telescope distance far beyond the characteristic size of the light pool ($\sim$ 120 m in radius) will have the effect of raising the low-energy threshold of the array, since low-energy showers are faint and can only be effectively imaged from within the light pool.

There are therefore competing design constraints which prevent simultaneous optimization over a large range of energies with a homogeneous array. The study of sources at low energies requires large, closely-spaced telescopes. High-energy studies require that the array cover a large geometric surface area, but the reflector size and spacing constraints are relaxed. Financial constraints limit the number and size of the telescopes as well. CTAO will thus construct arrays which consist of sub-arrays

[2] In this context the term "light pool" refers to the area on the ground, typically $\sim$ 120 meters in radius, where most of the Cherenkov light is focused (see Chapter 2).

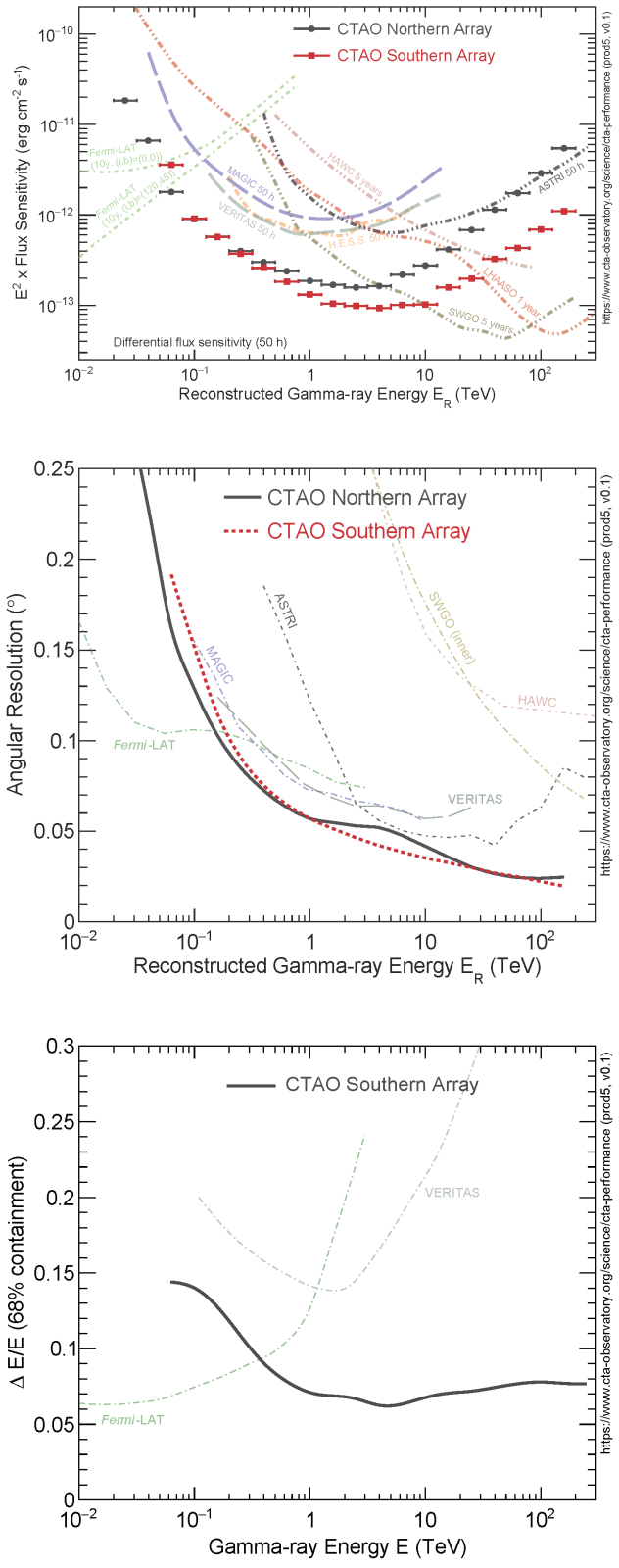

Figure 8.2: The differential sensitivity (top) and angular resolution (middle) of both CTAO arrays, compared to current instruments. The bottom panel shows the energy resolution of the Southern Array. Images available at [34].

of different types of telescopes. CTAO-South, in its initial "Alpha" configuration, will consist of 14 MSTs and 37 SSTs. The layout of the array will be a superposition of more compactly-spaced MSTs and sparsely-spaced SSTs, covering a total area of ~ 3 km^2. CTAO-North will comprise 4 LSTs and 9 MSTs and will cover a total area of ~ 0.25 km^2. CTAO-South is therefore more specialized for high energies, while CTAO North will boast a low-energy threshold of about 20 GeV [34]. The unique layout of the arrays also has the consequence that many more Cherenkov showers will be entirely contained within the array, allowing for greater numbers of telescopes to participate in event reconstruction. This will result in vastly improved energy and angular resolution, relative to current instruments (Figure 8.2, [320]).

Gamma-ray Binaries with CTAO

CTAOs improved sensitivity (about 10 times as sensitive as current IACTs) will allow it to detect faint sources which are unseen by current instruments. It will also allow it to conduct flux and spectral measurements of currently known sources 10 times faster. The former will result in the discovery of new gamma-ray binary systems, while the latter will result in the study of spectral variability of known systems on unprecedentedly small timescales. Increased energy resolution will also allow for much tighter constraints on features in the energy spectra of gamma-ray binaries (such as cutoff energies), which in turn constrain underlying parameters such as the magnetic field in the shock environment.

Given the relatively small size of the current population of gamma-ray binary systems, the discovery and analysis of new systems is critical to learning more about the population as a whole. Dubus (2017, [160]) posits that few systems remain to be discovered by current IACTs, due largely to their insufficient sensitivity to fainter sources. The increased sensitivity of CTAO will likely result in the discovery of several new sources: potentially four new gamma-ray binaries could be discovered in the first two years alone of CTAO operations [160]. This would represent a nearly 50% increase in the number of known systems. The discovery of additional gamma-ray binaries

can eventually allow for broader population studies which allow us to examine the statistical distribution of properties like luminosity, orbital size, spectral features, etc. similar to studies done for PWNe [321] and other more numerous sources.

In gamma-ray binaries, the physical conditions at the location of the shock are continuously changing. As the shock experiences varying stellar wind densities and magnetic and radiation fields, its spectral shape and overall luminosity will change. If the size of the emission region scales with separation distance between the compact object and massive star, there is reason to expect variability on timescales of minutes. Modern IACTs cannot approach these timescales with any level of precision. PSR J2032+4127/MT91 213 ranges in flux from 1-10% that of the Crab Nebula, typical among gamma-ray binaries. VERITAS can detect a 1% Crab source in 20-30 hours of exposure; a 10% source takes only 20-30 minutes [109]. Significantly more time is required to construct a precise energy spectrum. It is therefore difficult to study spectral evolution throughout the orbit of a gamma-ray binary on timescales smaller than days to weeks (although this has been done in the case of LS 5039 after integration over many orbits [21]).

The impact of CTAO observations on existing gamma-ray binaries has been studied in detail by Cherenyakova et al (2019, [322]), who simulated CTAO observations of known gamma-ray binaries in order to estimate how CTAO may improve the precision and resolution of current measurements. CTAO will be able to construct high-precision light curves with $\sim$30 minute observations, allowing for the detailed investigation of features like the recurrent dip in the light curve of PSR B1259-63, attributed to absorption. The construction of precise spectra in under 5 hours of exposure time will allow for the study of spectral variability on short timescales, placing strong constraints on the underlying physical processes and potentially allowing for investigation into the density profile of the stellar wind [322]. The lower energy threshold of CTAO will allow for observations of gamma-ray binaries at GeV energies, where there is significant overlap with *Fermi*-LAT. This will allow for detailed study of the high-energy component of the emission, which is currently thought to originate from a

different particle population than the VHE component. CTAOs increased sensitivity and energy resolution will also place tighter constraints on spectral features commonly observed in gamma-ray binaries, such as cutoff energies.

The influx of new sources, together with studies of existing sources in vastly greater detail, will greatly improve our understanding of gamma-ray binaries and how they work. In summary, the prospects for gamma-ray binary studies with CTAO are good, despite the limited source population.

BIBLIOGRAPHY

[1] A. U. Abeysekara, A. Archer, T. Aune, et al. A very high energy gamma-ray survey toward the Cygnus region of the galaxy. *The Astrophysical Journal*, 861(2):134, July 2018.

[2] VERITAS collaboration, E Aliu, T Arlen, et al. Detection of pulsed gamma rays above 100 GeV from the Crab pulsar. *Science*, 334(6052):69–72, 2011.

[3] I. F. Mirabel. Very energetic γ-rays from microquasars and binary pulsars. *Science*, 312(5781):1759–1760, 2006.

[4] H. Abdalla, R. Adam, F. Aharonian, et al. A very-high-energy component deep in the γ-ray burst afterglow. *Nature*, 575(7783):464–467, November 2019.

[5] Mathieu de Naurois and Daniel Mazin. Ground-based detectors in very-high-energy gamma-ray astronomy. *Comptes Rendus Physique*, 16(6-7):610–627, August 2015.

[6] Gernot Maier. The origin of cosmic rays and TeV gamma-ray astronomy. *EPJ Web of Conferences*, 52:10001, 2013.

[7] Jamie Holder. Atmospheric Cherenkov Gamma-ray Telescopes. *arXiv e-prints*, page arXiv:1510.05675, October 2015.

[8] F. Schmidt and J. Knapp. Corsika shower images, 2005. Available at: https://www-zeuthen.desy.de/~jknapp/fs/showerimages.html [Accessed: 2024-09-23].

[9] F Aharonian, J Buckley, T Kifune, and G Sinnis. High energy astrophysics with ground-based gamma ray detectors. *Reports on Progress in Physics*, 71(9):096901, August 2008.

[10] K. Tayabaly, D. Spiga, R. Canestrari, et al. Roughness tolerances for Cherenkov telescope mirrors. In Stephen L. O'Dell and Giovanni Pareschi, editors, *Optics for EUV, X-Ray, and Gamma-Ray Astronomy VII*. SPIE, September 2015.

[11] A. McCann, D. Hanna, J. Kildea, and M. McCutcheon. A new mirror alignment system for the VERITAS telescopes. *Astroparticle Physics*, 32(6):325–329, January 2010.

[12] D. B. Kieda. The gamma ray detection sensitivity of the upgraded VERITAS Observatory. In *International Cosmic Ray Conference*, volume 33 of *International Cosmic Ray Conference*, page 1124, January 2013.

[13] Hamamatsu Photonics K. K. *Photomultiplier Tubes: Basics and Applications*, 3a edition, 2007.

[14] A.N. Otte. The upgrade of VERITAS with high efficiency photomultipliers. In *Proceedings of the 32nd ICRC*, International Cosmic Ray Conference, January 2011.

[15] A. Weinstein. The VERITAS trigger system. In *International Cosmic Ray Conference*, volume 3 of *International Cosmic Ray Conference*, pages 1539–1542, January 2008.

[16] David Hanna. Calibration techniques for VERITAS. In *30th International Cosmic Ray Conference*, volume 3, pages 1417–1420, 7 2007.

[17] J. Holder. Exploiting VERITAS timing information. In *29th International Cosmic Ray Conference (ICRC29), Volume 5*, volume 5 of *International Cosmic Ray Conference*, page 383, January 2005.

[18] M. Wood, G. Blaylock, S. M. Bradbury, et al. A search for dark matter annihilation with the Whipple 10 m telescope. *The Astrophysical Journal*, 678(2):594, May 2008.

[19] M. Chernyakova, A. A. Abdo, A. Neronov, et al. Multiwavelength observations of the binary system PSR B1259-63/LS 2883 around the 2010-2011 periastron passage. *Monthly Notices of the Royal Astronomical Society*, 439(1):432–445, January 2014.

[20] H. Abdalla, R. Adam, F. Aharonian, et al. H.E.S.S. and Fermi-LAT observations of PSR B1259–63/LS 2883 during its 2014 and 2017 periastron passages. *Astronomy & Astrophysics*, 633:A102, January 2020.

[21] F. Aharonian, A. G. Akhperjanian, A. R. Bazer-Bachi, et al. 3.9 day orbital modulation in the TeV γ-ray flux and spectrum from the X-ray binary LS 5039. *Astronomy and Astrophysics*, 460(3):743–749, December 2006.

[22] S. Archambault, A. Archer, T. Aune, et al. Exceptionally bright TeV flares from the binary LS I +61 303. *The Astrophysical Journal Letters*, 817(1):L7, January 2016.

[23] M. L. Ahnen, S. Ansoldi, L. A. Antonelli, et al. Super-orbital variability of LS I +61°303 at TeV energies. *Astronomy & Astrophysics*, 591:A76, June 2016.

[24] G. Maier, O. Blanch, D. Hadasch, et al. Long-term gamma-ray observations of the binary HESS J0632+057 with H.E.S.S., MAGIC and VERITAS. In *36th International Cosmic Ray Conference (ICRC2019)*, volume 36 of *International Cosmic Ray Conference*, page 732, July 2019.

[25] H. E. S. S. Collaboration, A. Abramowski, F. Aharonian, et al. Discovery of variable VHE γ-ray emission from the binary system 1FGL J1018.6-5856. *Astronomy & Astrophysics*, 577:A131, May 2015.

[26] N. Komin, M. Haupt, and H. E. S. S. Collaboration. Discovery of VHE gamma-ray emission from the binary system LMC P3. In *35th International Cosmic Ray Conference (ICRC2017)*, volume 301 of *International Cosmic Ray Conference*, page 730, January 2017.

[27] Guillaume Dubus. Gamma-ray binaries and related systems. *The Astronomy and Astrophysics Review*, 21(1), August 2013.

[28] J. Takata, P. H. T. Tam, C. W. Ng, et al. High-energy emissions from the pulsar/Be binary system PSR J2032+4127/MT91 213. *The Astrophysical Journal*, 836(2):241, February 2017.

[29] K. L. Li, J. Takata, C. W. Ng, et al. The X-ray modulation of PSR J2032+4127/MT91 213 during the periastron passage in 2017. *The Astrophysical Journal*, 857(2):123, April 2018.

[30] A. U. Abeysekara, W. Benbow, R. Bird, et al. Periastron Observations of TeV Gamma-Ray Emission from a Binary System with a 50-year Period. *Astrophys. J.*, 867(1):L19, 2018.

[31] E. Aliu, T. Aune, B. Behera, et al. Observations of the unidentified gamma-ray source TeV J 2032+4130 by VERITAS. *The Astrophysical Journal*, 783(1):16, February 2014.

[32] M J Coe, A T Okazaki, I A Steele, et al. The semicentennial binary system PSR J2032+4127 at periastron: X-ray photometry, optical spectroscopy, and SPH modelling. *Monthly Notices of the Royal Astronomical Society*, 485(2):1864–1875, 02 2019.

[33] M Chernyakova, D Malyshev, P Blay, B van Soelen, and S Tsygankov. Multi-wavelength observations of PSR J2032+4127 during the 2017 periastron passage. *Monthly Notices of the Royal Astronomical Society*, May 2020.

[34] Cherenkov Telescope Array. https://www.cta-observatory.org.

[35] Victor F. Hess. Über Beobachtungen der durchdringenden Strahlung bei sieben Freiballonfahrten. *Phys. Z.*, 13:1084–1091, 1912.

[36] Thomas K. Gaisser. *Cosmic Rays and Particle Physics*. Cambridge University Press, 1991.

[37] R. L. Workman and Others. Review of particle physics. *PTEP*, 2022:083C01, 2022.

[38] Luke O'C Drury. Origin of cosmic rays. *Astroparticle Physics*, 39:52–60, 2012.

[39] M. Ackermann, M. Ajello, W. B. Atwood, et al. *Fermi*-LAT observations of the diffuse γ-ray emission: Implications for cosmic rays and the interstellar medium. *The Astrophysical Journal*, 750(1):3, April 2012.

[40] P Sreekumar, DL Bertsch, BL Dingus, et al. Constraints on the cosmic rays in the Small Magellanic Cloud. *Physical review letters*, 70(2):127, 1993.

[41] Abdo, A. A., Ackermann, M., Ajello, M., et al. Detection of the Small Magellanic Cloud in gamma-rays with Fermi/LAT. *A&A*, 523:A46, 2010.

[42] GV Kulikov and GB Khristiansen. On the size spectrum of extensive air showers. *Sov. Phys. JETP*, 35(8):441–444, 1959.

[43] S.P. Swordy, L.F. Fortson, J. Hinton, et al. The composition of cosmic rays at the knee. *Astroparticle Physics*, 18(2):129–150, 2002.

[44] WD Apel, JC Arteaga-Velàzquez, K Bekk, et al. Ankle-like feature in the energy spectrum of light elements of cosmic rays observed with KASCADE-Grande. *Physical Review D*, 87(8):081101, 2013.

[45] Karl-Heinz Kampert. Cosmic rays from the knee to the ankle–status and prospects. *Nuclear Physics B-Proceedings Supplements*, 165:294–306, 2007.

[46] W. Baade and F. Zwicky. Cosmic rays from super-novae. *Contributions from the Mount Wilson Observatory*, 3:79–83, January 1934.

[47] AW Strong, TA Porter, SW Digel, et al. Global cosmic-ray-related luminosity and energy budget of the Milky Way. *The Astrophysical Journal Letters*, 722(1):L58, 2010.

[48] Daniel Kasen and SE Woosley. Type II supernovae: model light curves and standard candle relationships. *The Astrophysical Journal*, 703(2):2205, 2009.

[49] G. A. Tammann, W. Loeffler, and A. Schroeder. The galactic supernova rate. *The Astrophysical Journal Supplemental Series*, 92:487, June 1994.

[50] Anthony M Hillas. The origin of ultra-high-energy cosmic rays. *Annual review of Astronomy and Astrophysics*, 22(1):425–444, 1984.

[51] M. J. Hardcastle. Which radio galaxies can make the highest energy cosmic rays? *Monthly Notices of the Royal Astronomical Society*, 405(4):2810–2816, 07 2010.

[52] Enrico Fermi. On the origin of the cosmic radiation. *Phys. Rev.*, 75:1169–1174, April 1949.

[53] Malcolm S. Longair. *High Energy Astrophysics*. Cambridge University Press, 2011.

[54] WI Axford, E Leer, and G Skadron. The acceleration of cosmic rays by shock waves. In *International Cosmic Ray Conference*, volume 11. Springer, 1977.

[55] GF Krymskii. A regular mechanism for the acceleration of charged particles on the front of a shock wave. In *Akademiia Nauk SSSR Doklady*, volume 234, pages 1306–1308, 1977.

[56] AR Bell. The acceleration of cosmic rays in shock fronts–I. *Monthly Notices of the Royal Astronomical Society*, 182(2):147–156, 1978.

[57] Roger D Blandford and James P Ostriker. Particle acceleration by astrophysical shocks. *Astrophysical Journal, Part 2-Letters to the Editor, vol. 221, Apr. 1, 1978, p. L29-L32.*, 221:L29–L32, 1978.

[58] S. P. Reynolds. Supernova remnants at high energy. *Annual Review of Astronomy and Astrophysics*, 46:89–126, September 2008.

[59] George R. Blumenthal and Robert J. Gould. Bremsstrahlung, synchrotron radiation, and compton scattering of high-energy electrons traversing dilute gases. *Rev. Mod. Phys.*, 42:237–270, April 1970.

[60] Arthur H. Compton. A quantum theory of the scattering of X-rays by light elements. *Phys. Rev.*, 21:483–502, May 1923.

[61] Felix A Aharonian, Lars Bergström, Charles Dermer, and Roland Walter. *Astrophysics at Very High Energies*. Springer, 2013.

[62] Armin Rest, DL Welch, NB Suntzeff, et al. Scattered-light echoes from the historical galactic supernovae cassiopeia a and tycho (sn 1572). *The Astrophysical Journal*, 681(2):L81, 2008.

[63] Kate Scholberg. Supernova neutrino detection. *Annual Review of Nuclear and Particle Science*, 62:81–103, 2012.

[64] S. P. Wakely and D. Horan. TeVCat: An online catalog for Very High Energy Gamma-Ray Astronomy. In *International Cosmic Ray Conference*, volume 3 of *International Cosmic Ray Conference*, pages 1341–1344, January 2008.

[65] Jacco Vink. *Physics and Evolution of Supernova Remnants*. Springer, 2020.

[66] H. J. Völk, E. G. Berezhko, and L. T. Ksenofontov. Magnetic field amplification in Tycho and other shell-type supernova remnants. *Astronomy & Astrophysics*, 433(1):229–240, April 2005.

[67] Markus Ackermann, Marco Ajello, A Allafort, et al. Detection of the characteristic pion-decay signature in supernova remnants. *Science*, 339(6121):807–811, 2013.

[68] AU Abeysekara, A Archer, W Benbow, et al. Evidence for proton acceleration up to TeV energies based on VERITAS and Fermi-LAT observations of the Cas A SNR. *The Astrophysical Journal*, 894(1):51, 2020.

[69] Ke Fang, Matthew Kerr, Roger Blandford, Henrike Fleischhack, and Eric Charles. Evidence for PeV proton acceleration from *Fermi*-LAT observations of SNR G 106.3+ 2.7. *Physical Review Letters*, 129(7):071101, 2022.

[70] MAGIC Collaboration, H. Abe, S. Abe, et al. MAGIC observations provide compelling evidence of hadronic multi-TeV emission from the putative PeVatron SNR G106.3+2.7. *Astronomy & Astrophysics*, 671:A12, March 2023.

[71] Zhen Cao, F Aharonian, Q An, et al. The first LHAASO catalog of gamma-ray sources. *The Astrophysical Journal Supplement Series*, 271(1):25, 2024.

[72] J. Chadwick. The existence of a neutron. *Proceedings of the Royal Society of London. Series A, Containing Papers of a Mathematical and Physical Character*, 136(830):692–708, 1932.

[73] J. R. Oppenheimer and G. M. Volkoff. On massive neutron cores. *Phys. Rev.*, 55:374–381, February 1939.

[74] A. Hewish, S. J. Bell, J. D. H. Pilkington, P. F. Scott, and R. A. Collins. Observation of a rapidly pulsating radio source. *Nature*, 217(5130):709–713, February 1968.

[75] Franco Pacini. Energy emission from a neutron star. *Nature*, 216(5115):567–568, 1967.

[76] Victor A Acciari, S Ansoldi, LA Antonelli, et al. Detection of the Geminga pulsar with MAGIC hints at a power-law tail emission beyond 15 GeV. *Astronomy & Astrophysics*, 643:L14, 2020.

[77] M. Spir-Jacob, A. Djannati-Ataï, L. Mohrmann, et al. Detection of sub-100 GeV gamma-ray pulsations from PSR B1706-44 with H.E.S.S. In *36th International Cosmic Ray Conference*, 8 2019.

[78] H. E. S. S. Collaboration, H. Abdalla, A. Abramowski, et al. The H.E.S.S. Galactic plane survey. *Astronomy & Astrophysics*, 612:A1, April 2018.

[79] *Neutron Stars and Pulsars*, volume 357 of *Astrophysics and Space Science Library*, January 2009.

[80] T. C. Weekes, M. F. Cawley, D. J. Fegan, et al. Observation of TeV gamma rays from the Crab Nebula using the Atmospheric Cherenkov Imaging Technique. *The Astrophysical Journal*, 342:379, July 1989.

[81] H. E. S. S. Collaboration, F. Aharonian, F. Ait Benkhali, et al. Time-resolved hadronic particle acceleration in the recurrent nova RS Ophiuchi. *Science*, 376(6588):77–80, April 2022.

[82] H. E. S. S. Collaboration, H. Abdalla, R. Adam, et al. Detection of very-high-energy γ-ray emission from the colliding wind binary η Car with H.E.S.S. *Astronomy & Astrophysics*, 635:A167, March 2020.

[83] F. Brun, M. de Naurois, W. Hofmann, et al. Discovery of VHE gamma-ray emission from the W49 region with H.E.S.S. In Frank M. Rieger, Christopher van Eldik, and Werner Hofmann, editors, *25th Texas Symposium on Relativistic Astrophysics*, page 201, January 2010.

[84] H. E. S. S. Collaboration, A. Abramowski, F. Acero, et al. Very-high-energy gamma-ray emission from the direction of the Galactic globular cluster Terzan 5. *Astronomy & Astrophysics*, 531:L18, July 2011.

[85] H Abdalla, A Abramowski, F Aharonian, et al. Characterising the VHE diffuse emission in the central 200 parsecs of our Galaxy with HESS. *Astronomy & Astrophysics*, 612:A9, 2018.

[86] Henric Krawczynski and Ezequiel Treister. Active galactic nuclei — the physics of individual sources and the cosmic history of formation and evolution. *Frontiers of Physics*, 8(6):609–629, December 2013.

[87] Grzegorz (Greg) Madejski and Marek Sikora. Gamma-ray observations of active galactic nuclei. *Annual Review of Astronomy and Astrophysics*, 54:725–760, September 2016.

[88] Matteo Cerruti. Leptonic and hadronic radiative processes in supermassive-black-hole jets. *Galaxies*, 8(4), 2020.

[89] C. Megan Urry and Paolo Padovani. Unified schemes for radio-loud active galactic nuclei. *Publications of the Astronomical Society of the Pacific*, 107:803, September 1995.

[90] P. Mészáros. Gamma-ray bursts. *Reports on Progress in Physics*, 69(8):2259–2321, August 2006.

[91] Xiang-Yu Wang, Ruo-Yu Liu, Hai-Ming Zhang, Shao-Qiang Xi, and Bing Zhang. Synchrotron self-compton emission from external shocks as the origin of the sub-TeV emission in GRB 180720B and GRB 190114C. *The Astrophysical Journal*, 884(2):117, October 2019.

[92] MAGIC Collaboration, V. A. Acciari, S. Ansoldi, et al. Teraelectronvolt emission from the γ-ray burst GRB 190114C. *Nature*, 575(7783):455–458, November 2019.

[93] H.E.S.S. Collaboration, H. Abdalla, F. Aharonian, et al. Revealing X-ray and gamma ray temporal and spectral similarities in the GRB 190829A afterglow. *Science*, 372(6546):1081–1085, 2021.

[94] H Abe, S Abe, VA Acciari, et al. MAGIC detection of GRB 201216C at z= 1.1. *Monthly Notices of the Royal Astronomical Society*, 527(3):5856–5867, 2024.

[95] Yong Huang, Shicong Hu, Songzhan Chen, et al. LHAASO observed GRB 221009A with more than 5000 VHE photons up to around 18 TeV. *GRB Coordinates Network*, 32677:1, October 2022.

[96] F. Acero, F. Aharonian, A. G. Akhperjanian, et al. Detection of gamma rays from a starburst galaxy. *Science*, 326(5956):1080, November 2009.

[97] VERITAS Collaboration, V. A. Acciari, E. Aliu, et al. A connection between star formation activity and cosmic rays in the starburst galaxy M82. *Nature*, 462(7274):770–772, December 2009.

[98] Chia-Chun Lu, Felix Aharonian, Francois Brun, et al. H.E.S.S. observations of the Large Magellanic Cloud. In *AAS/High Energy Astrophysics Division #14*, volume 14 of *AAS/High Energy Astrophysics Division*, page 403.05, August 2014.

[99] W. Galbraith and J. V. Jelley. Light pulses from the night sky associated with cosmic rays. *Nature*, 171(4347):349–350, February 1953.

[100] Michael Punch, Carl W Akerlof, Michael F Cawley, et al. Detection of TeV photons from the active galaxy Markarian 421. *Nature*, 358(6386):477–478, 1992.

[101] J. Quinn, C. W. Akerlof, S. Biller, et al. Detection of gamma rays with $E > 300$ GeV from Markarian 501. *The Astrophysical Journal Letters*, 456:L83, January 1996.

[102] A. Daum, G. Hermann, and HEGRA Collaboration. The Stereoscopic System of Imaging Atmospheric Cherenkov Telescopes of the HEGRA-Collaboration. In *International Cosmic Ray Conference*, volume 5 of *International Cosmic Ray Conference*, page 117, January 1997.

[103] G Pühlhofer, O Bolz, N Götting, et al. The technical performance of the HEGRA system of imaging air Cherenkov telescopes. *Astroparticle Physics*, 20(3):267–291, 2003.

[104] F Aharonian, A Akhperjanian, J Barrio, et al. Evidence for TeV gamma ray emission from Cassiopeia A. *Astronomy & Astrophysics*, 370(1):112–120, 2001.

[105] F. Aharonian, A. Akhperjanian, M. Beilicke, et al. An unidentified TeV source in the vicinity of Cygnus OB2. *Astronomy and Astrophysics*, 393:L37–L40, October 2002.

[106] F Aharonian, A Akhperjanian, M Beilicke, et al. Is the giant radio galaxy M 87 a TeV gamma-ray emitter? *Astronomy & Astrophysics*, 403(1):L1–L5, 2003.

[107] Mathieu De Naurois. The HESS experiment: Current status and future prospects. In *36th international cosmic ray conference (ICRC2019)*, volume 36, page 656, 2019.

[108] Jelena Aleksić, Stefano Ansoldi, Lucio Angelo Antonelli, et al. The major upgrade of the MAGIC telescopes, Part I: The hardware improvements and the commissioning of the system. *Astroparticle Physics*, 72:61–75, 2016.

[109] Nahee Park. Performance of the VERITAS experiment. In *Proceedings of The 34th International Cosmic Ray Conference — PoS(ICRC2015)*. Sissa Medialab, August 2016.

[110] C. van Eldik, M. Holler, D. Berge, et al. Observations of the Crab Nebula with H.E.S.S. Phase II. In *34th International Cosmic Ray Conference (ICRC2015)*, volume 34 of *International Cosmic Ray Conference*, page 847, July 2015.

[111] R.W. Springer. The High Altitude Water Cherenkov (HAWC) Observatory. *Nuclear and Particle Physics Proceedings*, 279-281:87–94, 2016. Proceedings of the 9th Cosmic Ray International Seminar.

[112] V. Schonfelder, R. Diehl, G. G. Lichti, et al. The imaging compton telescope COMPTEL on the Gamma Ray Observatory. *IEEE Transactions on Nuclear Science*, 31(1):766–770, 1984.

[113] Jeremy Perkins and Amego Team. All-Sky Medium Energy Gamma-ray Observatory (AMEGO) - A discovery mission for the MeV gamma-ray band. In *APS April Meeting Abstracts*, volume 2018 of *APS Meeting Abstracts*, page H16.001, January 2018.

[114] David J. Thompson. Space detectors for gamma rays (100 MeV–100 GeV): From EGRET to Fermi-LAT. *Comptes Rendus Physique*, 16(6-7):600–609, August 2015.

[115] W. B. Atwood, A. A. Abdo, M. Ackermann, et al. The Large Area Telescope on the Fermi Gamma-Ray Space Telescope Mission. *The Astrophysical Journal*, 697(2):1071–1102, May 2009.

[116] M Ajello, WB Atwood, L Baldini, et al. 3FHL: The third catalog of hard Fermi-LAT sources. *The Astrophysical Journal Supplement Series*, 232(2):18, 2017.

[117] Trevor C. Weekes. *Very high energy gamma-ray astronomy*. Institute of Physics Pub., 2003.

[118] Walter.1904 Heitler. *Quantum theory of radiation*. Dover Publications, 1954.

[119] Oliver Heaviside. On the electromagnetic effects due to the motion of electrification through a dielectric. *The London, Edinburgh, and Dublin Philosophical Magazine and Journal of Science*, 27(167):324–339, April 1889.

[120] P.A. Cerenkov. Visible emission of clean liquids by action of γ radiation. *Doklady Akad. Nauk SSSR*, 2:451, 1934.

[121] IE Tamm and IM Frank. Coherent radiation of fast electrons in a medium. In *Dokl. Akad. Nauk SSSR*, volume 14, pages 107–112, 1937.

[122] A M Hillas. The sensitivity of Cherenkov radiation pulses to the longitudinal development of cosmic-ray showers. *Journal of Physics G: Nuclear Physics*, 8(10):1475–1492, October 1982.

[123] M. Heß, K. Bernlöhr, A. Daum, et al. The time structure of Cherenkov images generated by TeV γ-rays and by cosmic rays. *Astroparticle Physics*, 11(3):363 – 377, 1999.

[124] Peter K. F. Grieder. *Exentsive Air Showers and High Energy Phenomena*. Springer Berlin Heidelberg, 2010.

[125] Maurizio Spurio. *Particles and Astrophysics*. Springer International Publishing, 2015.

[126] J. Matthews. A Heitler model of extensive air showers. *Astroparticle Physics*, 22(5-6):387–397, January 2005.

[127] Dennis Sivers, Stanley J. Brodsky, and Richard Blankenbecler. Large transverse momentum processes. *Physics Reports*, 23(1):1–121, January 1976.

[128] Andrew J. Smith. The MILAGRO Gamma Ray Observatory. In *29th International Cosmic Ray Conference (ICRC29), Volume 10*, volume 10 of *International Cosmic Ray Conference*, page 227, January 2005.

[129] Paolo Montini, ARGO-YBJ collaboration, et al. Cosmic ray physics with ARGO-YBJ. *Nuclear and particle physics proceedings*, 279:7–14, 2016.

[130] Michihiro Amenomori, XJ Bi, D Chen, et al. Tibet air shower array: results and future plan. In *Journal of Physics: Conference Series*, volume 120, page 062024. IOP Publishing, 2008.

[131] E. Roache, R. Irvin, J. S. Perkins, et al. Mirror facets for the VERITAS telescopes. In *International Cosmic Ray Conference*, volume 3 of *International Cosmic Ray Conference*, pages 1397–1400, January 2008.

[132] E. Gazda, T. Nguyen, N. Otte, and G. Richards. Photon detection efficiency measurements of the VERITAS Cherenkov telescope photomultipliers after four years of operation. *Journal of Instrumentation*, 11(11):P11015–P11015, November 2016.

[133] A.M. Hillas. Cherenkov light images of EAS produced by primary gamma rays and by nuclei. In *19th International Cosmic Ray Conference (ICRC19), Volume 3*, volume 3 of *International Cosmic Ray Conference*, page 445, August 1985.

[134] John M. Davies and Eugene S. Cotton. Design of the quartermaster solar furnace. *Solar Energy*, 1(2):16 – 22, 1957.

[135] Simon Archambault, Sean Griffin, and David Hanna. In-situ measurements of whole-dish reflectivity for VERITAS. In *International Cosmic Ray Conference*, volume 33 of *International Cosmic Ray Conference*, page 2878, January 2013.

[136] T.C Weekes, H Badran, S.D Biller, et al. VERITAS: the Very Energetic Radiation Imaging Telescope Array System. *Astroparticle Physics*, 17(2):221 – 243, 2002.

[137] F. Krennrich, I.H. Bond, P.J. Boyle, et al. VERITAS: the Very Energetic Radiation Imaging Telescope Array System. *New Astronomy Reviews*, 48(5-6):345–349, April 2004.

[138] Scott Tyler Griffiths. *Exploring the limits of Lorentz invariance with VERITAS gamma-ray observations of Markarian 421.* PhD thesis, University of Iowa, 2015.

[139] Tomoyuki Nagai, R. McKay, G. Sleege, and D. Petry. Focal plane instrumentation of VERITAS. In *30th International Cosmic Ray Conference*, volume 3, pages 1437–1440, 7 2007.

[140] J. Hall, V. V. Vassiliev, D. B. Kieda, et al. VERITAS CFDs. In *International Cosmic Ray Conference*, volume 5 of *International Cosmic Ray Conference*, page 2851, July 2003.

[141] S.M Bradbury and H.J Rose. Pattern recognition trigger electronics for an Imaging Atmospheric Cherenkov Telescope. *Nuclear Instruments and Methods in Physics Research Section A: Accelerators, Spectrometers, Detectors and Associated Equipment*, 481(1):521 – 528, 2002.

[142] Benjamin Zitzer and VERITAS Collaboration. The VERITAS upgraded telescope-level trigger systems: Technical details and performance characterization. In *International Cosmic Ray Conference*, volume 33 of *International Cosmic Ray Conference*, page 3076, January 2013.

[143] D. Hanna, A. McCann, M. McCutcheon, and L. Nikkinen. An LED-based flasher system for VERITAS. *Nuclear Instruments and Methods in Physics Research Section A: Accelerators, Spectrometers, Detectors and Associated Equipment*, 612(2):278–287, January 2010.

[144] R. J. White, H. J. Rose, S. M. Bradbury, M. Daniel, and P. Marshall. The VERITAS digital asynchronous transceiver. In *International Cosmic Ray Conference*, volume 3 of *International Cosmic Ray Conference*, pages 1527–1530, January 2008.

[145] P. F. Rebillot, J. H. Buckley, P. Dowkontt, and K. Kosack. The VERITAS flash ADC electronics system. In *International Cosmic Ray Conference*, volume 5 of *International Cosmic Ray Conference*, page 2827, July 2003.

[146] Elizabeth Hays. VERITAS data acquisition. In *30th International Cosmic Ray Conference*, volume 3, pages 1543–1546, 7 2007.

[147] Jeremy S. Perkins, G. Maier, and VERITAS Collaboration. VERITAS Telescope 1 relocation: Details and improvements. In *AAS/High Energy Astrophysics Division #11*, volume 11 of *AAS/High Energy Astrophysics Division*, page 39.04, March 2010.

[148] D. Hanna, A. McCann, M. McCutcheon, and L. Nikkinen. An LED-based flasher system for VERITAS. *Nuclear Instruments and Methods in Physics Research Section A: Accelerators, Spectrometers, Detectors and Associated Equipment*, 612(2):278–287, 2010.

[149] A. Kohnle, F. Aharonian, A. Akhperjanian, et al. Stereoscopic imaging of air showers with the first two HEGRA Cherenkov telescopes. *Astroparticle Physics*, 5(2):119–131, 1996.

[150] D. Heck and Forschungszentrum Karlsruhe. Technik und Umwelt. *CORSIKA : a Monte Carlo code to simulate extensive air showers.* Wissenschaftliche Berichte, FZKA 6019. Forschungszentrum Karlsruhe, Karlsruhe, 1998.

[151] Gernot Maier. Monte Carlo studies of the VERITAS array of Cherenkov telescopes. In *International Cosmic Ray Conference*, volume 3 of *International Cosmic Ray Conference*, pages 1413–1416, January 2008.

[152] Kneizys. F. X. The MODTRAN 2/3 report and LOWTRAN 7 model. *PL/GPOS*, 261, 1996.

[153] H. Krawczynski, D.A. Carter-Lewis, C. Duke, et al. Gamma–hadron separation methods for the VERITAS array of four imaging atmospheric cherenkov telescopes. *Astroparticle Physics*, 25(6):380–390, 2006.

[154] M. K. Daniel. The VERITAS standard data analysis. In *International Cosmic Ray Conference*, volume 3 of *International Cosmic Ray Conference*, pages 1325–1328, January 2008.

[155] Maria Krause, Elisa Pueschel, and Gernot Maier. Improved γ/hadron separation for the detection of faint γ-ray sources using boosted decision trees. *Astroparticle Physics*, 89:1–9, 2017.

[156] T. P. Li and Y. Q. Ma. Analysis methods for results in gamma-ray astronomy. *The Astrophysical Journal*, 272:317–324, September 1983.

[157] V. P. Fomin, A. A. Stepanian, R. C. Lamb, et al. New methods of atmospheric Cherenkov imaging for gamma-ray astronomy. I. The false source method. *Astroparticle Physics*, 2(2):137–150, May 1994.

[158] D. Berge, S. Funk, and J. Hinton. Background modelling in very-high-energy γ-ray astronomy. *Astronomy and Astrophysics*, 466(3):1219–1229, May 2007.

[159] S. S. Wilks. The large-sample distribution of the likelihood ratio for testing composite hypotheses. *The Annals of Mathematical Statistics*, 9(1):60 – 62, 1938.

[160] Guillaume Dubus, Nicolas Guillard, Pierre-Olivier Petrucci, and Pierrick Martin. Sizing up the population of gamma-ray binaries. *Astronomy & Astrophysics*, 608:A59, December 2017.

[161] The Fermi LAT Collaboration, A. A. Abdo, M. Ackermann, et al. Modulated high-energy gamma-ray emission from the microquasar Cygnus X-3. *Science*, 326(5959):1512–1516, 2009.

[162] P M Chadwick, T J L McComb, and K E Turver. Very high energy gamma rays from X-ray binary pulsars. *Journal of Physics G: Nuclear and Particle Physics*, 16(12):1773–1803, December 1990.

[163] Trevor C. Weekes. Tev radiation from Galactic sources. *Space Science Reviews*, 59(3-4):315–364, February 1992.

[164] Rene A. Ong. Very high-energy gamma-ray astronomy. *Physics Reports*, 305(3):93–202, 1998.

[165] J C A Miller-Jones, A T Deller, R M Shannon, et al. The geometric distance and binary orbit of PSR B1259–63. *Monthly Notices of the Royal Astronomical Society*, 479(4):4849–4860, July 2018.

[166] J. Casares, M. Ribo, I. Ribas, et al. A possible black hole in the γ-ray microquasar LS 5039. *Monthly Notices of the Royal Astronomical Society*, 364(3):899–908, December 2005.

[167] Christina Aragona, M. Virginia McSwain, Erika D. Grundstrom, et al. The orbits of the γ-ray binaries LS I +61 303 and LS 5039. *The Astrophysical Journal*, 698(1):514–518, May 2009.

[168] D. A. Frail and R. M. Hjellming. Distance and total column density to the periodic radio star LSI+61 303. *The Astronomical Journal*, 101:2126, June 1991.

[169] J. Casares, M. Ribó, I. Ribas, et al. On the binary nature of the γ-ray sources AGL J2241+4454 (= MWC 656) and HESS J0632+057 (= MWC 148). *Monthly Notices of the Royal Astronomical Society*, 421(2):1103–1112, April 2012.

[170] Yuki Moritani, Takafumi Kawano, Sho Chimasu, et al. Orbital solution leading to an acceptable interpretation for the enigmatic gamma-ray binary HESS J0632+057. *Publications of the Astronomical Society of Japan*, 70(4):61, August 2018.

[171] I. M. Monageng, V. A. McBride, L. J. Townsend, et al. The orbit of the gamma-ray binary 1FGL J1018.6-5856. *The Astrophysical Journal*, 847(1):68, September 2017.

[172] Vanessa J. Napoli, M. Virginia McSwain, Amber N. Marsh Boyer, and Rachael M. Roettenbacher. The distance of the γ-ray binary 1FGL J1018.6-5856. *Publications of the Astronomical Society of the Pacific*, 123(909):1262, November 2011.

[173] B van Soelen, N Komin, A Kniazev, and P Väisänen. The orbital parameters of the gamma-ray binary LMC P3. *Monthly Notices of the Royal Astronomical Society*, 484(3):4347–4351, January 2019.

[174] Wynn C G Ho, C.-Y Ng, Andrew G Lyne, et al. Multiwavelength monitoring and X-ray brightening of Be X-ray binary PSR J2032+4127/MT91 213 on its approach to periastron. *MNRAS*, 000:1–9, 2016.

[175] Simon Johnston, R. N. Manchester, A. G. Lyne, et al. PSR 1259-63 - a binary radio pulsar with a Be star companion. *The Astrophysical Journal*, 387:L37, March 1992.

[176] Ignacio Negueruela, Marc Ribó, Artemio Herrero, et al. Astrophysical parameters of LS 2883 and implications for the PSR B1259-63 gamma-ray binary. *The Astrophysical Journal*, 732(1):L11, April 2011.

[177] C. B. Stephenson and N. Sanduleak. Luminous stars in the Southern Milky Way. *Publications of the Warner & Swasey Observatory*, 1:1, January 1971.

[178] R. M. Shannon, S. Johnston, and R. N. Manchester. The kinematics and orbital dynamics of the PSR B1259-63/LS 2883 system from 23 yr of pulsar timing. *Monthly Notices of the Royal Astronomical Society*, 437(4):3255–3264, December 2013.

[179] F. Aharonian, A. G. Akhperjanian, K.-M. Aye, et al. Discovery of the binary pulsar PSR B1259-63 in very-high-energy gamma rays around periastron with HESS. *Astronomy & Astrophysics*, 442(1):1–10, September 2005.

[180] F. Aharonian, A. G. Akhperjanian, G. Anton, et al. Very high energy γ-ray observations of the binary PSR B1259–63/SS2883 around the 2007 periastron. *Astronomy & Astrophysics*, 507(1):389–396, September 2009.

[181] A. Abramowski, F. Acero, F. Aharonian, et al. H.E.S.S. observations of the binary system PSR B1259-63/LS 2883 around the 2010/2011 periastron passage. *Astronomy & Astrophysics*, 551:A94, March 2013.

[182] A. A. Abdo, M. Ackermann, M. Ajello, et al. Discovery of high-energy gamma-ray emission from the binary system PSR B1259-63/LS 2883 around periastron with Fermi. *Astrophysical Journal Letters*, 736(1):L11, July 2011.

[183] P. H. T. Tam, R. H. H. Huang, J. Takata, et al. Discovery of GeV γ-ray emission from PSR B1259-63/LS 2883. *The Astrophysical Journal*, 736(1):L10, June 2011.

[184] G. A. Caliandro, C. C. Cheung, J. Li, et al. Gamma-ray flare activity from PSR B1259-63 during 2014 periastron passage and comparison to its 2010 passage. *Astrophysical Journals*, 811(1):68, September 2015.

[185] P. H. T. Tam, X.-B. He, P. S. Pal, and Yudong Cui. The hour-timescale GeV flares of PSR B1259–63 in 2017. *The Astrophysical Journal*, 862(2):165, August 2018.

[186] T. J. Johnson, K. S. Wood, M. Kerr, et al. A luminous and highly variable gamma-ray flare following the 2017 periastron of PSR B1259-63/LS 2883. *The Astrophysical Journal*, 863(1):27, August 2018.

[187] Lynn Cominsky, Mallory Roberts, and Simon Johnston. Detection of X-ray emission from the PSR 1259-63/SS 2883 binary system. *The Astrophysical Journal*, 427:978, June 1994.

[188] M. Chernyakova, A. Neronov, A. Lutovinov, J. Rodriguez, and S. Johnston. XMM-Newton observations of PSR B1259-63 near the 2004 periastron passage. *Monthly Notices of the Royal Astronomical Society*, 367(3):1201–1208, April 2006.

[189] M. Chernyakova, A. Neronov, F. Aharonian, Y. Uchiyama, and T. Takahashi. X-ray observations of PSR B1259-63 near the 2007 periastron passage. *Monthly Notices of the Royal Astronomical Society*, 397(4):2123–2132, August 2009.

[190] M. Chernyakova, A. Neronov, B. van Soelen, et al. Multi-wavelength observations of the binary system PSR B1259-63/LS 2883 around the 2014 periastron passage. *Monthly Notices of the Royal Astronomical Society*, 454(2):1358–1370, 10 2015.

[191] George G. Pavlov, Chulhoon Chang, and Oleg Kargaltsev. Extended emission from the PSR B1259-63/SS 2883 binary detected with Chandra. *The Astrophysical Journal*, 730(1):2, February 2011.

[192] Jeremy Hare, Oleg Kargaltsev, George Pavlov, and Paz Beniamini. Evolution of the extended X-ray emission from the PSR B1259-63/LS 2883 binary in the 2014-2017 binary cycle. *The Astrophysical Journal*, 882(2):74, September 2019.

[193] Oleg Kargaltsev, George G. Pavlov, Martin Durant, Igor Volkov, and Jeremy Hare. The dynamic X-ray nebula powered by the pulsar B1259-63. *The Astrophysical Journal*, 784(2):124, March 2014.

[194] George G. Pavlov, Jeremy Hare, Oleg Kargaltsev, Blagoy Rangelov, and Martin Durant. An extended X-ray object ejected from the PSR B1259 –63/LS 2883 binary. *The Astrophysical Journal*, 806(2):192, June 2015.

[195] S. Johnston, L. Ball, N. Wang, and R. N. Manchester. Radio observations of PSR B1259-63 through the 2004 periastron passage. *Monthly Notices of the Royal Astronomical Society*, 358(3):1069–1075, April 2005.

[196] S. Johnston, R. N. Manchester, D. McConnell, and D. Campbell-Wilson. Transient radio emission from the PSR B1259-63 system near periastron. *Monthly Notices of the Royal Astronomical Society*, 302(2):277–287, January 1999.

[197] Javier Moldón, Simon Johnston, Marc Ribó, Josep M. Paredes, and Adam T. Deller. Discovery of extended and variable radio structure from the gamma-ray binary system PSR B1259-63/LS 2883. *The Astrophysical Journal*, 732(1):L10, April 2011.

[198] F. Aharonian. Discovery of very high energy gamma rays associated with an X-ray binary. *Science*, 309(5735):746–749, July 2005.

[199] A. A. Abdo, M. Ackermann, M. Ajello, et al. Fermi/LAT observations of LS 5039. *The Astrophysical Journal Letters*, 706(1):L56–L61, November 2009.

[200] D. Hadasch, D. F. Torres, T. Tanaka, et al. Long-term monitoring of the high-energy γ-ray emission from LS I $+61°303$ and LS 5039. *The Astrophysical Journal*, 749(1):54, April 2012.

[201] C. Motch, F. Haberl, K. Dennerl, M. Pakull, and E. Janot-Pacheco. New massive X-ray binary candidates from the ROSAT Galactic Plane Survey. I. Results from a cross-correlation with OB star catalogues. *Astronomy and Astrophysics*, 323:853–875, July 1997.

[202] Tadayuki Takahashi, Tetsuichi Kishishita, Yasunobu Uchiyama, et al. Study of the spectral and temporal characteristics of X-ray emission of the gamma-ray

binary LS 5039 with Suzaku. *The Astrophysical Journal*, 697(1):592–600, May 2009.

[203] Tetsuichi Kishishita, Takaaki Tanaka, Yasunobu Uchiyama, and Tadayuki Takahashi. Long-term stability of nonthermal X-ray modulation in the gamma-ray binary LS 5039. *The Astrophysical Journal*, 697(1):L1–L5, April 2009.

[204] A. Martocchia, C. Motch, and I. Negueruela. The low X-ray state of LS 5039 / RX J1826.2-1450. *Astronomy & Astrophysics*, 430(1):245–253, January 2005.

[205] A. D. Hoffmann, D. Klochkov, A. Santangelo, et al. INTEGRAL observation of hard X-ray variability of the TeV binary LS 5039/RX J1826.2-1450. *Astronomy & Astrophysics*, 494(3):L37–L40, January 2009.

[206] W. Collmar and S. Zhang. LS 5039 - the counterpart of the unidentified MeV source GRO J1823-12. *Astronomy & Astrophysics*, 565:A38, April 2014.

[207] Martin Durant, Oleg Kargaltsev, George G. Pavlov, Chulhoon Chang, and Gordon P. Garmire. Extended X-ray emission in the vicinity of the microquasar LS 5039: pulsar wind nebula? *The Astrophysical Journal*, 735(1):58, June 2011.

[208] N. Rea, D. F. Torres, G. A. Caliandro, et al. Deep chandra observations of TeV binaries - II. LS 5039. *Monthly Notices of the Royal Astronomical Society*, 416(2):1514–1521, July 2011.

[209] J. Marti, J. M. Paredes, and M. Ribo. The system LS 5039: a new massive radio emitting X-ray binary. *Astronomy & Astrophysics*, 338:L71–L74, October 1998.

[210] M. Ribó, P. Reig, J. Martí, and J. M. Paredes. X-ray and radio observations of RX J1826.2-1450/LS 5039. *Astronomy & Astrophysics*, 347:518–523, July 1999.

[211] J. Moldón, M. Ribó, and J. M. Paredes. Periodic morphological changes in the radio structure of the gamma-ray binary LS 5039. *Astronomy & Astrophysics*, 548:A103, November 2012.

[212] Sagar Godambe, Subir Bhattacharyya, Nilay Bhatt, and Manojendu Choudhury. Low-frequency radio spectrum and spectral turnover of LS 5039. *Monthly Notices of the Royal Astronomical Society: Letters*, 390(1):L43–L45, October 2008.

[213] Subir Bhattacharyya, Sagar Godambe, Nilay Bhatt, Abhas Mitra, and Manojendu Choudhury. Low-frequency radio spectrum of LS 5039 during periastron and apastron passages. *Monthly Notices of the Royal Astronomical Society: Letters*, 421(1):L1–L5, December 2011.

[214] J. Casares, I. Ribas, J. M. Paredes, J. Martí, and C. Allende Prieto. Orbital parameters of the microquasar LS I +61 303. *Monthly Notices of the Royal Astronomical Society*, 360(3):1105–1109, July 2005.

[215] M. Chernyakova, Iu. Babyk, D. Malyshev, et al. Study of orbital and superorbital variability of LSI +61° 303 with X-ray data. *Monthly Notices of the Royal Astronomical Society*, 470(2):1718–1728, May 2017.

[216] Shan-Shan Weng, Lei Qian, Bo-Jun Wang, et al. Radio pulsations from a neutron star within the gamma-ray binary LS I +61° 303. *Nature Astronomy*, 6:698–702, March 2022.

[217] J. Albert, E. Aliu, H. Anderhub, et al. Variable very-high-energy gamma-ray emission from the microquasar LS I +61 303. *Science*, 312(5781):1771–1773, June 2006.

[218] J. Albert, E. Aliu, H. Anderhub, et al. Periodic very high energy γ-ray emission from LS I +61°303 observed with the MAGIC telescope. *The Astrophysical Journal*, 693(1):303–310, March 2009.

[219] V. A. Acciari, M. Beilicke, G. Blaylock, et al. VERITAS observations of the γ-ray binary LS I +61 303. *The Astrophysical Journal*, 679(2):1427–1432, June 2008.

[220] Payel Kar. *High mass X-ray binaries at extreme energies with VERITAS*. PhD thesis, University of Utah, 2017.

[221] A. A. Abdo, M. Ackermann, M. Ajello, et al. Fermi LAT observations of LS I +61°303: First detection of an orbital modulation in GeV gamma rays. *Astrophysical Journal Letters*, 701(2):L123–L128, August 2009.

[222] L. Saha, V. R. Chitnis, A. Shukla, A. R. Rao, and B. S. Acharya. The multi-wavelength characteristics of the TeV binary LS I+61°303. *The Astrophysical Journal*, 823(2):134, May 2016.

[223] G. F. Bignami, P. A. Caraveo, R. C. Lamb, T. H. Markert, and J. A. Paul. Einstein X-ray identification of the variable radio star LS I +61 303. *Astrophysical Journal Letters*, 247:L85–L88, July 1981.

[224] M. Chernyakova, A. Neronov, and R. Walter. INTEGRAL and XMM-Newton observations of LS I +61 303. *Monthly Notices of the Royal Astronomical Society*, 372(4):1585–1592, November 2006.

[225] F. A. Harrison, P. S. Ray, D. A. Leahy, E. B. Waltman, and G. G. Pooley. Simultaneous X-ray and radio monitoring of the unusual binary LS I +61o303: Measurements of the light curve and high-energy spectrum. *The Astrophysical Journal*, 528(1):454–461, January 2000.

[226] M. Chernyakova, A. Neronov, S. Molkov, et al. Superorbital modulation of X-ray emission from gamma-ray binary LS I +61 303. *The Astrophysical Journal*, 747(2):L29, February 2012.

[227] Jian Li, Diego F. Torres, Shu Zhang, et al. Unveiling the super-orbital modulation of LS I +61°303 in X-rays. *The Astrophysical Journal*, 744(1):L13, December 2011.

[228] A. Smith, P. Kaaret, J. Holder, et al. Long-term X-ray monitoring of the TeV binary LS I +61 303 with the Rossi X-ray Timing Explorer. *The Astrophysical Journal*, 693(2):1621–1627, March 2009.

[229] R. van Dijk, K. Bennett, H. Bloemen, et al. COMPTEL detection of the high-energy γ-ray source 2CG 135+01. *Astronomy & Astrophysics*, 315:485–492, November 1996.

[230] P. C. Gregory and A. R. Taylor. New highly variable radio source, possible counterpart of γ-ray source CG135+1. *Nature*, 272(5655):704–706, April 1978.

[231] P. C. Gregory, M. Peracaula, and A. R. Taylor. Bayesian periodic signal detection. II. discovery of periodic phase modulation in LS I +61 303 radio outbursts. *The Astrophysical Journal*, 520(1):376–390, July 1999.

[232] P. C. Gregory. Bayesian analysis of radio observations of the Be X-ray binary LS I +61 303. *The Astrophysical Journal*, 575(1):427–434, August 2002.

[233] M. Massi and M. Kaufman Bernadó. Radio spectral index analysis and classes of ejection in LS I +61°303. *The Astrophysical Journal*, 702(2):1179–1189, September 2009.

[234] Vivek Dhawan, Amy Mioduszewski, and M. Rupen. LS I +61 303 is a Be-Pulsar binary, not a Microquasar. In *VI Microquasar Workshop: Microquasars and Beyond*, page 52.1, January 2006.

[235] Christina Aragona, M. Virginia McSwain, and Michaël De Becker. HD 259440: The proposed optical counterpart of the γ-ray binary HESS J0632+057. *The Astrophysical Journal*, 724(1):306–312, November 2010.

[236] F. A. Aharonian, A. G. Akhperjanian, A. R. Bazer-Bachi, et al. Discovery of a point-like very-high-energy γ-ray source in Monoceros. *Astronomy & Astrophysics*, 469(1):L1–L4, March 2007.

[237] V. A. Acciari, E. Aliu, T. Arlen, et al. Evidence for long-term gamma-ray and X-ray variability from the unidentified TeV source HESS J0632+057. *The Astrophysical Journal Letters*, 698(2):L94–L97, June 2009.

[238] S. D. Bongiorno, A. D. Falcone, M. Stroh, et al. A new TeV binary: The discovery of an orbital period in HESS J0632+057. *The Astrophysical Journal Letters*, 737(1):L11, August 2011.

[239] E. Aliu, S. Archambault, T. Aune, et al. Long-term TeV and X-ray observations of the gamma-ray binary HESS J 0632+057. *The Astrophysical Journal*, 780(2):168, December 2013.

[240] G. Maier and VERITAS Collaboration. VHE observations of galactic binary systems with VERITAS. In *35th International Cosmic Ray Conference (ICRC2017)*, volume 301 of *International Cosmic Ray Conference*, page 729, January 2017.

[241] Jian Li, Diego F. Torres, K. S. Cheng, et al. GeV Detection of HESS J0632+057. *The Astrophysical Journal*, 846(2):169, September 2017.

[242] J. A. Hinton, J. L. Skilton, S. Funk, et al. HESS J0632+057: a new gamma-ray binary? *The Astrophysical Journal Letters*, 690(2):L101–L104, January 2009.

[243] E. Aliu, S. Archambault, T. Aune, et al. Long-term TeV and X-ray observations of the gamma-ray binary HESS J0632+057. *The Astrophysical Journal*, 780(2):168, January 2014.

[244] Denys Malyshev, Maria Chernyakova, Andrea Santangelo, and Gerd Pühlhofer. Decade-long X-ray observations of HESS J0632+057. *Astronomische Nachrichten*, 340(6):465–474, July 2019.

[245] J. L. Skilton, M. Pandey-Pommier, J. A. Hinton, et al. The radio counterpart of the likely TeV binary HESS J 0632+057. *Monthly Notices of the Royal Astronomical Society*, 399(1):317–322, October 2009.

[246] J. Moldón, M. Ribó, and J. M. Paredes. Revealing the extended radio emission from the gamma-ray binary HESS J0632+057. *Astronomy & Astrophysics*, 533:L7, September 2011.

[247] Fermi LAT Collaboration, M. Ackermann, M. Ajello, et al. Periodic emission from the gamma-ray binary 1FGL J1018.6-5856. *Science*, 335(6065):189, January 2012.

[248] H. E. S. S. Collaboration, A. Abramowski, F. Acero, et al. Discovery of VHE emission towards the Carina arm region with the H.E.S.S. telescope array: HESS J1018-589. *Astronomy & Astrophysics*, 541:A5, May 2012.

[249] Hongjun An, Eric Bellm, Varun Bhalerao, et al. Broadband X-ray properties of the gamma-ray binary 1FGL J1018.6-5856. *The Astrophysical Journal*, 806(2):166, June 2015.

[250] HESS Collaboration, H. Abdalla, A. Abramowski, et al. Detection of variable VHE γ-ray emission from the extra-galactic γ-ray binary LMC P3. *Astronomy & Astrophysics*, 610:L17, March 2018.

[251] M. Ackermann, A. Albert, W. B. Atwood, et al. Deep view of the Large Magellanic Cloud with six years of Fermi-LAT observations. *Astronomy & Astrophysics*, 586:A71, January 2016.

[252] R. H. D. Corbet, L. Chomiuk, M. J. Coe, et al. A luminous gamma-ray binary in the Large Magellanic Cloud. *The Astrophysical Journal*, 829(2):105, October 2016.

[253] Philip Massey and A. B. Thompson. Massive stars in CYG OB2. *Astronomical Journal*, 101:1408, April 1991.

[254] Daniel C. Kiminki, Henry A. Kobulnicky, Carlos A. Vargas Álvarez, Michael J. Alexander, and Michael J. Lundquist. Predicting GAIA's parallax distance to the Cygnus OB2 association with eclipsing binaries. *The Astrophysical Journal*, 811(2):85, September 2015.

[255] C.-Y. Ng, W. C. G. Ho, E. V. Gotthelf, et al. X-ray and radio variabilities of PSR J2032+4127 near periastron. *The Astrophysical Journal*, 880(2):147, August 2019.

[256] Partha Sarathi Pal, P. H. T. Tam, Y. Cui, et al. X-ray spectral evolution of PSR J2032+4127 during the 2017 periastron passage. *The Astrophysical Journal*, 882(1):25, August 2019.

[257] HESS Collaboration, A. Abramowski, F. Acero, et al. Discovery of the VHE gamma-ray source HESS J1832-093 in the vicinity of SNR G22.7-0.2. *Monthly Notices of the Royal Astronomical Society*, 446(2):1163–1169, January 2015.

[258] P. Eger, H. Laffon, P. Bordas, et al. Discovery of a variable X-ray counterpart to HESS J1832-093: a new gamma-ray binary? *Monthly Notices of the Royal Astronomical Society*, 457(2):1753–1758, April 2016.

[259] Pak-Hin Thomas Tam, K. K. Lee, Yudong Cui, et al. A multiwavelength study of the γ-ray binary candidate HESS J1832-093. *The Astrophysical Journal*, 899(1):75, August 2020.

[260] G. Martí-Devesa and O. Reimer. X-ray and γ-ray orbital variability from the γ-ray binary HESS J1832-093. *Astronomy & Astrophysics*, 637:A23, May 2020.

[261] Aous A Abdo, Markus Ackermann, Marco Ajello, et al. Fermi large area telescope first source catalog. *The Astrophysical Journal Supplement Series*, 188(2):405, 2010.

[262] RHD Corbet, L Chomiuk, MJ Coe, et al. Discovery of the galactic high-mass gamma-ray binary 4FGL J1405. 1- 6119. *The Astrophysical Journal*, 884(1):93, 2019.

[263] R Schlickeiser and J Ruppel. Klein–Nishina steps in the energy spectrum of galactic cosmic-ray electrons. *New Journal of Physics*, 12(3):033044, March 2010.

[264] Rafał Moderski, Marek Sikora, Paolo S. Coppi, and Felix Aharonian. Klein-Nishina effects in the spectra of non-thermal sources immersed in external radiation fields. *Monthly Notices of the Royal Astronomical Society*, 363(3):954–966, November 2005.

[265] Robert J. Gould and Gérard P. Schréder. Pair production in photon-photon collisions. *Phys. Rev.*, 155:1404–1407, March 1967.

[266] Iurii Sushch and Brian van Soelen. Gamma–gamma absorption in the γ-ray binary system PSR B 1259-63/LS 2883. *The Astrophysical Journal*, 837(2):175, March 2017.

[267] G. Dubus, B. Cerutti, and G. Henri. The modulation of the gamma-ray emission from the binary LS 5039. *Astronomy & Astrophysics*, 477(3):691–700, November 2007.

[268] Markus Böttcher and Charles D. Dermer. Photon-photon absorption of very high energy gamma rays from microquasars: Application to LS 5039. *The Astrophysical Journal*, 634(1):L81–L84, November 2005.

[269] G. Dubus. Gamma-ray absorption in massive X-ray binaries. *Astronomy & Astrophysics*, 451(1):9–18, April 2006.

[270] W. Bednarek. Cascade initiated by VHE γ-rays in the radiation field of a close massive companion. *Astronomy & Astrophysics*, 322:523–532, June 1997.

[271] D. Khangulyan, F. Aharonian, and V. Bosch-Ramon. On the formation of TeV radiation in LS 5039. *Monthly Notices of the Royal Astronomical Society*, 383(2):467–478, January 2008.

[272] V. Bosch-Ramon, D. Khangulyan, and F. A. Aharonian. Non-thermal emission from secondary pairs in close TeV binary systems. *Astronomy & Astrophysics*, 482(2):397–402, February 2008.

[273] C. F. Kennel and F. V. Coroniti. Confinement of the Crab pulsar's wind by its supernova remnant. *The Astrophysical Journal*, 283:694–709, August 1984.

[274] G. Dubus, B. Cerutti, and G. Henri. Relativistic doppler-boosted emission in gamma-ray binaries. *Astronomy and Astrophysics*, 516:A18, June 2010.

[275] Ben Margalit and Brian D. Metzger. Constraining the maximum mass of neutron stars from multi-messenger observations of GW170817. *The Astrophysical Journal*, 850(2):L19, November 2017.

[276] G. Dubus. Gamma-ray binaries: pulsars in disguise? *Astronomy & Astrophysics*, 456(3):801–817, September 2006.

[277] F Aharonian, L Anchordoqui, D Khangulyan, and T Montaruli. Microquasar LS 5039: a TeV gamma-ray emitter and a potential TeV neutrino source. *Journal of Physics: Conference Series*, 39:408–415, May 2006.

[278] A. A. Abdo, M. Ackermann, M. Ajello, et al. Detection of 16 gamma-ray pulsars through blind frequency searches using the Fermi LAT. *Science (80-.).*, 325(5942):840–844, 2009.

[279] Fernando Camilo, Paul S Ray, Scott M Ransom, et al. Radio detection of LAT PSRs J1741–2054 and J2032+ 4127: no longer just gamma-ray pulsars. *The Astrophysical Journal*, 705(1):1, 2009.

[280] A. G. Lyne, B. W. Stappers, M. J. Keith, et al. The binary nature of PSR J2032+4127. *Monthly Notices of the Royal Astronomical Society*, 451(1):581–587, 05 2015.

[281] N. Gehrels. The swift gamma-ray burst mission. In *AIP Conference Proceedings*. AIP, 2004.

[282] David N. Burrows, J. E. Hill, J. A. Nousek, et al. The Swift X-Ray Telescope. *Space Science Reviews*, 120(3-4):165–195, October 2005.

[283] NASA High Energy Astrophysics Science Archive Research Center (HEASARC).

[284] K. A. Arnaud. *XSPEC: The First Ten Years*, volume 101 of *Astronomical Society of the Pacific Conference Series*, page 17. 1996.

[285] J. Aleksić, S. Ansoldi, L. A. Antonelli, et al. The major upgrade of the MAGIC telescopes, Part II: A performance study using observations of the Crab Nebula. *Astroparticle Physics*, 72:76–94, January 2016.

[286] G. Maier and J. Holder. Eventdisplay: An analysis and reconstruction package for ground-based gamma-ray astronomy. In *35th International Cosmic Ray Conference (ICRC2017)*, volume 301 of *International Cosmic Ray Conference*, page 747, January 2017.

[287] R. Bird. PSR J2032+4127, the counterpart of TeV J2032+4130? multiwavelength monitoring of the approach to periastron. In *proceedings of the 35th International Cosmic Ray Conference (ICRC2017)706*, January 2017.

[288] O. Helene. Upper limit of peak area. *Nuclear Instruments and Methods in Physics Research*, 212(1):319 – 322, 1983.

[289] Alice K. Harding and T. K. Gaisser. Acceleration by pulsar winds in binary systems. *The Astrophysical Journal*, 358:561, August 1990.

[290] Marco Tavani and Jonathan Arons. Theory of high-energy emission from the pulsar/Be star system PSR 1259-63. I. radiation mechanisms and interaction geometry. *The Astrophysical Journal*, 477(1):439–464, March 1997.

[291] M Petropoulou, G Vasilopoulos, I M Christie, D Giannios, and M J Coe. X-ray mapping of the stellar wind in the binary PSR J 2032+4127/MT91 213. *Monthly Notices of the Royal Astronomical Society: Letters*, 474(1):L22–L26, November 2017.

[292] D. Khangulyan, S. Hnatic, F. Aharonian, and S. Bogovalov. TeV light curve of PSR B1259-63/SS2883. *Monthly Notices of the Royal Astronomical Society*, 380(1):320–330, September 2007.

[293] J. Takata, A. T. Okazaki, S. Nagataki, et al. Modeling high-energy light curves of the PSR B1259-63/LS 2883 binary based on 3D SPH simulations. *The Astrophysical Journal*, 750(1):70, April 2012.

[294] I. Sushch. Probing orbital parameters of gamma-ray binaries with TeV light curves. In *proceedings of the 36th International Cosmic Ray Conference (ICRC2019)1178*, 2019.

[295] M. Kerschhaggl. TeV flux modulation in PSR B1259-63/LS2883. *Astronomy & Astrophysics*, 525:A80, December 2010.

[296] Yasunobu Uchiyama, Takaaki Tanaka, Tadayuki Takahashi, Koji Mori, and Kazuhiro Nakazawa. Suzaku observations of PSR B 1259-63: a new manifestation of relativistic pulsar wind. *The Astrophysical Journal*, 698(1):911–921, May 2009.

[297] Włodek Bednarek, Piotr Banasiński, and Julian Sitarek. Gamma-rays from the binary system containing PSR J2032+4127 during its periastron passage. *Journal of Physics G: Nuclear and Particle Physics*, 45(1):015201, December 2017.

[298] Andrii Neronov and Maria Chernyakova. Radio-to-TeV γ-ray emission from PSR B1259-63. *Astrophysics and Space Science*, 309(1-4):253–259, April 2007.

[299] T. P. Li and Y. Q. Ma. Analysis methods for results in gamma-ray astronomy. *Astrophysical Journal*, 272:317–324, September 1983.

[300] J. Michael Burgess, Henrike Fleischhack, Giacomo Vianello, et al. The Multi-Mission Maximum Likelihood framework (3ML). November 2021.

[301] Axel Donath, Régis Terrier, Quentin Remy, et al. Gammapy: A Python package for gamma-ray astronomy. *Astronomy & Astrophysics*, 678:A157, October 2023.

[302] Jea Knödlseder, M Mayer, C Deil, et al. Gammalib and ctools—a software framework for the analysis of astronomical gamma-ray data. *Astronomy & Astrophysics*, 593:A1, 2016.

[303] A. M. Read, S. R. Rosen, R. D. Saxton, and J. Ramirez. A new comprehensive 2D model of the point spread functions of the XMM-Newton EPIC telescopes: spurious source suppression and improved positional accuracy. *Astronomy & Astrophysics*, 534:A34, October 2011.

[304] J. Cardenzana. *A 3D maximum likelihood analysis for studying highly extended sources in VERITAS data*. PhD thesis, Iowa State University, 2017.

[305] J. R. Mattox, D. L. Bertsch, J. Chiang, et al. The likelihood analysis of EGRET data. *The Astrophysical Journal*, 461:396, April 1996.

[306] A. U. Abeysekara, A. Albert, R. Alfaro, et al. Measurement of the Crab Nebula spectrum past 100 TeV with HAWC. *The Astrophysical Journal*, 881(2):134, August 2019.

[307] K. Meagher and VERITAS Collaboration. Six years of VERITAS observations of the Crab Nebula. In *34th International Cosmic Ray Conference (ICRC2015)*, volume 34 of *International Cosmic Ray Conference*, page 792, July 2015.

[308] J. Aleksić, S. Ansoldi, L. A. Antonelli, et al. Measurement of the Crab Nebula spectrum over three decades in energy with the MAGIC telescopes. *Journal of High Energy Astrophysics*, 5:30–38, March 2015.

[309] R. Alfaro, C. Alvarez, J. C. Arteaga-Velázquez, et al. Understanding the emission and morphology of the unidentified gamma-ray source TeV J2032+4130. *arXiv e-prints*, page arXiv:2407.02879, July 2024.

[310] Wolfgang A Rolke, Angel M López, and Jan Conrad. Limits and confidence intervals in the presence of nuisance parameters. *Nuclear Instruments and Methods in Physics Research Section A: Accelerators, Spectrometers, Detectors and Associated Equipment*, 551(2-3):493–503, 2005.

[311] T. M. Tauris and E. P. J. van den Heuvel. Formation and evolution of compact stellar X-ray sources. In Walter H. G. Lewin and Michiel van der Klis, editors, *Compact stellar X-ray sources*, volume 39, pages 623–665. 2006.

[312] CTA Consortium et al. *Science with the Cherenkov Telescope Array*. World Scientific, 2018.

[313] G. Maier, L. Arrabito, K. Bernlöhr, et al. Performance of the Cherenkov Telescope Array. In *35th International Cosmic Ray Conference (ICRC2017)*, volume 301 of *International Cosmic Ray Conference*, page 846, July 2017.

[314] R. White, J. P. Amans, D. Berge, et al. The small-sized telescopes for the southern site of the Cherenkov Telescope Array. In *37th International Cosmic Ray Conference*, page 728, March 2022.

[315] J.A. Barrio. Status of the large size telescopes and medium size telescopes for the cherenkov telescope array observatory. *Nuclear Instruments and Methods in Physics Research Section A: Accelerators, Spectrometers, Detectors and Associated Equipment*, 952:161588, 2020. 10th International Workshop on Ring Imaging Cherenkov Detectors (RICH 2018).

[316] Federico Di Pierro et al. Status of the large-sized telescope of the cherenkov telescope array. In *Journal of Physics: Conference Series*, volume 2429, page 012020. IOP Publishing, 2023.

[317] Werner Hofmann and Roberta Zanin. The Cherenkov Telescope Array. In *Handbook of X-ray and Gamma-ray Astrophysics*, pages 2787–2833. Springer, 2024.

[318] JS Lapington, CTA SST Collaboration, et al. The silicon photomultiplier-based camera for the Cherenkov Telescope Array small-sized telescopes. *Nuclear Instruments and Methods in Physics Research Section A: Accelerators, Spectrometers, Detectors and Associated Equipment*, 1055:168433, 2023.

[319] Pierre Colin and Stephan LeBohec. Optimization of large homogeneous air Cherenkov arrays and application to the design of a 1–100 TeV γ-ray observatory. *Astroparticle Physics*, 32(5):221–230, 2009.

[320] O. Gueta. The Cherenkov Telescope Array: layout, design and performance. In *37th International Cosmic Ray Conference*, page 885, March 2022.

[321] Giulia Pagliaroli, Saqib Hussain, Vittoria Vecchiotti, and Francesco Lorenzo Villante. The galactic population of pulsar wind nebulae and the contribution of its unresolved component to the diffuse high-energy gamma-ray emission. *Universe*, 9(9), 2023.

[322] M Chernyakova, D Malyshev, Adamantia Paizis, et al. Overview of non-transient γ-ray binaries and prospects for the Cherenkov Telescope Array. *Astronomy & Astrophysics*, 631:A177, 2019.